

# The circuit basis of olfactory mate recognition and localisation

István Taisz

Peterhouse

Neurobiology Division  
MRC Laboratory of Molecular Biology

A thesis submitted to the University of Cambridge  
for the degree of Doctor of Philosophy

30 June 2021

“Én azt tapasztaltam, hogyha a hegyet előnytelen oldalon mászzuk meg, az sem elveszett munka, mert mászás közben igen sokat tanulhatunk, olyat is, amit emberek, akik hibát nem követnek el, sohasem tudhatnak meg.”

“In my experience, climbing a mountain from the wrong side is not a futile effort. As we climb, we learn things that someone who never made that mistake, would never have known.”

— György Békésy

## **Preface**

All the work described in this thesis was carried out in the Neurobiology Division of the Medical Research Council Laboratory of Molecular Biology under the supervision of Dr Gregory S.X.E Jefferis. All the experiments and analysis were conducted from October 2017 to June 2021.

This thesis has not been submitted, in whole or in part, for a degree, diploma or any other qualification at the University of Cambridge or any other university. The dissertation does not exceed 60,000 words, excluding figures, tables, appendices and bibliography, as specified by the Degree Committee.

I, István Taisz, declare that the words and data analysis presented in this thesis is the result of my own, independent work, unless otherwise stated. Due to the collaborative nature of this project, this work contains behavioural and anatomical data generated and kindly provided by Dr Dana Galili. Dr Erika Donà contributed a genetic driver line and anatomical data. Shanice Bailey, William Morris, Irene Varela, Kimberly Meechan, Katie Stevens, and Kai Liang took part in reconstructing neuron morphologies in an EM dataset for this project; all research assistants in the Wellcome Drosophila Connectomics group hosted at the Department of Zoology and managed by Dr Marta Costa. I take care to note my use of others' efforts in the following text.

*István Taisz, June 2021*

## Acknowledgements

I am deeply grateful to Greg Jefferis, my supervisor, for giving me the opportunity to learn from him, and for giving me the freedom to pursue any question, method, or course I was interested in. Your endless knowledge and rigorous scientific thinking paired with genuine kindness and attention to people set an example that I can only hope to live up to. Thank you for your continuous support and guidance.

I would like to thank Dana Galili for all the energy, encouragement, and discussions we had throughout our work together. Thank you for helping me get started in the lab, probably the hardest task in my PhD. I learned a lot from working with you.

Special thanks to Alex Bates, Marina Gkantia, and Philip Myers for your friendship. Our trips to Torquay, Little Snoring, and Budapest are strangely my fondest memories of Cambridge.

A huge thank you to all the other members of the lab. Seba Cachero, Erika Donà, Shahar Frechter, Markus Pleijzier, Philipp Schlegel, Bella Beckett you made my days in the lab easy regardless of what happened with experiments. Thank you for giving me a sense of community, and for never hesitating to answer my questions or give insightful comments on my work.

Thank you to all members of the Drosophila Connectomics Group at Zoology, especially to those, with essential contributions to this work. Shanice Bailey, Billy Morris, Irene Varela, Kimberly Meechan, Katie Stevens, and Kai Liang together have reconstructed a substantial proportion of neurons shown in this work.

I would like to thank Csaba Sóti, Péter Csermely, and Zoltán Antal, my mentors in Hungary, for nurturing my scientific interest, and encouraging me to think independently in my research projects as an undergraduate.

I feel privileged to have attended two excellent courses, and learned about neuroscientific concepts and areas directly from experts. Thank you to every organiser, TA, student, and lecturer at the NS&B course in Woods Hole, and the Cajal Course on Behaviour of Neural Systems in Lisbon. These experiences taught me that science is best when it is creative, fun, and collaborative. A special thanks to Woods Hole TAs Stephen Holtz, and Yvette Fisher for their inspiring way of thinking, and their continuous help with my questions since.

Thank you to Amalia Braun, for her support, and for all our conversations.

Lastly, I would like to thank my family and friends in Hungary, for always making me feel home in Budapest. Thank you to my parents, my grandparents, and my sisters for creating an environment where I could aspire to do the things I find most interesting.

# Summary

István Taisz

## The circuit basis of olfactory mate recognition and localisation

Finding a mate has two essential steps: recognising an appropriate partner and locating it. Sex pheromones are used in solving both tasks; they carry qualitative information to recognise, and positional information to locate a mate. How does the brain extract both a qualitative and a quantitative message from a single signal, like a pheromone smell?

We used the pheromone sensing circuit of *Drosophila melanogaster* as a model to understand how such a signal is processed in the brain and how that instructs sexual behaviours. We used connectomics, functional imaging, and behavioural tests to investigate the anatomy and function of a circuitry dedicated to processing cis-vaccenyl acetate (cVA) a male pheromone signal. We discovered a previously unknown second order projection neuron class (PN) that senses cVA, and relays this signal to a neural hub for sexual behaviours - including female receptivity. We imaged the activity of sensory neurons and second order PNs in the cVA pathway while presenting the female with a male fly at defined positions and asked what features of the stimulus can be decoded from neuronal activity. We show that both sensory neurons and PNs carry information about male position by cell type-specific distance tuning properties and lateralisation ability. Additionally, we found an interneuron that is only activated by contralateral input and is well placed in the circuit to create mutual inhibition between the two sides. We propose that this mechanism underlies improved lateralisation in PNs compared to sensory neurons.

To further understand cVA processing we characterised the responses of two third-order neurons. We found that one is selectively tuned to an approaching male, and the response magnitude is strongly dependent on approach speed. A second, previously described, sexually dimorphic third-order neuron receives taste input besides cVA, and integrates these signals at its dendrites. Following the flow of information downstream of the taste and cVA integrating neurons we discovered a layered axo-axonic circuit; this layout suggests a hierarchical gating of different sensory modalities. Through connectomics and functional experiments, we showed that signals from the abdominal ganglion - controlling reproductive organs - and leg muscle load information enter this axo-axonic motif, and that manipulating any of these neurons during behaviour affects female receptivity bidirectionally.

These findings together extend our understanding of cVA's function as a pheromone that signals positional information. Supporting this function we propose an olfactory lateralisation mechanism previously unknown in *Drosophila*. Our observations about third order neurons suggest that quantitative and qualitative signals are separated at the third layer of cVA processing and that integrating other relevant modalities plays a role in this separation.

## List of Figures and Tables

Figure 1: Architecture of olfactory systems and cVA processing	20
Figure 2: Genetic and connectomic tools in flies	26
Figure 3: A novel PN pathway for cVA	45
Figure 4: Presenting a male fly as an olfactory stimulus	47
Figure 5: ORNs, IPNs, and lvPNs respond to a male fly in a distance dependent manner	49
Figure 6: cVA lateralisation in ORNs does not depend on bilateral input	57
Figure 7: cVA lateralisation in IPNs depends on bilateral input	59
Figure 8: i13LN6 shows bilateral contrast with larger contralateral responses	61
Figure 9: i13LN6, a candidate ALLN for enhancing odour lateralisation	63
Figure 10: IPNs encode angular position	65
Figure 11: Decoding male position from left and right IPN responses	67
Figure 12: AV2a2 responds to male approach in a speed dependent manner	73
Figure 13: AV2a2 responses correlate with the speed of IPN activity change	75
Figure 14: pC1 shows sustained responses to cVA, similarly to presynaptic lvPNs	77
Figure 15: Parallel pheromone pathways have distinct effects on female receptivity	79
Figure 16: Sensory integration steps in cVA processing	87
Figure 17: The aSP-g clone consists of three morphological subtypes	89
Figure 18: aSP-g integrates taste inputs with cVA	91
Figure 19: aSP-g controls female receptivity independent of pC1	93
Figure 20: A layered axo-axonic circuit downstream of aSP-g regulates female receptivity	102
Figure 21: mAL1 is a subtype of the mAL clone with inputs from an abdominal ascending neuron	104
Figure 22: dMS6 is a third-order neuron to multiple leg sensory modalities	106
Figure 23: dMS6 is activated by increased leg muscle load	108
Figure 24: An excitation-inhibition model for receptivity control by mAL1 and AVL29 via dMS6	110
Figure 25: Separation of positional and identity cues in cVA processing	121
Table 1: Fly stocks used in this study	29
Table 2: Neuron identifiers from EM datasets (FAFB, hemibrain)	123
Table 3: List of synaptic weights from FAFB and hemibrain for relevant connections across cell types	127
Table 4: Neuron identifiers from the FANC EM dataset	130
Table 5: List of synaptic weights from FANC across cell types	130

# Contents

<b>Preface</b>	<b>2</b>
<b>Acknowledgements</b>	<b>3</b>
<b>Summary</b>	<b>5</b>
<b>List of Figures and Tables</b>	<b>6</b>
<b>Contents</b>	<b>7</b>
<b>Abbreviations</b>	<b>10</b>
<b>1 Introduction</b>	<b>13</b>
1.1 Extracting distinct features of a sensory stimulus	14
1.2 Sex pheromones signal mate identity and location	15
1.3 cVA processing as a model for parallel positional and identity coding	16
Figure 1: Architecture of olfactory systems and cVA processing	20
1.4 Circuit neuroscience in <i>Drosophila</i>	22
Figure 2: Genetic and connectomic tools in flies	26
<b>2 Materials and Methods</b>	<b>28</b>
2.1 Fly stocks	29
Table 1: Fly stocks used in this study	29
2.2 <i>Drosophila</i> husbandry	31
2.3 Split-GAL4 hemidriver combination screening	31
2.4 Neuron tracing in FAFB and FANC	32
2.5 Computational neuroanatomy and connectomic analysis	34
2.6 Immunohistochemistry and confocal microscopy	35
2.7 In vivo calcium imaging and stimulus presentation	35
2.8 Calcium imaging quantification and statistical analyses	38
2.9 Courtship assays and behavioural analysis	39
<b>3 Parallel pheromone pathways</b>	<b>41</b>
3.1 Characterisation of a novel cVA pathway	42
3.2 IPNs and lvPNs differ in sensitivity and adaptation properties	43
Figure 3: A novel PN pathway for cVA	45
Figure 4: Presenting a male fly as an olfactory stimulus	47
Figure 5: ORNs, IPNs, and lvPNs respond to a male fly in a distance dependent manner	49
<b>4 cVA as a positional signal</b>	<b>51</b>
4.1 A male fly is a lateralised olfactory stimulus	52
4.2 IPN lateralisation is dependent on an active mechanism	53
4.3 <i>il3LN6</i> , a candidate for contralateral inhibition	54

4.4. Decoding position from a pheromone signal	55
<b>5 Separation of positional and identity information at third order neurons</b>	<b>69</b>
5.1 Extracting male approach speed information from cVA	70
5.2 Tonic cVA response persists downstream of lvPNs	71
5.3 Distinct behavioural effects by positional and identity signals	71
Figure 12: AV2a2 responds to male approach in a speed dependent manner	73
Figure 13: AV2a2 responses correlate with the speed of IPN activity change	75
Figure 14: pC1 shows sustained responses to cVA, similarly to presynaptic lvPNs	77
Figure 15: Parallel pheromone pathways have distinct effects on female receptivity	79
<b>6 Multimodal sensory integration increases signal specificity</b>	<b>81</b>
6.1 aSP-g integrates smell and taste	83
6.2 aSP-g increases female receptivity via a pC1 independent pathway	85
Figure 16: Sensory integration steps in cVA processing	87
Figure 17: The aSP-g clone consists of three morphological subtypes	89
Figure 18: aSP-g integrates taste inputs with cVA	91
Figure 19: aSP-g controls female receptivity independent of pC1	93
<b>7 A layered axo-axonic circuit for hierarchical processing of multimodal signals</b>	<b>95</b>
7.1 Behavioural dissection of an axo-axonic circuit	96
7.2 Characterisation of mAL1 and dMS6 inputs	97
7.3 A model for receptivity control by hierarchical sensory integration	100
Figure 20: A layered axo-axonic circuit downstream of aSP-g regulates female receptivity	102
Figure 21: mAL1 is a subtype of the mAL clone with inputs from an abdominal ascending neuron	104
Figure 22: dMS6 is a third-order neuron to multiple leg sensory modalities	106
Figure 23: dMS6 is activated by increased leg muscle load	108
Figure 24: An excitation-inhibition model for receptivity control by mAL1 and AVLP29 via dMS6	110
<b>8 Discussion</b>	<b>111</b>
8.1 Olfactory positional coding	112
8.2 Separate pathways for what and where	116
8.3 Dendritic and axonal sensory integration steps shape sexual decision making	118
Figure 25: Separation of positional and identity cues in cVA processing	122
Table 2: Neuron identifiers from EM datasets (FAFB, hemibrain)	123
Table 3: List of synaptic weights from FAFB and hemibrain for relevant connections across cell types	127
Table 4: Neuron identifiers from the FANC EM dataset	130
Table 5: List of synaptic weights from FANC across cell types	130
<b>9 References</b>	<b>131</b>



## Abbreviations

abdSMP	abdominal (to) superior medium protocerebrum neuron
Ach	Acetyl-choline
AD	Activation Domain
AL	Antennal Lobe
ALLN	Antennal Lobe Local Neuron
AN	Ascending Neuron
AON	Anterior Olfactory Nucleus
asc-Ms	ascending-Mesothoracic neuron
BDSC	Bloomington Drosophila Stock Center
CATMAID	Collaborative Annotation Toolkit for Massive Amounts of Image Data
cfRN	campaniform (sensillum) Receptor Neuron
CMTK	Computational Morphometry Toolkit
CNS	Central Nervous System
cVA	cis-vaccenyl acetate
DA1	Dorsal Anterior (glomerulus) 1
DBD	DNA-binding domain
DN	Descending Neuron
EM	Electron Microscopy
FAFB	Full Adult Female Brain
FANC	Full Adult Nerve Cord
FCWB	FlyCircuit Whole Brain
FIBSEM	Focussed Ion-Beam Scanning Electron Microscopy
FLP	Flippase
FRT	Flippase Recognition Site
G2N-SLP1	Gustatory second-order Neuron to Superior Lateral Protocerebrum
GABA	$\gamma$ -aminobutyric acid
GFP	Green Fluorescent Protein
GNG	Gnathal Ganglion
GRN	Gustatory Receptor Neuron
Ir94e	Ionotropic receptor 94e
IS2	Intersex 2 <i>D. melanogaster</i> template brain

JAABA	Janelia Automatic Animal Behaviour Annotator
Kir2.1	Inwardly-rectifying potassium channel 2.1
LC4	Lobula Column 4
LED	Light Emitting Diode
IGRN	labellar Gustatory Receptor Neuron
LH	Lateral Horn
LN	Local Neuron
LPLC2	Lobula Plate Lobula Column 2
IPN	lateral Projection Neuron
lvPN	lateroventral Projection Neuron
MARCM	Mosaic Analysis with a Repressible Cell Marker
MB	Mushroom Body
MCFO	Multi-Colour Flip-Out
MIP	Mean Intensity Projection
ML	methyl-laurate
NBLAST	Neuron-BLAST (Basic Local Alignment Search Tool)
OR67d	Olfactory receptor 67d
OR75a	Olfactory receptor 75a
ORN	Olfactory Receptor Neuron
pGRN	pharyngeal Gustatory Receptor Neuron
PMT	Photomultiplier Tube
PN	Projection Neuron
ROI	Region of Interest
SEM	Standard Error of the Mean
SIP	Superior Intermediate Protocerebrum
SLP	Superior Lateral Protocerebrum
SMP	Superior Medial Protocerebrum
ssTEM	serial section Transmission Electron Microscopy
T1	Thoracic (segment) 1
T2	Thoracic (segment) 2
T3	Thoracic (segment) 3
UAS	Upstream Activating Segment
VNC	Ventral Nerve Cord
vpoDN	vaginal plate opening Descending Neuron

vpoEN	vaginal plate opening Excitatory Neuron
vpoIN	vaginal plate opening Inhibitory Neuron
VT	Vienna Tiles - driver line collection

# 1 Introduction

This work aims to understand how (i) a brain can extract and encode two different aspects of the same sensory stimulus, and (ii) how these aspects instruct specific behaviours. In this introduction, I lay out why I have chosen to examine this phenomenon using an olfactory pheromone of *Drosophila melanogaster* that guides courtship behaviours. Olfaction, and specifically, sparsely tuned odour channels provide an entry point to investigate sensory processing with known signal identity at deeper circuit layers. Therefore I chose sex pheromones, signalling mate identity and location, with dedicated olfactory pathways to uncover how these features of a stimulus are encoded in the brain. I briefly introduce sex pheromones and their behavioural role as first described in moth species, and discuss the function and processing of a male pheromone of *Drosophila melanogaster* in detail. Finally, I provide an overview of the extremely powerful genetic and connectomic tools uniquely available in the vinegar fly, *Drosophila melanogaster* that allow us to probe our question at multiple levels of neuroscientific investigation.

## **1.1 Extracting distinct features of a sensory stimulus**

Sensory stimuli carry information about their identity, timing, intensity, and location (Fechner 1860). Sensory systems translate such stimuli to an efficient neural code representing these features to instruct behaviour (Laughlin 1981; Heng, Woodford, and Polania 2020). Out of these four characteristics of a signal, timing is encoded most trivially: neurons are active when the stimulus is either present or absent, often with specific neurons responding to stimulus onset and offset. The next aspect, stimulus intensity and its coding may provide the most successful example of understanding a part of the neural code: in general the higher the stimulus intensity, the higher the neuronal firing rate (Adrian and Zotterman 1926). Both timing and intensity coding have many additional layers of complexity to ensure reliable and efficient encoding of a signal. However, stimulus identity and location are different from timing and intensity, as their availability varies across sensory modalities. The sense of smell is excellent in encoding stimulus identity by relying on a wide variety of distinct receptor proteins and a combinatorial neural code (Buck and Axel 1991; Malnic et al. 1999). In contrast, the spatial arrangement and number of sensilla make olfaction suboptimal for fast and precise directional processing. Vision, on the other hand, relies on a receptor geometry that allows quick and excellent coding of stimulus location already at the sensory neurons, while identity can be only established by complex neural computations.

The visual streams of identity and location information are believed to be separately processed in mammalian brains, and the neural circuits were named the *what* and *where* pathways (Goodale and Milner 1992). The computations required to extract identity or location seem specific to the feature, arguing for separate streams during processing steps. However, creating a coherent percept about a stimulus requires a representation that encodes all of its features together. To address this problem, we use a sparsely tuned olfactory pathway – specifically activated by an odour, as this system relays the identity of the stimulus unchanged to deeper layers of sensory processing circuits.

## **1.2 Sex pheromones signal mate identity and location**

We set out to investigate this question by focussing on sex pheromone processing. Pheromones evolved to act as chemical communication channels between organisms and are widely used in the animal kingdom. Sex pheromones are specific to either males or females, therefore, they carry essential information about the sex of an individual and provide important messages for reproductive behaviours. The first described sex pheromone, bombykol, signals the identity and direction of a female moth, and males use this information to identify and locate potential mates from large distances (Butenandt, Beckmann, and Hecker 1961). Pheromonal communication is mostly used among conspecifics and evokes innate behavioural responses, implying that the circuits underlying pheromone processing are stereotyped across individuals, which facilitates neuroscientific inquiry.

The example of bombykol and similar moth pheromones have been studied extensively to understand odour navigation strategies in flying and walking moths (Kennedy and Marsh 1974; Baker et al. 1985; Takasaki, Namiki, and Kanzaki 2012). Moths turn towards pheromones as fast as a few tens of ms following the stimulus, followed by local circling search for olfactory information upon the stimulus ends. Recordings of sensory and second order neurons of the bombykol sensing pathways showed that they are able to resolve odour pulses at 10 Hz frequency (Bau, Justus, and Cardé 2002; Chu et al. 2020). Flying moths use this information to start positive anemotaxis, upwind flight, which at such large distances is a more reliable navigational signal than odour concentration gradients. In walking moths, however, it was also demonstrated that bilateral information is used to determine walking direction, suggesting that once the odour source is closer, gradient information (i.e. odour concentration difference at the antennae) is highly relevant (Takasaki, Namiki, and Kanzaki 2012). These studies are foundational to our understanding of olfactory

navigation, however, further characterisation of the underlying neural circuits and computations is limited by the lack of genetic tools to reproducibly record or manipulate specific cell types deeper in the brain. In order to understand how pheromone-based positional and identity information are processed and translated to behaviour, we can use the genetically tractable model, *Drosophila melanogaster*.

### **1.3 cVA processing as a model for parallel positional and identity coding**

Cis-vaccenyl acetate (cVA) is a male-specific pheromone in *Drosophila* produced in the ejaculatory bulbs. cVA is a low-volatility, therefore short-range pheromone, that evokes distinct behaviours in the sexes. Male flies are repulsed by cVA, their courtship is suppressed towards a fly carrying cVA, and male aggression is increased in the presence of this compound (Wang and Anderson 2010; Tachibana, Touhara, and Ejima 2015). Females, on the other hand, are attracted to the pheromone and show increased receptivity towards courting males when they sense cVA (Kurtovic, Widmer, and Dickson 2007; Ronderos and Smith 2010). Importantly, placing cVA in a behavioural chamber was sufficient to evoke these effects, suggesting that the general abundance of the odour is relevant rather than the stimulus' temporal and spatial structure.

Flies have two olfactory organs, the antennae, and the maxillary palps, which house olfactory receptor neurons (ORNs). ORNs fall into roughly 50-60 types defined by their odorant receptor expression responsible for their odour responses. The sensory neurons enter the brain and form synapses with second order projection neuron (PN) dendrites in the antennal lobe (AL). The AL is organised into discrete compartments: glomeruli, like its analogous brain region in vertebrates, the olfactory bulb. Tens of ORNs with the same receptor project into the same glomerulus, and connect to one or multiple sister PNs, most of which have glomerulus-specific dendrites (Vosshall, Wong, and Axel 2000; Stocker et al. 1990). Odour information is processed in the AL by reciprocal interactions of ORNs, PNs, and primarily inhibitory local neurons (LNs). LNs are the substrates of olfactory processing phenomena like lateral inhibition, lateral excitation, and gain control, which are achieved by a diverse set of LN cell types suggestive of specialised functions (Schlegel et al. 2021). Olfactory PNs relay information with stereotyped projection patterns to two higher-order brain centres, the mushroom body (MB), and the lateral horn (LH), which have been established as essential brain areas for learned (MB) and innate (LH) odour driven behaviours (Jefferis et al. 2007; Heisenberg et al. 1985; Dolan et al. 2018); (Figure 1A-C).

cVA is sensed by two types of olfactory receptor neurons (ORNs) housed in trichoid sensilla, Or67d and Or65a, which send this signal to DA1 and DL3 PN, respectively. Previous work has shown that Or67d ORNs and DA1 PN selectively respond to cVA, and it was proposed that this pathway functions as a labelled line for cVA (Schlief and Wilson 2007). Although male flies have more Or67d ORNs than females, resulting in a larger glomerular volume, PN responses were shown to be identical in males and females (Datta et al. 2008). While the sexually dimorphic anatomy and physiology of some third-order LH neurons have been characterised (Kohl et al. 2013; Jeanne and Wilson 2015; Ruta et al. 2010), we lack an understanding of how this signal is transformed into behaviour (Figure 1D).

A key circuit element for sexual behaviours was described to respond to cVA in female flies. These neurons, called pC1, are widely considered as master regulators of female receptivity. Indeed, they integrate the likely most salient cues of a courting male's quality: courtship song and cVA, and control the activity of vpoDNs, a descending command neuron for vaginal plate opening (Zhou et al. 2014; K. Wang et al. 2021). pC1 is one of the best known example of sexually dimorphic neurons in flies; a male specific subset of pC1 neurons, P1, is known to regulate male sexual behaviours: courtship, and aggression (Philipsborn et al. 2011; Kohatsu, Koganezawa, and Yamamoto 2011; Hoopfer et al. 2015). pC1 is one of many sexually dimorphic neurons in *Drosophila* that provided key insights into the morphology - function relationship of nervous systems. Two central transcription factors, *fruitless* and *doublesex* are members of the sex determination hierarchy, and are known to be central for sex-specific neuron morphology (Kimura et al. 2005, 2008). Investigating neurons that express either one or both of these factors has been an entry point to understand the genetic and neural basis of behavioural differences in the sexes (Demir and Dickson 2005; Rideout et al. 2010). Ever since, our understanding of sexually dimorphic neurons is growing, with a special focus on trying to provide a circuit mechanism underlying courtship (Zhang et al. 2018; McKellar et al. 2019; K. Wang et al. 2021).

The complex dialogue of a courting male and female *Drosophila* relies on most, if not all sensory modalities (Pavlou and Goodwin 2013; Aranha and Vasconcelos 2018). Male flies sample contact pheromones to select optimal courtship targets by tapping other flies with their forelegs covered by gustatory receptor neurons (GRNs; Spieth 1952; Koganezawa et al. 2010; Seeholzer et al. 2018). If the approached fly is a conspecific virgin female, the tap will be most likely followed by courtship, which includes the close following of the target and vibration of a wing to produce a species-specific set of auditory stimuli: the courtship song

(Zhang et al. 2018). If the female is receptive, it will slow down and pause more frequently, groom its abdomen, and open the vaginal plates to make copulation possible. The male modulates the chasing speed and song depending on the proximity of the female (Coen et al. 2014). After detecting signals of receptivity, the male will engage in a behavioural sequence to attempt mating: a lick of the female's genitalia, curling of the abdomen, and lifting of the forelegs to mount the female (McKellar et al. 2019). Other communication channels include abdominal vibrations (Mazzoni, Anfora, and Virant-Doberlet 2013; Fabre et al. 2012) and visual cues involved in male following behaviour (Ribeiro et al. 2018). Such an abundance of signals creates an interesting problem: females need to integrate inputs from many modalities to make a binary decision, mate or not to mate. (Spieth 1952; Koganezawa et al. 2010; Seeholzer et al. 2018)

Odours have been suggested to play an important role in the initial part of courtship in males to select ideal mating targets (Agrawal, Safarik, and Dickinson 2014), while for females, it is unclear whether cVA elicits its aphrodisiac effect at a specific phase. It is also not known how other sensory modalities are used in females to instruct the mating decision and what aspects of the cVA signal are integrated with them. When comparing the response differences to delayed bilateral antennal nerve stimulation across odour channels the cVA responsive DA1 PNs were shown to detect stimulus timing differences better than other glomeruli (Agarwal and Isacoff 2011). This feature could underlie odour localisation behaviour, as was shown for moth pheromone sensing PNs. A similar idea was proposed for the role of methyl-laurate (ML), a general fly pheromone, in guiding male courtship (Root et al. 2008).

PNs responsive to general odours were shown to be activated more strongly by ipsilateral stimulation than contralateral (Gaudry et al. 2013), and flies can detect odour direction during walking and flight (Borst and Heisenberg 1982; Duistermars, Chow, and Frye 2009). However, all these experiments required odour presentations where the stimulus was strongly lateralised artificially. The proximity of the antennae (~250  $\mu\text{m}$ ) raises the question whether a volatile stimulus can have sufficient concentration difference in space at such a short distance to evoke lateralised responses. The problem is further complicated by the fact that most ORN types (including DA1) innervate glomeruli bilaterally, relaying odour information to PNs from both antennae (Figure 1A). Although this bilateral information is biased at the level of connectivity: ipsilateral ORNs (the ones with their soma on the same side) give more inputs to PNs than contralateral ORNs (soma on the opposite side) of the

same type (Tobin, Wilson, and Lee 2017; Schlegel et al. 2021), it is unclear if detecting bilateral odour contrast – lateralisation – of naturalistic stimuli, like another fly, is possible.

Our current understanding of cVA processing and its role in female receptivity provides an entry point to study how a pheromone signal can be used both as a transient positional cue and as a signal of male identity that tonically regulates sexual behaviours.

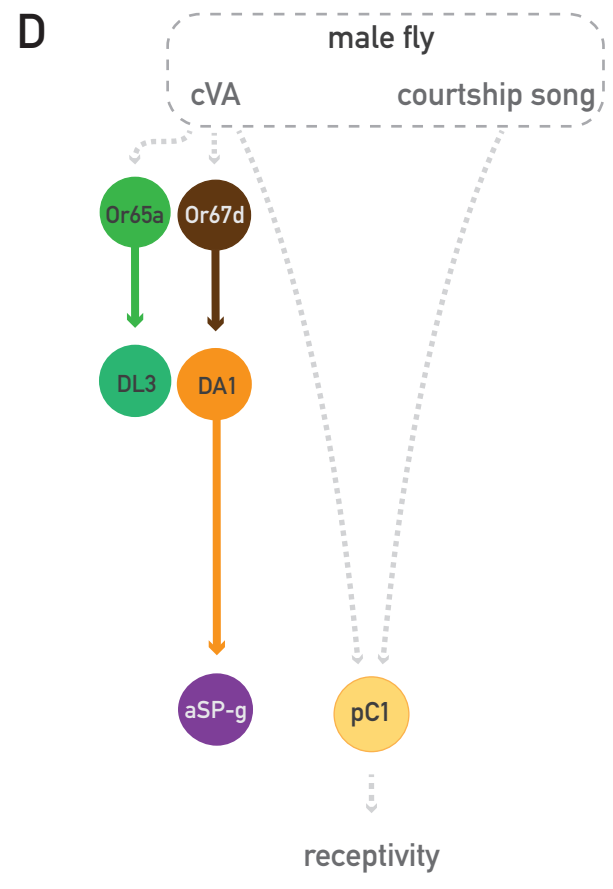
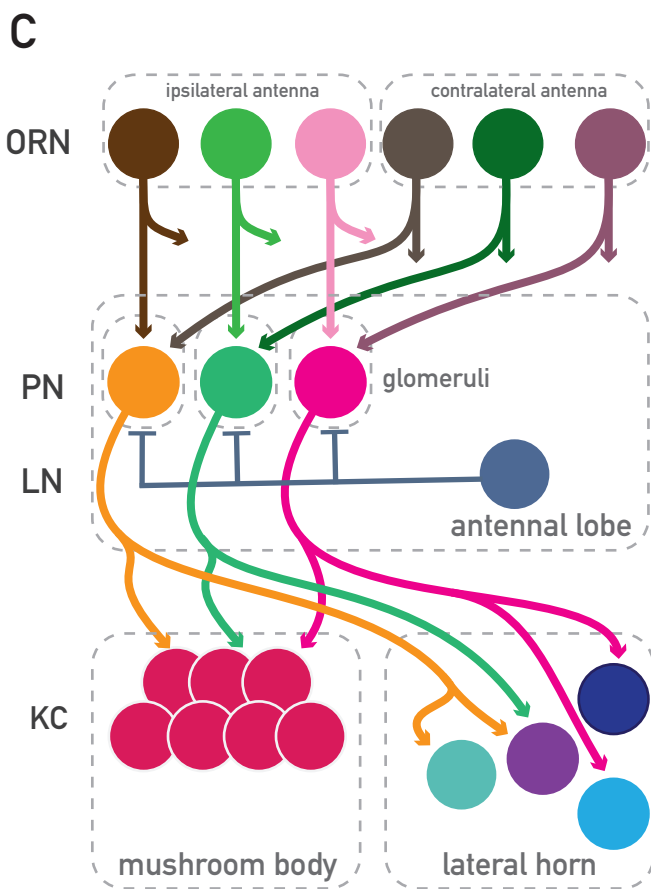
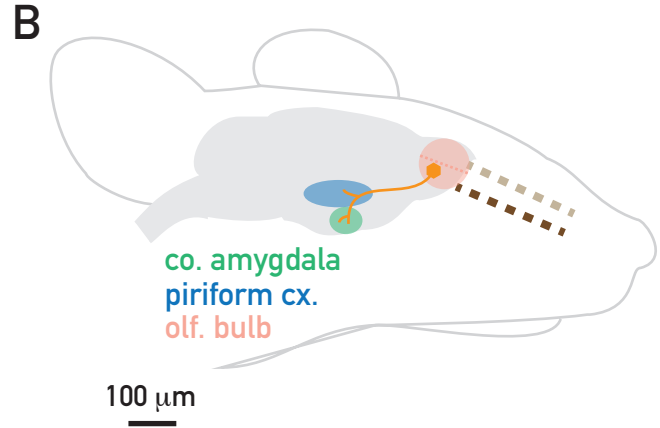
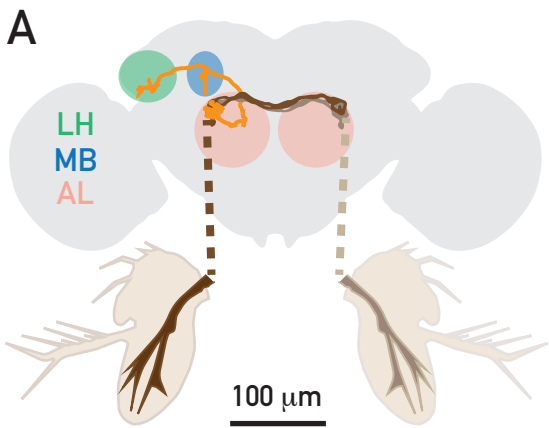


## Figure 1: Architecture of olfactory systems and cVA processing

**A:** Anatomy of the olfactory system of *D. melanogaster*. Olfactory receptor neurons project from the antennae (and maxillary palps) bilaterally to specific glomeruli in the antennal lobes (AL). Second-order projection neurons relay the information to higher-order centers: the lateral horn (LH) and the mushroom body (MB). **B:** Anatomy of the olfactory system in *Mus musculus*. Olfactory receptor neurons have sensory endings in the olfactory epithelium and project unilaterally to a specific glomerulus of the olfactory bulb. Second order mitral, and tufted cells relay this information to higher-order brain centers, including the cortical amygdala and the piriform cortex. **C:** Circuit schematic of the olfactory system of *D. melanogaster*. A given cell type of olfactory receptor neurons projects to a single glomerulus in the antennal lobe, and connects with projection and local neurons (PN, LN). Projection neurons forward this signal to third-order Kenyon cells (KC) in the mushroom body, and to third-order lateral horn neurons (LHN). PN to KC connectivity is close to random, while PN to LHN connectivity is largely stereotyped. (Throughout this work a circle and an arrow represent a neuronal cell-type, irrespective of the number of neurons in a given cell-type.) **D:** Known cVA processing pathways. Two ORN types (both consisting of a few tens of neurons), Or67d and Or65a respond to cVA, projecting to DA1 and DL3 glomeruli, respectively. aSP-g is a cVA responsive, *fruitless*<sup>+</sup> lateral horn neuron innervated by DA1 PNs in female flies. pC1 is a *doublesex*<sup>+</sup> central brain neuron that integrates cVA and male courtship song, and regulates female receptivity. The role of *fruitless* and *doublesex* is explained on page 18.

## 1.4 Circuit neuroscience in *Drosophila*

Circuit neuroscience aims to understand the computational functions of the brain at the level of interacting neuronal populations – circuits, placing itself between neuroscientific disciplines with longer history: studying single neurons or whole areas of the brain. Using *Drosophila melanogaster* for circuit neuroscience allows us to bring together multiple levels of investigation: circuit anatomy, physiology, and behaviour. All these possibilities originate from the rich ethological, genetic, and genomic advances achieved in flies over the 20th century. A key problem in circuit neuroscience is to gain access reproducibly to the same neurons to probe their function across individuals. The combination of two separate transgenic lines that express a transcription factor and a reporter engineered to be transcribed by this factor we call a binary expression system. These provide a fast, efficient, and uniquely precise solution to this problem in *Drosophila*. Large libraries of driver lines, relying on the yeast transcription factor, GAL4, can be combined with reporter lines using the UAS promoter. Importantly, two orthogonal binary expression systems, LexA/LexAop and QF/QUAS, are commonly combined with GAL4/UAS to drive multiple reporters with independent expression patterns. This study relied on the GMR (Gerry M. Rubin) and VT (Vienna Tiles) driver line libraries, generated at Janelia Research Campus, and IMP Vienna, respectively, to generate specific lines for neurons of interest. These libraries use single transcriptional enhancers, an approximately 3000 base sequence from a gene expressed in adult brains, to specify the expression of GAL4 or LexA inserted at a defined location by site-specific recombination (Pfeiffer et al. 2008; Jenett et al. 2012; Tirian and Dickson 2017). These drivers rarely label single neurons but an intersectional strategy can further specify the neuronal labelling pattern. Using a split version of the GAL4 transcription factor in which the activation domain (AD) and the DNA-binding domain (DBD) are controlled by distinct enhancers, one can create a combined driver line, where the reporter is only expressed where both the AD and DBD components are present in a neuron (Figure 2A; Luan et al. 2006; Pfeiffer et al. 2010). These libraries were made available as searchable image databases, including sparse and stochastic multi-colour labelling by these drivers, that facilitate finding neurons of interest, and selecting split-GAL4 hemidriviers to be combined for specific access (Meissner et al. 2020; Otsuna, Ito, and Kawase 2018). Further intersectional strategies to limit expression include the FLP/FRT (flippase / flippase recognition target) site-directed recombination system, and the GAL80 transcriptional repressor of GAL4. The FLP/FRT system uses a defined expression pattern for FLP recombinase via an enhancer, and the

reporter's expression is dependent on FLP recombination guided by FRT sites in the inserted transgene (Konsolaki et al. 1992). GAL80 can repress GAL4 driven transactivation by binding to its activation domain, thereby limiting the reporter's expression to neurons with GAL4 but without GAL80 (Giniger, Varnum, and Ptashne 1985). Combination of GAL4, GAL80, and FLP is used by the MARCM method (mosaic analysis with a repressible cell marker, (Lee and Luo 2001)). MARCM uses a FLP driven recombination of the heterozygous GAL80 during mitosis to create two daughter cells, one homozygous for GAL80, and one without any GAL80. The progenitor cell without GAL80, and all of its daughter cells - a clone, will express the reporter driven by GAL4. A further variation, FLPout MARCM labels individual cells of a clone (J. Wang et al. 2002).

Using such labelling strategies for neuroanatomical studies further developed our understanding that flies have conserved neuron morphologies across individuals (E. C. Marin et al. 2002; Chiang et al. 2011). Being able to identify the same neuron or cell type across animals is crucial to reproducibly test the function of a circuit element (Bates et al. 2019). A vital step in making comparisons of neuron morphology across different flies is to use a common template space, and image registration tools to place neurons from individuals into the same brain space (Bates, Manton, et al. 2020; Bogovic et al. 2020). After registration, expert inspection at small scales, or algorithmic comparison of morphological similarity at large scales can provide a consensus on a neuron's identity and cell type (Costa et al. 2016). Using MARCM studies to define developmental clones, and large databases of individual neuron morphologies registered to a single template brain provided a rich and systematic but far from comprehensive description of neuronal cell types in *D. melanogaster* (Chiang et al. 2011; Ito et al. 2013; Cachero et al. 2010).

Currently, electron microscopy (EM) is the only method that achieves sufficient resolution to create a neuron level wiring diagram, or connectome. Following pioneering studies by Sydney Brenner's lab in the worm, *Caenorhabditis elegans* (White et al. 1986), EM based connectomics aimed to account for all cell types and explore synaptic connectivity in the fly. The small size of the fly brain, the recognisable neurons across individuals, and the wide variety of neuroscientific methods available in flies made it an attractive target to acquire and annotate a connectome of its nervous system (reviewed in Schlegel, Costa, and Jefferis 2017). After studies acquiring and analysing smaller brain regions like the visual and antennal lobes (Takemura et al. 2017; Tobin, Wilson, and Lee 2017; Horne et al. 2018), a full adult fly brain (FAFB) was imaged at 4x4x40 nm resolution by serial section transmission EM (ssTEM), followed by approximately one-third of a fly brain, dubbed the 'hemibrain',

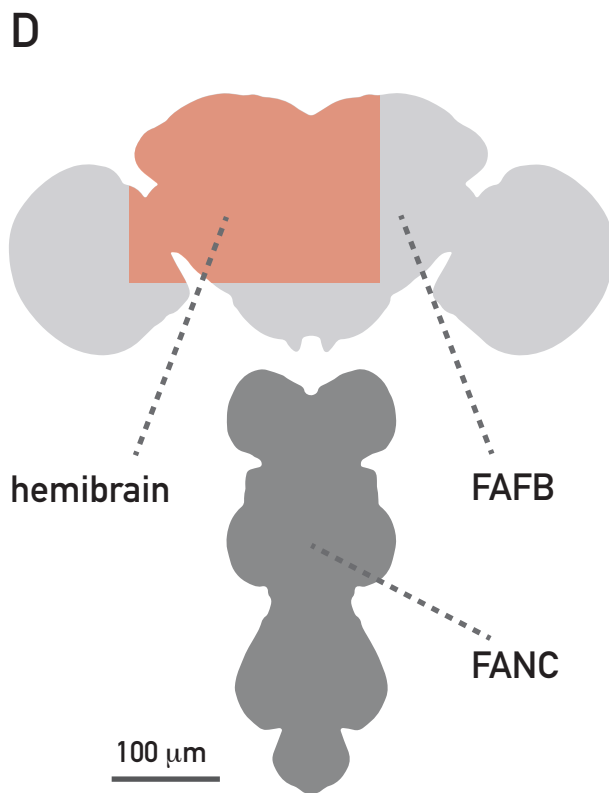
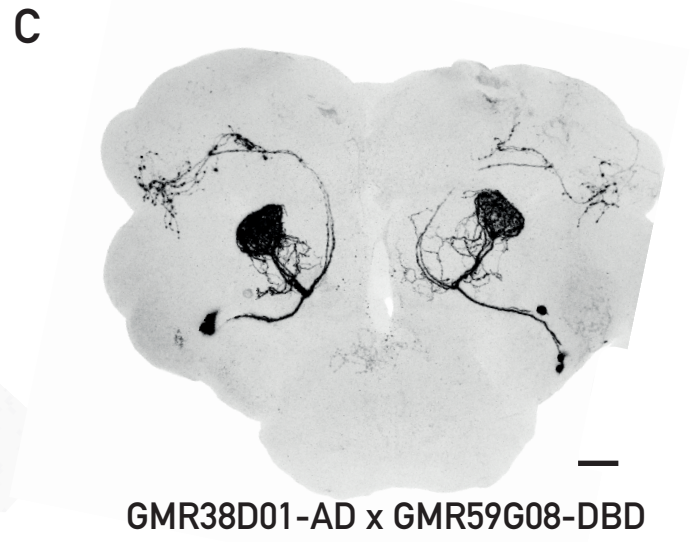
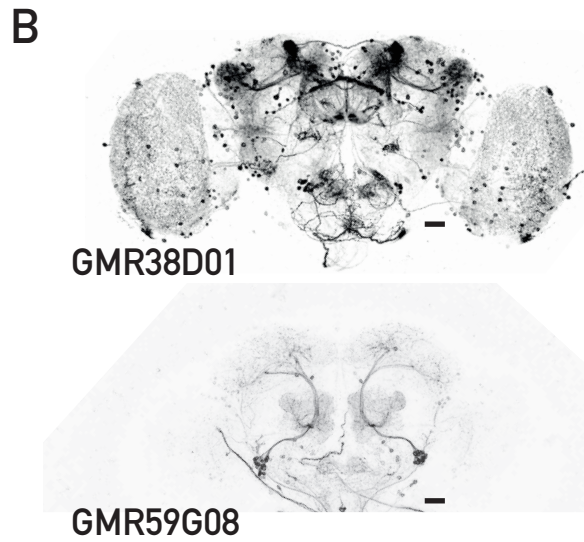
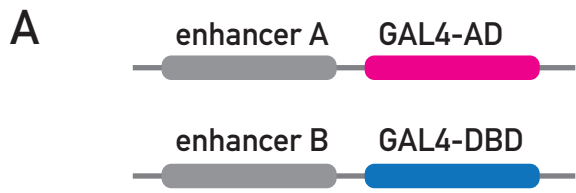
with focussed ion beam scanning EM (FIBSEM), and a full adult nerve cord (FANC) with ssTEM (Zheng et al. 2018; Scheffer et al. 2020; Phelps et al. 2021). The ssTEM datasets are primarily used for sparse reconstruction of circuits of interest via manual tracing of neuron morphologies and annotation of synapses. This method was superseded by automated segmentation of neurons and synapses, that is followed by manual proofreading for FAFB and FANC (P. H. Li et al. 2020; Dorkenwald et al. 2020; Buhmann et al. 2018). This strategy was first used to achieve a dense reconstruction of the hemibrain dataset. Currently neuron morphologies and connectivity from the hemibrain dataset are accessible via a web interface and programmatic tools, allowing large scale analyses of full sensory systems or specific brain regions like the mushroom body or central complex (Schlegel et al. 2021; F. Li et al. 2020; Hulse et al. 2020). In parallel, the FAFB dataset is continued to be used for sparse reconstructions with special focus on circuits with components in the gnathal ganglion (GNG) or descending and ascending neurons (DNs, ANs), which are fully or partially absent in the hemibrain. FANC, the first ssTEM dataset of the VNC (ventral nerve cord) incorporates sensory and motor circuits of the leg and abdomen, also, it is a useful complement to FAFB to investigate DN and ANs. Having two datasets about parts of the fly brain allows comparisons across individuals. Surprisingly, innate olfactory circuits across individuals are conserved to the extent that interindividual variability (FAFB compared to hemibrain) is not bigger than interhemispheric variability (FAFB right compared to FAFB left, Schlegel et al. 2021).

These connectomic resources help us understand the flow of information from sensory input to motor output at an unprecedented detail. In order to reveal the computations performed throughout this flow we need to functionally test, measure, and manipulate the activity of neurons. *In vivo* whole-cell electrophysiology and GCaMP calcium imaging, complementary methods to record neural activity, were adopted in flies early on, and were efficiently combined with existing genetic tools (Wilson, Turner, and Laurent 2004; Jayaraman and Laurent 2007). These techniques unravelled neural computations such as olfactory gain control in the antennal lobe, odour representation and associative learning mechanisms in the mushroom body, and the emergence of a heading direction signal in the central complex (Olsen and Wilson 2008; Root et al. 2008; Caron et al. 2013; Hige et al. 2015; Seelig and Jayaraman 2013). These studies are further extended or challenged by novel connectomic insights. In the case of understanding directional selectivity in visual processing, early connectomic resources already proved their value, demonstrating how they aid forming hypotheses about circuit function (Takemura et al. 2017; Strother et al. 2017). Current work

in fly neuroscience can exclude circuit models incompatible with connectomic data, and constrain and develop hypotheses based on the observed circuit layout.

Recording neural activity allows us to understand sensory coding and information processing, but is limited in answering the question what aspects of sensory stimuli were relevant to changing an animal's behaviour. Early descriptions of *Drosophila* behaviour both in the wild and the laboratory provide rich information about the merkwelt (perceptual world, (Tinbergen 1951) of flies. Recent technological advances in computer vision and machine learning methods made it possible to track, quantify, and cluster fly behaviour, organise it into hierarchical or sequential modules, and ultimately, to gain the best possible read out of the fly's goals (Branson et al. 2009; Kabra et al. 2013; Berman et al. 2014; Pereira et al. 2019; Mathis et al. 2018). The rigid body parts of flies make their movement easier to track than that of mammals, making behavioural classification more accurate. An impactful analysis pipeline, which we also use in this study, JAABA (Janelia Automatic Animal Behaviour Annotator), can incorporate positional data about fly body, wings, and legs from multiple tracking methods (Kabra et al. 2013). The data is processed to generate more complex features based on other available information, e.g. distance to arena wall, distance and facing angle relative to another fly. After manual marking of frames with positive and negative examples of a given behaviour a machine learning algorithm uses the descriptor features to find the function that best detects examples of the behaviour. Iterative teaching and testing steps achieve human-level accuracy in detecting fly social behaviours, like chasing, wing-extension, copulation attempt, or aggressive lunge (Robie et al. 2017). This supervised learning method can be extended by unsupervised tools, to detect and cluster unknown behavioural elements (Berman et al. 2014; Calhoun, Pillow, and Murthy 2019). As an alternative to video based tracking, behaviour can be quantified in a tethered walking or flying fly based on measuring proxies of velocity (Borst and Heisenberg 1982; Lehmann and Dickinson 1997). These approaches come with the great advantage of recording neural activity while measuring behaviour (Maimon, Straw, and Dickinson 2008; Seelig et al. 2010), although social behaviours are limited in a head-fixed fly. More recent efforts to measure neural activity in freely behaving flies are promising, but rather constrained by the low signal to noise ratio (Grover et al. 2020; Mercier et al. 2018).

This work relies on most of these techniques, including intersectional genetic labelling methods, computational neuroanatomy, connectomics, *in vivo* functional calcium imaging, and supervised classification of social behaviours.



**E**

	FAFB	hemibrain	FANC
part of CNS	whole brain	1/3 brain	VNC
acquisition method	ssTEM	FIBSEM	ssTEM
resolution	4x4x40 nm	8x8x8 nm	4.3x4.3x43 nm
reconstruction method	first manual; currently segmentation based	segmentation based	first manual; currently segmentation based
resulting data	sparse	dense	sparse

## Figure 2: Genetic and connectomic tools in flies

**A:** Schematic of split-GAL4 labelling strategy. Two components of the GAL4 transcription factor, the activation, and the DNA-binding domain, have specific expression patterns defined by upstream enhancer regions. If these expression patterns overlap the cells in the intersection will carry both components, and they can assemble to a functional transcription factor to drive reporter expression. **B:** Expression pattern of two enhancer trap lines from the GMR collection. Top: confocal image of the GMR38D01-GAL4 enhancer line's expression, maximum projection. Bottom: confocal image of the GMR59G08-GAL4 enhancer line's expression, maximum projection. Scale bar is 20  $\mu\text{m}$ . **C:** An example of the split-GAL4 technique to sparsely label a cell type in the fly brain. Confocal image of combining the GMR38D01-AD GMR59G08-DBD enhancer lines, maximum projection. Scale bar is 20  $\mu\text{m}$ . **D:** Coverage of the central nervous system by recent EM datasets for fly connectomics. **E:** Comparison of the largest EM datasets for fly connectomics, also used in this study. Sparse reconstruction: focussed reconstruction of selected neurons to gain an understanding of a circuit of interest. Dense reconstruction: unbiased tracing of every neuron to create a comprehensive connectome.

## **2 Materials and Methods**

## 2.1 Fly stocks

**Table 1: Fly stocks used in this study**

name and genotype	source	identifier
lPN SS: w[1118]; GMR54A11-AD; BJD_115F09	gift from Dr Yoshi Aso	SS01189
lvPN SS: w[1118]; GMR38D01-AD; GMR59G08-DBD	gift from Dr Mike Dolan	LH467
yw, UAS-CD8::GFP, UAS-CD8::GFP		
w[1118]; 20XUAS-opGCaMP6s su(Hw)attP5;	gift from Dr Yonil Jung, Dr Barrett Pfeiffer, and Dr David Anderson	NA
w[1118]; 20XUAS-opGCaMP6f su(Hw)attP5;	gift from Dr Yonil Jung, Dr Barrett Pfeiffer, and Dr David Anderson	NA
w, Or67d-GAL4;;	BDSC	RRID: BDSC_9998
w[1118];; GMR24A10-GAL4	BDSC	RRID: BDSC_49059
w[1118];; VT046100-GAL4	BDSC	RRID: BDSC_75076
w[1118];; GMR53A03-GAL4	BDSC	RRID: BDSC_38858 (currently not available)
pC1 SS2: w[1118]; VT002064-p65ADZp in attP2, dsx-DBD	Janelia FlyLight	SS59911
w[1118], 13XLexAop-IVS-jGCaMP7f su(Hw)attP8;;	BDSC	RRID: BDSC_80910
w;; dsx-LexA	gift from Dr David Deutsch and Dr Mala Murthy	NA
w[1118];; 20XUAS-CsChrimson-mCherry	gift from Dr Marta Zlatic and Dr Vivek Jayaraman	NA
w[1118]; 20XUAS-CsChrimson-mVenus;	BDSC	RRID: BDSC_55135
w[1118], UAS-Hid, UAS-Reaper	gift from Dr Barry J.	

	Dickson	
AV2a2 SS: w[1118]; GMR30A10-AD; GMR53A03-DBD	gift from Dr Mike Dolan	LH907
aSP-g SS1: w[1118]; GMR76G09-DBD, JK1029-AD	this study	
w[1118]; P{y[+t7.7] w[+mC]=20XUAS-IVS-GCaMP6f}attP40	BDSC	RRID: BDSC_42747
yw, Or67d-QF;;	gift from Dr Chris Potter	NA
;QUAS-CsChrimson-mVenus;	gift from Dr Chris Potter	NA
w[1118]; Ir94e-GAL4	gift from Dr Richard Benton	NA
w[1118]; GMR81A04-LexA;	BDSC	RRID: BDSC_54390
aSP-g SS1/aSP-g SS2: w[1118];GMR76G09-DBD,JK1029/GMR81A0 4-DBD,JK1029	this study	
JK1029, empty-DBD: w[1118]; JK1029,GAL4-DBD.empty control (BPZpGDBD)	this study	
w[1118]; <i>fru</i> FLP	gift from Dr Barry J. Dickson	
aSP-g FLP1: w[1118]; 76G09-GAL4, <i>fru</i> FLP	this study	
aSP-g FLP2: w[1118]; 81A04-GAL4, <i>fru</i> FLP	this study	
empty-GAL4 FLP: w[1118]; empty-GAL4 (pBDPGAL4Uw), <i>fru</i> FLP		
w;; UAS>mCherry>eGFP:Kir2.1	gift from Dr Rebecca Yang and Dr Barry J. Dickson	
aSP-g LexA FLP: w[1118]; 81A04-GAL4, <i>fru</i> FLP	this study	
w;; 20xUAS>dsFRT>CsChrimson:mVenus	gift from Dr Taketoshi Kiya	
mAL1 SS:	this study	

w[1118]; VT033636-AD; VT013555-DBD		
w; pJFRC-10xUAS-IVS-eGFP-Kir2.1;;	Janelia Research Campus	NA
w;; pJFRC-10xUAS-IVS-eGFP-Kir2.1;	Janelia Research Campus	NA
dMS6 SS: w[1118]; 22B10-AD;VT059003-DBD	this study	
abdSMP SS: w[1118]; 42D03-AD; 20C05-DBD	this study	
w[1118]; GMR67E08-LexA;	BDSC	RRID: BDSC_54092
w[1118];; GMR22B10-GAL4	BDSC	RRID: BDSC_48969

## 2.2 *Drosophila* husbandry

Standard techniques were used for fly stock maintenance. Flies for experiments were raised and kept at 25°C in an incubator with a 12 hour light:dark cycle, and grown on iberian *Drosophila* food. For optogenetic experiments the food was supplemented with all-trans retinal.

## 2.3 Split-GAL4 hemidriver combination screening

The split-GAL4 hemidriver lines were selected based on the full expression pattern of GAL4 using the same enhancer, and multi colour flip-out (MCFO) labelling of these drivers. Expression was assessed by both visual screening of mean intensity projections from the FlyLight database, and Colour depth MIP mask search relying on FlyLight MCFO data of GMR and VT hemidriver lines that were generated at Janelia Research Campus, and IMP Vienna (Otsuna, Ito, and Kawase 2018; Meissner et al. 2020; Jenett et al. 2012; Tirian and Dickson 2017). Split-GAL4 lines contain two hemidrivers, the p65ADZp in attP40 and the ZpGAL4DBD in attP2, with a few exceptions where a hemidriver of a non-GMR enhancer was used (JK1029-AD, *dsx*-DBD). Split-GAL4 line candidates for confocal imaging were selected by choosing two hemidriver lines (an AD and DBD) whose GAL4 patterns seemed to contain the target cell type. The lines were screened by combining the two hemidrivers and a UAS reporter: Enhancer-p65ADZp (attP40); Enhancer-ZpGAL4DBD (attP2) crossed to 20xUAS-csChrimson::mVenus (attP18) or UAS-CD8::GFP; UAS-CD8::GFP.

## 2.4 Neuron tracing in FAFB and FANC

Definitions of terms and expressions used in connectomics:

**Sparse reconstruction:** focussed reconstruction of selected neurons to gain an understanding of a circuit of interest. **Dense reconstruction:** unbiased tracing of every neuron to create a comprehensive connectome. **Manual reconstruction:** tracing of neuronal morphology and annotation of synapses across EM sections by a human annotator. This results in a neuron skeleton, a point and line representation of 3D neuron structure. **Automated reconstruction:** software based segmentation of neuronal morphology, machine learning algorithms are trained to detect the contiguous neuron parts across EM sections, and synapses based on human generated ground truth datasets. This results in neuron segments, volumetric representation of neuron structure. **Segment concatenation:** automated reconstruction algorithms make errors where neurons are split into several segments which are joined by a human proofreader - this is segment concatenation. False merge errors are also common which need to be cut by a proofreader. **Upstream neuron, input neuron:** neuron A is upstream to neuron B if A is presynaptic to B, i.e. A forms directional synapses that transmit the signal to B, therefore A is an input neuron of B. **Downstream neuron, output neuron:** neuron A is downstream to neuron B if A is postsynaptic to B, i.e. B forms directional synapses that transmit the signal from A, therefore A is an output neuron of B. **(Trans)-synaptic sampling:** EM datasets relying on sparse reconstruction, tracing a given neuron or cell type does not inform us about the identity of its synaptic partners. In order to reveal these partners we have to reconstruct the neuronal profiles (a small part of a neuron on a single EM section) that were annotated as a synaptic partner. We can sample synapses either up- or downstream of our neuron of interest to identify pre- or postsynaptic neurons, respectively. **Top synaptic partner:** the neuron or cell-type that has the highest synaptic weight with our neuron of interest (can be either upstream or downstream). **Synaptic weight:** the number of annotated synapses for a given connection between two neurons, e.g. if neuron A is presynaptic to neuron B, and there are 10 individual synapses annotated between these neurons in this direction, the synaptic weight of this connection is 10. When specified this can refer to the sum of synaptic weights across all members of two cell-types. **Synapse strength:** in this work this is used only as a synonym of synaptic weight. In general, there is an underlying assumption that more synapses result in a physiologically stronger synapse. While proving this statement is technically challenging, there have been studies that demonstrated synapse size linearly scales synapse number (Barnes, Bonn ry, and Cardona

2022), and that synapse size linearly scales with synapse strength (Holler et al. 2021), furthermore in *Drosophila* it was found that synapse density and location jointly predict synapse strength (Liu et al. 2022). **Brain space:** in order to compare neurons across brains a common template space can be used. This template may be made by averaging the 3D image of many brains – usual for light microscopy, or by using a single brain specimen – usual for EM. Neuron images from other sources (e.g. confocal images of driver line expression, or different EM datasets) can be registered onto this template and compared with neurons from different brains. **Biassed input, biassed connectivity:** much of this work focusses on the comparison of bilateral signals from the antennae. Biassed input here means that a neuron or cell-type with bilateral input forms more synapses with one side than the other.

We used ssTEM (serial section transmission electron microscope) volumes to sparsely reconstruct the morphology and connectivity of neurons of interest in a female fly brain volume (FAFB) and a female VNC volume (FANC), (Zheng et al. 2018; Phelps et al. 2021). Neurons were either fully manually reconstructed or leveraging a partial segmentation of the FAFB database (P. H. Li et al. 2020). Tracing and segment concatenation was done using CATMAID (Saalfeld et al. 2009), a Web-based environment for working on large image datasets and for tracing of neuronal morphologies. Annotated synapses represent chemical synapses (both inhibitory and excitatory) based on previously described criteria.

aSP-g upstream sampling: Sampling was done as described in (P. H. Li et al. 2020). In brief, we combined an automated segmentation of the FAFB dataset with manually annotated presynaptic locations. The presynaptic locations were mapped onto the volumetric neuron segments, that allowed us to rank upstream segments by the number of presynapses inside the volume. We traced all upstream segments with more than one presynapse, thereby covering 56% of all inputs to aSP-g neurons. To reconstruct upstream neuron morphologies we concatenated skeletonised versions of the segments as described in Bates et al. 2020.

G2N-SLP1 upstream sampling: Sampling relied on another automated segmentation of the FAFB dataset, and the related FlyWire proofreading environment (Dorkenwald et al. 2020). We ranked upstream segments by the number of manually marked synaptic locations in them, and all of those containing more than two synapses (75% of all inputs) were reconstructed via concatenating segments.

aSP-g2 downstream sampling: Manual tracing was used to randomly sample 27% of the 1120 post-synaptic profiles of two aSPg2 neurons. 152 profiles were traced to their soma, and clustered by morphology to rank downstream cell types by synaptic weight.

mAL1 downstream sampling: Manual tracing was used to randomly sample 20% of the 1501 post-synaptic profiles of two mAL1 neurons. 134 profiles were traced to their soma, and clustered by morphology to rank downstream cell types by synaptic weight.

dMS6 upstream sampling: Manual tracing was used to fully reconstruct the 849 post-synaptic profiles of two dMS6 neurons. Profiles were traced to their soma, and neurons with three or more dMS6 connections were clustered by morphology to rank upstream cell types by the number of connections.

Identifying sensory neurons in FANC: Putative sensory neurons have dark cytosol, granular appearance, frequent invaginations with neighbouring neurons. Upstream neurons that possessed one or more of these traits were traced until evident that they were not sensory neurons or exiting the VNC through a nerve fibre. This method was used to find sensory neurons presynaptic to exemplar neurons of the five strongest dMS6 upstream neuron groups.

## **2.5 Computational neuroanatomy and connectomic analysis**

A dense reconstruction of one third of a female fly brain imaged with FIBSEM (focussed ion-beam scanning electron microscopy), referred to as hemibrain, was used to investigate connectivity in the antennal lobe (Scheffer et al. 2020). The website displaying the data (neuprint.org) and the natverse R package family was used to find connectivity information, and to visualise neuronal morphologies (Bates, Manton, et al. 2020).

For morphological clustering we calculated mean NBLAST similarity scores of neuron skeletons (point and line representations) and used Ward's hierarchical clustering on these scores and expert inspection to find morphological cell types (Costa et al. 2016).

Quantification of dendritic cable length in the lateral horn (i.e. what proportion of the dendritic arbour is in the LH) was done with natverse R package. Neuron skeletons were resampled at 1  $\mu\text{m}$ , to get an even distribution of nodes throughout the neuronal cable. We pruned these skeletons to dendrites by manually selecting a node on the skeleton before the axon branching (in aSP-g neurons axons are easily distinguished based on the large number of presynaptic boutons in those arbours, while dendrites almost completely lack these), and removing all nodes distal to the axonal branching. After this we took the proportion of nodes that were inside the lateral horn, divided by the number of all nodes that remained after pruning, i.e. the nodes that make up the dendrite part of the neuron's skeleton. For FAFB neurons, we used the LH\_L volume (lateral horn left) to define which nodes are inside or outside the LH. For FlyCircuit neurons we used the LH volume of the FCWB reference brain,

which is the template that these neurons were registered to in the dataset. For MCFO data, neuron skeletons were traced in Fiji (Schindelin et al. 2012) with the Simple Neurite Tracer plugin (Longair, Baker, and Armstrong 2011) and then registered to the IS2 template brain with CMTK - Computational Morphometry Toolkit as described in Cachero et al. (2010). We used the LH volume of the IS2 template brain to calculate the dendritic cable inside the LH for neurons from MCFO data.

## **2.6 Immunohistochemistry and confocal microscopy**

Immunohistochemistry was done as described in (Jefferis et al. 2007) except that the blocking step was overnight at 4°C. Primary antibodies: mouse anti-nc82 (DSHB, AB\_2314866) 1:40, chicken anti-GFP (Abcam, ab13970) 1:1000, rabbit anti-RFP (antibodies-online, ABIN129578) 1:1000, mouse anti-ChAT4B (DSHB, AB\_528122), rabbit anti-GABA (Sigma, A2052). Secondary antibodies: Alexa-568 anti-mouse (Invitrogen) 1:400, Alexa-488 anti-chicken (Invitrogen) 1:400, Alexa-633 anti-mouse (Invitrogen) 1:400, Alexa-568 anti-rabbit (Invitrogen) 1:400.

Prolonged incubation of brains (2–3 days at 4°C) with primary and secondary antibodies was required for homogeneous staining. Brain specimens were whole mounted in Vectashield (Vector Labs) on charged slides to avoid movement. Confocal stacks were acquired using a Zeiss 780 confocal microscope. Brains were imaged at  $768 \times 768$  pixel resolution every  $1 \mu\text{m}$  ( $0.46 \times 0.46 \times 1 \mu\text{m}$ ) using an EC Plan-Neofluar  $40\times/1.30$  oil objective and 0.6 zoom factor in the ZEN confocal imaging software. VNCs were imaged with the same conditions with two subsequent acquisitions to fully capture a single specimen, followed by manual stitching of mean intensity projections for presentation. All images were acquired at 16 bit colour depth. Maximum projections of z stacks were made in Fiji (Schindelin et al. 2012).

## **2.7 *In vivo* calcium imaging and stimulus presentation**

Functional imaging experiments of neurons were performed on virgin female flies aged 3 to 7 days, containing one copy of codon optimised GCaMP6f, unless other GCaMP is specified. Flies were placed into custom built holders, leaving the head and thorax exposed, under ice anaesthesia and secured in place with UV curable glue (Norland Optical Adhesive, NOA 68). Low melting point wax was used for securing the legs and the proboscis, unless otherwise specified. A window was then cut into the head capsule with a 30G needle, and trachea and air sacks were removed with forceps in order to uncover the brain. Fly brains

were bathed in external saline adjusted to 275mM and 7.3 pH, and bubbled with 5% CO<sub>2</sub> - 95% O<sub>2</sub> mixture. The saline had the following composition (Concentration, mM): NaCl 104.75; KCl 5; NaH<sub>2</sub>PO<sub>4</sub> 1; MgCl<sub>2</sub>·6H<sub>2</sub>O 1; CaCl<sub>2</sub>·2H<sub>2</sub>O 1; NaHCO<sub>3</sub> 26; TES 5; glucose 10; trehalose 10. The antennae were left under the holder so that they could be exposed to odour stimuli. A custom-built setup based on the Sutter (Novato, CA) Movable Objective Microscope with a Zeiss W Plan-Apochromat 20x/1.0 objective was used for the two photon imaging. A Coherent (Santa Clara, CA) Chameleon Vision Ti-Sapphire laser provided excitation, and image acquisition was controlled by Vidrio ScanImage Premium software (Leesburg, VA Pologruto, Sabatini, and Svoboda 2003). Image acquisition and stimulus delivery were triggered by a separate computer via Igor Pro software (Wavemetrics, Lake Oswego, OR) running Neuromatic. Images were captured at 7 Hz at 200 x 200 or 140 x 280 pixels for most experiments. Responses to an approaching male with varying speed were captured at 21 Hz, with two 80 x 80 pixel ROIs. Two-photon excitation was provided at 900 nm.

cVA delivery was done with a custom built olfactometer with two odour channels, each equipped with a solenoid valve (SH360T041, Neptune Research). Carrier airflow rate was 600 ml/min and odour channels entered the airstream approximately 3 cm from the fly's antennae with a flow rate of 200 ml/min, all regulated by separate mass flow controllers (Alicat Scientific Tucson, AZ, MC Series). Clean air from both odour channels was constantly flowing to the fly until a trigger pulse arrived to one of the valves, redirecting the odourised air from waste to the fly. Odours were 10% cVA (Pherobank, 6186-98-7) diluted in mineral oil, and the solvent control. The odour path containing cVA had a manual valve between the mass flow controller and the odour bottle, that was used to send the air to waste in between presentations to avoid depletion of cVA from the bottle with constant airflow.

Males used as stimuli were 4-8 days old Canton S flies, collected upon hatching and raised in groups of 5-10 individuals. A single male was selected and had its legs and wings removed under ice anaesthesia, and glued onto a metal needle with UV-curable glue (Norland Optical Adhesive, NOA 68). The glue was applied onto the proboscis, thorax, and abdomen of the male to inhibit any movement, but the genitalia were left free to avoid covering the regions where cVA is most abundant. A female fly was placed in the imaging holder (and later discarded) to position the male relative to the imaged fly's antennae. A Luigs Neumann Mini 23 compact *in vivo* micromanipulator was used to move the male, controlled by an Luigs Neumann SM-5 system. The SM-5 was connected to the imaging PC to externally trigger movements of the stimulus fly to defined locations with custom MATLAB scripts.

The male, facing up with its genitalia, was positioned manually directly in front of the female's antennae by the help of a camera equipped with a high magnification lens (FLIR BlackFly S3, and 3.3X Macro Zoom Lens, Computar). The zero position was reset on the manipulator in this position, so that any subsequent movement of the male happened relative to this origin. Male movement via the manipulator and two photon imaging was triggered as described above. To infer the timing of male movement a camera (same as above) was triggered together with the imaging experiment, and recorded throughout the acquisition at 33 frames per second. The start and end frames for each movement were noted down, and male movement traces were generated based on these in R, assuming constant velocity. An IR LED was used for illumination during imaging, and the camera was protected from 2-photon light with an 800 nm short pass filter.

For all stimulus protocols the starting position of the male was 10 mm below the female's antennae. For single male presentations we moved the male to 0.75 mm distance for 10 s (Figure 4B). For speed tuning experiments, the presentation length at lower speeds was shorter, as the time of movement start (both up and down) was kept constant. We used three speeds: 1.41, 4.30, and 8.04 mm/s, which correspond to speed settings 7, 11, and 15 (maximal) on the micromanipulator, respectively. For distance tuning experiments we used ten distances: 5, 3.5, 3, 2.5, 2, 1.5, 1, 0.75, 0.5, 0.25 mm. For each distance the male was moved up for 5 s, and then lowered back to the starting positions (10 mm) for 12 s. For lateralisation experiments the male was moved to 0.5 mm distance in z, 1.25 mm laterally to one side with respect to the antennae (Figure 6A). For 2D spatial coding experiments we used sixteen positions defined by a hexagonal lattice centred around the imaged fly. The points had a distance of 1, 1.732, or 2 mm from the antennae, and an angular position ranging from  $\pm 150^\circ$ . We did not use  $180^\circ$  presentations, as the imaged fly's body takes up these positions defined by the lattice.

Antennae were blocked for lateralisation experiments with Kwik-Sil (world Precision Instruments), a fast curing, low toxicity adhesive. The two components of Kwik-Sil were mixed and fumed silica (microscopic droplets of amorphous silica, Sigma, S5130) was added until curing was imminent. The mixture was gently applied on one of the antennae under a dissection scope, with care taken not to touch the other antenna. All flies used for these experiments were imaged with intact antennae prior to the antennal block, and the resulting data is included in the relevant figures and analyses.

Optogenetic stimulation of CsChrimson (a red-light gated cation channel) during imaging was done by a fibre-coupled 617 nm LED (M617F2, Thorlabs, Ely, UK). The light

was passed through a 600 nm long-pass filter, to avoid any light bleedthrough into the imaging PMT (GCaMP emission filter was 525/70 nm band-pass). An optic fibre was placed approximately 0.5 mm away from the fly's head from below, and the LED was turned on via external triggering, described as above. In all experiments the LED was constantly on for the specified period, except for lvPN - pC1 experiments, where the LED sent 50 ms light pulses for 5 s with 10 Hz frequency.

For experiments with a platform under the fly a metal cooling pad was used during dissection to extend anaesthesia, and to allow positioning of the fly without fixing the legs with wax. After five minutes of recovery under the objective, once the flies started moving their legs vigorously, a platform was lifted by a manipulator, approximately to 0.5 mm distance from the fly, so it could comfortably stand on it. Calcium imaging and video recording of behaviour was triggered simultaneously as described above. The time of events when the fly pushed on the platform was manually detected by the following criteria: these events last at least 0.5 s, and all visible legs are in flexion at the tibio-tarsal joints. These time points were used to generate event-triggered averages of the  $\Delta F/F_0$  imaging traces.

## **2.8 Calcium imaging quantification and statistical analyses**

Images were registered with the NoRMCorre algorithm implemented in MATLAB using the signal channel ("NoRMCorre: An Online Algorithm for Piecewise Rigid Motion Correction of Calcium Imaging Data" 2017) <https://github.com/flatironinstitute/NoRMCorre>, flies with notable movement in the z axis were removed from analysis. Image analysis was performed with custom scripts written in R employing the open source scanimage package (see <https://github.com/jefferis/scanimage>). Raw  $\Delta F/F_0$  traces were gently smoothed with a low-pass Butterworth filter, except for speed tuning and distance tuning experiments (Figure 12, 13, and 5). For distance and angular tuning curves, largest values from a given ROI over an experiment were used for normalisation. Response maxima and means were calculated in R.

For lateralisation experiments – where bilateral response contrast was assessed based on ipsi- and contralateral stimulation – (Figure 6, 7, 8) the mean value was taken from six responses for all imaging ROIs, and these data were checked for normality (Shapiro-Wilk's test), and the variance of ipsilateral and contralateral ROIs were compared with F-test. If a condition passed both tests (  $p > 0.05$ ), unpaired t-test was used to test the statistical

significance of response differences in ipsi- and contralateral ROIs. Where either conditions failed (normality, equal variance), Wilcoxon-test was used instead.

Distance tuning curves were calculated based on the mean normalised response maxima to a given male distance, and fitted with a sigmoid curve. Curve fitting was done with nonlinear least squares method, self-started by a logistic function and parameters from the data.

For 2D positional coding experiments we used a hexagonal lattice centred around the imaged fly to define male positions, thereby sampling 2D space at equal distances between neighbouring stimulus positions. This resulted in three possible distances from the imaged fly's antennae: 1, 1.732, and 2 mm, and eleven angular positions (30° steps between -150° to +150° with 0° being frontal to the imaged fly). To create the angular tuning curves of left and right IPNs we used a fixed distance (1.732 mm), for which mean responses at six angular positions were recorded directly, and mean responses at five positions were linearly interpolated based on mean responses to 1 mm and 2 mm presentations at these angles. A single multivariate linear model was used to predict the x and y position (equal to the cosine and sine of the angular position on a unit circle, respectively) of the male based on the difference and the sum of right and left IPN responses. Based on these predictions of x and y position the angular position was calculated and compared with the actual position and angular direction to get prediction errors in mm and degrees (Figure 11).

For speed dependence experiments, mean response maxima from six trials per fly were compared by Friedman-test to assess if male approach speed had a significant effect on responses. Where the Friedman-test rejected the null-hypothesis (AV2a2) it was followed by paired Wilcoxon-test for pairwise comparisons across speeds with Benjamini-Hochberg correction for multiple comparisons (Figure 12). All analyses were done in R.

Representative 2-photon images with intensity colour coding were made in Fiji (Schindelin et al. 2012).

## **2.9 Courtship assays and behavioural analysis**

A courtship assay modified from Hoopfer et al. (2015) was used to measure female receptivity. 4-8 day old virgin females of the experimental genotype and Canton S males were placed with gentle aspiration in a transparent behavioural plate with eight chambers, 16 mm in diameter, equipped with sliding separators. Walls were covered with teflon-like material (polytetrafluorethylene) and the lid was covered with Sigma-coat to prevent flies from

climbing and holding onto the walls and lid. The plate was placed into a 23°C incubator and males and females were allowed to habituate to the chamber for a few minutes after transfer. The separators were removed upon the start of the experiment, and flies behaved and interacted freely in the chambers. The behavioural plate was backlit with homogenous IR light from an LED panel, and a Teledyne FLIR Grasshopper 3 camera was used to record behaviour for 20 minutes at 30 frames per second. Dim ambient light was provided to the flies to stimulate courtship by the males. The intensity of the ambient light was adjusted in experiments for a given cell-type manipulation for all conditions, to set the baseline rate of courtship and thereby the latency to copulation. This was necessary to avoid situations where genetic controls mated immediately, in which case a receptivity increase by a manipulation could not be detected due to a ceiling effect.

Video files were converted to a compressed format (ufmf), and fly positions were tracked with FlyTracker software (Eyjólfsdóttir 2014). Tracking data was fed into a JAABA analysis pipeline with custom behavioural classifiers, also detecting the time of mating (Kabra et al. 2013). Mating was defined when both flies in the chamber were classified as mating for at least 30s, and mating events were eventually manually checked and corrected for errors. Survival analysis of mating latency, followed by log-rank test, was used to test statistical significance of differences in latency to copulation. When multiple comparisons were made, it was followed by post-hoc Benjamini-Hochberg corrections. Data processing was done in MATLAB, statistical analyses were done in R with the survminer package.

For neuronal manipulations we used driver lines specific to the neuron of interest and expressed an actuator or a pair of apoptosis promoting proteins to perturb function. The same LED panel that provided IR light was equipped with 617 nm LEDs as well to activate CsChrimson. For most experiments the activation LED was kept on throughout the 20 minutes of the experiment, providing constant light intensity of 40 uW/mm<sup>2</sup>. For IPN and lvPN activation we used 5 s long periods of 50 ms light pulses at 10 Hz, separated by 5 s of no stimulation light periods, throughout the experiment. Hyperpolarisation via Kir2.1, and genetic ablation of manipulated neurons via Hid and Reaper were constitutive. Genetic controls carried an empty GAL4 insertion (or split-GAL4, where a split-GAL4 line was used) at the same landing site where the driver was inserted (attP2 for GAL4 lines, and attP40 and attP2 for split-GAL4 hemidrivers). For cases where a non-GMR or VT hemidriver was used (JK1029-AD), the genetic control carried this transgene together with an empty-DBD.

### **3 Parallel pheromone pathways**

Previous work has described two types of DA1 PNs, the excitatory DA1 IPNs (lateral lineage) projecting to the mushroom body and the lateral horn (Figure 3A, B), and the inhibitory DA1 vPNs (ventral lineage) which project only to the lateral horn (E. C. Marin et al. 2002). To explore other potential cVA pathways we relied on a comprehensive description of olfactory projection neurons (Bates, Schlegel, et al. 2020; Zheng et al. 2018). These studies used an EM volume of a female Full Adult Fly Brain (FAFB) and reconstructed all olfactory PNs. In this dataset, we found a previously uncharacterised uniglomerular PN type from the lateroventral lineage consisting of three neurons, with dendritic arbours in the DA1 glomerulus (Figure 3C, D). We identified the same cell type based on morphological similarity in another EM dataset of a female fly brain, the hemibrain (Scheffer et al. 2020). We refer to these neurons as lvPN in this work (cell type M\_lvPNm45 in the hemibrain). lvPN dendrites are largely confined to the volume of the DA1 glomerulus (defined based on the dendritic arbours of DA1 IPNs; Bates et al. 2020). lvPNs project to the superior intermediate protocerebrum (SIP), not innervated by IPNs, and the LH where the axons of the two PN types overlap in space. Together, these observations suggest that cVA information diverges at the first synapse (from a single cell type, Or67d ORNs, to two PN types) and is relayed onto distinct third order neurons by parallel pathways.

### **3.1 Characterisation of a novel cVA pathway**

We used the hemibrain dataset to explore the input connectivity of lvPNs. DA1 ORNs, the ORN type that responds selectively to cVA, are the strongest presynaptic cell type of lvPNs, and provide 99% of all ORN inputs to lvPNs (270 synapses out of 273). Therefore anatomically speaking, lvPNs are sparsely tuned to cVA, although uniglomerular PNs have been shown to have wider tuning profile than the ORNs of the same glomerulus due to lateral excitation by local neurons (Olsen, Bhandawat, and Wilson 2007). There are 90 ORN input synapses per lvPN in this dataset, which is more than an order of magnitude smaller than in IPNs (1252 synapses / IPN), indicating different response properties to similar ORN activity (Figure 3F).

We identified a split-GAL4 genetic driver line generated in a previous study in our lab that sparsely labels lvPNs (line LH467 in Dolan et al. 2019). We used this line to drive GFP expression and showed colocalisation of GFP signal and ChaT4B, an enzyme known to synthesise acetyl-choline, in lvPN cell bodies by immunostaining (Figure 3I), therefore we expect lvPNs to be cholinergic. When we compared the anatomy of lvPNs in male and female

brains we did not observe a gross morphological difference in the sexes (Figure 3G, H). Next we expressed a genetically encoded calcium indicator, GCaMP6s, under the control of lvPN Stable Split to perform *in vivo* two photon calcium imaging. We observed a strong axonal calcium increase when presenting cVA from an olfactometer (Figure 3J). Earlier findings about IPNs and these data together show that IPNs and lvPNs are sexually monomorphic, parallel excitatory pathways, relaying cVA information.

### 3.2 IPNs and lvPNs differ in sensitivity and adaptation properties

Using olfactometers to deliver cVA in physiology experiments is a widely used method, but relating cVA concentration to ethological events is non-trivial. A rarely used alternative stimulus to cVA is a male fly (Clowney et al. 2015; Tachibana, Touhara, and Ejima 2015). In this case the distance of the male or a directed air puff can be used to temporally control cVA presentation. While using a male fly is a more complex odour stimulus than cVA alone, we wanted to control not only the temporal but also the spatial structure (distance and angular direction) of the stimulus. Given that DA1 (Or67d) ORNs and IPNs were shown to be sparsely tuned to cVA (Schlief and Wilson 2007) we attribute calcium responses in these cell-types to this odour upon male presentation. However, we cannot exclude that the presence of other fly odours modulates PN activity. We used an externally controlled micromanipulator to present a male at defined positions relative to the imaged female fly's antennae, and measured the activity of DA1 ORN, IPN, or lvPN axons with *in vivo* two-photon calcium imaging by using specific driver lines to drive GCaMP expression in the respective cell types (Figure 4). We used 10 mm distance from the antennae as the male's starting position in all experiments, which is approximately five body lengths for a fly.

Moving the male to 0.75 mm distance for 10 s evoked a large calcium increase in all three cell types (Figure 5A, E, I). ORN and IPN responses are consistent with previous reports about other olfactory glomeruli in flies, ORN responses reach their maximal activity slower than PNs, and PNs adapt stronger during the stimulus ((Bhandawat et al. 2007), see also Chapter 2.7). Interestingly, we found that DA1 lvPNs did not adapt throughout the 10 s stimulus, and to our knowledge there is no published physiological data about PNs from the lvPN lineage that we could use for comparison. The sustained responses in lvPNs shows a basic difference in what these PN pathways can signal about an odour. IPNs are responding stronger to changes in cVA concentration (stimulus onset) while lvPNs may signal the absolute level of cVA concentration. Another key result of these experiments is the fact that a

male from 10 mm distance did not activate the ORNs or PNs. Based on this our next question was whether cVA can be used to signal the distance of a male.

We presented a male at ten distances between 5 and 0.25 mm in sequence (see Methods) and measured GCaMP signal in ORNs and PNs. All three cell types show a strong concentration dependent and therefore indirectly distance dependent activation (Figure 5C, G, K). To describe the distance tuning of these cell types we fit a sigmoidal function to their maximal responses to each distance (Figure 5D, H, L). ORNs respond reliably at 5 mm distance and have a wide dynamic range, resulting in monotonously increasing responses as distances get shorter. We did not expect ORNs to be saturated by these stimuli as it was previously shown that touching cVA to the antenna results in higher ORN firing rate than just moving cVA close to the sensilla (van der Goes van Naters and Carlson 2007). IPNs on the other hand have a sigmoidal tuning curve, with a plateau at shorter distances than 1 mm. IvPNs respond weaker to mid range distances (5 - 2 mm) and their response grows sharply at distances under 2 mm without saturation at 0.25 mm. These data show that IPNs are more sensitive to cVA than IvPNs, which is consistent with their large difference in the number of Or67d ORN synaptic inputs (Figure 3F). As there is no airflow in the experiment, we expect that cVA forms a steady concentration gradient around the male, resulting in cVA concentration increase at the imaged fly's antennae when the male is closer. This allows ORNs to report male distance in a windless environment, which signal is then split into different sensitivity ranges at the PN level. This differential distance tuning of IPNs and IvPNs might allow improved distance estimation if the two signals are compared by downstream circuits.

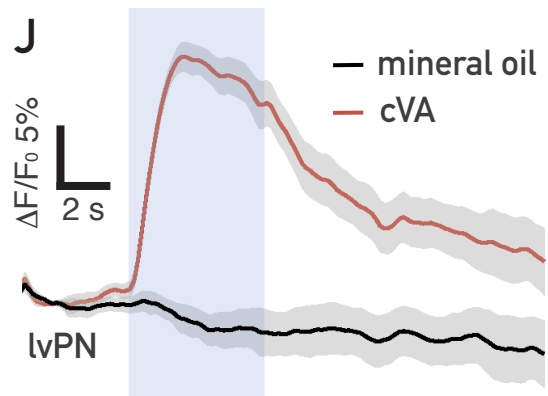
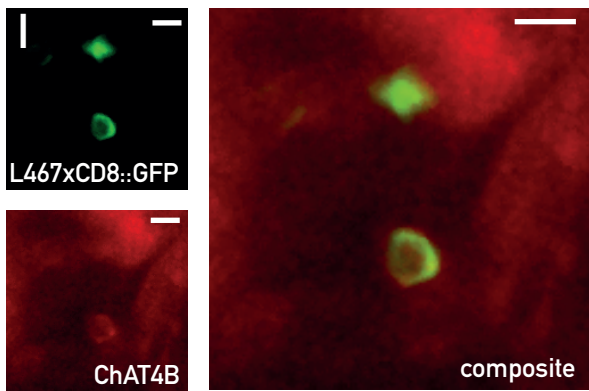
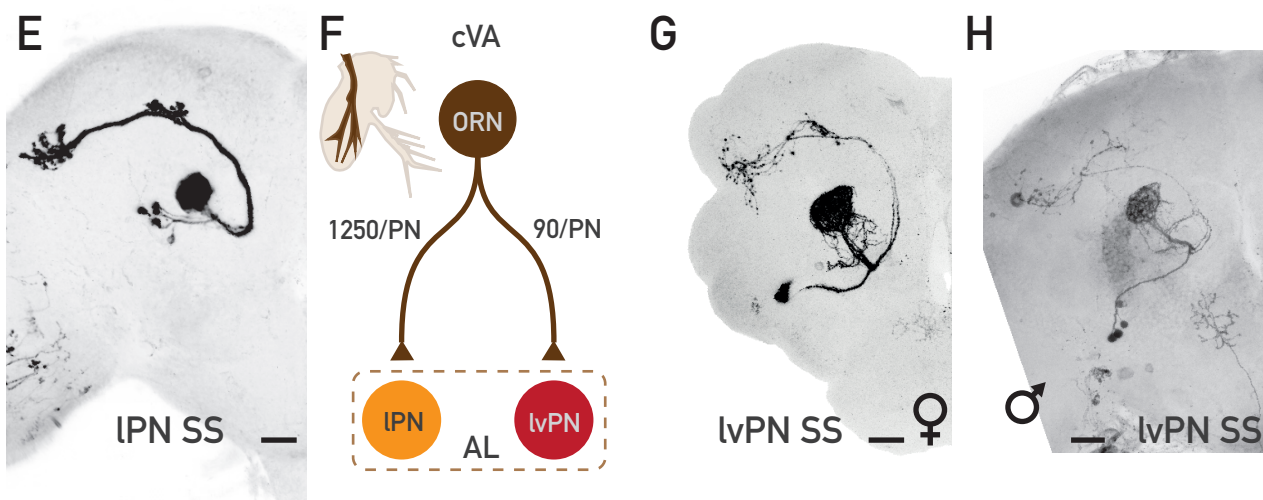
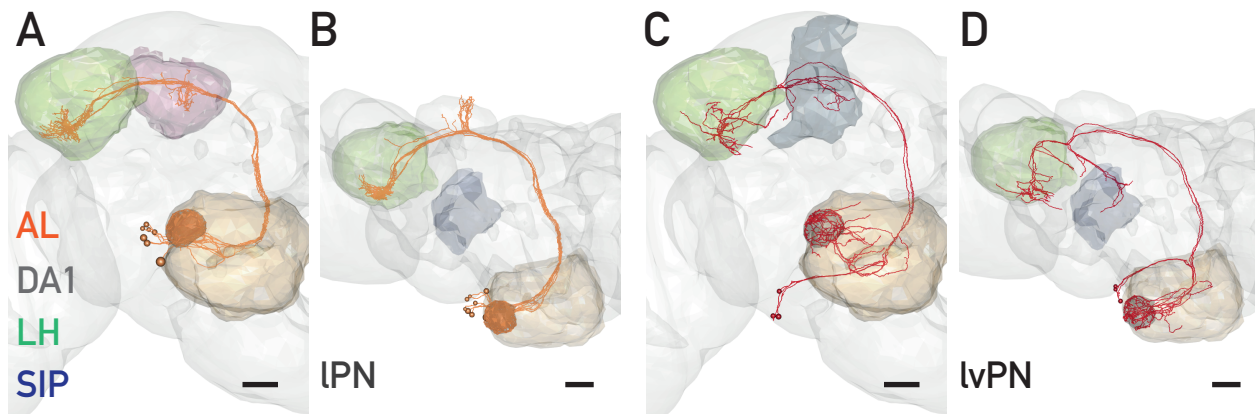


### **Figure 3: A novel PN pathway for cVA**

**A:** EM reconstructions of DA1 IPNs from the right hemisphere of the FAFB dataset; frontal view, AL: antennal lobe, DA1: dorsal anterior (glomerulus) 1, LH: lateral horn, SIP: superior intermediate protocerebrum. **B:** Same as A; dorsal view. **C:** EM reconstructions of DA1 lvPNs from the right hemisphere of the FAFB dataset; frontal view. **D:** same as C; dorsal view. **E:** Confocal image of DA1 IPN in a female brain, reporter expression driven by IPN Stable Split, maximum projection. Image kindly provided by Dr Yoshi Aso. **F:** Circuit diagram of Or67d ORNs, DA1 IPNs, and DA1 lvPNs based on the hemibrain dataset. Top left inset: schematic of an antenna and the antennal nerve. The numbers show the average number of Or67d ORN input synapses per neuron for a PN type. In the hemibrain dataset there are 143 Or67d ORNs (both left and right), 7 DA1 IPNs (right), and 3 DA1 lvPNs (right). **G:** Confocal image of DA1 lvPN in a female brain, reporter expression driven by lvPN Stable Split, maximum projection. **H:** same as G, in a male brain. Scale bars for A, B, C, D, E, G, and H are 20  $\mu\text{m}$ . **I:** Confocal image of co-immunostaining of lvPN somata (top) and ChAT4B enzyme (bottom), single imaging channels on the left, composite image on the right. Scale bars are 5  $\mu\text{m}$ . **J:** GCaMP responses in lvPN axons to cVA and mineral oil presented from an olfactometer. Mean trace from 5 flies, 6 odour presentations each, grey area is SEM.

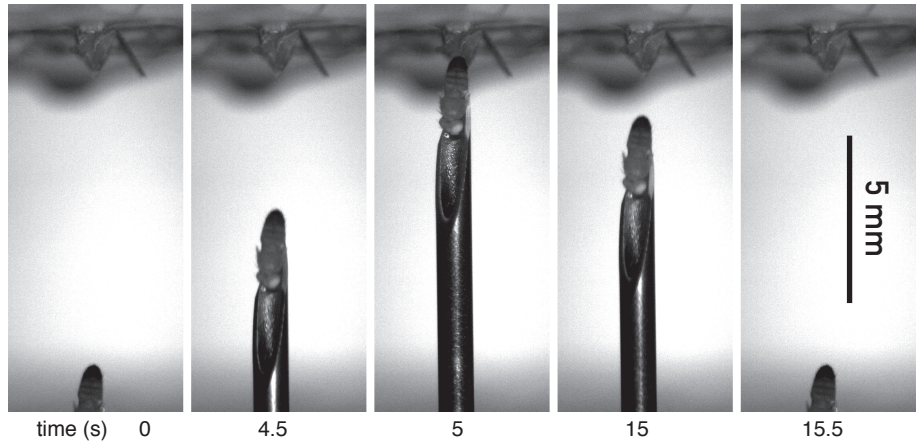
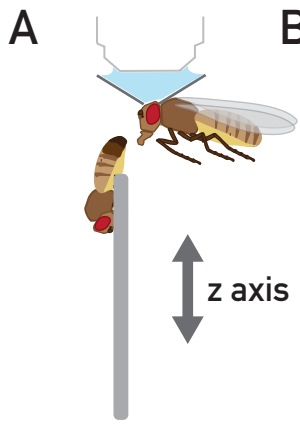


#### **Figure 4: Presenting a male fly as an olfactory stimulus**

**A:** Schematic of the experimental setup for *in vivo* 2-photon imaging and male presentation. A female fly is mounted in a holder under the objective with the head cuticle removed to gain access to the brain for imaging. A male fly is glued onto a metallic needle with the abdomen towards the imaged fly. The wings and legs of the male are removed. An externally triggered micromanipulator moves the male to a predefined location relative to the female's antennae during GCaMP imaging. **B:** Frames from a video recording of the male being moved from 10 mm distance to 0.75 mm and back during an experiment.

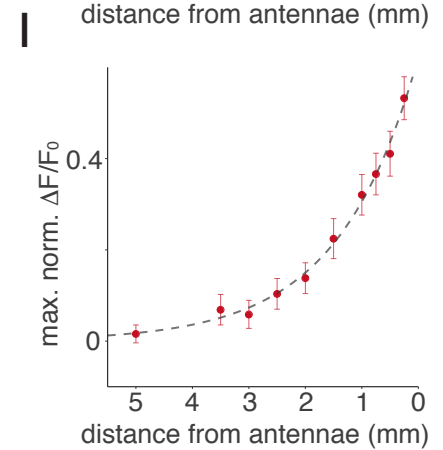
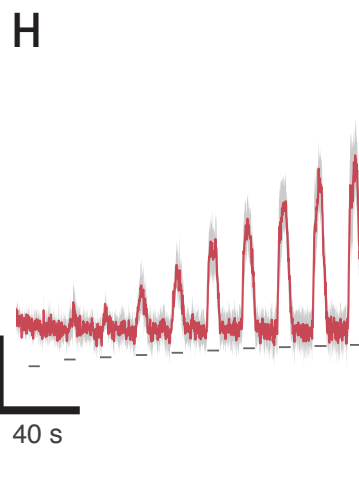
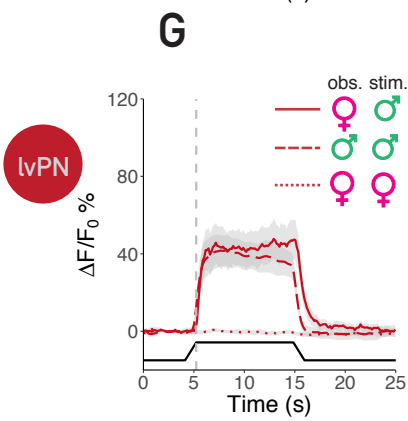
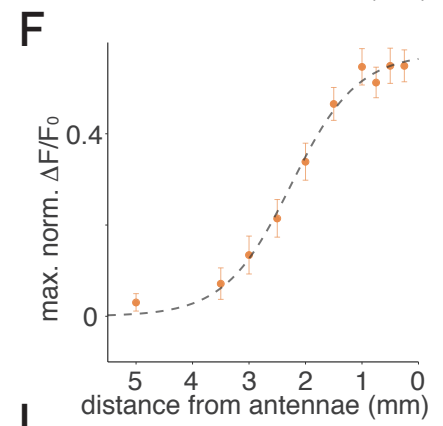
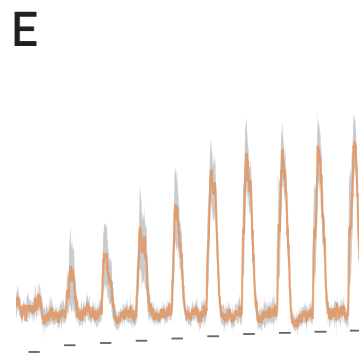
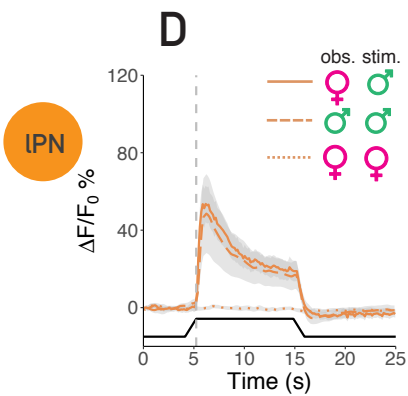
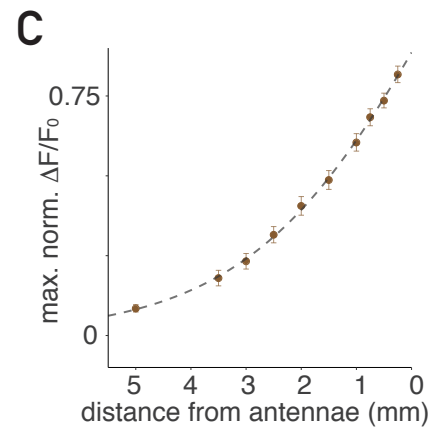
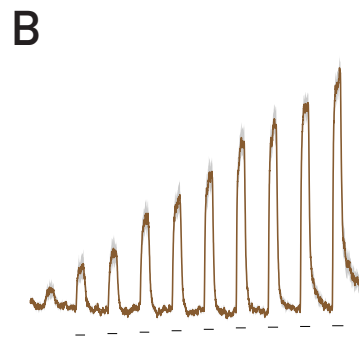
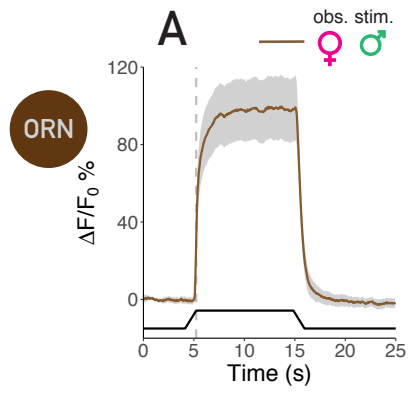


## **Figure 5: ORNs, IPNs, and lvPNs respond to a male fly in a distance dependent manner**

**A:** ORN GCaMP response to moving a male fly from 10 mm to 0.75 mm distance from the antennae of a female fly (imaged fly is female). Mean trace from 10 flies, 6 male presentations each, grey area is SEM. Bottom black trace is the male's position based on a video recording of the presentation, baseline is 10 mm, plateau is 0.75 mm. **B:** ORN GCaMP response to a sequence of ten distance steps ranging from 5 to 0.25 mm, all starting from 10 mm. Mean trace from 10 flies, 3 presentations for all distances, grey area is SEM. **C:** ORN distance tuning curve, responses are the maximum values of the normalised responses for every distance from 10 flies, 3 presentations, error bars are SEM. Residual standard error = 0.0087. **D:** IPN GCaMP responses in females to a male stimulus (solid line), in males to a male stimulus (dashed line) and in females to a virgin female stimulus (dotted line) in axon boutons.  $n = 10, 7, 6$ , respectively. **E:** Same as B, but responses measured in IPN axons;  $n = 9$ . **F:** Same as C, but for IPN responses;  $n = 9$ , residual standard error = 0.020. **G:** Same as D, but responses measured in lvPN axons.  $n = 9, 7, 6$ , respectively. **H:** Same as B, but responses measured in lvPN axons;  $n = 7$ . **F:** Same as C, but for lvPN responses;  $n = 7$ , residual standard error = 0.016.

## **4 cVA as a positional signal**

Intrigued by the PN's sensitivity to detect small differences in a male's distance, we were curious if cVA can be used to infer the angular direction of a male. Such coding would require bilaterally different responses when a male is presented on the side of the fly. As introduced earlier, the behavioural relevance and mechanism of odour lateralisation was described for general odours with highly artificial stimulus presentation paradigms, leaving doubts that this also occurs with real odour stimuli given the tiny (0.25 mm) inter-antennal distance in flies. We asked whether cVA from a male can reach sufficient concentration difference at the antennae to evoke bilaterally different responses.

#### **4.1 A male fly is a lateralised olfactory stimulus**

To test cVA lateralisation we presented a male fly on the two sides of a female sequentially while performing *in vivo* 2-photon calcium imaging to record the activity of ORNs or IPNs on both sides of the female's brain (Figure 6A). We averaged trials from glomeruli on both sides when the male was on the ipsilateral or contralateral side with respect to the imaged glomerulus. We found a strongly lateralised response: ORNs are activated more by ipsilateral male presentation (Figure 6B, D). The mean response is larger for ipsilateral stimulus than for contralateral stimulus (Figure 6E). The lateralisation was similar in IPNs, but the contralateral responses were close to baseline and had a faster decay than responses to ipsilateral stimuli (Figure 6B); neither of which is true for ORNs. This strong lateralisation at both the ORN and PN levels to a natural stimulus with intact antennae suggests that cVA can be used as a positional cue not only for male distance but potentially also for angular position.

Given that ORNs innervate the antennal lobes bilaterally, the previous experiment measured combined activity of left and right ORNs, yet there was a stronger response to ipsilateral presentation. In order to understand how these responses are built we performed antennal block experiments by sealing one antenna with a fast curing low-toxicity adhesive before male presentation. Blocking an antenna means that we measure the responses from ORNs originating from one antenna that innervate both hemispheres, therefore we expect responses on both sides of the brain. When we imaged from glomeruli that had the contralateral antenna blocked we did not see a change in response magnitude or in the ratio of responses evoked by an ipsi- and contralateral male stimulus (Figure 6F, G). Imaging from glomeruli with the ipsilateral antenna blocked decreased the response magnitude to both stimuli, and reversed the lateralisation: a contralateral stimulus evoked a stronger response

(Figure 6H, I). This is in agreement with the fact that the ORNs imaged in this condition originate from the intact, contralateral antenna, which is closer to a stimulus presented on the contralateral side, resulting in a higher cVA concentration. If ORN responses are lateralised with a single intact antenna, as we observed, we can conclude that cVA is low volatility enough to produce a detectable concentration difference even at the short inter-antennal distance of flies. This is in line with the ORN responses being different at 1000, 750, 500, and 250  $\mu\text{m}$  distances, as shown in Figure 5C.

#### **4.2 IPN lateralisation is dependent on an active mechanism**

We saw that with intact antennae, IPNs show a larger bilateral contrast than ORNs (Figure 6J), suggesting that there may be an active circuit mechanism underlying this increased difference. Blocking an antenna had strikingly different effects on IPN responses. Lacking contralateral inputs rendered the lateralisation less efficient in IPNs, with smaller than control responses to ipsilateral and larger than control responses to contralateral stimulation (Figure 7D, E). This suggests that blocking the contralateral input not only affects the contralateral ORN input – rendering ipsilateral responses smaller, but also releases an inhibition on the IPNs – making responses to contralateral stimuli larger. In this layout, depending on the exact position of the stimulus the net effect of contralateral inputs onto IPNs might be excitatory (ipsilateral stimulus) or inhibitory (contralateral stimulus). Accordingly, blocking the ipsilateral antenna caused the responses to be smaller and more transient than in control, and the contralateral excitation was followed by sustained inhibition of IPNs (Figure 7F, G). When we present the male in front of the female (the same protocol as in Figure 5E), blocking an antenna results in an artificially lateralised stimulus, as only one antenna senses cVA. IPN responses decreased by blocking the ipsilateral antenna, while blocking the contralateral antenna caused an even more pronounced inhibition than we saw with the lateralisation protocol (Figure 7H-J). These data strongly suggest that IPN lateralisation depends on a contralateral inhibition mechanism, however the exact nature of the inhibition is unclear: it could be a direct synaptic effect onto IPN dendrites or potentially a presynaptic mechanism inhibiting ORN axons. This is surprising, as previous work found no evidence of GABA antagonists affecting odour lateralisation ability, and that lateralisation has a presynaptic origin in DM6 PNs (Gaudry et al. 2013).

### 4.3 il3LN6, a candidate for contralateral inhibition

What could be the circuit substrate of this apparent contralateral inhibition on DA1 IPNs? A comprehensive description of the fly olfactory system pointed out a pair of antennal lobe local neurons, il3LN6 as a potential source of contralateral inhibition based on its connectivity (Schlegel et al. 2021). il3LN6 bilaterally innervates the AL and forms arbours in most glomeruli (Figure 9A, C, D). Importantly this local neuron receives biased input from ORNs: more synapses from contralateral ORNs than from ipsilateral ones, atypical of ALLNs, and is presynaptic to PNs (Figure 9F). We used a GAL4 driver from the Vienna Tiles collection to gain genetic access to il3LN6 neurons (Tirian and Dickson 2017), and expressed GFP to perform co-immunostaining with GABA. We observed co-labelling with GABA at the il3LN6 soma (Figure 9B), therefore this cell type is likely to be GABAergic and inhibitory.

Next we recorded calcium responses from il3LN6 neurons, specifically from the arbours in the DA1 glomerulus on both sides, using the lateralisation stimulus protocol we showed earlier with ORNs and IPNs. il3LN6 showed inverted lateralisation to a male in the DA1 glomerulus: a contralateral stimulus evoked a larger response (Figure 8D, E). This is consistent with the connectivity: contralateral ORNs provide more than five times as many synapses to il3LN6 than ipsilateral ones. Blocking the contralateral antenna caused il3LN6 responses to completely disappear (Figure 8F, G), indicating that only the contralateral ORN input is functional. In line with this, blocking the ipsilateral antenna had no effect on either the size of the responses or the lateralisation ability of il3LN6 (Figure 8H, I).

We did not observe responses in il3LN6 in other glomeruli than DA1 (data not shown), suggesting that this neuron is highly compartmentalised and operates independently in glomeruli. Indeed, the neuron that is considered to be the larval equivalent of il3LN6 was recently reported to show compartmentalised odour responses in first instar larva (Si et al. 2021). Similarly high level of compartmentalisation was observed in an amacrine cell in the fly and it was shown that tortuous branching and loops in the arbour facilitate the necessary electrotonic separation of the arbours of a single cell (Meier and Borst 2019). Similarly to this amacrine cell, il3LN6 neurites form many loops where branches follow a tract for a while only to turn back; also il3LN6 splits into branches far outside the AL which then continue in the same tract parallel to each other. In general the splitting of il3LN6 neurites happens much earlier than the actual spatial separation of these branches (Figure 9E). These anatomical

features and responses to lateralised male presentation are consistent with a model where il3LN6 performs contralateral inhibition in a glomerulus specific manner.

To assess how general this computation could be in other olfactory channels we compared the ratio of contra- and ipsilateral ORN inputs to il3LN6 and the fraction of inputs from il3LN6 to canonical uniglomerular PNs for all glomeruli. Both of these measures are indicators of potential contralateral inhibition efficiency via il3LN6. DA1 IPNs receive a higher than average proportion of their inputs from il3LN6, but in other glomeruli like DC2, and VC1 PNs also get strong il3LN6 inputs while the ORN contra-ipsi bias is stronger in these odour channels than in DA1 (Figure 9G). Importantly, DM6 PNs receive very little il3LN6 input, consistent with earlier work by Gaudry et al (2013), where they showed that GABAergic blockade does not affect lateralisation in DM6 PNs. These together suggest that il3LN6 could have a similar role in other glomeruli as in DA1, likely to enhance lateral contrast of selected odours.

A recent study suggested that contralateral inhibition plays a role in enhancing lateral contrast of odours in third-order lateral horn neurons, and suggested that this inhibition is presynaptic at the PN-LHN synapse (Mohamed, Hansson, and Sachse 2019) feedback mechanisms originating from the LHN level, however they did not investigate the possibility of an inhibition mechanism in the antennal lobe.

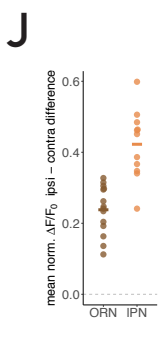
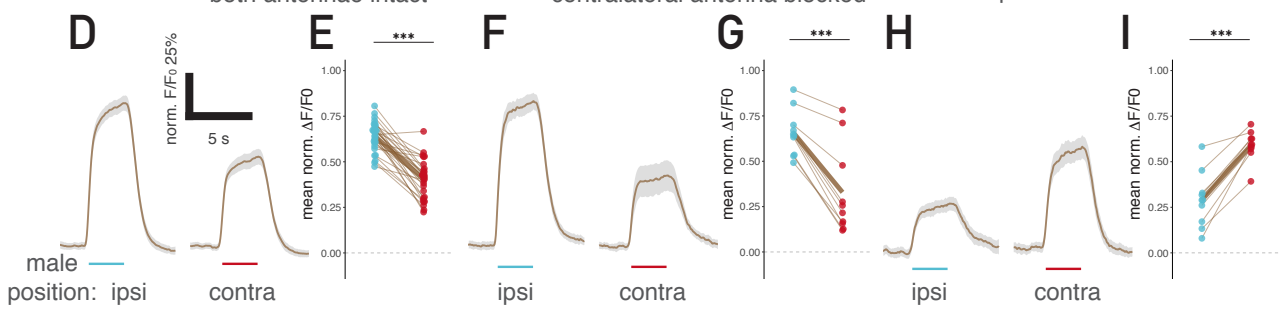
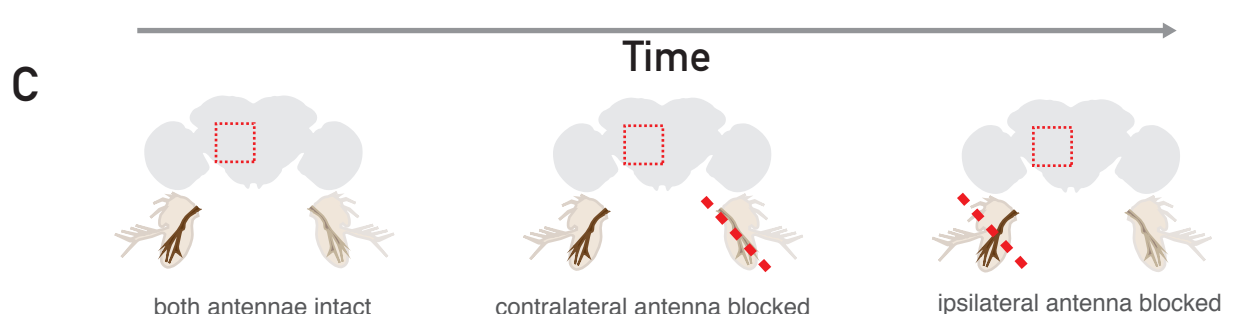
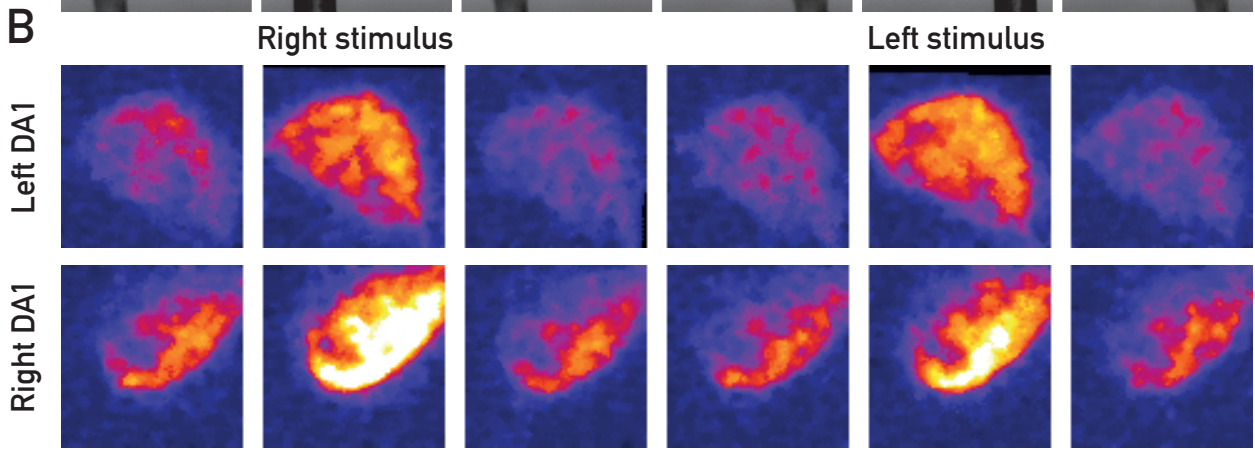
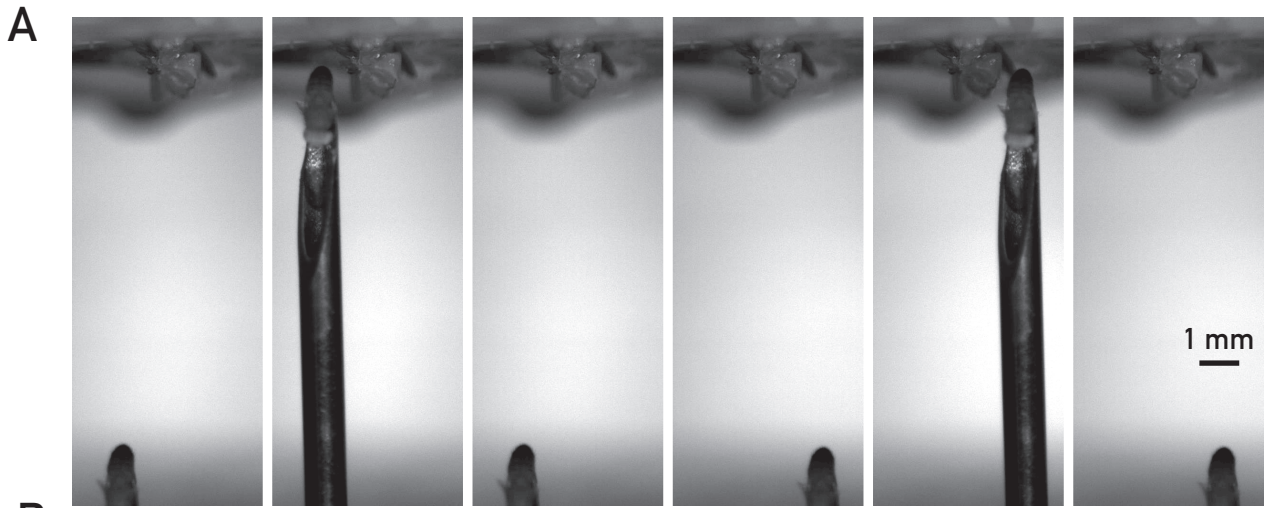
#### **4.4. Decoding position from a pheromone signal**

Encoding male distance and angular direction is sufficient to create a representation of male position in 2D space. IPN responses to a male are distance dependent and clearly lateralised. To test 2D positional coding we presented the male at sixteen positions which were defined by the centerpoints of a hexagonal lattice around the imaged fly (Figure 10A). This protocol sampled the space at 1, 1.732, and 2 mm distances, and at 30° steps in the range between -150° to +150° angular positions (with 0° being the direction that the fly faces). We imaged the IPNs on both sides of the brain and found that responses show a spatial gradient with strongest responses with the male presented closest (1 mm) and slightly ipsilateral (30° or 60°) with respect to the imaged PN (Figure 10A). We then calculated mean responses for eleven angles at 1.7 mm distance (six of these means are direct measurements, five of them are based on interpolation from responses at 1 and 2 mm distance, see Methods). Left and right IPNs show symmetric angular tuning: responses were larger for stimulation ipsilateral to

the imaged PN, and identical for both sides when the male was in front of the fly (Figure 11A).

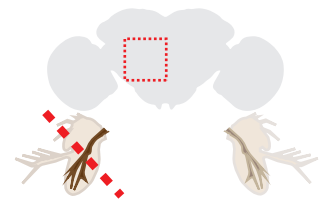
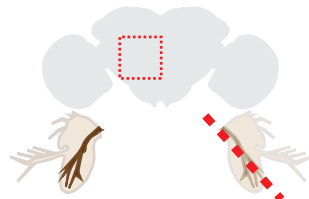
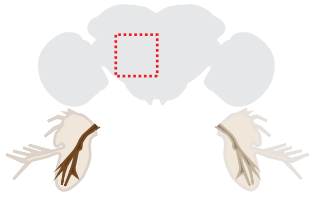
Could the fly infer a male's angular direction by using IPN responses from both sides of the brain? We found that the difference and the sum of the left and right responses strongly correlate with the sine and the cosine of the male's angular position (Figure 11B, C, E, F). The sine and the cosine together give a unique solution to angular position around a full rotation of a circle. The difference and the sum of bilateral IPN responses therefore provide measures to predict a male's angular direction. Moreover, the sine and cosine of an angle are equal to the Cartesian  $x$  and  $y$  coordinates of a point on the unit circle. We devised a bivariate linear model using IPN responses from the two hemispheres, where the difference and the sum of the right and left IPN responses are used as predictors, and the male's  $x$  and  $y$  position are the response variables. This model accurately predicts stimulus position when given the response of left and right PNs (Figure 10D median error 1.3 mm). For angular direction the median prediction error was  $26^\circ$  (Figure 10G). This model shows that, using IPN responses from both sides of the brain, a fly could estimate a male's angular position based only on cVA information.

In this chapter we focussed on IPNs and did not characterise lvPNs, yet their contribution to positional coding will be interesting to explore in the future.



## Figure 6: cVA lateralisation in ORNs does not depend on bilateral input

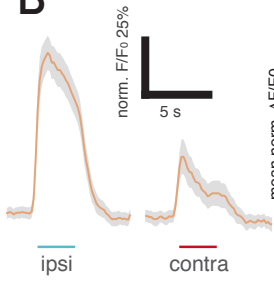
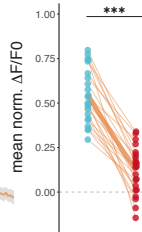
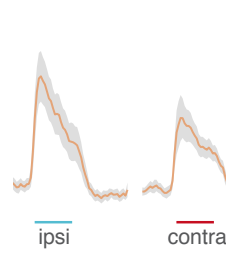
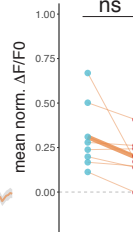
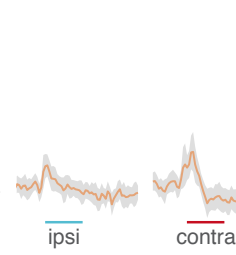
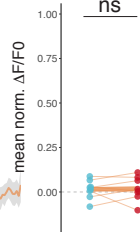
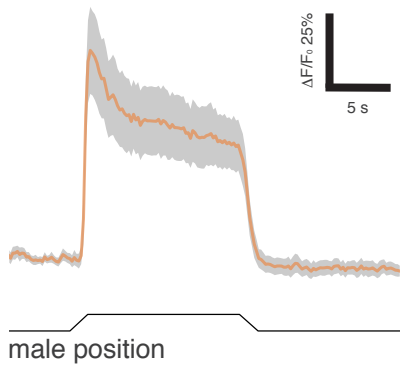
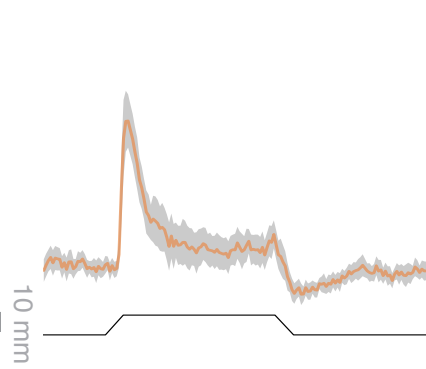
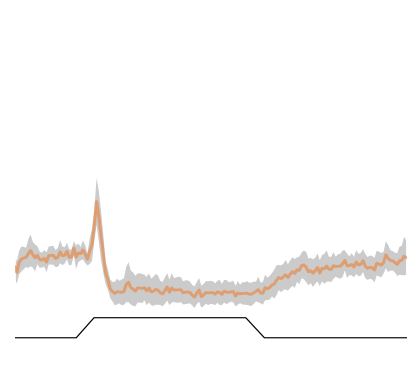
**A:** Frames from a video recording of the male being moved first to the right, then to the left side of the imaged fly during a lateralisation experiment. **B:** Representative 2-photon images of Or67d ORN GCaMP signal from a left (top row) and right (bottom row) DA1 glomerulus at the time points shown in A. Warmer colours indicate higher signal intensity. **C:** Schematics of antennal manipulations with respect to an imaging ROI (red square over the antennal lobe). Left: both antennae intact, middle: contralateral antenna relative to the imaging ROI is blocked, right: ipsilateral antenna relative to the imaging ROI is blocked. **D:** ORN GCaMP response to ipsilateral and contralateral male presentation. The male is presented during the time marked by blue and red horizontal bars. Mean traces from 14 flies, 6 presentations for both sides, grey area is SEM. **E:** ORN GCaMP mean during ipsi- (blue) and contralateral (red) male presentation. One datapoint is the average of 6 presentations from a hemisphere (1 ROI / hemisphere);  $n = 28$ , unpaired t-test  $p < 0.001$ . **F:** Same as D, but the contralateral antenna is blocked,  $n = 10$ . **G:** Same as E, but the contralateral antenna is blocked;  $n = 10$ , unpaired t-test  $p < 0.001$ . **H:** Same as D, but the ipsilateral antenna is blocked,  $n = 10$ . **I:** Same as E, but the ipsilateral antenna is blocked;  $n = 1$ , Wilcoxon-test  $p < 0.001$ . **J:** Bilateral contrast is larger in IPNs than in ORNs. Bilateral contrast was calculated as the difference of mean responses to ipsi- and contralateral male presentation.

**A**

both antennae intact

contralateral antenna blocked

ipsilateral antenna blocked

**B****C****D****E****F****G****H****I****J**

## Figure 7: cVA lateralisation in IPNs depends on bilateral input

**A:** Schematics of antennal manipulations with respect to an imaging ROI (red square over the antennal lobe). Left: both antennae intact, middle: contralateral antenna relative to the imaging ROI is blocked, right: ipsilateral antenna relative to the imaging ROI is blocked. **B:** IPN GCaMP response to ipsilateral and contralateral male presentation measured in the calyx axons. The male is presented during the time marked by blue and red horizontal bars. Mean traces from 10 flies, 6 presentations on both sides, grey area is SEM. **C:** IPN GCaMP response mean during ipsi- (blue) and contralateral (red) male presentation. One datapoint is the average of 6 presentations from a hemisphere;  $n = 20$ , Wilcoxon-test  $p < 0.0001$ . **D:** Same as B, but the contralateral antenna is blocked,  $n = 8$ . **E:** Same as F, but the contralateral antenna is blocked;  $n = 8$ , unpaired t-test  $p = 0.348$ . **F:** Same as B, but the ipsilateral antenna is blocked,  $n = 8$ . **G:** Same as C, but the ipsilateral antenna is blocked;  $n = 8$ , unpaired t-test  $p = 0.717$ . **H:** IPN GCaMP response to moving the male from 10 mm to 0.75 mm distance from the antennae. Mean trace from 8 flies, 6 male presentations each, grey area is SEM. Bottom black trace is the male's position based on a video recording of the presentation, baseline is 10 mm, plateau is 0.75 mm. This same data is included in the trace shown in Figure 5D. **I:** same as H, but the contralateral antenna is blocked. **J:** same as H, but the ipsilateral antenna is blocked.

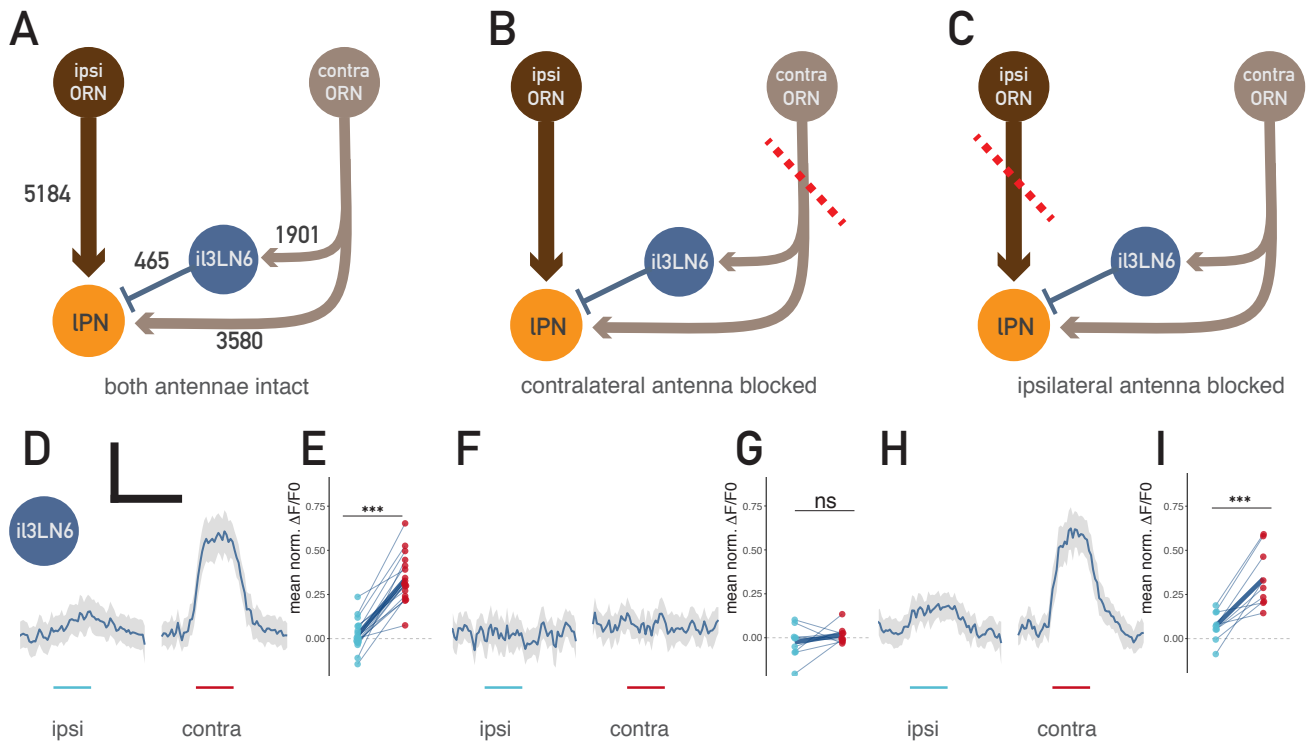


## **Figure 8: il3LN6 shows bilateral contrast with larger contralateral responses**

**A:** Simplified circuit diagram of the ORN, IPN, il3LN6 circuit based on the hemibrain dataset. ORN interconnectivity is not shown. Numbers show the number of synaptic connections between the two connected cell-types. **B:** The effect of contralateral antenna block on the circuit in A. **C:** The effect of ipsilateral antenna block on the circuit in A. **D:** il3LN6 GCaMP response to ipsilateral and contralateral male presentation measured in the DA1 glomerulus. The male is presented during the time marked by blue and red horizontal bars. Mean traces from 11 flies, 6 presentations for both sides, grey area is SEM. **E:** il3LN6 GCaMP mean response during ipsi- (blue) and contralateral (red) male presentation. One datapoint is the average of 6 presentations from a hemisphere;  $n = 22$  Wilcoxon-test  $p < 0.001$ . **F:** Same as D, but the contralateral antenna is blocked,  $n = 9$ . **G:** Same as E, but the contralateral antenna is blocked;  $n = 9$ , two sample t-test  $p = 0.39$ . **H:** Same as D, but the ipsilateral antenna is blocked;  $n = 9$ , two sample t-test  $p < 0.001$ . **I:** Same as E, but the ipsilateral antenna is blocked,  $n = 9$ .

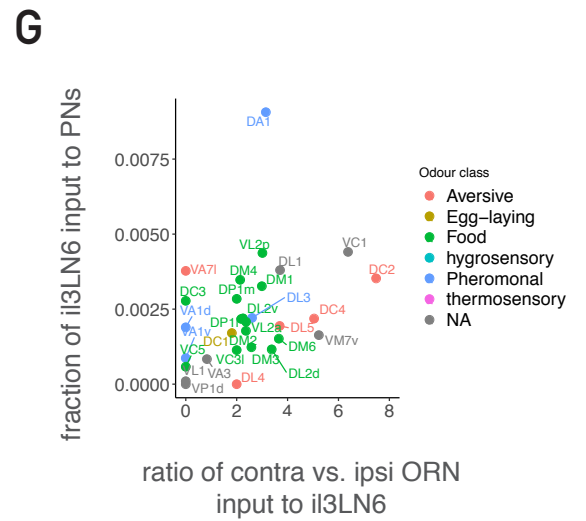
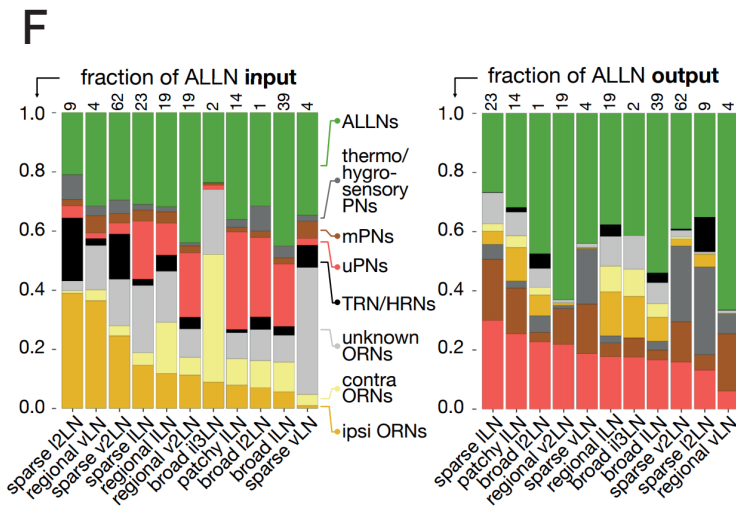
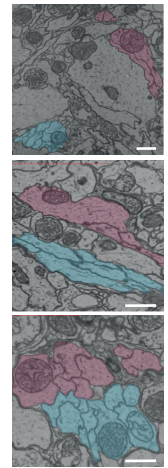
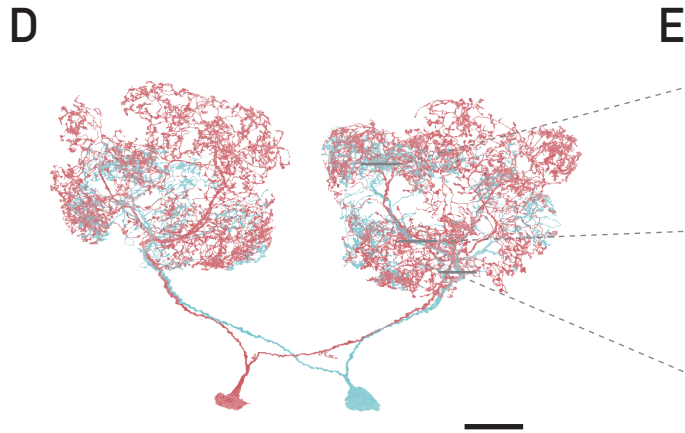
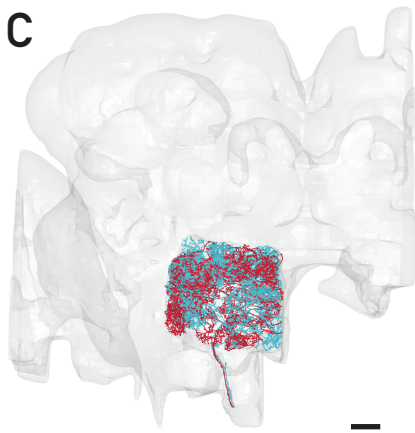
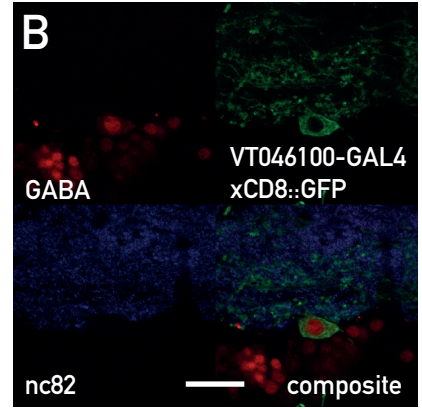
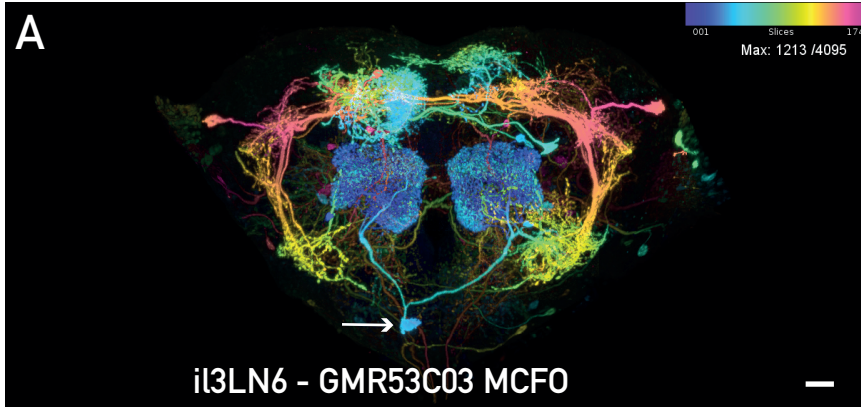


## **Figure 9: il3LN6, a candidate ALLN for enhancing odour lateralisation**

**A:** Colour coded mean intensity projection of a brain labelling a single il3LN6 with MCFO using 53C03-GAL4, image acquired and processed by FlyLight at Janelia Research Campus. Arrow indicates il3LN6 soma. **B:** Confocal image of co-immunostaining of an il3LN6 soma and GABA, imaging channels are GABA: red, nc82 neuropil stain: blue, VT046100-GAL4: green. **C:** EM morphology of il3LN6 arbores in the right antennal lobe from the hemibrain dataset, red: right il3LN6, blue: left il3LN6. **D:** Same as C but from the FAFB dataset, reconstructed with FlyWire, white lines represent locations where EM sections were taken for E. Scale bars for A, B, C and D are 20  $\mu\text{m}$ . **E:** ssTEM sections from the FAFB dataset showing multiple profiles in a tract that belong to the pair of il3LN6, colours as in D. The place of sections relative to the neuron's morphology is shown in D. Scale bars are 750 nm. **F:** Input (left) and output (right) connectivity of major LN classes with AL neuron types from the hemibrain dataset. The il3LN class consists of the pair of il3LN6 neurons only. Adapted from Schlegel et al. (2021) Figure 5. **G:** Lateralisation measures based on connectivity for glomeruli: x axis shows the ratio of contralateral and ipsilateral ORN input to il3LN6 in a glomerulus, y axis shows the fraction of il3LN6 inputs to canonical, uniglomerular PNs in a glomerulus. For glomeruli where the contra / ipsi ORN input ratio is shown as zero the real value is unknown due to limitations in assigning ORNs into contra- or ipsilateral groups. Glomeruli are coloured by the ethological relevance of odours that activate them according to Huoviala et al. (2018).

A

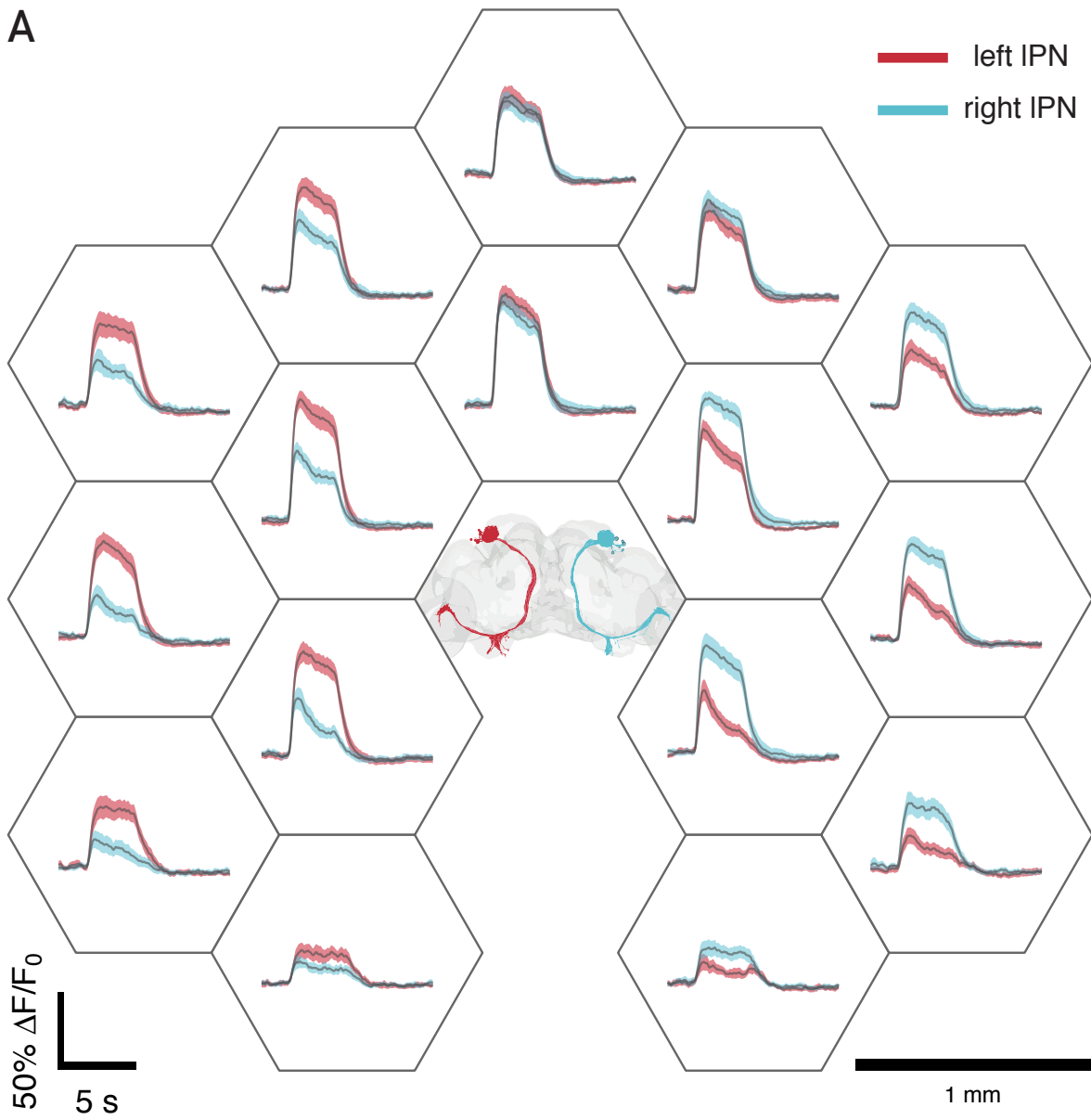


### **Figure 10: IPNs encode angular position**

**A:** GCaMP6 responses of left (red) and right (cyan) IPN dendrites to male presentations. Positions of the male during the stimulation protocol are indicated by the centerpoints of the hexagons around the respective responses. Positions are at 1, 1.732, and 2 mm distances, and at 30° steps in the range between -150° to +150° angular positions; the fly faces 0°, negative angles are on the left, positive angles on the right side. The position of the imaged female fly is indicated by the brain volume in the centre (top view), IPNs colored based on their side as the corresponding GCaMP traces. Average response from 8 flies, 3 trials, shaded area is SEM. Scale bar: 1 mm.

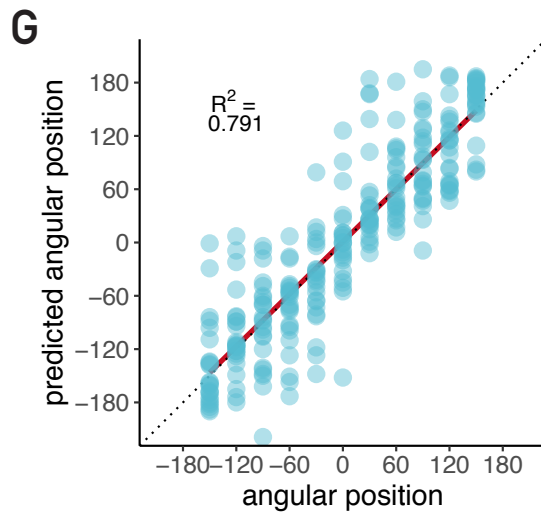
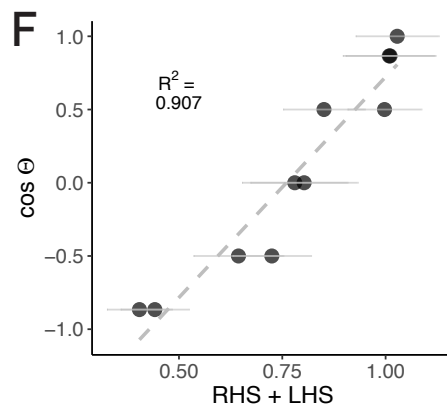
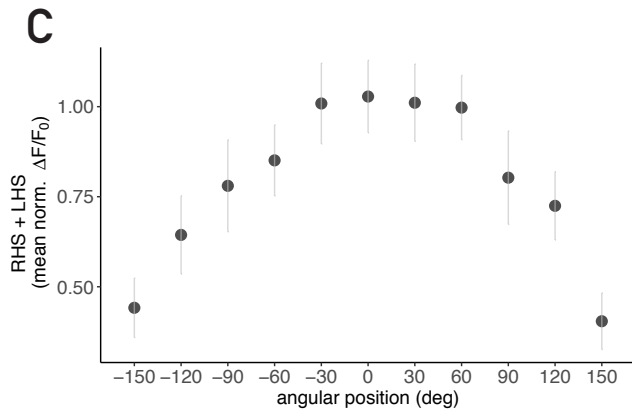
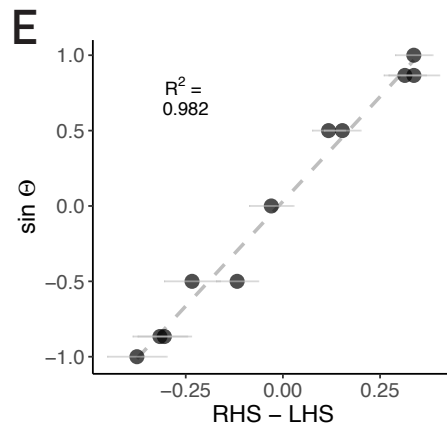
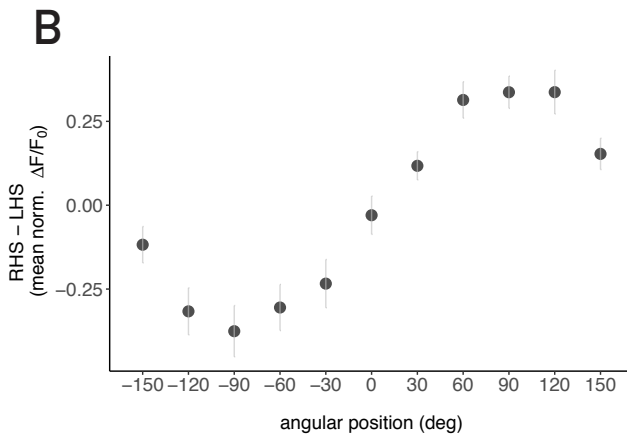
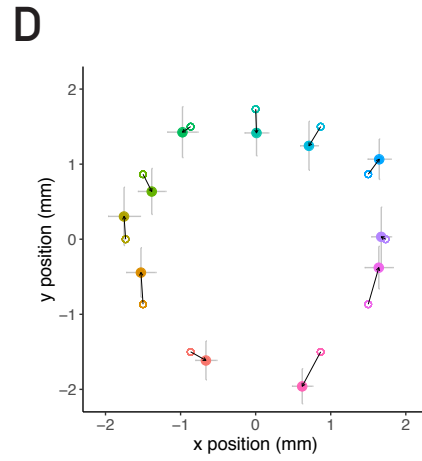
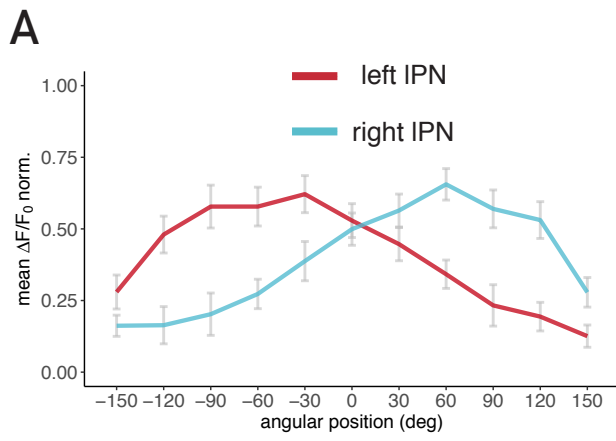


## Figure 11: Decoding male position from left and right IPN responses

**A:** Angular tuning curves of left (red) and right (cyan) IPNs based on A. Six of these positions are direct measurements, five of these (at angles  $-120^\circ$ ,  $-60^\circ$ ,  $0^\circ$ ,  $+60^\circ$ ,  $+120^\circ$ ) are based on linear interpolation from responses at 1 and 2 mm at these angular directions (see Methods). Error bars are SEM. **B:** The difference of mean right and left IPN responses at given male angular positions. Error bars are SEM. **C:** The sum of mean right and left IPN responses at given male angular positions. Error bars are SEM. **D:** A linear model predicts male position based on bilateral IPN responses. Model formula in Wilkinson notation:  $(x, y) \sim (\text{IPN}_R - \text{IPN}_L) + (\text{IPN}_R + \text{IPN}_L)$ . Where  $x$  and  $y$  are the Cartesian coordinates of the male fly, and  $\text{IPN}_R$ ,  $\text{IPN}_L$  are right and left IPN responses, respectively. The predicted position is calculated from the  $x$  and  $y$  predictions for single trials from (A). Small circles show the original positions, large points show the mean predictions by positions of the model with SEM error bars. Mean error of position prediction in mm, mean: 1.46, median: 1.28. **E:** The difference of right and left IPN responses correlates with the sine of the male angular position.  $R^2 = 0.982$ , dashed line shows linear fit. **F:** The sum of right and left IPN responses correlates with the cosine of the male angular position.  $R^2 = 0.907$ , dashed line shows linear fit. **G:** Using the model in D, predicted male angular positions correlate with the actual angular position,  $R^2 = 0.791$ . Red solid line shows the linear fit, the dotted line shows  $x = y$ . Prediction error in angles, mean =  $35^\circ$ , median =  $26^\circ$ .

## **5 Separation of positional and identity information at third order neurons**

We demonstrated that IPN responses reflect male distance, and bilateral comparison of IPN activity can inform a fly about the male's angular position, while lvPNs tonically respond to cVA on a male, ideal for signalling the presence of a male. How is this information read out by downstream circuits? We chose third order neuron types postsynaptic to one of the PNs to investigate this question. AV2a2 is a sexually monomorphic, lateral horn output neuron projecting to the SIP (Figure 12H) with strong IPN input (115 synapses across 4 AV2a2 neurons, numbers from the hemibrain), and we can access it genetically by two driver lines (Figure 12I, J). Downstream to lvPNs, we found pC1 neurons (59 synapses across 5 pC1 neurons), a well known *doublesex*<sup>+</sup> sexually dimorphic cluster (Figure 14F, G) which integrate cVA with male courtship song and bidirectionally regulate female receptivity: activating these neurons promotes, silencing these neurons abolishes mating in females; furthermore pC1 also regulates female aggression (Zhou et al. 2014; Deutsch et al. 2020; Schretter et al. 2020).

### 5.1 Extracting male approach speed information from cVA

A single presentation of a male for 10 s evoked a transient response in AV2a2 dissimilar to the response of upstream IPNs (Figure 12D). The observation that AV2a2 filters out the sustained component of the IPN response suggests that they selectively respond to an increase in IPN activity. To test this hypothesis we varied the approach speed of the male stimulus, aiming to evoke a slower rise in IPN activity. We measured responses in ORNs, IPNs, and AV2a2 to three approach speeds. ORNs of another glomerulus were shown to code both odour concentration and the speed of change in odour concentration (A. J. Kim, Lazar, and Slutskiy 2011), but how downstream circuits read these streams of information out is unclear (Wilson 2013). In ORNs and IPNs we observed a speed-dependent rise-time in intracellular calcium, but no difference in maximal responses with different approach speeds (Figure 12B, C, E, F). In contrast, peak responses were strongly dependent on approach speed in AV2a2 (Figure 12D, G).

How is IPN activity transformed to create the responses observed in AV2a2? By taking the differential of the IPN trace we found that its positive part is qualitatively similar to the AV2a2 responses (Figure 13A). Furthermore the size of the peaks on the IPN differential trace are strongly correlated with the evoked peaks in AV2a2 at different speeds (Figure 13C). This correlation suggests that AV2a2 acts as a differentiator on IPN responses. As the first derivative of position is speed, taking the differential of the IPN's male distance signal

allows AV2a2 to represent male speed. A differentiation would also signal (with a negative deflection) when the male is moving away (also see Figure 13A). The fact that this is not present in AV2a2 responses might be a result of low baseline activity in these neurons, in which case an inhibition is not detected by a calcium sensor. These results indicate that AV2a2 is selectively tuned to encode the speed of an approaching male, an example of extracting specific features of positional information relayed by IPNs.

## 5.2 Tonic cVA response persists downstream of lvPNs

We tested the response of a cell type downstream of lvPNs, pC1, to sustained presentation of a male. pC1 neurons were tonically activated over a 10 s period by a male, and showed little adaptation. This is in stark contrast with the responses observed on the IPN - AV2a2 pathway, and may suggest that pC1, following lvPNs, could signal male presence rather than fast changes in cVA concentration. pC1 was shown to respond to cVA (Zhou et al. 2014), but the circuit responsible for this was unknown. The connection from lvPN to pC1 is present in the hemibrain and both sides of the FAFB dataset (59, and 73 connections on one hemisphere, respectively). To test whether lvPNs are sufficient to activate pC1s we expressed CsChrimson under the control of lvPN-SS and recorded calcium activity in pC1s by expressing GCaMP7f driven by *dsx*-LexA while imaging at a pC1 specific location in the brain. When we activated CsChrimson in lvPNs we observed an increase in pC1 calcium level (Figure 14E). This shows that the lvPN - pC1 synapse is functional, but we cannot exclude that other pathways contribute to responses in pC1 when presented with a male fly.

## 5.3 Distinct behavioural effects by positional and identity signals

To understand the behavioural relevance of these parallel cVA pathways we used a courtship assay and activated these neurons in females optogenetically via expressing CsChrimson, a red-light gated cation channel. We measured mating latency, tracked the position of flies and their wings using Caltech FlyTracker (Eyjólfsdóttir 2014), and developed classifiers for modules of sexual behaviours in JAABA (Kabra et al. 2013). Activating IPNs did not affect mating rate, while lvPN activation decreased the latency to copulation and the number of pairs copulated (Figure 15A, D). This implies that the receptivity increasing effect of cVA in females can be attributed to lvPNs but not to IPNs. Genetically ablating these neurons by expressing apoptosis promoting genes showed consistent effects: IPN ablation did not affect female receptivity, while lvPN ablation made females mate less and later (Figure

15B, E). The effects on female receptivity by lvPN mimic manipulations of pC1 neurons (Figure 15H, I, reproduced from Zhou et al. 2014). In contrast, the IPN downstream AV2a2 differed in its effect from IPNs. Both optogenetic activation of AV2a2, and silencing by constitutive expression of an inward rectifying potassium channel (Kir2.1) resulted in decreased female mating rate.

The direct and constant activation of AV2a2 neurons interferes with the neurons' ability to signal an approaching male, hence perturbs female behaviour. Hyperpolarising AV2a2 could lead to a very similar effect on neuronal activity, that is in line with the similar behavioural phenotype. These results show that, while manipulation of the lvPN - pC1 pathways bidirectionally regulates female receptivity, a similar manipulation of IPNs and AV2a2 has either no effect, or disrupted female behaviour by both activation and inhibition. This is in line with a role for lvPN and pC1 with a role in signalling male quality, and a role for IPN and AV2a2 in positional coding where temporal changes in activity are necessary for informative signalling. A limitation of our behavioural experiments with AV2a2 neurons is that a sparse driver line, 53A03-GAL4 (Figure 12I), used for calcium imaging had motor defects when crossed to CsChrimson (data not shown), therefore we used a split-GAL4 line from Dolan et al. 2018, which labelled other LHNs and two pairs of bilateral neurons innervating the lateral accessory lobes. We cannot rule out the possibility that the behavioural effects seen with this line are partially, or completely due to these neurons.

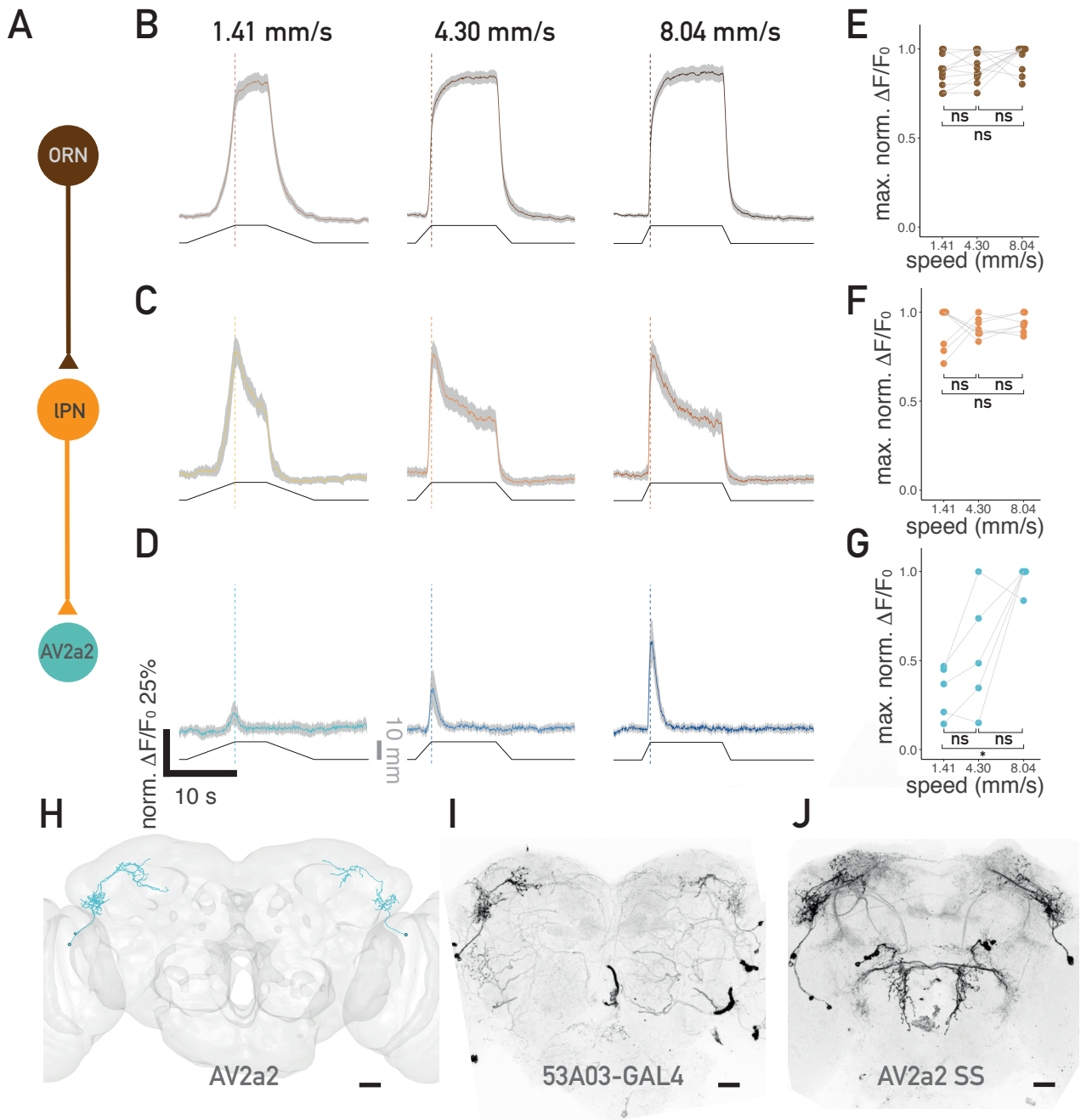


## **Figure 12: AV2a2 responds to male approach in a speed dependent manner**

**A:** Circuit schematic of Or67d ORNs, DA1 IPNs and AV2a2 LHNs. **B:** ORN response traces to moving a male from 10 mm to 0.75 mm distance from the antennae at different speeds; speeds shown at the top. Mean traces from 11 flies, 6 presentations each, grey area is SEM. Bottom black trace is the male's position based on a video recording of the presentation, baseline is 10 mm, plateau is 0.75 mm, dashed line shows the male's arrival time. (The trace for the highest speed is the same as Figure 5A.) **C:** Same as B but for IPNs. Imaged in the MB calyx axons. (n = 7) **D:** Same as B but for AV2a2 neurons. Imaged in the SIP axons. (n = 5) **E:** ORN mean maximal responses to male presentations at different speeds, based on data shown in B. Lines connect values from the same fly. Statistical significance was tested by pairwise Wilcoxon test followed by Bonferroni-correction for multiple comparisons. **F:** Same as E, but for IPNs based on data shown in C. **G:** Same as E, but for AV2a2 neurons based on data shown in D. Responses to 1.41 mm/s and 8.04 mm/s are significantly different (p = 0.029). **H:** EM reconstructions of AV2a2 neurons from the FAFB dataset **I:** Confocal image of AV2a2 in a female brain, reporter expression driven by 53A03-GAL4, the driver used for measurements in D, maximum projection. **J:** Confocal image of AV2a2 in a female brain, reporter expression driven by AV2a2 SS, the driver used in Figure 15, maximum projection. Scale bars in H, I, and J are 20  $\mu$ m. The images presented in panels I and J were contributed by Dr Dana Galili.

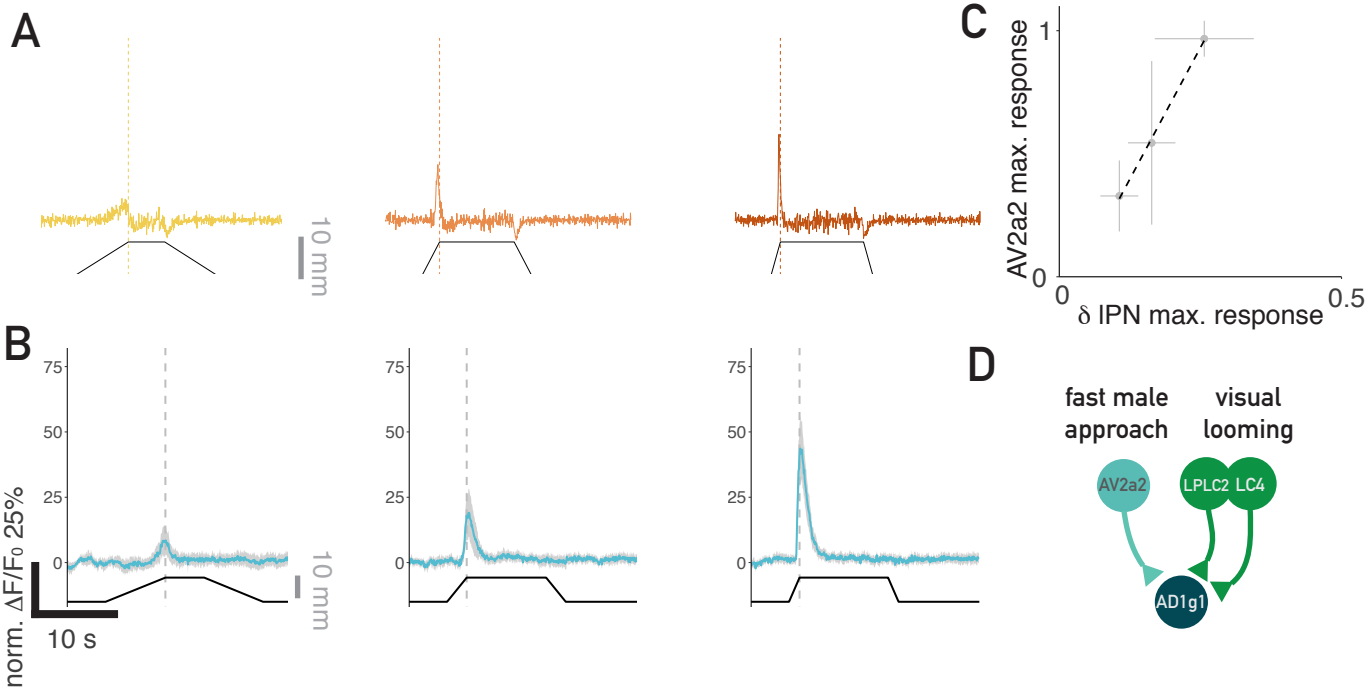


### **Figure 13: AV2a2 responses correlate with the speed of IPN activity change**

**A:** The differential of the IPN response trace to presenting a male at different speeds, based on data in Figure 12C.  $n = 10$ . **B:** AV2a2 response traces to moving a male from 10 mm to 0.75 mm distance from the antennae at different speeds; speeds shown at the top, dashed line shows the male's arrival time. Mean traces from 5 flies, 6 presentations each, grey area is SEM. Bottom black trace is the male's position based on a video recording of the presentation, baseline is 10 mm, plateau is 0.75 mm. (Same as Figure 12D.) **C:** Correlation of the IPN response differential trace maxima, and the AV2a2 response trace maxima to male presentation at different speeds. Error bars are standard deviation. Dashed line shows the linear fit,  $R^2 = 0.9976$ ,  $p = 0.031$ . **D:** Circuit diagram showing inputs of AD1g1 neurons: AV2a2, and looming sensitive visual neuron types: LPLC2, and LC4, based on the hemibrain dataset.

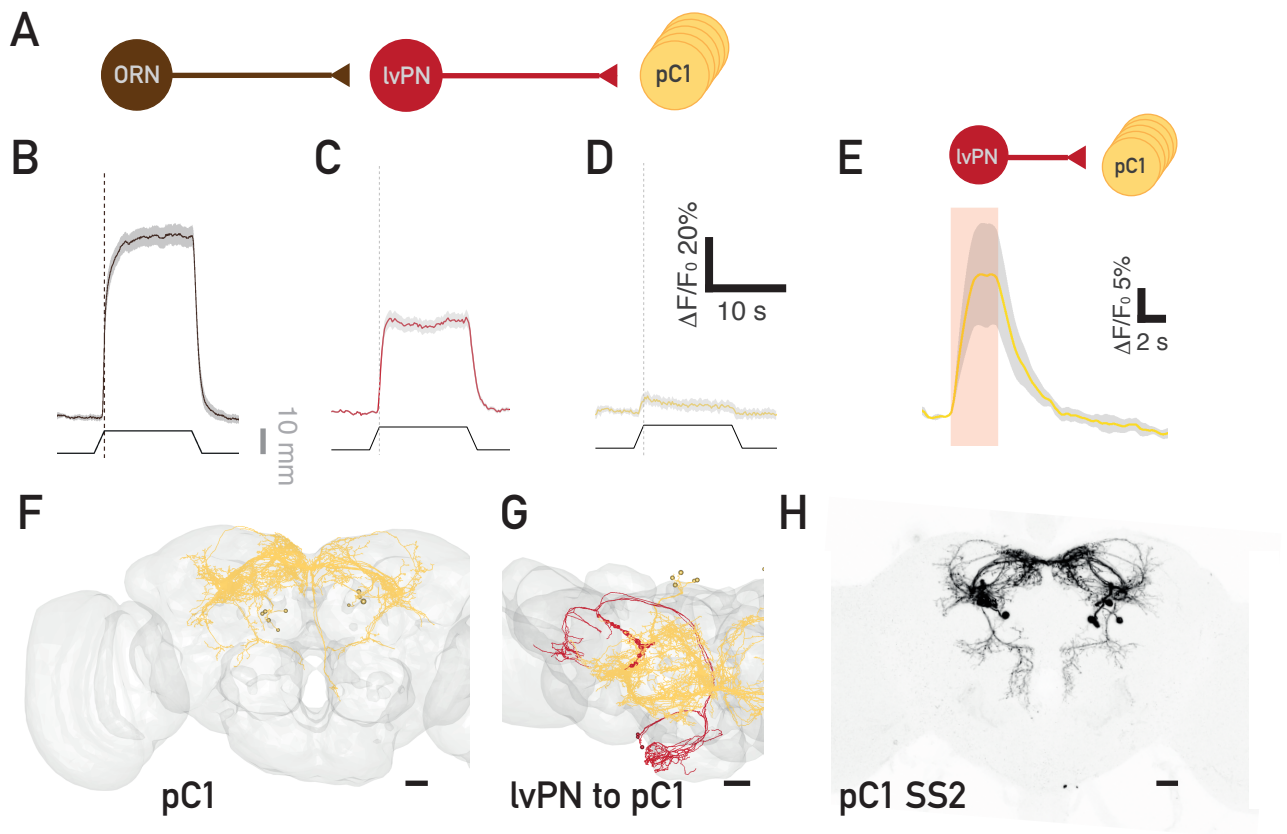


## Figure 14: pC1 shows sustained responses to cVA, similarly to presynaptic lvPNs

**A:** The connectivity diagram of Or67d ORNs, DA1 lvPNs and pC1 based on the hemibrain dataset. **B:** ORN response traces to moving a male from 10 mm to 0.75 mm distance from the antennae, dashed line shows the male's arrival time. Mean traces from 10 flies, 6 presentations each, grey area is SEM. Bottom black trace is the male's position based on a video recording of the presentation, baseline is 10 mm, plateau is 0.75 mm. (Data also shown in Figure 5A.) **C:** Same as B, but measured in lvPN axons. (Data also shown on Figure 5G.) **D:** Same as B, but measured in pC1 axons. (n = 6) **E:** pC1 responses to lvPN optogenetic activation. lvPN SS was used to drive the expression of CsChrimson, and *dsx*-LexA to drive GCaMP7f. Red area shows the time of optogenetic stimulation by an LED (n = 5). **F:** EM reconstructions of pC1 neurons from the FAFB dataset; frontal view. pC1 neuron reconstructions were made publicly available by Wang et al. (2020). **G:** EM reconstruction of lvPN (red) and pC1 (yellow), and lvPN to pC1 synapses (red circles in the SIP). **H:** Confocal image of pC1 neurons in a female brain (top) and VNC (bottom), reporter expression driven by pC1 Stable Split 2, maximum projection., image from FlyLight - Janelia Research Campus, driver line published in Wang et al. (2020). Scale bars are 20  $\mu$ m.

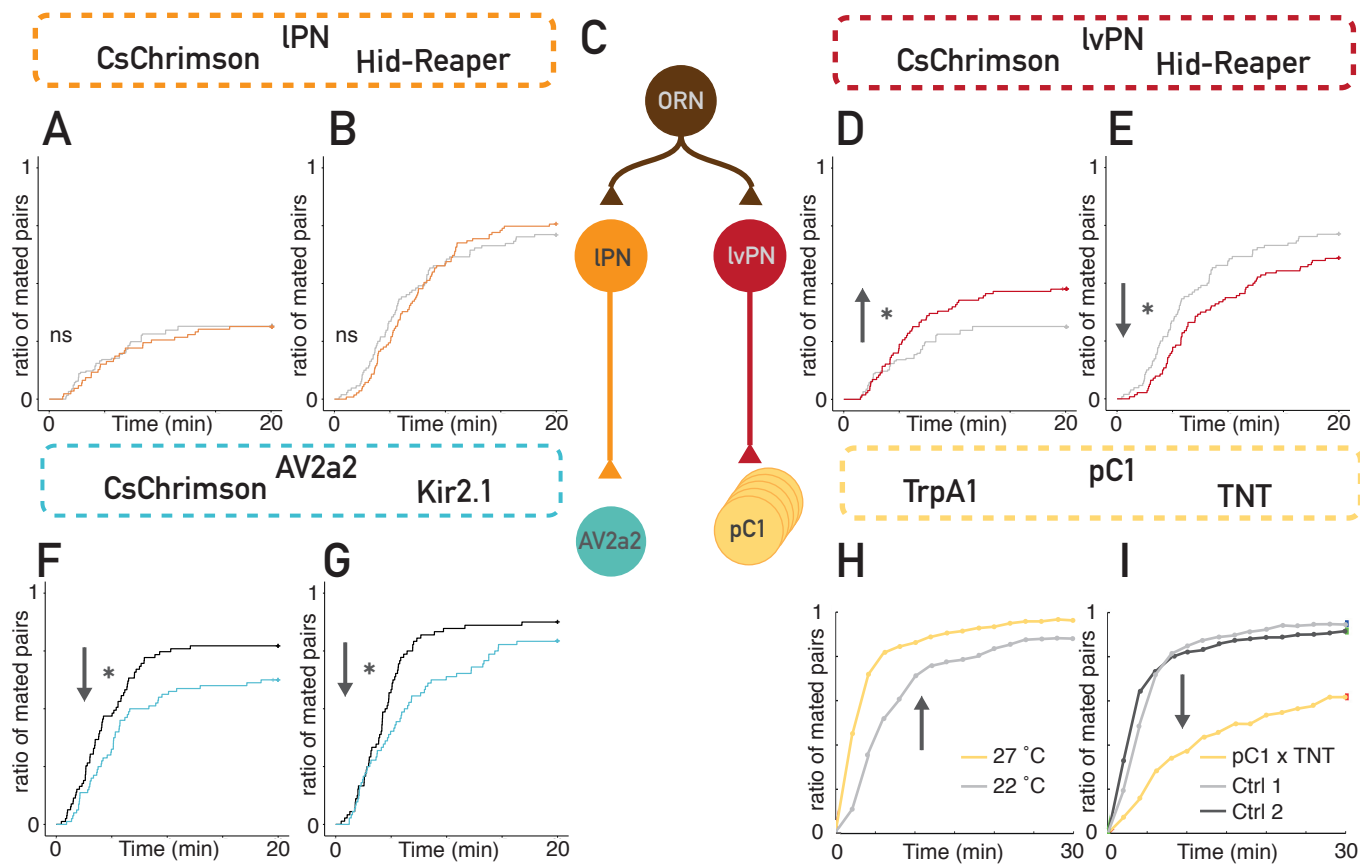


## Figure 15: Parallel pheromone pathways have distinct effects on female receptivity

**A:** Copulation rate of IPN CsChrimson activated virgin females (orange) and genetic control (grey). Log-rank test, n.s, n = 88-105. **B:** Copulation rate of IPN Hid-Reaper ablated virgin females (orange) and genetic control (grey). Log-rank test, n.s, n = 110. **C:** Simplified connectivity diagram of Or67d ORNs, DA1 IPNs and lvPNs, AV2a2 neurons, and pC1 neurons. (In the hemibrain dataset there are 143 ORNs, 7 IPNs, 3 lvPNs, 4 AV2a2 neurons, and 5 pC1 neurons in one hemisphere.) **D:** Copulation rate of lvPN CsChrimson activated virgin females (red) and genetic control (grey). Log-rank test, p = 0.01, n = 88-105. **E:** Copulation rate of lvPN Hid-Reaper ablated virgin females (red) and genetic control (grey). Log-rank test, p = 0.046, n = 110. **F:** Copulation rate of AV2a2 CsChrimson activated virgin females (blue) and genetic control (black). Log-rank test, p = 0.02, n = 80. **G:** Copulation rate of AV2a2 Kir2.1 blocked virgin females (blue) and genetic control (black). Log-rank test, p = 0.02, n = 72. **H:** Copulation rate of TrpA1 activated virgin females (yellow) and temperature control (grey). Genotype: 71G01-LexA/LexAop2-FLP; dsx-GAL4/UAS>stop>dTrpa1. (Adapted from Zhou et al. 2014.) **I:** Copulation rate of Tetanus Toxin blocked females (yellow) and parental control (light grey), and inactivated toxin control (dark grey). Genotypes in this order: 71G01-LexA/LexAop2-FLP; dsx-GAL4/UAS>stop>TNT, LexAop2-FLP/+; dsx-GAL4/UAS>stop>TNT, 71G01-LexA/LexAop2-FLP; dsx-GAL4/UAS>stop>TNT<sup>m</sup>. (Adapted from Zhou et al. 2014.) The behavioural data and analyses presented in panels A, B, D, E, F, and G were contributed by Dr Dana Galili.

## **6 Multimodal sensory integration increases signal specificity**

The previous chapters demonstrated that cVA, a single odour, can encode male identity, distance, angular position, and speed. This impressive repertoire is made possible by specific neurons tuned to features like the signal's intensity, rate of change, or laterality. However, these signals are not always reliable. The amount of cVA on males is age- and social context dependent (Bartelt, Schaner, and Jackson 1985; Krupp et al. 2008), older males may be perceived closer based on just PN signals than a freshly eclosed one, a mated female may appear as a male, or males outside the range of cVA sensitivity may remain simply undetected. A solution to these problems is offered by integrating cVA with information from other sensory modalities. The pathways characterised above clearly make use of this.

pC1 has been shown to integrate cVA and male courtship song (Zhou et al. 2014), although a recent study has questioned whether pC1 neurons directly respond to song (F. Wang et al. 2020). This controversy may be a result of different physiology reagents. Zhou et al. used *dsx-LexA* to image calcium in pC1 neurons, which labels many other song responsive neurons like pC21 and pMN2 / vpoDN (Deutsch et al. 2019). Alternatively, differences in song presentation methods could cause such different results. However, it was clearly demonstrated by Wang et al. that a pC1 downstream neuron, vpoDN (vaginal plate opening Descending Neuron), integrates pC1 activity and courtship song, therefore vpoDNs could be an alternative site for integrating cVA and male song. This is also consistent with vpoDN's function of acting as a command neuron for vaginal plate opening, a necessary step for mating.

We inspected the connectivity of AV2a2 neurons in the hemibrain, to understand what other sensory modalities may be relevant to AV2a2 activity. There are no strong inputs from other PN types or non-olfactory sensory pathways to AV2a2. However, on the output side, connectivity suggests that the strongest downstream partner of AV2a2 is likely to be a site of multimodal integration. These neurons, one per hemisphere, called AD1g1 (Figure 16B), receive strong visual input from neurons that were shown to be selectively tuned to the size (LPLC2 neurons) or the velocity (LC4 neurons) of a looming stimulus (Klapoetke et al. 2017; Ache et al. 2019). It is tempting to speculate that AD1g1 neurons integrate visual looming with their input from AV2a2 (which themselves do not receive visual input), and thereby AD1g1 creates a specific representation of an approaching male by integrating olfactory and visual information (Figure 13D, Figure 16A).

IPN neurons have numerous other downstream partners in the lateral horn than AV2a2, one of which was characterised earlier in our lab (Kohl et al. 2013). This study described a developmental switch that underlies sexually dimorphic wiring in a pair of third

order neuron types. aSP-g respond to cVA in females but not in males, and the relationship is reversed in aSP-f neurons (Figure 16E, reproduced from Kohl et al. 2013). This study also showed that aSP-g is not sparsely tuned to cVA like the IPNs, but they also respond to food odours, furthermore they have extensive dendritic arbours outside the LH where taste projection neurons terminate (Figure 16D; H. Kim, Kirkhart, and Scott 2017b). Following these observations we hypothesised that aSP-g integrates cVA with other stimuli to signal a specific chemosensory scene related to a male's presence.

### **6.1 aSP-g integrates smell and taste**

A previous study showed that taste projection neurons innervate the SLP medial to the LH (H. Kim, Kirkhart, and Scott 2017a), where aSP-g dendrites are abundant. To fully reconstruct these circuits we used the FAFB dataset, as the hemibrain does not contain the GNG, where taste sensory neurons form their presynapses. We traced out the morphology of aSP-g neurons in confocal light microscopy stacks and transformed these to EM brain space with the *natverse* neuroanatomy toolbox (Bates, Manton, et al. 2020), and used their registered location to identify aSP-g neurons in FAFB. We fully reconstructed all 11 aSP-g neurons on the left hemisphere of the FAFB volume, and found that IPNs but not lvPNs are presynaptic to them. Interestingly, we found another lvPN cell type (lvPN2 in this work) that innervates aSP-g, but no other olfactory PN forms strong inputs to aSP-g. lvPN2 are multiglomerular PNs, typical of the latero-ventral lineage, and have most of their dendrites in DA1, DC3, and VC4 glomeruli. DC3 and VC4 are known to respond to fruit odours (Münch and Galizia 2016), consistent with findings of aSP-g odour tuning in Kohl et al. (2013). We matched lvPN2s to their corresponding cell type in the hemibrain, and found that they have little direct ORN input in the DA1 glomerulus, but are postsynaptic to DA1 IPNs at their dendrites (Figure 18A). This suggests that if lvPN2 neurons respond to cVA that may be dependent on IPN activity.

Consistent with recordings from Kohl et al., where only 70% of aSP-g neurons responded to cVA, only a subset of aSP-g neurons (five out of eleven) were connected to IPNs and lvPN2s in FAFB. In line with this, hierarchical clustering of FAFB aSP-g neurons based on NBLAST morphology similarity scores (Costa et al. 2016) revealed three distinct subtypes (numbered based on dendrite position from anterior to posterior, Figure 17Ai, Ci), which are most different in the amount and position of their dendritic arbour. To confirm that these subtypes are conserved across individuals we searched for aSP-g neurons in the

FlyCircuit database that contains light microscopy images and traces of single neurons from MARCM experiments. We found nine examples of female aSP-g neurons in FlyCircuit which fell into the same three groups after clustering (Figure 17Aii, Cii). We performed multi-colour flip-out experiments to label single cells in a split-GAL4 line labelling aSP-g neurons (Figure 17D), and found the same three morphology groups after image registration and clustering (Figure 17Aiii, Ciii). These subtypes were found and similarly named in the hemibrain dataset based on our suggestion. Of these three types, aSP-g2 neurons have the largest proportion of dendritic arbour in the LH across all datasets (Figure 17B), and are the only aSP-g subtype that receives DA1 innervation. This applies to IPN and lvPN2 in both FAFB and the hemibrain. To further confirm that our driver line, aSP-g SS, labels the aSP-g2 subtype we imaged their activity by driving GCaMP expression, while activating Or67d ORNs optogenetically via CsChrimson driven by Or67d-QF. Activating Or67d ORNs evoked a strong increase in neurons labelled by aSP-g SS, therefore we conclude that aSP-g2 is labelled by our driver line.

To explore non-olfactory aSP-g input pathways we carried out a sampling of aSP-g postsynapses, reconstructing the morphology of aSP-g input neurons first manually, later by the help of partial segmentation of the FAFB volume (P. H. Li et al. 2020). We found that the single strongest upstream neuron, G2N-SLP1 (gustatory second-order neuron - superior lateral protocerebrum 1; Figure 18A, B) provides 60 synapses, 4.8% of all inputs to aSP-g2. G2N-SLP1 is a projection neuron with dendrites in the GNG, suggesting gustatory inputs. We sampled 75% of all G2N-SLP1 inputs, which revealed that indeed they receive inputs from gustatory receptor neurons (GRNs). The GRNs fall into two types, one enters the brain via the labellar nerve and provides 71 synapses (8.9% of all inputs - lGRN, Figure 18A, B) and the other type enters via the accessory pharyngeal nerve to provide 163 synapses (20.4% of all inputs, pGRN, Figure 18A, B). These data suggest that aSP-g2 neurons are third-order in the processing of both olfactory and gustatory stimuli, serving as a point of intra- and intermodal sensory convergence.

In parallel to reconstructing upstream partners of aSP-g2 neurons, we have sampled inputs of aSP-g1 and aSP-g3 (Figure 18A). We found that the strongest dendritic input of aSP-g1 neurons is also G2N-SLP1, and their strongest upstream cell type in general is aSP-g2 neurons via axo-axonic connections. Therefore aSP-g1 neurons seem to process similar information to aSP-g2 even though they are not directly connected to DA1 PNs. In contrast, the three strongest inputs to aSP-g3 are putative taste pathways, two GNG PNs and one ascending neuron. aSP-g3 is therefore likely to integrate multiple gustatory channels.

GRN anatomy and receptor expression has been extensively studied in *Drosophila* both for Gr and Ir receptors (Kwon et al. 2014; Sánchez-Alcañiz et al. 2018). Based on morphological similarity we identified the G2N-SLP1 upstream labellar GRNs to be the population labelled by Ir94e-GAL4 (Koh et al. 2014; Sánchez-Alcañiz et al. 2018; Jaeger et al. 2018). To test how aSP-g integrates cVA and taste we imaged intracellular calcium in aSP-g by expressing GCaMP6s with 81A04-LexA, and drove CsChrimson by Ir94e-GAL4 (Croset et al. 2016). As expected, cVA presentation evoked a transient activation of aSP-g neurons, while optogenetic activation of Ir94e GRNs caused a small and slowly decaying signal increase in aSP-gs. Presenting these two stimuli together caused a superlinear activation of aSP-g (Figure 18D). These anatomical and calcium imaging data show that aSP-g indeed integrates multimodal stimuli: cVA, and an unknown taste substance. Ir94e GRNs have been shown to weakly respond to salts (Jaeger et al. 2018), but it is not known whether contact pheromones activate them. Although females normally do not sample male pheromones by licking (typical of courting males), it has been shown that deposits from males contain cVA, sufficient to activate Or67d ORNs (Mercier et al. 2018). These deposits, with all their pheromonal content, may be also sampled by the proboscis, which could expose the labellar Ir94e GRNs and the pharyngeal GRNs upstream of G2N-SLP1 to male specific molecules, potentially providing a multimodal signal about male identity and quality. A similar phenomenon was shown with behavioural experiments in males: cVA and a male specific contact pheromone regulate male-male aggression together (L. Wang et al. 2011).

## **6.2 aSP-g increases female receptivity via a pC1 independent pathway**

aSP-g integrates taste with cVA, well placed to recognise a conspecific male, or male deposit. To test the behavioural effect of aSP-gs on female sexual behaviours we used a courtship assay, described above, and manipulated the activity of aSP-g neurons. The driver aSP-g SS labels  $4.7 \pm 1.33$  neurons per hemisphere, out of 11-12 neurons. To access more neurons we added a second split-GAL4 DBD (DNA-binding domain) known to label aSP-gs. This combined line (aSP-g SS1-2) labels  $5.2 \pm 1.2$  neurons, and we used this in our courtship assay for activation experiments. Activating aSP-g neurons with CsChrimson and constant red light increased female receptivity (Figure 19A). In order to block aSP-g activity we generated driver lines that label even more aSP-gs ( $7.6 \pm 2$  and  $6.7 \pm 1$ ), by intersecting fruFLP with the GAL4 lines with the GMR insertions used as DBDs in aSP-g SS1-2. Blocking aSP-g activity with Kir2.1 expression resulted in a small but significant decrease in female

receptivity (Figure 19B), while activating these lines with CsChrimson reproduced the receptivity increase phenotype seen with aSP-g SS1-2 (data not shown). These results demonstrate that aSP-g bidirectionally regulates female receptivity, like lvPNs and pC1 neurons. Interestingly, activation or genetic ablation of IPNs did not affect receptivity (Figure 15A, B), suggesting that cVA alone is insufficient for aSP-g to express its behavioural effect, rather the integration with taste is a necessary step for this.

Next we asked how the lvPN-pC1 and IPN-aSP-g pathways might interact to control female receptivity. We have shown earlier that lvPNs do not innervate aSP-gs, similarly aSP-g is not connected strongly to pC1 in FAFB or the hemibrain. This connectivity suggests that these cVA responsive pathways act independently to affect female receptivity. To test this idea, we devised a behavioural epistasis experiment, where aSP-g neurons are activated by driving CsChrimson with the intersection of FruFLP and a GMR LexA line labelling aSP-g neurons, while pC1s were genetically ablated by driving Hid, and Reaper apoptotic factors by pC1 SS2 (F. Wang et al. 2020). As expected, ablating pC1 neurons alone suppressed female receptivity, and aSP-g activation alone increased female receptivity compared to genetic control (Figure 19C). In the epistasis genotype we saw a significant increase of receptivity compared to the pC1 ablated condition, which shows that aSP-g neurons are able to elicit their receptivity increasing effect without functional pC1 neurons. It is important to note that our driver line for aSP-g (aSP-g FLP-LexA) labels a few neurons in the midline of the brain, projecting from the peri-esophageal region to the pars intercerebralis. We cannot exclude the possibility that these neurons contribute to the behavioural effects in this experiment.

Receptivity is not a single behaviour, rather a drive, or arousal state, that affects the likelihood of expressing specific behavioural modules related to accepting a courting male for mating. pC1 has been elegantly linked to such a specific module, vaginal plate opening (K. Wang et al. 2021). aSP-g may elicit its effect on this step, by converging on the same descending neuron as pC1, although aSP-g is not directly presynaptic to the relevant cell type, according to data from the hemibrain. Alternatively, aSP-g may regulate other steps of female acceptance via a pC1 independent complete sensory-motor circuit (Figure 19D).

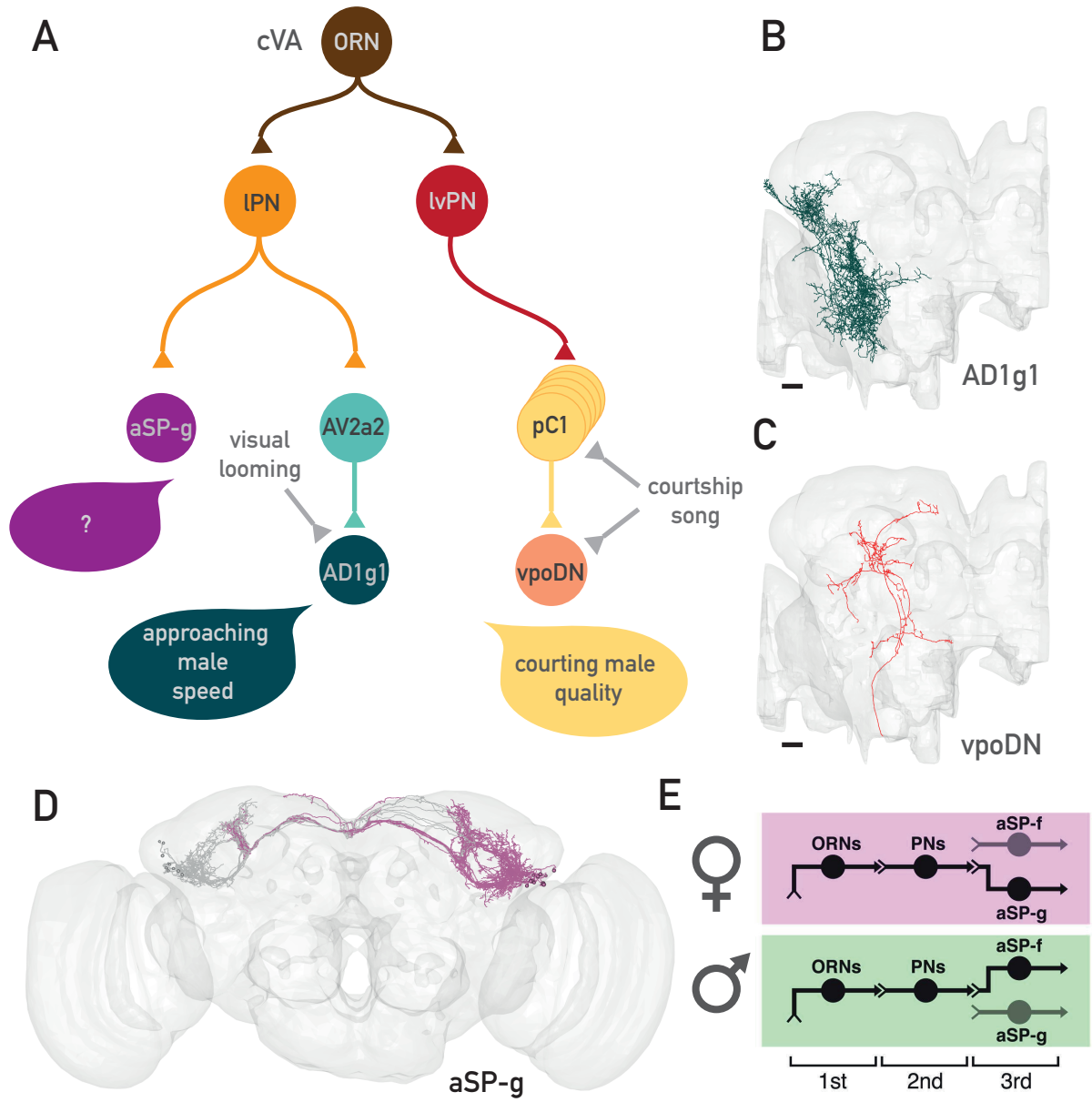


### **Figure 16: Sensory integration steps in cVA processing**

**A:** Connectivity diagram of cVA processing pathways downstream of Or67d ORNs with other sensory modalities. IPN to ORN connection not shown. (In the hemibrain dataset there are 143 ORNs, 7 IPNs, 3 lvPNs, 4 AV2a2 neurons, 1 AD1g1 neuron, 5 pC1 neurons, 1 vpoDN, 11 aSP-g neurons in one hemisphere.) **B:** EM reconstruction of the AD1g1 neuron in the hemibrain dataset. **C:** EM reconstruction of vpoDN in the hemibrain dataset. Scale bars in B and C are 20  $\mu\text{m}$ . **D:** EM reconstruction of aSP-g neurons in the FAFB dataset. 11 neurons from both hemispheres, left: purple, right: grey. **E:** Schematic of a sexually dimorphic circuit switch at the level of third-order lateral horn neurons: aSP-g and aSP-f. Adapted from Kohl et al. (2013).

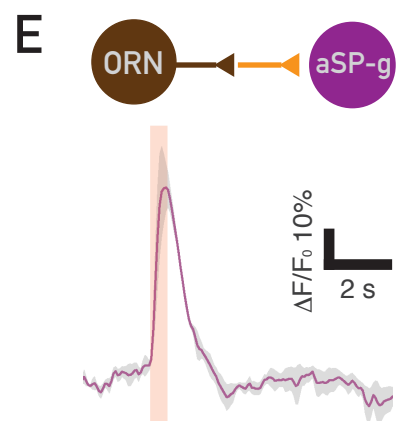
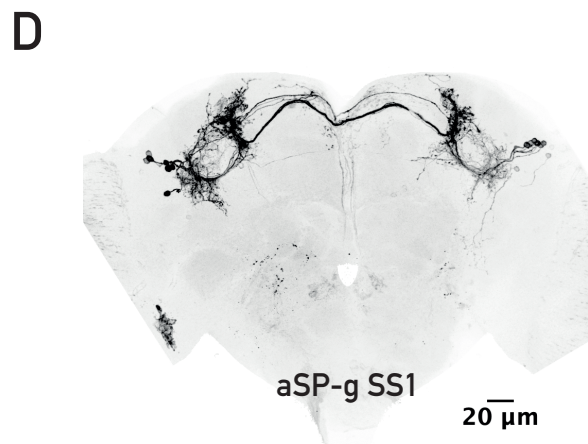
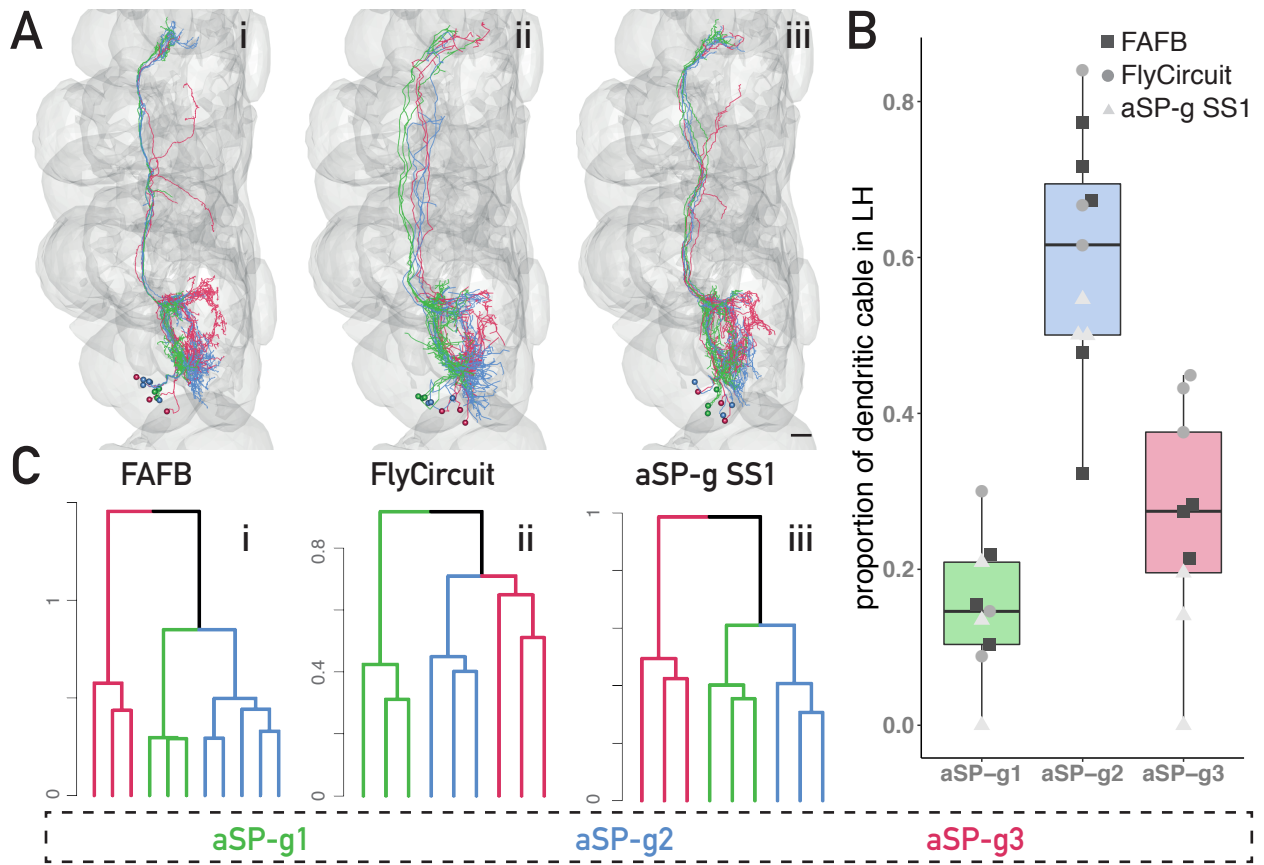


### **Figure 17: The aSP-g clone consists of three morphological subtypes**

**A:** Reconstructions of aSP-g neurons coloured based on NBLAST morphological clustering from the FAFB dataset (left), the FlyCircuit dataset (middle), and MCFO data from aSP-g Stable Split (right). Scale bar is 20  $\mu\text{m}$ . **B:** The proportion of dendritic cable inside the lateral horn for aSP-g subtypes across three datasets. Squares: FAFB, circles: FlyCircuit, triangles: aSP-g SS MCFO. **C:** Hierarchical clustering based on NBLAST morphological similarity scores using ward's method,  $k = 3$ . Order and colours are the same as in A. **D:** Confocal image of aSP-g neurons in a female brain, reporter expression driven by aSP-g Stable Split, maximum projection. **B:** aSP-g responses to Or67d ORN optogenetic activation. Or67d-QF was used to drive the expression of CsChrimson, and aSP-g SS1 to drive GCaMP6f. Red area shows the time of optogenetic stimulation by an LED ( $n = 5$ ). The image presented in panel D was contributed by Dr Dana Galili. The aSP-g SS1 MCFO labelling and the resulting neuron traces presented in panel A (right) were contributed by Dr Erika Donà.

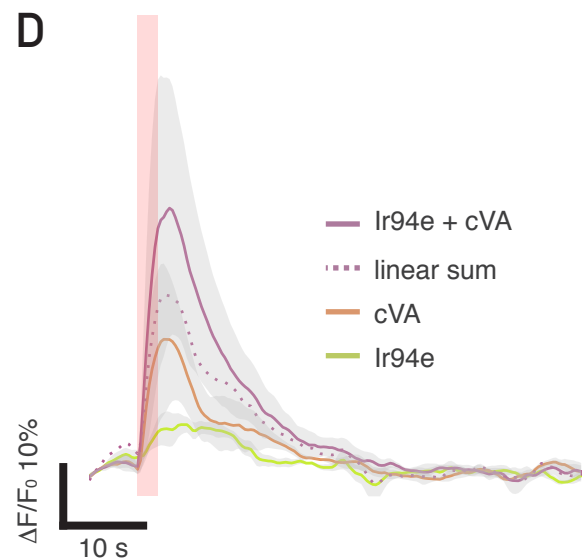
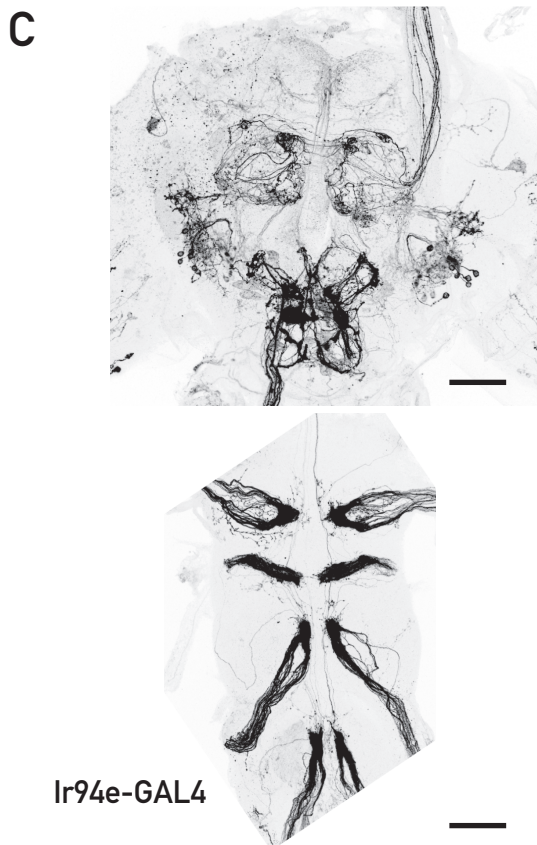
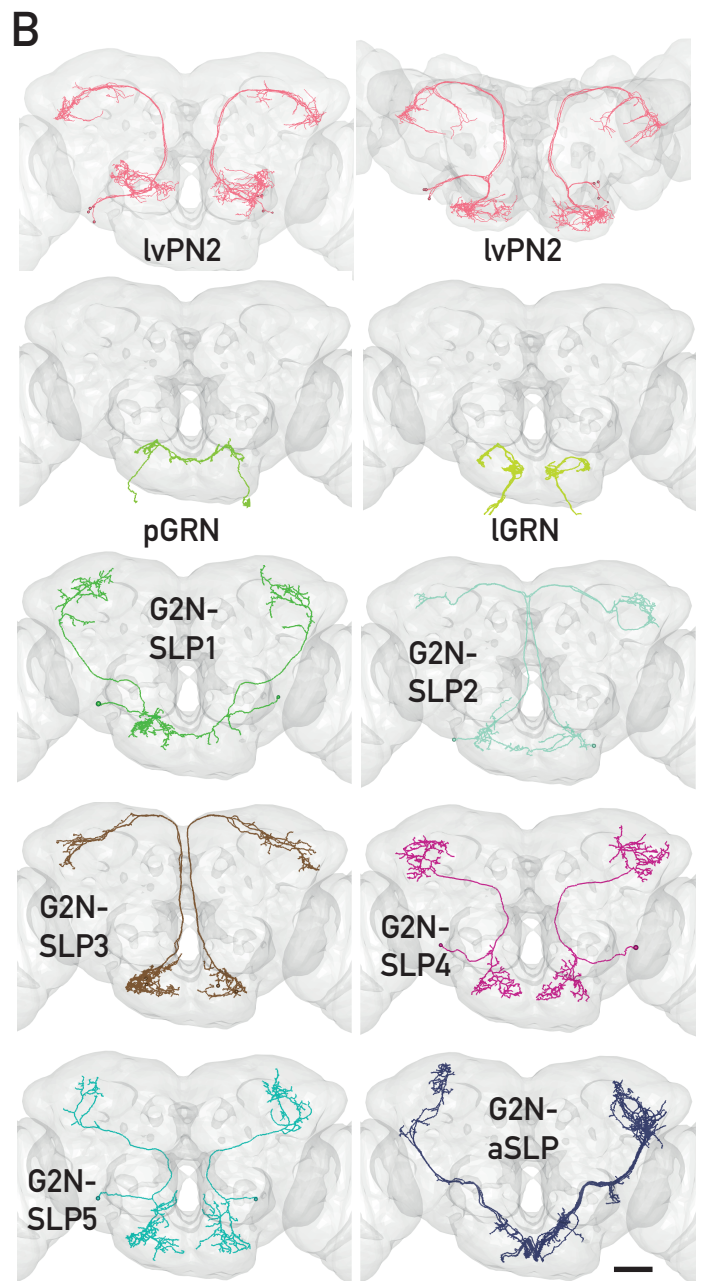
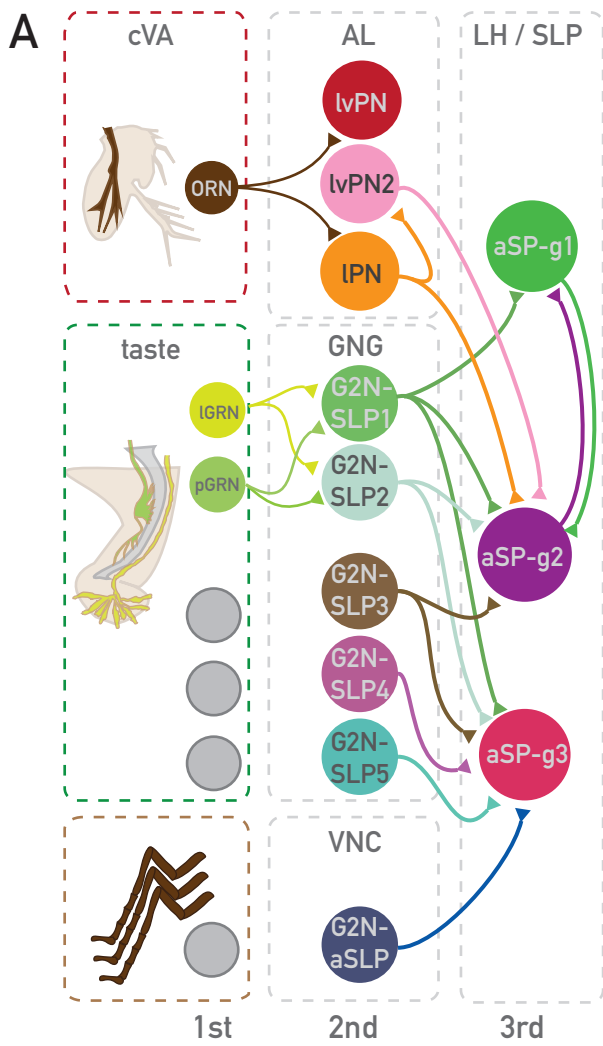
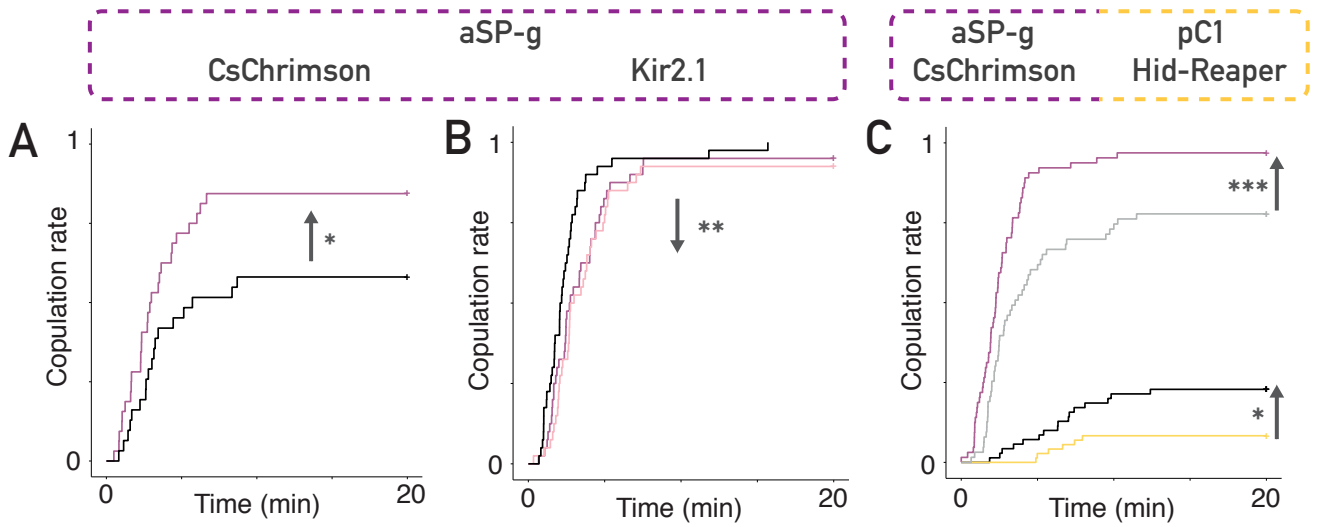


## Figure 18: aSP-g integrates taste inputs with cVA

**A:** Connectivity diagram of aSP-g subtypes with olfactory and gustatory pathways based on FAFB presynaptic sampling, and hemibrain connectivity in the antennal lobe (AL). **B:** EM reconstruction of aSP-g input neurons in the FAFB dataset. First row left: lvPN2; frontal view, right: dorsal view. Second row left: pharyngeal GRNs, right: labellar GRNs. Third row left: G2N-SLP1, right: G2N-SLP2. Fourth row left: G2N-SLP3, right: G2N-SLP4. Fifth row left: G2N-SLP5, right: G2N-aSLP. **C:** Confocal image of Ir94e labellar GRNs in a female brain (top) and VNC (bottom), reporter expression driven by Ir94e-GAL4, maximum projection. Driver line generated by Croset et al. (2016). Scale bars in B and C are 40  $\mu\text{m}$ . **D:** aSP-g responses to Ir94e ORN optogenetic activation, cVA presentation, and simultaneous stimulation. Ir94e-GAL4 was used to drive the expression of CsChrimson, and 81A04-LexA to drive GCaMP6s and image aSP-g neurons. Red area shows the time of optogenetic stimulation by an LED, and / or the delivery of cVA from an olfactometer (n = 3 - statistical significance not tested). Dotted purple line shows the linear sum of responses to single stimuli.



**D**

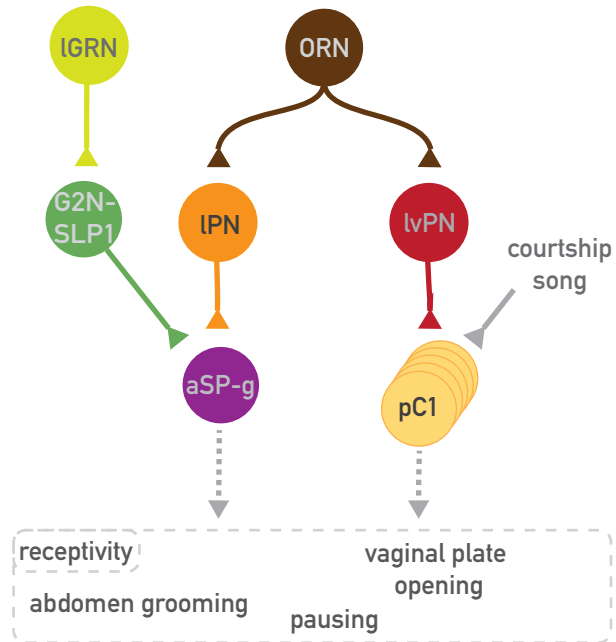


### **Figure 19: aSP-g controls female receptivity independent of pC1**

**A:** Copulation rate of aSP-g CsChrimson activated virgin females (purple) and genetic control (black); log-rank test  $p = 0.017$ ,  $n = 31-32$ . **B:** Copulation rate of aSP-g Kir2.1 blocked virgin females (aSP-g FLP1 driver: purple, aSP-g FLP2 driver: pink) and genetic control (black).  $n = 40$  for each group; log-rank test  $p = 0.008$ , pairwise comparisons with Benjamini-Hochberg correction: aSP-g FLP1 vs. empty FLP  $p = 0.036$ , aSP-g FLP2 vs. empty FLP  $p = 0.013$ . **C:** Behavioural epistasis with pC1 block and aSP-g activation. Copulation rate for genetic control: grey; pC1 Hid-Reaper ablation: yellow; aSP-g CsChrimson activation: purple; pC1 ablation and aSP-g activation: black; log-rank test  $p < 0.001$ , pairwise comparisons with Benjamini-Hochberg correction: aSP-g activation against control:  $p < 0.001$ , aSP-g activation with pC1 ablation, against pC1 ablation alone:  $p = 0.017$ . **D:** Connectivity diagram of cVA and Ir94e pathways upstream of aSP-g and pC1 neurons based on the FAFB dataset with behavioural outputs. The behavioural data and analyses presented in panels A, B, and C were contributed by Dr Dana Galili.

## **7 A layered axo-axonic circuit for hierarchical processing of multimodal signals**

We established that aSP-g neurons integrate cVA with an unknown taste signal and affect female receptivity via a pC1 independent pathway. These results extend previous work demonstrating that aSP-g neurons are *fruitless*<sup>+</sup>, sexually dimorphic, third-order neurons that receive cVA information in females but not in males (Kohl et al. 2013). Next, we asked what circuits read out the multimodal information from aSP-g to instruct female behaviour independent of pC1.

Using the aSP-g neurons reconstructed in the FAFB volume we chose two aSP-g2 neurons with strong cVA input from PNs, and carried out a pseudo-random sampling of their postsynaptic partners. We clustered the resulting neurons based on their morphology, and ranked the clusters by the number of connections from aSP-g2 neurons. We found that a type of mAL neurons (medial to antennal lobe) are the strongest downstream partners of aSP-g2 in our sample, and we named them mAL1 (Figure 20A, B). To follow the flow of information we carried out a second sampling, now of mAL1 postsynaptic partners. We found two cell types strongly downstream of mAL1, and focussed on one of them, a pair of *fruitless*<sup>+</sup> neurons, ascending from the nerve cord, called dMS6 (Philipsborn et al. 2011, Figure 20D, E). Intriguingly, both aSP-g2 to mAL1, and mAL1 to dMS6 synapses are axo-axonic, that is, the axons of the presynaptic neurons form synapses that are on the axonal arbours of the postsynaptic neurons exclusively. This circuit layout is unusual as axons are usually the output compartments of neurons, while dendrites receive inputs. This circuit motif suggests that aSP-g2 may be part of a hierarchical gating mechanism, where its multimodal signal modulates the information coming from mAL1 and dMS6 dendrites to instruct female sexual behaviour.

### **7.1 Behavioural dissection of an axo-axonic circuit**

We screened split-GAL4 combinations to selectively label mAL1 and dMS6 neurons resulting in a sparse driver line for each cell type (Figure 20C, E). We used these lines to test the role of mAL1 and dMS6 in female receptivity by either optogenetically activating them via CsChrimson or constitutively hyperpolarising these neurons by Kir2.1 during a courtship assay. Both mAL1 and dMS6 bidirectionally modulates female receptivity, but they act in opposite directions. Activating mAL1 in female flies results in a drastic decrease in mating rate and the number of mated pairs, while blocking mAL1 increases the rate and chance of copulation (Figure 20F, G). On the other hand, dMS6 activation increased receptivity, while Kir2.1 block elicited a small but significant mating rate decrease (Figure 20H, I), rather

similarly to the same manipulations in aSP-g (Figure 19A, C). To better understand the relationship between these neurons we performed co-immunostaining with neurotransmitter markers. Consistent with previous results about mAL neurons in males we found co-labelling of GABA and mAL1 neurons, while dMS6 somata showed overlap with ChAT4B staining, suggesting that mAL1s are GABAergic and dMS6 are cholinergic (Figure 20J, L).

Based on these results and previous work showing that aSP-g are cholinergic (Kohl et al. 2013) we devised a circuit model that is compatible with the behavioural data (Figure 20K). Walking through the circuit from inside out: we propose that dMS6 forms excitatory synapses with an unknown downstream neuron with a positive effect on female receptivity. mAL1 neurons gate this effect by GABAergic presynaptic inhibition onto dMS6 axons. aSP-g neurons have a positive effect on female receptivity by providing a disinhibition: aSP-g activity blocks mAL1 neurotransmission, thereby dMS6 is relieved of its presynaptic inhibition. In this model the cholinergic aSP-g - mAL1 synapse blocks transmission. This could be a result of metabotropic ACh receptors on mAL1 axons with an inhibitory effect (as was shown in proprioceptive sensory neuron axons in locusts, (Wolf and Burrows 1995); alternatively a second neurotransmitter could be used in the aSP-g - mAL1 synapse; or it may be an effect of cholinergic subthreshold depolarisation of the mAL1 boutons inactivating sodium channels and thereby stopping dendritic signals to evoke normal levels of vesicle release upon firing. In order to better understand the nature of this layered axo-axonic circuit we asked what information enters via mAL1 and dMS6 dendrites.

## 7.2 Characterisation of mAL1 and dMS6 inputs

mAL neurons are sexually dimorphic, *fruitless*<sup>+</sup>, GABAergic neurons, responsive to male and female gustatory pheromones in males. They have a role in guiding male courtship towards conspecific females, and male-male aggression (Kimura et al. 2005; Kallman, Kim, and Scott 2015; Clowney et al. 2015; Koganezawa, Kimura, and Yamamoto 2016; Seeholzer et al. 2018). Cachero et al. described that there are  $28.6 \pm 8.02$  mAL neurons (*fruitless* clone aDT-b) in females, but their role in female social behaviour was not explored. We exhaustively reconstructed neurons in the axon tract that contained mAL1 neurons on the right hemisphere of the FAFB volume, and found 35 mAL neurons, comprising six morphological subtypes we define by axonal morphology based clustering (Figure 21A). These subtypes were similarly grouped and named in the hemibrain dataset based on our suggestion.

mAL1 neurons have three separate dendritic branches: two of them go ventrally around the oesophagus towards the GNG, and one, most proximal to the soma, innervates the protocerebrum. These proximal dendrites are found uniquely in mAL1, and the ipsilateral peri-oesophageal dendrite is only present in mAL1 and mAL2, whereas all other mAL subtypes have a single contralateral dendrite, larger than mAL1's. The ipsilateral dendrites of mAL1 make them similar to male mALs, however the dendrites end more dorsally on both sides of the GNG for mAL1 than for male mALs (Kimura et al. 2005).

To learn about mAL1 inputs we carried out a full reconstruction of presynaptic partners of a single mAL1 neuron in FAFB (7.5% of inputs were left as fragments due to tracing ambiguity). We found that the strongest dendritic upstream cell type is a pair of ascending neurons contributing 9.3% of the total input to mAL1 dendrites, we refer to them as abdSMP (abdominal ganglion to superior medial protocerebrum, Figure 21B, C). Morphologically similar neurons were labelled by the intersection of *fru*FLP and *Abdominal-B-GAL4* in earlier work, suggesting that abdSMP are *fruitless*<sup>+</sup> (Bussell et al. 2014). abdSMP presynapses are distributed across all dendritic regions of mAL1, but do not reach the axons where aSP-g2 inputs onto mAL1 (Figure 21E). To test the effect of abdSMP on mAL1 activity we generated a splitGAL4 driver line labelling them (Figure 21D), and drove CsChrimson expression to activate it optogenetically while imaging intracellular calcium in mAL1 axons via GCaMP7f driven by 67E08-LexA. abdSMP stimulation resulted in a strong activation of mAL1 (Figure 21F). Although our driver for abdSMP labels two other ascending neurons and some interneurons of the abdominal ganglion, none of them overlap with mAL1 neurons, therefore we interpret our imaging results as the abdSMP - mAL1 synapse is excitatory.

The abdominal ganglion sends and receives information from all abdominal organs including the reproductive system. Signals relevant for sexual behaviour enter the CNS here, such as mating status, copulation and oviposition related cues, or stimuli associated with the lick of a courting male. In order to better understand what abdSMP neuron activity might relay we leveraged another recently acquired EM volume, the Female Adult Nerve Cord, FANC, (Phelps et al. 2021). This dataset contains a full adult female VNC including the neck connective and small parts of the GNG from the brain. We compared the structures in the FAFB and FANC neck connectives and chose a location in FANC where we expected abdSMP neurons to be based on their FAFB position. To confirm the identity of the VNC abdSMP neuron we used MCFO data from the FlyLight GMR MCFO database, where we could find whole CNS stainings with only abdSMP labelled on a channel (Meissner et al.

2020). Unfortunately the FANC dataset is incomplete in the abdominal ganglion, and the quality of the EM staining is poorest in this region. Due to these limitations the abdSMP dendritic tracings are incomplete and sampling presynaptic inputs was mostly unsuccessful. We found a few examples of sensory neurons entering via the abdominal nerve that are upstream of abdSMP, suggesting that abdSMP is second- and mAL1 is third-order cell type in this pathway. However, the limited number of connections and poor reconstruction of sensory neurons does not allow us to better characterise the signals that reach mAL1.

Next we turned to dMS6 neurons to characterise their inputs. dMS6 neurons ascend from the VNC, form axons ventral to the GNG and in the SMP, where mAL1 synapses onto them (Figure 20D). dMS6 has not been characterised functionally, but it was briefly described as a *fruitless* clone in a PhD thesis by Dr Tianxio Liu in Dr Barry Dickson's lab. Based on MARCM labelling in this work dMS6 neurons are *fruitless*<sup>+</sup> and sexually dimorphic, with larger dendritic arbours in females in the wing neuropil of the VNC. To understand what dendritic signals are modulated by mAL1 axonal inputs at dMS6 axons we reconstructed dMS6 dendrites in the FANC volume with the strategy used for finding abdSMP (Figure 20D). dMS6 innervates the VNC medially with arbours in all leg neuropils and the wing neuropil, and it does not enter regions where sensory neuron axons could synapse onto them based on published maps (Tuthill and Wilson 2016; Tsubouchi et al. 2017).

We traced out all presynaptic partners to the two dMS6 neurons (one per hemisphere). We ranked morphological clusters based on the number of dMS6 connections and fully reconstructed exemplar neurons from the top five strongest upstream clusters which together provide 19.2% of all inputs to dMS6 (Figure 22A). We then manually screened all the profiles presynaptic to the five dMS6 upstream exemplars, to find putative sensory neurons based on their distinct, electron-dense cytosol (Figure 22B). With this biased upstream sampling strategy we identified multiple sensory inputs that belong to distinct modalities originating in different neuromeres (Figure 22C, D). The fraction of sensory inputs from all inputs is given for the five dMS6 upstream clusters in Figure 22C. The cluster with the highest ratio of sensory inputs (33%) we call asc-Ms (ascending, mesothoracic neuron), which receives innervation from neurons originating in the campaniform sensillum based on their morphology. In stick insects campaniform sensilla are known to sense muscle load and contribute to motor control (Zill et al. 2012). Based on their morphology sensory inputs to other dMS6 upstream clusters include mechanosensory bristle neurons involved in sensing touch in the hindleg (T3 neuromere), and leg GRNs relaying gustatory signals from the front

and middle leg (T1 and T2 neuromeres, Figure 22D). Based on connectivity dMS6 neurons are third order neurons with respect to multiple sensory modalities, including muscle load, touch, and taste. This suggests that dMS6 may integrate a combination of stimuli that together represent an event in courtship, e.g. male tap, or attempted copulation.

To test the functional relevance of dMS6 inputs we focussed on the pathway with the strongest sensory input: asc-Ms neurons and campaniform sensilla (Figure 23A). We imaged intracellular calcium in dMS6 axons by driving GCaMP6s under the control of dMS6-SS, while we placed a stationary platform under the fly that could freely move its legs (Figure 23B). We observed frequent spontaneous events of tibio-tarsal flexion, with all legs simultaneously pressed onto the platform. We believe this happens when the fly is trying to free its thorax from the imaging holder and applies force on the platform with the legs. These events were manually labelled on a video recording, and overlaid with the GCaMP trace (Figure 23C). We found that this behaviour is followed by a strong activation of dMS6 neurons. While we cannot rule out the possibility that dMS6 activity reflects some other component of the behaviour than increased muscle load on the legs, the relative timing and the input connectivity of dMS6 makes this explanation likely. The load on leg muscles is increased by the males weight upon copulation attempt, and during copulation. We speculate that dMS6 could function as a final checkpoint before copulation, or potentially contribute to the female's sustained engagement in mating that can last up to twenty minutes.

### **7.3 A model for receptivity control by hierarchical sensory integration**

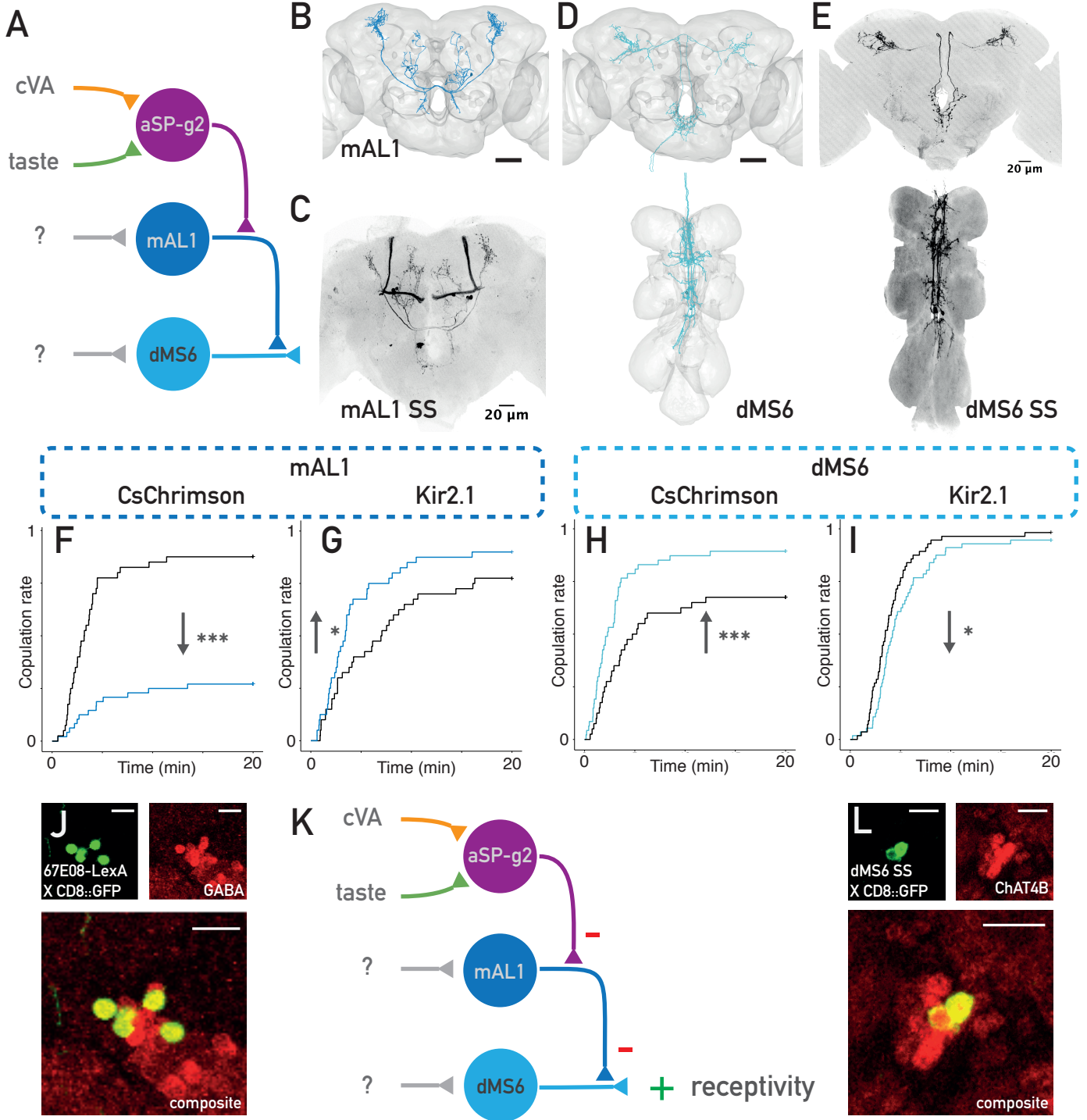
Based on the anatomy, neurotransmitter identity and behavioural results we proposed a model how the axo-axonic motif of aSP-g, mAL1, and dMS6 could interact to regulate female receptivity (Figure 20K). Reconstructing two layers of upstream circuitry of mAL1 and dMS6 allows us to extend our model with more specific information about the identity of dendritic signals to these nodes (Figure 24A). Based on these results we see a hierarchy of distinct channels, smell and taste gating an abdominal signal, which then regulates another multimodal, likely strongly proprioceptive input that positively controls female receptivity.

To test our model of disinhibition, we imaged mAL1 activity while activating the cVA pathway. As imaging mAL1 activity with the 67E08-LexA driver can be done unambiguously only from axonal signals we used DA1 IPN SS (labelling cVA responsive PNs upstream of aSP-g) to drive CsChrimson and thereby provide an artificial cVA stimulus. Initial experiments where we drove CsChrimson expression directly in aSP-g neurons were

unsuccessful, as axonal mAL1 imaging required us to scan over aSP-g axons with the imaging laser, which was sufficient to activate CsChrimson in them. This means that our stimulation via IPNs only provides the cVA aspect of the aSP-g signal. Activating IPNs resulted in a large increase in mAL1 intracellular calcium (Figure 24B). These results contradict our initial circuit model of aSP-g inhibiting mAL1 axons (Figure 20K).

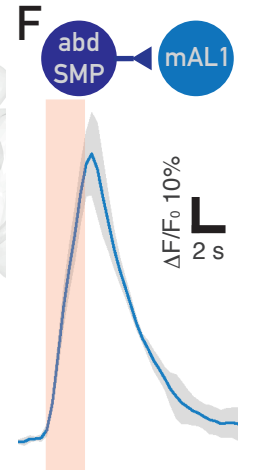
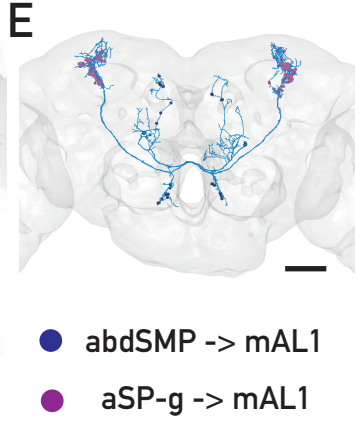
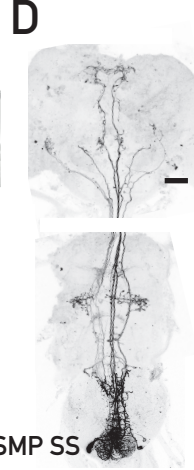
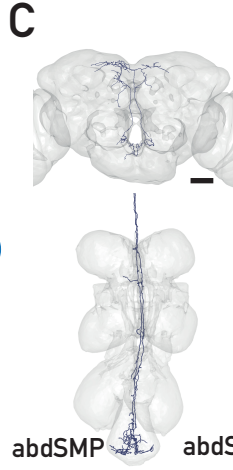
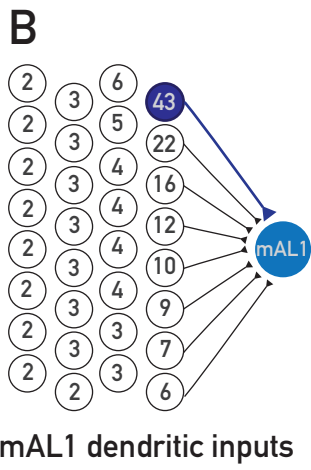
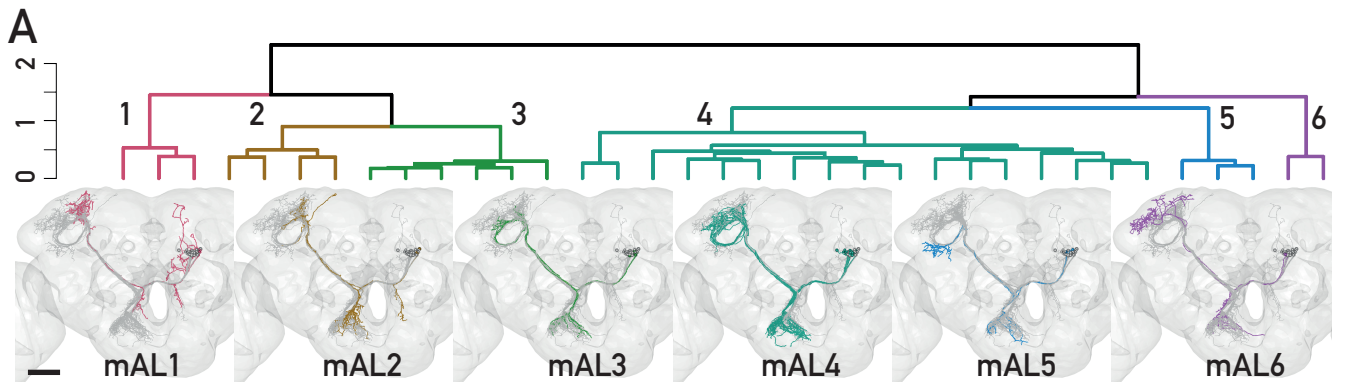
We looked for other pathways between IPN and mAL1 in the hemibrain to explain this, but we found no cell type directly linking them with more than three synapses at each step other than aSP-g2. On the other hand, when we looked at pathways between aSP-g2 and dMS6 we found that a single neuron, called AVL29, shares the same place in the circuit as mAL1: directly postsynaptic to aSP-g2 (and indirectly via aSP-g1), and directly presynaptic to dMS6 axons (Figure 24C). Based on our imaging data and the connectomic findings we revisited our model, and we suggest that AVL29 and mAL1 may provide an excitation-inhibition balance on dMS6 axons, which aSP-g2 can trigger, but may be separately modulated by other factors.

mAL neurons in males are part of a similar excitation-inhibition balance motif. Both female and male contact pheromones strongly activate mALs in males, while a parallel pathway converging on the same downstream neurons responds strongly only to female pheromones (Clowney et al. 2015; Kallman, Kim, and Scott 2015 Figure 23E). This layout allows the flexible control of male courtship, by keeping the activity of downstream neurons under tight control, but biasing responses to a specific sex. A recent study has found another example of excitation-inhibition balance to control female receptivity (Figure 24F). vpoEN and vpoIN (vaginal plate opening Excitatory, and Inhibitory Neuron) both respond to courtship song. vpoEN is closely tuned to conspecific song elements, while vpoIN is a broadly tuned auditory neuron responding to non-*melanogaster* song as well. vpoEN activates, vpoIN inhibits vpoDN, resulting in highly specific responses in vpoDN to conspecific song, showing how such a circuit motif can enhance the detection of relevant signals to instruct behaviour (F. Wang et al. 2020). Interestingly, using the hemibrain dataset we found that vpoIN is also presynaptic to AVL29 and dMS6 axons. The connectivity suggests that besides mAL1, an inhibitory pathway of another sensory modality can also gate the receptivity promoting effect of dMS6. Although the exact behavioural events and temporal kinetics of the circuit interactions remain to be explored, we propose that mAL1 and AVL29 balance the activity of dMS6 to control the mating decision in female flies.



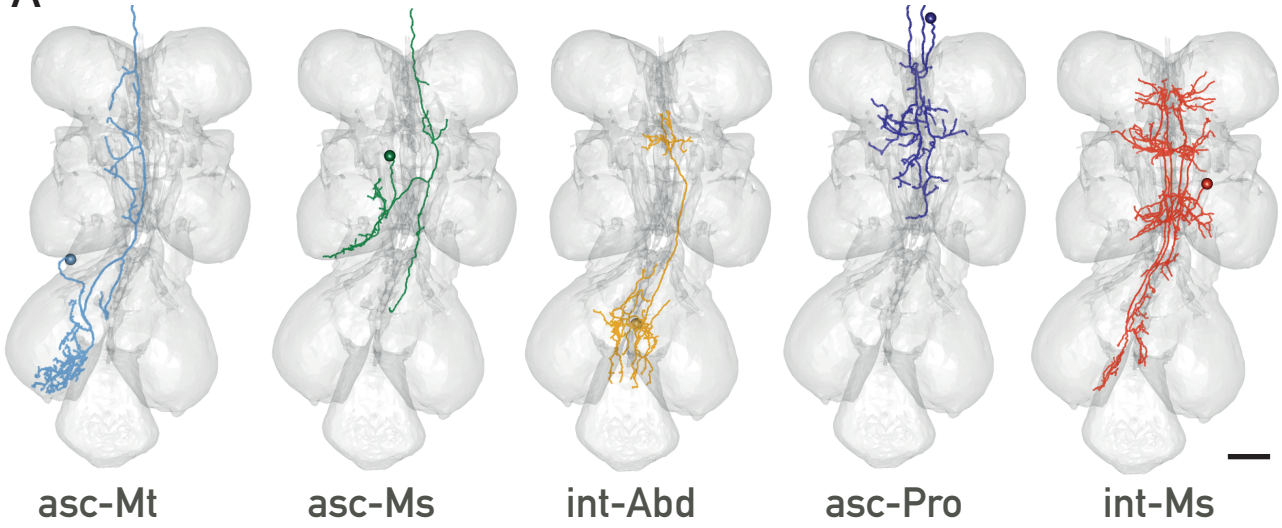
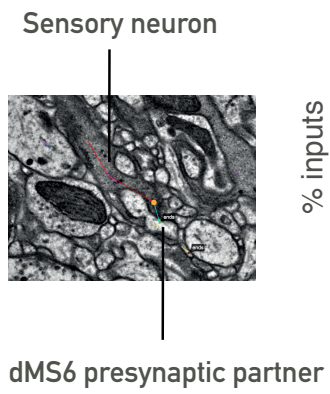
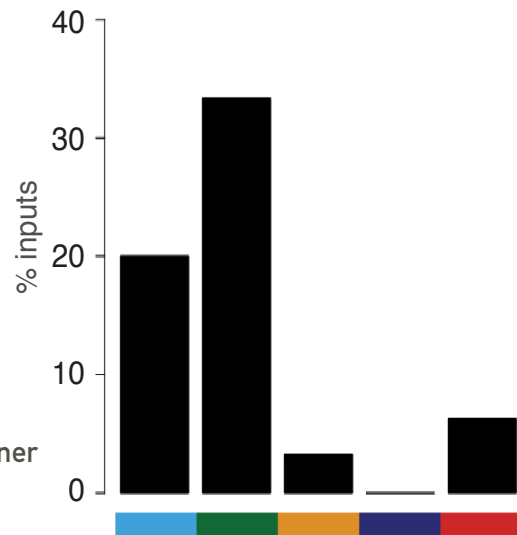
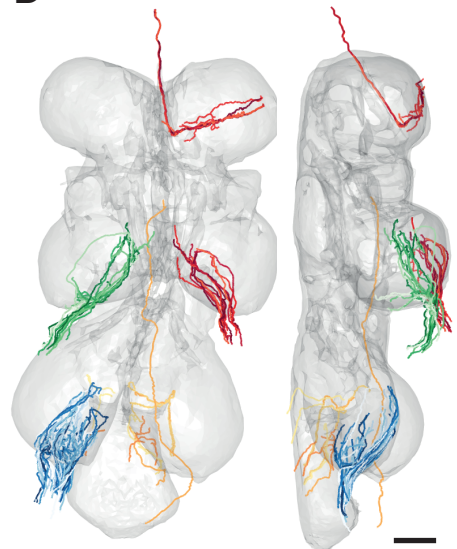
## **Figure 20: A layered axo-axonic circuit downstream of aSP-g regulates female receptivity**

**A:** Connectivity diagram of aSP-g downstream steps based on the FAFB dataset. Connections onto other connectors represent axo-axonal synapses. **B:** EM reconstruction of mAL1 neurons in the FAFB dataset (3 neuron / hemisphere). **C:** Confocal image of mAL1 in a female brain, reporter expression driven by mAL1 Stable Split, maximum projection. **D:** EM reconstruction of dMS6 neurons in the FAFB (top) and FANC (bottom) datasets. 1 neuron / hemisphere. Scale bars in B and D are 20  $\mu\text{m}$ . **E:** Confocal image of dMS6 in a female brain (top) and VNC (bottom), reporter expression driven by dMS6 Stable Split, maximum projection. **F:** Copulation rate of mAL1 CsChrimson activated virgin females (blue) and genetic control (black); n = 40-48, log rank test  $p < 0.001$ . **G:** Copulation rate of mAL1 Kir2.1 blocked virgin females (blue) and genetic control (black); n = 40, log rank test  $p = 0.024$ . **H:** Copulation rate of dMS6 CsChrimson activated virgin females (blue) and genetic control (black); n = 38-40, log rank test  $p < 0.001$ . **I:** Copulation rate of dMS6 Kir2.1 blocked virgin females (blue) and genetic control (black); n = 48, log rank test  $p = 0.039$ . **J:** Confocal image of co-immunostaining of mAL1 (3) and mAL2 (2) somata labelled by 67E08-LexA and GABA, single imaging channels on top, composite image at the bottom. Scale bars are 10  $\mu\text{m}$ . **K:** A circuit model for controlling female receptivity by a layered axo-axonic motif. **L:** Confocal image of co-immunostaining of dMS6 (2) somata labelled by dMS6 SS and ChAT4B, single imaging channels on top, composite image at the bottom. Scale bars are 10  $\mu\text{m}$ . The behavioural data and analyses presented in panels F, G, H and I, and the anatomical data in panels C, E, and J were contributed by Dr Dana Galili.



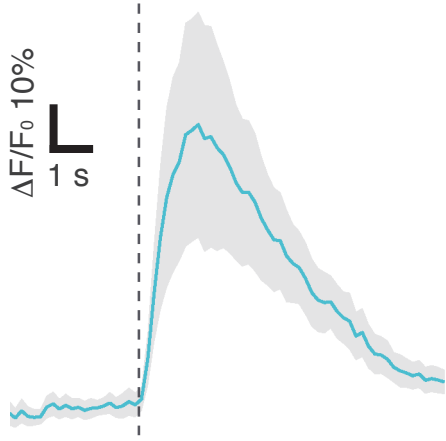
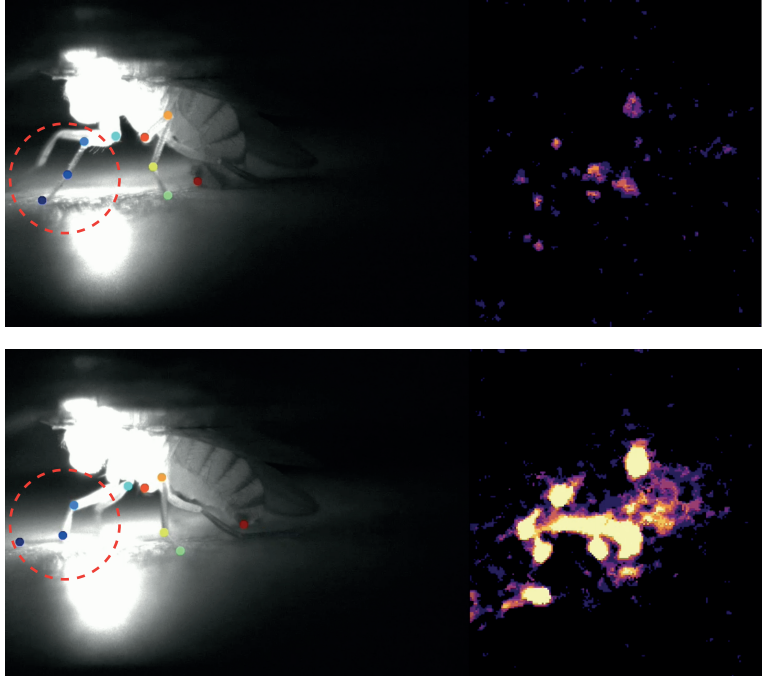
## **Figure 21: mAL1 is a subtype of the mAL clone with inputs from an abdominal ascending neuron**

**A:** Reconstructions of 35 mAL neurons from the FAFB dataset. Coloured based on NBLAST morphological clustering. Top: dendrogram of hierarchical clustering (Ward's method,  $k = 6$ ); bottom: mAL subtypes coloured by clusters, all other mAL neurons in grey for each brain. **B:** Representation of mAL1 inputs connectivity. Small circles represent a cell type with numbers showing the synaptic inputs to mAL1 neurons. The strongest upstream partner (dark blue) with 43 connections is abdSMP. **C:** Reconstructions of abdSMP neurons from the FAFB and FANC datasets; top: brain, bottom: VNC, 1 neuron / hemisphere. **D:** Confocal image of abdSMP in a female brain (top) and VNC (bottom), reporter expression driven by abdSMP Stable Split, maximum projection. **E:** The placement of synapses on mAL1 arbores from the top dendritic (abdSMP, dark blue circles), and the top axonal (aSP-g, purple circles) input cell types. Scale bars in B and D are 20  $\mu\text{m}$ . **F:** mAL1 responses to abdSMP optogenetic activation. abdSMP SS was used to drive the expression of CsChrimson, and 67E08-LexA to drive GCaMP7f. Red area shows the time of optogenetic stimulation by an LED ( $n = 5$ ).

**A****B****C****D**

**Figure 22: dMS6 is a third-order neuron to multiple leg sensory modalities**

**A:** Reconstructions of a single representative from the top five dMS6 upstream cell types in the FANC dataset. **B:** A representative EM section of an electron dense sensory neuron synapsing onto a dMS6 upstream partner in the FANC dataset. **C:** The percentage of sensory inputs to representative dMS6 upstream neurons. The order and colour bars at the bottom are the same as in A. **D:** Reconstructions of sensory neurons that synapse onto dMS6 upstream neurons in A. Colours of sensory neurons match the colour of their downstream cell in A. Left: frontal view, Right: lateral view. Scale bars in A and D are 20  $\mu\text{m}$ . These data and analyses were contributed by Shanice Bailey and William Morris.

**A****C****B**

### **Figure 23: dMS6 is activated by increased leg muscle load**

**A:** Circuit schematic of the dMS6 upstream pathway with the largest proportion of sensory inputs. cfRN: campaniform sensilla receptor neurons, asc-Ms: ascending mesothoracic neuron. **B:** Example frames from video recording of a fly at rest (top), and while pushing on the platform (bottom). Red dashed circles show the tibiotarsal joint on the foreleg that is in flexion while pushing down the platform. Next to it 2-photon images of GCaMP signal in dMS6 axons at the respective timepoints. Warmer colours represent higher intensity. **C:** Event triggered average of dMS6 GCaMP responses to the legs being pressed down on the platform by the fly. Joint position was manually scored;  $n = 3$ .

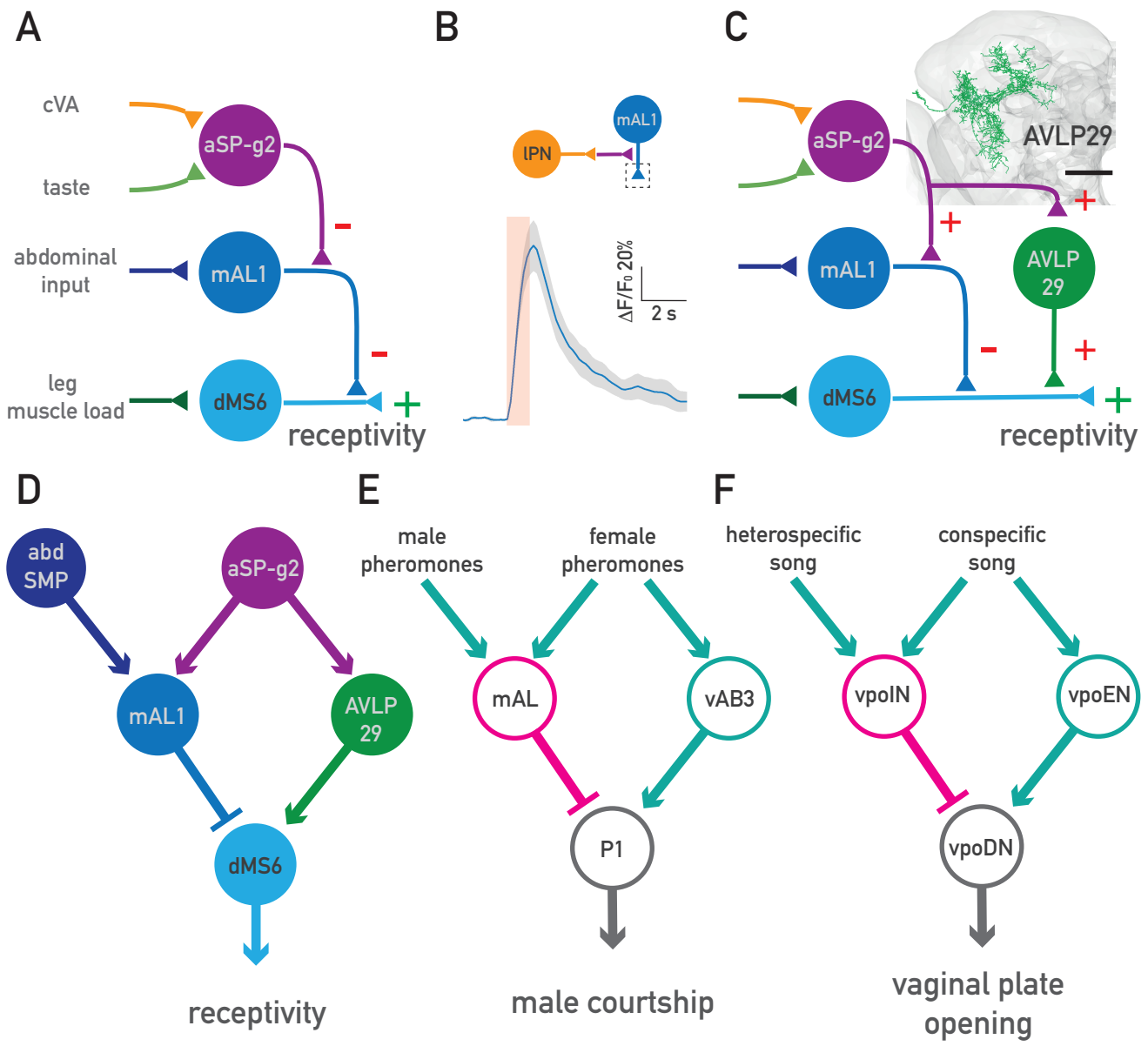


**Figure 24: An excitation-inhibition model for receptivity control by mAL1 and AVL29 via dMS6**

**A:** Circuit schematic of a single dMS6 upstream pathway showing the synaptic partners that provide the highest fraction of presynapses to their downstream partner. **B:** mAL1 responses to IPN optogenetic activation. IPN SS was used to drive the expression of CsChrimson, and 67E08-LexA to drive GCaMP7f. Red area shows the time of optogenetic stimulation by an LED (n = 5). **C:** Extended circuit model with AVL29 of receptivity control. Inset: EM reconstruction of AVL29 in the hemibrain dataset, scale bar is 20  $\mu\text{m}$ . **D:** Excitation - inhibition model for receptivity control based on C. **E:** Excitation - inhibition model of male courtship (adapted from Clowney et al. 2015) **F:** Excitation - inhibition model of vaginal plate opening (adapted from Wang et al. 2020).

## **8 Discussion**

This study described two parallel pathways for cVA processing in *Drosophila melanogaster* that preferentially signal male sex and position. The lvPN - pC1 route signals absolute levels of cVA on a 10 s timescale and promotes female receptivity. These features are consistent with coding male identity and improves our understanding of how pC1 gathers information about a courting male to guide the female mating decision. In contrast, the lPN - AV2a2 pathway is tuned to cVA concentration change and can extract features like male distance, angular position, and speed. lPNs are aided by an active antennal lobe mechanism enhancing bilateral contrast, and we identify a cell type that is a strong candidate to provide contralateral inhibition. This work establishes cVA as a pheromone that encodes positional information, demonstrates how identity and positional features of this signal are separately processed, and characterises a neuron likely responsible for improved olfactory lateralisation for many glomeruli.

We extensively reconstructed and analysed the wider cVA processing circuitry by using two connectomic datasets, and showed that cell types and connectivity are stereotyped across all neurons, in line with their role in innate, sexual behaviours. The circuit provides numerous examples of multimodal sensory integration. Connectivity and functional imaging shows that aSP-g neurons integrate cVA with taste information at their dendrites. This complex signal is sent onto a layered axo-axonic motif of mAL1 and dMS6 neurons. dMS6 neurons integrate information from leg sensory neurons that are likely from multiple modalities. We propose a model, consistent with connectivity, calcium imaging, and behavioural results, for how these multimodal signals regulate female receptivity. In this model aSP-g activates a pair of neurons, mAL1 and AVL29, which together provide an excitation - inhibition balance onto dMS6 axons to gate ascending inputs controlling female mating decision. This work suggests that axo-axonal connections and multimodal sensory integration are frequent motifs in the fly brain.

## **8.1 Olfactory positional coding**

Previous work on cVA has shown that the presence of cVA without any spatial or temporal structure is sufficient to alter male aggression and courtship, and female receptivity, clearly demonstrating how tonic stimulation of the cVA sensing Or67d ORNs affects behaviour in both sexes (Kurtovic, Widmer, and Dickson 2007; Wang and Anderson 2010). These findings defined our understanding of cVA's role, but other work suggested that cVA may do more than signal male sex. Agarwal and Isacoff (2011) claimed that DA1 lPNs have

characteristics that enable them to report stimulus differences between the two antennae better than other PNs, suggesting that they could encode male position.

Our study explores this possibility using a male fly as a spatially controlled stimulus and shows that IPN responses are dependent on male position. First we demonstrated that intracellular calcium responses in both ORNs and IPNs depend strongly on male distance, with the IPN dynamic range between 5 and 1 mm (Figure 5). Presenting the male on the side of a fly with or without unilateral antennal block evoked lateralised responses in ORNs, suggesting that the interantennal distance is sufficiently large to distinguish between ipsi- and contralateral male location on the ORN level (Figure 6). Notably, Or67d ORNs are housed in sensilla close to the lateral edge of the antennae, likely helping lateralisation by maximising the distance between the sensors (van der Goes van Naters and Carlson 2007; Grabe et al. 2016). ORNs from both sides converge onto PNs, although with a bias towards ipsilateral connections, this introduces a problem of reading out male angular position at the PN level.

Earlier work in DM6 PNs, which respond to volatile food odours, showed that biased ORN input connectivity underlies odour lateralisation in this glomerulus and excluded a contribution of GABAergic inhibition (Gaudry et al. 2013; Tobin, Wilson, and Lee 2017). However, recording IPN activity during lateralised male presentations with antennal manipulations revealed that inhibition shapes the responses in DA1 PNs (Figure 7). A pair of broad antennal lobe local neurons, il3LN6, were found to have strongly biased input connectivity from contralateral ORNs and inversely lateralised responses, consistent with a role in providing contralateral inhibition onto IPNs (Figure 8). The lack of a GABAergic mechanism in DM6 PN lateralisation is consistent with the fact that il3LN6 gives very little input (34 synapses) to them, compared to DA1 PNs, which receive 436 synapses from il3LN6. The morphology of this interneuron strongly suggests compartmentalised odour responses (Figure 9); in line with this, using a male fly as a stimulus specifically activated il3LN6 arbours in the DA1 glomerulus. These features make il3LN6 a strong candidate underlying enhanced lateral contrast of odour signals in many glomeruli.

Sampling the space with the male stimulus while recording IPN responses illustrates how the signal from both hemispheres can be used to decode angular direction and distance ( $\sim 30^\circ$  angular precision, 1.3 mm spatial precision; Figure 11). The sum of the activity on the sides correlates with the cosine of the male's angular direction (y-axis), and the difference between the sides correlates with the sine of the male's angular direction (x-axis) (Figure 11). Therefore these neurons are sufficient to estimate male position in 2D space using cartesian coordinates.

Our work also demonstrates that the concentration dependence of first and second order olfactory neurons translates well to distance tuning. As in many sensory systems, there is an inverse relation between signal intensity and distance, which leads to ambiguity in estimating these features. Additionally, cVA amount on males and cVA sensitivity depends on odour context, mating history and age (Das et al. 2017; Kuo et al. 2012; Lebreton et al. 2014; Park et al. 2020). Therefore cVA alone is always an ambiguous signal on its own for estimating distance but flies could use cVA for male localisation while incorporating sensory information from other modalities and temporal correlations in the signal, thereby overcoming these limitations.

These results extend our understanding of how cVA instructs behaviour. We showed that the stimulus' fine temporal and spatial aspects are closely followed by ORN and IPN activity, which would be superfluous for a role in shifting the arousal state for sexual behaviours on a time scale of minutes. Notably, flies cannot differentiate between males and females only using visual cues (Agrawal, Safarik, and Dickinson 2014), and this statement can be likely extended to other similarly sized *Drosophilids*. Using cVA to estimate a fly's position comes with the advantage of adding identity information to an ambiguous visual cue, and the possibility of tracking a male's movement in the dark. During courtship the male spends most of the time following the female from behind, while the female runs away from the male by orienting away from it, and running forward. Orienting away from a male is a behaviour where knowing the angular position of a male is essential, and cVA could be used to estimate this. Methyl laureate, another low volatility pheromone carried by both males and females, might extend the localisation range defined by cVA, and use a similar mechanism to detect female flies, as proposed by Root et al (2008), where they showed that males in a large dark arena can use methyl laureate to find females.

Previous work has shown that ORN and IPN responses to cVA are isomorphic in the sexes (Datta et al. 2008), our work showed that not only IPNs but also lvPNs respond similarly to a male at a single distance (Figure 5D, G). Potentially cVA based positional coding has a more prominent role in male behaviours like aggression or courtship suppression, as during these behaviours the cVA source (the male) is in front of the fly.

Olfactory lateralisation was shown to be relevant in detecting odour sources in many species, including flies, moths, moles, rats, and humans (Borst and Heisenberg 1982; Rajan, Clement, and Bhalla 2006; Catania 2013; Croy et al. 2014; von Békésy 1964; Takasaki, Namiki, and Kanzaki 2012). A recent review proposed contralateral inhibition as the most likely mechanism of efficient odour lateralisation in mice based on findings that a population

of anterior olfactory nucleus (AON) neurons are excited by ipsilateral and inhibited by contralateral odour presentation; furthermore, ablating crossing bilateral inputs to the AON disrupts odour localisation behaviour (Dalal, Gupta, and Haddad 2020; Esquivelzeta Rabell et al. 2017; Kikuta et al. 2010). These results and our work together strongly suggest that contralateral inhibition is another analogous aspect of insect and mammalian olfactory systems.

Using signal differences at two sensors to estimate the position of a stimulus is a general feature of sensory systems, most intensely studied in auditory processing (Gulick and von Békésy 1963; E. Knudsen and Konishi 1978). It was first demonstrated in barn owls that interaural time and intensity differences can be used to represent the position of auditory stimuli by neurons with specific receptive fields for spatial locations (E. I. Knudsen and Konishi 1979; E. Knudsen and Konishi 1978; Peña and Konishi 2001). Earlier, in von Békésy's foundational work he showed that humans can estimate the angular position of odour sources with 7-10° precision using similar information, despite the small distance between the nostrils (Gulick and von Békésy 1963). Whether there are neurons dedicated to representing the spatial aspect of olfactory information based on comparing bilateral signals, as is known for sound, is unclear.

Representing an arbitrary position in space by an abstract neural map comes with the advantage that this information is available independent of the behavioural task. In crickets, however, it was shown that females follow the song of males by reactive steering to single song pulses, without the time or the need to extract more complex features of the stimulus than azimuthal location (Hedwig and Poulet 2004), although the gain of turning is modulated by qualitative aspects of the song (Poulet and Hedwig 2005). Whether positional information in IPNs is used to create a map encoding male position based on cVA, or in general, whether there is a set of neurons with spatially localised olfactory receptive fields will be interesting to investigate. Potentially, the imbalance in the cVA signal levels at the two sides is sufficient to instruct lateralised behavioural responses without the need for a more abstract representation of male position. However, it is also possible that both kinds of circuit might coexist in the insect brain: fast acting circuits mediating reactive steering and more map-like representations that could interact for example with circuits mediating very long range navigation (Leitch et al. 2020).

Crucially, the mechanism of olfactory localisation we describe provides an instantaneous way to infer the location of the stimulus, similar to auditory and visual systems. Olfactory navigation strategies evolved to deal with the intermittent nature of odour stimuli,

and often rely on active sampling, integration over time, or other modalities like wind-sensing (Payne 1986; Khan, Sarangi, and Bhalla 2012; A. C. Marin, Schaefer, and Ackels 2021). We found that cVA, likely due to its low volatility, provides an olfactory signal that requires no temporal integration or multiple sampling events, rather it continuously informs the fly about a male's position. Recent work in mice showed that olfaction operates on a faster time scale than expected (Ackels et al. 2021), suggesting that a similar continuous positional code could be used by mammals to infer the location of stable odour stimuli.

An important limitation of our study is that our experiments used a male mounted with the abdomen facing the experimental fly during imaging. Clearly this orientation is very rare during behaviour, but based on the clear and reproducible responses in ORNs and PNs at different distances, and the lack of responses to only airflow (Figure 5) we assume that in a windless environment the cVA gradient around a male is largely unchanged as the male is moving along, other than it moves together with it. Likely, this “odour cloud” is not perfectly spherical, centred around the male genitalia, but we regard this as a useful first estimate, also based on mass spectrometry imaging where most cVA on a male was found at the top of the abdomen (Kaftan et al. 2020). An interesting possibility to consider is that males could also fan their smell towards a female during courtship song, a similar phenomenon was observed in silkworm moths (Loudon and Koehl 2000), furthermore antennal movements of the receiver fly could actively contribute to cVA sensing e.g. by modifying the interantennal distance.

## 8.2 Separate pathways for *what* and *where*

Above we concluded that cVA can be used for positional coding besides its well-known function of signalling male identity. How are these two distinct features, relevant on different time scales, extracted from a single sensory input? Connectomic work showed a previously unidentified cVA responsive PN type, lvPNs, which receive ORN input specifically from Or67d ORNs. lvPNs were shown to be a parallel excitatory cVA pathway to IPNs (Figure 3). lvPNs have lower sensitivity to cVA consistent with having fewer input synapses than IPNs. Furthermore, these neurons respond tonically to a male, while IPNs adapt fast, implying that they operate on different time scales (Figure 5). A tonic response can represent the presence of an object as long as it is there; e.g. as long as a male is courting. The physiology and behavioural role of other PNs from the latero-ventral lineage is

unexplored in adult flies, therefore it is an open question whether adaptation properties of DA1 lvPNs is common in this lineage.

Previous work has characterised how cVA information is transformed across three neuronal layers to improve the speed and accuracy of stimulus onset detection, however, it focussed on very short, 100 ms long, stimuli (Jeanne and Wilson 2015). Using two third-order neurons; AV2a2, a sexually non-dimorphic downstream partner of IPNs, and pC1, a sexually dimorphic downstream partner of lvPN; this work reveals a striking difference in response properties at the third layer. pC1 shows the tonic responses like lvPNs, while AV2a2 responses are even more phasic than their input, IPN, thereby specifically responding to stimulus onset (Figure 12, 14). Furthermore, AV2a2 responses are strongly dependent on the male's approach speed and correlate with the speed of change in the IPN signal (Figure 12, 13). These response profiles of the IPN - AV2a2 and lvPN - pC1 pathways are consistent with their behavioural effect on female receptivity. AD1g1, the neuron that AV2a2 gives most of its output synapses, also receives strong input from visual looming sensors, while pC1 is known to integrate cVA and courtship song (Figure 16). Intriguingly, AV2a2 is sexually monomorphic and does not express *fruitless* or *doublesex*, while pC1 is *doublesex+* and dimorphic. This suggests that identity-related features are processed differently in the sexes, while positional features could be processed identically in males and females.

IPNs have a wide variety of downstream partners in the lateral horn: twenty cell types receive at least 1% of their inputs from IPNs. AV2a2 is one that keeps the “labelled line” nature of the PNs based on connectivity, as it does not receive direct PN input from other glomeruli or non-olfactory modalities. aSP-g neurons, a *fruitless+*, sexually dimorphic IPN partner, integrate cVA with taste. aSP-g regulates female receptivity bidirectionally, similarly to pC1, however IPN manipulations were not sufficient to evoke these effects (Figure 15).

Based on these data, a model emerges in which distinct features are extracted from a single olfactory signal by specific pathways to encode male position and identity at the third layer of the circuits. The AV2a2 extracts a specific feature of positional information, approach speed, to integrate this with relevant visual signals, and manipulating AV2a2 activity in either direction disrupts temporal coding and negatively affects female receptivity. pC1 and aSP-g, on the other hand, could signal a male related signal. pC1 may represent a courting male by integrating cVA with courtship song, while aSP-g could assess a combination of male pheromones (olfactory and gustatory) to regulate female receptivity. This model does not account for the fact that lvPNs also carry information about male distance; thereby pC1, and aSP-g (via IPNs) might relay positional aspects of cVA.

Importantly, aSP-g neurons are bilateral, with overlapping axonal arbours in the two hemispheres and their downstream partners receive input from aSP-g neurons on both sides. This circuit layout may suggest that angular position information is lost downstream of aSP-g by summing signals from the two antennae. Intriguingly, pC1 and aSP-g are sexually dimorphic, while AV2a2 is identical in males and females. These findings together suggest that positional and identity features are represented in a strongly biased manner at the third layer of this olfactory circuit. Furthermore, we propose that identity-related features are encoded by sexually dimorphic circuit elements, consistent with their function in regulating sex-specific behaviours, while positional features are encoded by the same neurons in males and females (Figure 25).

It will be interesting to ask how these cell-types interact in male flies. P1 neurons, a hub for male social behaviours including aggression are a likely candidate for being downstream of lvPNs. If AV2a2 is indeed not only morphologically but also physiologically isomorphic, responding to male approach in both sexes, it might play a specific role in male aggression. The integration of visual and olfactory approach signals could be tested in AD1g1 neurons. Finally, all these pathways must reach descending neurons to instruct motor circuits in the VNC that are not identified yet.

### **8.3 Dendritic and axonal sensory integration steps shape sexual decision making**

Earlier work in our laboratory described a developmental circuit switch at the third layer of the cVA pathway (Kohl et al. 2013). aSP-g neurons respond to cVA in females, but not in males, while aSP-f neurons are wired oppositely. This dimorphism is a result of cell-autonomous mechanisms, driven by *fruitless*, a sex-determination factor. These findings provided a link between sexually dimorphic gene expression, neuroanatomy, and physiology (Kohl et al. 2013). Building on this work, our study advanced our understanding of how one of the female member's of this switch guides the expression of sexually dimorphic behaviours, and which downstream neurons are involved. Our efforts were led by connectomic tracing of information flow. With this largely unbiased approach, we found that the most relevant circuit components are also *fruitless*<sup>+</sup> (mAL1, abdSMP, dMS6). This suggests that *fruitless* specifies a subset of neurons that preferentially wire with each other to form extensive dimorphic circuits that guide sexual behaviours.

Showing that aSP-g neurons bidirectionally regulate female receptivity demonstrates the behavioural significance of the circuit switch described by Kohl et al. Contradicting

previous expectations in the field (Auer and Benton 2016) we show that aSP-g controls female receptivity via a pC1-independent pathway (Figure 19). This finding, together with the fact that DA1 lvPN is sufficient to activate pC1, suggests that cVA controls female receptivity via two pathways that already split at the first synapse. These results signify exploring the upstream and downstream circuits of aSP-g.

This study characterises anatomically and behaviourally the fourth and fifth layer of a cVA processing pathway and describes the distinct sensory modalities entering this circuit (Figure 21, 22). The third-order aSP-g neurons integrate cVA with a taste cue sensed by Ir94e+ labellar GRNs and relay this signal to the axons of mAL1 neurons (Figure 19, 20). It is important to note that the evidence of integration of taste signals with cVA by aSP-g neurons is limited. While the connectomic data is very clear, the calcium imaging experiments used only three flies, more data is needed to make this observation more robust. mAL1 is activated at its dendrites by an abdominal signal via abdSMP neurons, and also at its axons by aSP-g (Figure 21, 24). How these signals are integrated is unclear, but they could evoke presynaptic inhibition by mAL1 onto dMS6 axons, given that mAL1 are GABAergic. dMS6, an ascending neuron with dendrites in the VNC, is innervated by many modalities from the legs (Figure 22). These include external mechano- and proprioceptive pathways, and indeed dMS6 responds to increased load on leg muscles (Figure 23). dMS6 regulated receptivity similarly to aSP-g, while mAL1 activation negatively affects female mating drive, which would be consistent with the inhibitory relationship from mAL1 to dMS6 (Figure 20). We found AVL29 neurons to take a similar place in the circuit as mAL1, between aSP-g and dMS6. This connectivity suggests that aSP-g activates mAL1 and AVL29 together to switch on an excitation - inhibition balance onto dMS6 axons, likely affected by other signals (Figure 24). mAL neurons in male flies play a similar role in choosing the right target for courtship (Clowney et al. 2015; Kallman, Kim, and Scott 2015).

This study found several examples of sensory integration motifs. Presenting a male together with optogenetic taste stimulation caused a superlinear activation in aSP-g (Figure 18). Future work will characterise the precise quantitative nature of this dendritic integration. At the next two circuit elements, we found examples of axo-axonal synapses; we speculate that a different interaction emerges where dendritic signals are gated or modulated by presynaptic inputs. This is in line with findings from many other studies using connectomic data, that axo-axonal connections are prevalent in the fly brain (Bates, Schlegel, et al. 2020; F. Li et al. 2020). What computational rules apply to this type of connection needs to be

further investigated. Our work provides a circuit with defined behavioural roles and synaptic signs as an entry point to this problem.

The anatomical and functional data we present show a layered circuit with sensory integration at almost every step, including modalities (e.g. proprioception) that were not previously considered to play a role in female receptivity. These findings open up questions about the exact nature and ethological relevance of these sensory pathways: what stimuli activate Ir94e GRNs, abdSMP neurons, and other dMS6 inputs? Furthermore, we believe that the network we uncovered is a central part of the female mating decision: integrating a multitude of sensory inputs from a courting male to make a binary decision whether to reject or accept him. We propose that a motif of excitation-inhibition balance, similar to other pathways in fly sexual behaviours, is at the core of this circuit, improving signal specificity to fine-tune behaviour.

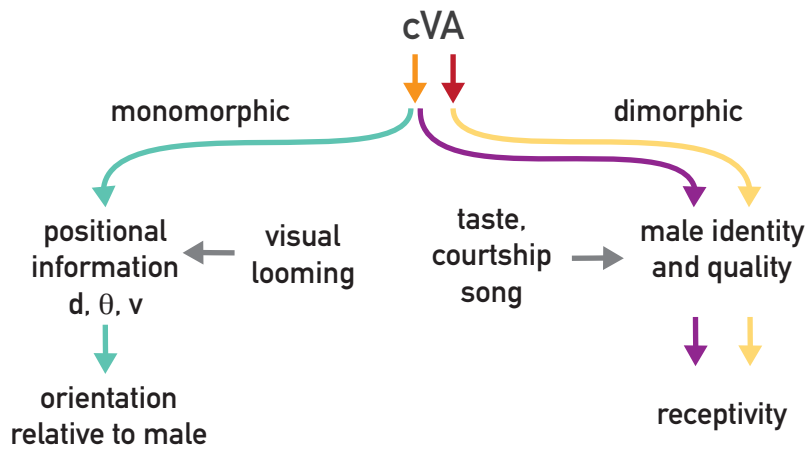


### **Figure 25: Separation of positional and identity cues in cVA processing**

cVA information diverges onto two parallel excitatory PN pathways at the first synapse. Third-order neurons mainly extract either positional or identity features and integrate these with other relevant sensory modalities. Neurons encoding male identity related information are sexually dimorphic and bidirectionally regulate female receptivity.

**Table 2: Neuron identifiers from EM datasets (FAFB, hemibrain)**

<b>cell type</b>	<b>FAFB skeleton id</b>	<b>hemibrain bodyid</b>
abdSMP	6536545, 4291069	519012059, 519603027
AD1g1	1316642	792326206
aSP-g1	1064888, 1100594, 1101176, 1070581, 1074687, 1079881, 1083904, 6649459	485430434, 485775679, 610916994, 887148641, 949534412
aSP-g2	1055936, 1064687, 7899781, 7918690, 534333, 1064853, 1086385, 1149437, 2477473	421992069, 641278400, 855414220, 5813115796
aSP-g3	7856299, 11322700, 8415303, 1041505, 1168923	329919036, 421650982, 485430336
AV2a2	1811965, 1870230, 6762450	486444499, 612285653, 674001478, 948135822
AVLP29	10977800, 7928068	580227374
DA1 IPN	4207871, 3239781, 2381753, 2380564, 2379517, 2345089, 2319457, 2863104, 61221, 57381, 755022, 57353, 57323, 57311, 27295	722817260, 754534424, 754538881, 1734350788, 1734350908, 1765040289, 5813039315
DA1 lvPN	4520197, 7710838, 7414894, 57179, 57158, 57035	757258507, 757591093, 792023887
DA1 lvPN2	7430367, 7423477, 7414916, 7414898, 57089, 57023, 57019, 57011	851684181, 1827473315, 792024028

DA1 ORN L	2285344	1671970331, 1764703462, 1574160129, 1574833154, 1575170261, 1639938708, 1669949998, 1670627821, 1671620813, 1671629267, 1671629301, 1671966114, 1671966254, 1671970212, 1671970367, 1671970683, 1672311578, 1672639485, 1672643988, 1703337673, 1703342190, 1703678670, 1704006659, 1704011227, 1734350776, 1734350800, 1734350801, 1734350808, 1734350882, 1734355450, 1734359876, 1734691780, 1734691853, 1734696429, 1734696604, 1735037273, 1735041817, 1735050696, 1735050861, 1735054428, 1735058800, 1735378225, 1735378236, 1735386920, 1764703552, 1765053669, 1765727039, 1766068129, 1766068153, 1766409090, 1766753982, 1766758683, 1796075469, 1796080038, 1796420624, 1796757192, 1796757522, 1796766157, 1797443721, 1797793830, 1826773830, 1827110060, 1827114589, 1827446803, 1827633289, 5812995356, 5812995402, 5812996926, 5812996943, 5813083386, 5813134848, 5901204334, 5901210481
DA1 ORN R	2253836	1734355466, 1827451271, 1671966064, 1671970238, 1671974365, 1672307311, 1672311668, 1672315788, 1672652372, 1702301766, 1703682799, 1703682848, 1703682852, 1703683023, 1703683156, 1734355247, 1734355428, 1734691670, 1734691865, 1734705240, 1735032816, 1735037070, 1735037194, 1735041965, 1735042035, 1735054607, 1735378183, 1735382530, 1735382574, 1735391275, 1735395504, 1735395524, 1764699151, 1765040222, 1765044896, 1765381455, 1765386030, 1765403303, 1766067809, 1766068147, 1766413024, 1766754285, 1766762919, 1795402166, 1795734015, 1795742734, 1796416505, 1796761826, 1797439276, 1797789401, 1826773768, 1858162227, 1858486077, 1858822939,

		1859190013, 5812995437, 5812996079, 5813020396, 5813054729, 5901204564, 1796757163
dMS6	1255100, 2125955	611262552, 704367157
G2N-aSLP	11463951, 11483002, 11490387, 11491648, 11491723, 11491809, 11491851, 11495175, 11968494, 11968950, 3917175	671618401, 5901195362
G2N-SLP1	7552826, 2434711	424379864
G2N-SLP2	1059970, 1064624	583042026, 614059839
G2N-SLP3	9484087, 11464526, 2686821, 3781311	330998071, 362024428
G2N-SLP4	9165878, 1102458	5813056890
G2N-SLP5	9040832, 2255652	515450389
iI3LN6	8964539	5813018460, 5901206553
LC4	NA	1158187240, 1158864995, 1189559257, 1218901359, 1249932198, 1251287671, 1281303666, 1405780725, 1438524573, 1466861327, 1471601440, 1498574596, 1503999967, 1562673627, 1590979045, 1621357756, 1625080038, 1627117134, 1688505620, 1715459859, 1745821751, 1749258134, 1781268241, 1782668028, 1809264255, 1810956698, 1815070402, 1838257401, 1839288696, 1840636280, 1845078711, 1874035952, 1876471221, 1876894387, 1876898200, 1876902545, 1877217777, 1877930505, 1877939213, 1878271377, 1906159299, 1906496111, 1907156409, 1907169406, 1907510214, 1907519001, 1907571222, 1907574944, 1907578957, 1907584319, 1907587934, 1907924777, 1907933561, 1908226457, 1936848448, 1937875810, 1938207942, 1938541380, 1938544937, 1998922583, 2121711447, 2215161310, 5812993692, 5812998136, 5813000577, 5813055129, 5813061197, 5813069053, 5813069377, 5813075607, 5901215446

IGRN	7759395, 7789757, 7789762, 7802087, 11302515, 11559749, 11987931, 10780443, 10795558, 11243248	NA
LPLC2	NA	1221971218, 1282007450, 1283013506, 1343749180, 1403392477, 1407179534, 1437850908, 1438908304, 1438912593, 1441598865, 1467548306, 1470971204, 1500598873, 1530636214, 1533683889, 1534363304, 1566411868, 1626482563, 1626827782, 1627131491, 1682707330, 1688164533, 1691259738, 1716496582, 1719225241, 1719595635, 1751329909, 1751670748, 1752016801, 1753674977, 1782364786, 1782369015, 1782369340, 1782369359, 1783051578, 1783051753, 1809614687, 1811630361, 1813403630, 1813403762, 1813403869, 1813403953, 1813403998, 1814414329, 1814418212, 1814422650, 1814426918, 1814777260, 1814780768, 1814781082, 1814781356, 1814781537, 1814781628, 1814781633, 1815126312, 1815126433, 1815131045, 1815471919, 1815480848, 1815809293, 1815826155, 1844750081, 1845449270, 1845453234, 1872033743, 1876147388, 1876147437, 1876484146, 1876492837, 1938195143, 2059978318, 5812987894, 5812996383, 5812998825, 5812999264, 5813034151, 5813038769, 5813038821, 5813038822, 5813038825, 5813039136, 5813046478, 5813050827, 5901214470, 5901226269
mAL1	1670287, 4119200, 8792484, 1182615, 1273130, 8167845	360958913, 390616496, 452694446
pC1	3838015, 3807212, 3212353, 3781621, 3837769, 3794183, 3884170, 3979930, 3883095, 3770805	5813046951, 267214250, 267551639, 5813063587, 514850616
pGRN	7108314, 5864214	NA
vpoDN	5094164	5813057864

pC1 neurons and vpoDN were reconstructed in FAFB and published by Wang et al. (2021). We reconstructed all cell types on both sides in FAFB with the following exceptions: AD1g1, AV2a2, AVL29, i3LN6, G2N-aSLP, IGRN, vpoDN. All cell types in the hemibrain come from one hemisphere, with the following exceptions: DA1 ORN, i3LN6, dMS6.

**Table 3: List of synaptic weights from FAFB and hemibrain for relevant connections across cell types**

As described above, most cell types in FAFB were reconstructed on both sides of the brain, with the following exceptions: AD1g1, AV2a2, AVL29, i3LN6, G2N-aSLP, IGRN, vpoDN. The presented FAFB synaptic weights are the sum from both sides for cell type pairs, where both pre- and postsynaptic partners are reconstructed on both sides. Synaptic weights from the hemibrain are based on the version 1.2.1 of the dataset, displayed at neurpint.org, and represent connectivity from a single hemisphere, with the following exceptions: DA1 ORN, i3LN6, dMS6. ORNs from the right hemisphere (DA1 ORN R) are ipsilateral to the antennal lobe in the hemibrain, and ORNs from the left hemisphere (DA1 ORN L) are contralateral.

<b>presynaptic cell type</b>	<b>postsynaptic cell type</b>	<b>FAFB # synapses</b>	<b>hemibrain # synapses</b>
abdSMP	mAL1	43	23
aSP-g1	AVLP29	44	75
aSP-g2	aSP-g1	129	77
aSP-g2	aSP-g2	74	29
aSP-g2	AVLP29	45	23
aSP-g2	mAL1	254	64
aSP-g2	pC1	2	17
aSP-g3	mAL1	12	25
AV2a2	AD1g1	NA	142
AV2a2	pC1	18	48
AVLP29	aSP-g1	27	42
AVLP29	aSP-g2	21	11
AVLP29	dMS6	84	148

DA1 IPN	aSP-g2	132	37
DA1 IPN	AV2a2	232	115
DA1 IPN	DA1 lvPN2	NA	114
DA1 IPN	DA1 ORN L	NA	43
DA1 lvPN	aSP-g2	13	3
DA1 lvPN	pC1	85	59
DA1 lvPN2	aSP-g2	113	28
DA1 ORN L	DA1 IPN	NA	3580
DA1 ORN R	DA1 IPN	NA	5184
DA1 ORN L	DA1 lvPN	NA	113
DA1 ORN R	DA1 lvPN	NA	157
DA1 ORN L	DA1 lvPN2	NA	9
DA1 ORN R	DA1 lvPN2	NA	28
DA1 ORN L	i13LN6	NA	1901
DA1 ORN R	i13LN6	NA	359
DA1 ORN L	DA1 ORN L	NA	1070
DA1 ORN R	DA1 ORN R	NA	1411
DA1 ORN L	DA1 ORN R	NA	959
DA1 ORN R	DA1 ORN L	NA	791
dMS6	AVLP29	33	37
dMS6	pC1	68	90
G2N-aSLP	aSP-g1	36	NA
G2N-aSLP	aSP-g2	11	NA
G2N-aSLP	aSP-g3	61	NA
G2N-SLP1	aSP-g1	79	80
G2N-SLP1	aSP-g2	85	28
G2N-SLP1	aSP-g3	25	19
G2N-SLP2	aSP-g1	3	11
G2N-SLP2	aSP-g2	34	29
G2N-SLP2	aSP-g3	33	45
G2N-SLP3	aSP-g2	70	27
G2N-SLP3	aSP-g3	24	18
G2N-SLP4	aSP-g3	33	15

G2N-SLP5	aSP-g3	66	20
i13LN6	DA1 lPN	NA	465
i13LN6	DA1 lvPN	NA	3
i13LN6	DA1 lvPN2	NA	5
i13LN6	DA1 ORN L	NA	165
i13LN6	DA1 ORN R	NA	297
LC4	AD1g1	NA	434
LPLC2	AD1g1	NA	474
lGRN	G2N-SLP1	63	NA
lGRN	G2N-SLP2	86	NA
mAL1	dMS6	87	29
pC1	pC1	426	347
pC1	vpoDN	386	92
pGRN	G2N-SLP1	166	NA
pGRN	G2N-SLP2	56	NA

**Table 4: Neuron identifiers from the FANC EM dataset**

cell type	FANC skeleton id
dMS6	206759, 206956
asc-MT	228730, 243758
asc-MS	228414, 230684, 232113, 233993
int-Abd	230179, 230735, 231741
asc-Pro	208452, 208721, 208759, 227353, 229411
int-Ms	231162, 247540
cfRN	334563, 334569, 334590, 334590, 338766, 342249, 343258, 391955, 392293

**Table 5: List of synaptic weights from FANC across cell types**

presynaptic cell type	postsynaptic cell type	FANC # synapses
asc-MT	dMS6	39
asc-MS	dMS6	34
int-Abd	dMS6	33
asc-Pro	dMS6	29
int-Ms	dMS6	25
cfRN	asc-MT	27

Synaptic weights including dMS6 are numbers based on both hemispheres.

## 9 References

- Ache, Jan M., Jason Polsky, Shada Alghailani, Ruchi Parekh, Patrick Breads, Martin Y. Peek, Davi D. Bock, Catherine R. von Reyn, and Gwyneth M. Card. 2019. “Neural Basis for Looming Size and Velocity Encoding in the *Drosophila* Giant Fiber Escape Pathway.” *Current Biology: CB* 29 (6): 1073–81.e4.
- Ackels, Tobias, Andrew Erskine, Debanjan Dasgupta, Alina Cristina Marin, Tom P. A. Warner, Sina Tootoonian, Izumi Fukunaga, Julia J. Harris, and Andreas T. Schaefer. 2021. “Fast Odour Dynamics Are Encoded in the Olfactory System and Guide Behaviour.” *Nature* 593 (7860): 558–63.
- Adrian, E. D., and Y. Zotterman. 1926. “The Impulses Produced by Sensory Nerve Endings: Part 3. Impulses Set up by Touch and Pressure.” *The Journal of Physiology* 61 (4): 465–83.
- Agarwal, Gautam, and Ehud Isacoff. 2011. “Specializations of a Pheromonal Glomerulus in the *Drosophila* Olfactory System.” *Journal of Neurophysiology*. <https://doi.org/10.1152/jn.00591.2010>.
- Agrawal, Sweta, Steve Safarik, and Michael Dickinson. 2014. “The Relative Roles of Vision and Chemosensation in Mate Recognition of *Drosophila Melanogaster*.” *The Journal of Experimental Biology* 217 (Pt 15): 2796–2805.
- Aranha, Márcia M., and Maria Luísa Vasconcelos. 2018. “Deciphering *Drosophila* Female Innate Behaviors.” *Current Opinion in Neurobiology*. <https://doi.org/10.1016/j.conb.2018.06.005>.
- Auer, Thomas O., and Richard Benton. 2016. “Sexual Circuitry in *Drosophila*.” *Current Opinion in Neurobiology*. <https://doi.org/10.1016/j.conb.2016.01.004>.
- Baker, T. C., M. A. Willis, K. F. Haynes, and P. L. Phelan. 1985. “A Pulsed Cloud of Sex Pheromone Elicits Upwind Flight in Male Moths.” *Physiological Entomology*. <https://doi.org/10.1111/j.1365-3032.1985.tb00045.x>.
- Barnes, Christopher L., Daniel Bonn ery, and Albert Cardona. 2022. “Synaptic Counts Approximate Synaptic Contact Area in *Drosophila*.” *PloS One* 17 (4): e0266064.
- Bartelt, Robert J., Angela M. Schaner, and Larry L. Jackson. 1985. “Cis-Vaccenyl Acetate as an Aggregation Pheromone in *Drosophila Melanogaster*.” *Journal of Chemical Ecology*. <https://doi.org/10.1007/bf01012124>.
- Bates, A. S., Jasper Janssens, Gregory Sxe Jefferis, and Stein Aerts. 2019. “Neuronal Cell Types in the Fly: Single-Cell Anatomy Meets Single-Cell Genomics.” *Current Opinion in Neurobiology* 56 (June): 125–34.
- Bates, A. S., James D. Manton, Sridhar R. Jagannathan, Marta Costa, Philipp Schlegel, Torsten Rohl ing, and Gregory Sxe Jefferis. 2020. “The Natverse, a Versatile Toolbox for Combining and Analysing Neuroanatomical Data.” *eLife* 9 (April). <https://doi.org/10.7554/eLife.53350>.
- Bates, A. S., Philipp Schlegel, Ruairi J. V. Roberts, Nikolas Drummond, Imaan F. M. Tamimi, Robert Turnbull, Xincheng Zhao, et al. 2020. “Complete Connectomic Reconstruction of Olfactory Projection Neurons in the Fly Brain.” *Current Biology: CB* 30 (16): 3183–99.e6.
- Bau, J., K. A. Justus, and R. T. Card e. 2002. “Antennal Resolution of Pulsed Pheromone Plumes in Three Moth Species.” *Journal of Insect Physiology* 48 (4). [https://doi.org/10.1016/s0022-1910\(02\)00062-8](https://doi.org/10.1016/s0022-1910(02)00062-8).
- B ek esy, G. von. 1964. “OLFACTORY ANALOGUE TO DIRECTIONAL HEARING.” *Journal of Applied Physiology* 19 (May): 369–73.
- Berman, Gordon J., Daniel M. Choi, William Bialek, and Joshua W. Shaevitz. 2014.

- “Mapping the Stereotyped Behaviour of Freely Moving Fruit Flies.” *Journal of the Royal Society, Interface / the Royal Society* 11 (99).  
<https://doi.org/10.1098/rsif.2014.0672>.
- Bhandawat, Vikas, Shawn R. Olsen, Nathan W. Gouwens, Michelle L. Schlieff, and Rachel I. Wilson. 2007. “Sensory Processing in the *Drosophila* Antennal Lobe Increases Reliability and Separability of Ensemble Odor Representations.” *Nature Neuroscience*.  
<https://doi.org/10.1038/nn1976>.
- Bogovic, John A., Hideo Otsuna, Larissa Heinrich, Masayoshi Ito, Jennifer Jeter, Geoffrey Meissner, Aljoscha Nern, et al. 2020. “An Unbiased Template of the *Drosophila* Brain and Ventral Nerve Cord.” *PloS One* 15 (12): e0236495.
- Borst, Alexander, and Martin Heisenberg. 1982. “Osmotropotaxis in *Drosophila Melanogaster*.” *Journal of Comparative Physiology ? A*.  
<https://doi.org/10.1007/bf00612013>.
- Branson, Kristin, Alice A. Robie, John Bender, Pietro Perona, and Michael H. Dickinson. 2009. “High-Throughput Ethomics in Large Groups of *Drosophila*.” *Nature Methods* 6 (6): 451–57.
- Buck, L., and R. Axel. 1991. “A Novel Multigene Family May Encode Odorant Receptors: A Molecular Basis for Odor Recognition.” *Cell* 65 (1): 175–87.
- Buhmann, Julia, Renate Krause, Rodrigo Ceballos Lentini, Nils Eckstein, Matthew Cook, Srinivas Turaga, and Jan Funke. 2018. “Synaptic Partner Prediction from Point Annotations in Insect Brains.” *Medical Image Computing and Computer Assisted Intervention – MICCAI 2018*. [https://doi.org/10.1007/978-3-030-00934-2\\_35](https://doi.org/10.1007/978-3-030-00934-2_35).
- Bussell, Jennifer J., Nilay Yapici, Stephen X. Zhang, Barry J. Dickson, and Leslie B. Vosshall. 2014. “Abdominal-B Neurons Control *Drosophila* Virgin Female Receptivity.” *Current Biology: CB* 24 (14): 1584–95.
- Butenandt, Adolf, Rüdiger Beckmann, and Erich Hecker. 1961. “Über Den Sexuallockstoff Des Seidenspinners, I. Der Biologische Test Und Die Isolierung Des Reinen Sexuallockstoffes Bombykol.” *Hoppe-Seyler's Zeitschrift Für Physiologische Chemie*.  
<https://doi.org/10.1515/bchm2.1961.324.1.71>.
- Cachero, Sebastian, Aaron D. Ostrovsky, Jai Y. Yu, Barry J. Dickson, and Gregory S. X. Jefferis. 2010. “Sexual Dimorphism in the Fly Brain.” *Current Biology*.  
<https://doi.org/10.1016/j.cub.2010.07.045>.
- Calhoun, Adam J., Jonathan W. Pillow, and Mala Murthy. 2019. “Unsupervised Identification of the Internal States That Shape Natural Behavior.” *Nature Neuroscience* 22 (12): 2040–49.
- Caron, Sophie J. C., Vanessa Ruta, L. F. Abbott, and Richard Axel. 2013. “Random Convergence of Olfactory Inputs in the *Drosophila* Mushroom Body.” *Nature* 497 (7447): 113–17.
- Catania, Kenneth C. 2013. “Stereo and Serial Sniffing Guide Navigation to an Odour Source in a Mammal.” *Nature Communications*. <https://doi.org/10.1038/ncomms2444>.
- Chiang, Ann-Shyn, Chih-Yung Lin, Chao-Chun Chuang, Hsiu-Ming Chang, Chang-Huain Hsieh, Chang-Wei Yeh, Chi-Tin Shih, et al. 2011. “Three-Dimensional Reconstruction of Brain-Wide Wiring Networks in *Drosophila* at Single-Cell Resolution.” *Current Biology: CB* 21 (1): 1–11.
- Chu, Xi, Stanley Heinze, Elena Ian, and Bente G. Berg. 2020. “A Novel Major Output Target for Pheromone-Sensitive Projection Neurons in Male Moths.” *Frontiers in Cellular Neuroscience* 14 (June): 147.
- Clowney, E. Josephine, E. Josephine Clowney, Shinya Iguchi, Jennifer J. Bussell, Elias Scheer, and Vanessa Ruta. 2015. “Multimodal Chemosensory Circuits Controlling Male Courtship in *Drosophila*.” *Neuron*. <https://doi.org/10.1016/j.neuron.2015.07.025>.

- Coen, Philip, Jan Clemens, Andrew J. Weinstein, Diego A. Pacheco, Yi Deng, and Mala Murthy. 2014. “Dynamic Sensory Cues Shape Song Structure in *Drosophila*.” *Nature* 507 (7491): 233–37.
- Costa, Marta, James D. Manton, Aaron D. Ostrovsky, Steffen Prohaska, and Gregory S. X. E. Jefferis. 2016. “NBLAST: Rapid, Sensitive Comparison of Neuronal Structure and Construction of Neuron Family Databases.” *Neuron* 91 (2): 293–311.
- Croset, Vincent, Michael Schleyer, J. Roman Arguello, Bertram Gerber, and Richard Benton. 2016. “A Molecular and Neuronal Basis for Amino Acid Sensing in the *Drosophila* Larva.” *Scientific Reports* 6 (December): 34871.
- Croy, Ilona, Max Schulz, Anna Blumrich, Cornelia Hummel, Johannes Gerber, and Thomas Hummel. 2014. “Human Olfactory Lateralization Requires Trigeminal Activation.” *NeuroImage* 98 (September): 289–95.
- Dalal, Tal, Nitin Gupta, and Rafi Haddad. 2020. “Bilateral and Unilateral Odor Processing and Odor Perception.” *Communications Biology* 3 (1): 150.
- Das, Sudeshna, Federica Trona, Mohammed A. Khallaf, Elisa Schuh, Markus Knaden, Bill S. Hansson, and Silke Sachse. 2017. “Electrical Synapses Mediate Synergism between Pheromone and Food Odors in.” *Proceedings of the National Academy of Sciences of the United States of America* 114 (46): E9962–71.
- Datta, Sandeep Robert, Maria Luisa Vasconcelos, Vanessa Ruta, Sean Luo, Allan Wong, Ebru Demir, Jorge Flores, Karen Balonze, Barry J. Dickson, and Richard Axel. 2008. “The *Drosophila* Pheromone cVA Activates a Sexually Dimorphic Neural Circuit.” *Nature* 452 (7186): 473–77.
- Demir, Ebru, and Barry J. Dickson. 2005. “Fruitless Splicing Specifies Male Courtship Behavior in *Drosophila*.” *Cell* 121 (5): 785–94.
- Deutsch, David, Jan Clemens, Stephan Y. Thiberge, Georgia Guan, and Mala Murthy. 2019. “Shared Song Detector Neurons in *Drosophila* Male and Female Brains Drive Sex-Specific Behaviors.” *Current Biology: CB* 29 (19): 3200–3215.e5.
- Deutsch, David, Diego Pacheco, Lucas Encarnacion-Rivera, Talmo Pereira, Ramie Fathy, Jan Clemens, Cyrille Girardin, et al. 2020. “The Neural Basis for a Persistent Internal State in Females.” *eLife* 9 (November). <https://doi.org/10.7554/eLife.59502>.
- Dolan, Michael-John, Ghislain Belliard-Guérin, Alexander Shakeel Bates, Shahar Frechter, Aurélie Lampin-Saint-Amaux, Yoshinori Aso, Ruairí J. V. Roberts, et al. 2018. “Communication from Learned to Innate Olfactory Processing Centers Is Required for Memory Retrieval in *Drosophila*.” *Neuron* 100 (3): 651–68.e8.
- Dolan, Michael-John, Shahar Frechter, Alexander Shakeel Bates, Chuntao Dan, Paavo Huoviala, Ruairí Jv Roberts, Philipp Schlegel, et al. 2019. “Neurogenetic Dissection of the Lateral Horn Reveals Major Outputs, Diverse Behavioural Functions, and Interactions with the Mushroom Body.” *eLife* 8 (May). <https://doi.org/10.7554/eLife.43079>.
- Dorkenwald, Sven, Claire McKellar, Thomas Macrina, Nico Kemnitz, Kisuk Lee, Ran Lu, Jingpeng Wu, et al. 2020. “FlyWire: Online Community for Whole-Brain Connectomics.” <https://doi.org/10.1101/2020.08.30.274225>.
- Esquivelzeta Rabell, José, Kadir Mutlu, João Noutel, Pamela Martin Del Olmo, and Sebastian Haesler. 2017. “Spontaneous Rapid Odor Source Localization Behavior Requires Interhemispheric Communication.” *Current Biology: CB* 27 (10): 1542–48.e4.
- Eyjólfssdóttir, Eyrún Arna. 2014. *Detecting Actions of Fruit Flies*.
- Fabre, Caroline C. G., Berthold Hedwig, Graham Conduit, Peter A. Lawrence, Stephen F. Goodwin, and José Casal. 2012. “Substrate-Borne Vibratory Communication during Courtship in *Drosophila Melanogaster*.” *Current Biology: CB* 22 (22): 2180–85.
- Fechner, Gustav Theodor. 1860. *Elements of Psychophysics, 1860*.

- Gaudry, Quentin, Elizabeth J. Hong, Jamey Kain, Benjamin L. de Bivort, and Rachel I. Wilson. 2013. "Asymmetric Neurotransmitter Release Enables Rapid Odour Lateralization in *Drosophila*." *Nature* 493 (7432): 424–28.
- Giniger, Edward, Susan M. Varnum, and Mark Ptashne. 1985. "Specific DNA Binding of GAL4, a Positive Regulatory Protein of Yeast." *Cell*. [https://doi.org/10.1016/0092-8674\(85\)90336-8](https://doi.org/10.1016/0092-8674(85)90336-8).
- Goes van Naters, Wynand van der, and John R. Carlson. 2007. "Receptors and Neurons for Fly Odors in *Drosophila*." *Current Biology: CB* 17 (7): 606–12.
- Goodale, M. A., and A. D. Milner. 1992. "Separate Visual Pathways for Perception and Action." *Trends in Neurosciences*. [https://doi.org/10.1016/0166-2236\(92\)90344-8](https://doi.org/10.1016/0166-2236(92)90344-8).
- Grabe, Veit, Amelie Baschwitz, Hany K. M. Dweck, Sofia Lavista-Llanos, Bill S. Hansson, and Silke Sachse. 2016. "Elucidating the Neuronal Architecture of Olfactory Glomeruli in the *Drosophila* Antennal Lobe." *Cell Reports* 16 (12): 3401–13.
- Grover, Dhruv, Takeo Katsuki, Jinfang Li, Thomas J. Dawkins, and Ralph J. Greenspan. 2020. "Imaging Brain Activity during Complex Social Behaviors in *Drosophila* with Flyception2." *Nature Communications* 11 (1): 623.
- Gulick, W. L., and George von Békésy. 1963. "Experiments in Hearing." *The American Journal of Psychology*. <https://doi.org/10.2307/1419812>.
- Hedwig, Berthold, and James F. A. Poulet. 2004. "Complex Auditory Behaviour Emerges from Simple Reactive Steering." *Nature* 430 (7001): 781–85.
- Heisenberg, M., A. Borst, S. Wagner, and D. Byers. 1985. "*Drosophila* Mushroom Body Mutants Are Deficient in Olfactory Learning." *Journal of Neurogenetics* 2 (1): 1–30.
- Heng, Joseph A., Michael Woodford, and Rafael Polania. 2020. "Efficient Sampling and Noisy Decisions." *eLife* 9 (September). <https://doi.org/10.7554/eLife.54962>.
- Hige, Toshihide, Yoshinori Aso, Mehrab N. Modi, Gerald M. Rubin, and Glenn C. Turner. 2015. "Heterosynaptic Plasticity Underlies Aversive Olfactory Learning in *Drosophila*." *Neuron* 88 (5): 985–98.
- Holler, Simone, German Köstinger, Kevan A. C. Martin, Gregor F. P. Schuhknecht, and Ken J. Stratford. 2021. "Structure and Function of a Neocortical Synapse." *Nature* 591 (7848): 111–16.
- Hoopfer, Eric D., Yonil Jung, Hidehiko K. Inagaki, Gerald M. Rubin, and David J. Anderson. 2015. "P1 Interneurons Promote a Persistent Internal State That Enhances Inter-Male Aggression in *Drosophila*." *eLife* 4 (December). <https://doi.org/10.7554/eLife.11346>.
- Horne, Jane Anne, Carlie Langille, Sari McLin, Meagan Wiederman, Zhiyuan Lu, C. Shan Xu, Stephen M. Plaza, Louis K. Scheffer, Harald F. Hess, and Ian A. Meinertzhagen. 2018. "A Resource for the *Drosophila* Antennal Lobe Provided by the Connectome of Glomerulus VA1v." *eLife*. <https://doi.org/10.7554/elife.37550>.
- Hulse, Brad K., Hannah Haberkern, Romain Franconville, Daniel B. Turner-Evans, Shinya Takemura, Tanya Wolff, Marcella Noorman, et al. 2020. "A Connectome of the *Drosophila* Central Complex Reveals Network Motifs Suitable for Flexible Navigation and Context-Dependent Action Selection." <https://doi.org/10.1101/2020.12.08.413955>.
- Ito, Masayoshi, Naoki Masuda, Kazunori Shinomiya, Keita Endo, and Kei Ito. 2013. "Systematic Analysis of Neural Projections Reveals Clonal Composition of the *Drosophila* Brain." *Current Biology: CB* 23 (8): 644–55.
- Jaeger, Alexandria H., Molly Stanley, Zachary F. Weiss, Pierre-Yves Musso, Rachel C. W. Chan, Han Zhang, Damian Feldman-Kiss, and Michael D. Gordon. 2018. "A Complex Peripheral Code for Salt Taste in *Drosophila*." *eLife*. <https://doi.org/10.7554/elife.37167>.
- Jayaraman, Vivek, and Gilles Laurent. 2007. "Evaluating a Genetically Encoded Optical Sensor of Neural Activity Using Electrophysiology in Intact Adult Fruit Flies." *Frontiers in Neural Circuits* 1 (November): 3.

- Jeanne, James M., and Rachel I. Wilson. 2015. "Convergence, Divergence, and Reconvergence in a Feedforward Network Improves Neural Speed and Accuracy." *Neuron*. <https://doi.org/10.1016/j.neuron.2015.10.018>.
- Jefferis, Gregory S. X. E., Christopher J. Potter, Alexander M. Chan, Elizabeth C. Marin, Torsten Rohlffing, Calvin R. Maurer Jr, and Liqun Luo. 2007. "Comprehensive Maps of *Drosophila* Higher Olfactory Centers: Spatially Segregated Fruit and Pheromone Representation." *Cell* 128 (6): 1187–1203.
- Jenett, Arnim, Gerald M. Rubin, Teri-T B. Ngo, David Shepherd, Christine Murphy, Heather Dionne, B. D. Pfeiffer, et al. 2012. "A GAL4-Driver Line Resource for *Drosophila* Neurobiology." *Cell Reports* 2 (4): 991–1001.
- Kabra, Mayank, Alice A. Robie, Marta Rivera-Alba, Steven Branson, and Kristin Branson. 2013. "JAABA: Interactive Machine Learning for Automatic Annotation of Animal Behavior." *Nature Methods*. <https://doi.org/10.1038/nmeth.2281>.
- Kaftan, Filip, Purva Kulkarni, Markus Knaden, Sebastian Böcker, Bill S. Hansson, and Aleš Svatoš. 2020. "*Drosophila* *Melanogaster* Chemical Ecology Revisited: 2-D Distribution Maps of Sex Pheromones on Whole Virgin and Mated Flies by Mass Spectrometry Imaging." *BMC Zoology*. <https://doi.org/10.1186/s40850-020-00053-7>.
- Kallman, Benjamin R., Heesoo Kim, and Kristin Scott. 2015. "Excitation and Inhibition onto Central Courtship Neurons Biases *Drosophila* Mate Choice." *eLife* 4 (November): e11188.
- Kennedy, J. S., and D. Marsh. 1974. "Pheromone-Regulated Anemotaxis in Flying Moths." *Science* 184 (4140): 999–1001.
- Khan, Adil Ghani, Manaswini Sarangi, and Upinder Singh Bhalla. 2012. "Rats Track Odour Trails Accurately Using a Multi-Layered Strategy with near-Optimal Sampling." *Nature Communications* 3 (February): 703.
- Kikuta, Shu, Kenichiro Sato, Hideki Kashiwadani, Koichi Tsunoda, Tatsuya Yamasoba, and Kensaku Mori. 2010. "From the Cover: Neurons in the Anterior Olfactory Nucleus Pars Externa Detect Right or Left Localization of Odor Sources." *Proceedings of the National Academy of Sciences of the United States of America* 107 (27): 12363–68.
- Kim, Anmo J., Aurel A. Lazar, and Yevgeniy B. Slutskiy. 2011. "System Identification of *Drosophila* Olfactory Sensory Neurons." *Journal of Computational Neuroscience* 30 (1): 143–61.
- Kim, Heesoo, Colleen Kirkhart, and Kristin Scott. 2017a. "Author Response: Long-Range Projection Neurons in the Taste Circuit of *Drosophila*." <https://doi.org/10.7554/elife.23386.020>.
- . 2017b. "Long-Range Projection Neurons in the Taste Circuit of *Drosophila*." *eLife*. <https://doi.org/10.7554/elife.23386>.
- Kimura, Ken-Ichi, Tomoaki Hachiya, Masayuki Koganezawa, Tatsunori Tazawa, and Daisuke Yamamoto. 2008. "Fruitless and Doublesex Coordinate to Generate Male-Specific Neurons That Can Initiate Courtship." *Neuron* 59 (5): 759–69.
- Kimura, Ken-Ichi, Manabu Ote, Tatsunori Tazawa, and Daisuke Yamamoto. 2005. "Fruitless Specifies Sexually Dimorphic Neural Circuitry in the *Drosophila* Brain." *Nature*. <https://doi.org/10.1038/nature04229>.
- Klapoetke, Nathan C., Aljoscha Nern, Martin Y. Peek, Edward M. Rogers, Patrick Breads, Gerald M. Rubin, Michael B. Reiser, and Gwyneth M. Card. 2017. "Ultra-Selective Looming Detection from Radial Motion Opponency." *Nature* 551 (7679): 237–41.
- Knudsen, E., and M. Konishi. 1978. "A Neural Map of Auditory Space in the Owl." *Science*. <https://doi.org/10.1126/science.644324>.
- Knudsen, Eric I., and Masakazu Konishi. 1979. "Mechanisms of Sound Localization in the Barn Owl (*Tyto Alba*)." *Journal of Comparative Physiology ? A*.

- <https://doi.org/10.1007/bf00663106>.
- Koganezawa, Masayuki, Daisuke Haba, Takashi Matsuo, and Daisuke Yamamoto. 2010. "The Shaping of Male Courtship Posture by Lateralized Gustatory Inputs to Male-Specific Interneurons." *Current Biology: CB* 20 (1): 1–8.
- Koganezawa, Masayuki, Ken-Ichi Kimura, and Daisuke Yamamoto. 2016. "The Neural Circuitry That Functions as a Switch for Courtship versus Aggression in *Drosophila* Males." *Current Biology: CB* 26 (11): 1395–1403.
- Kohatsu, Soh, Masayuki Koganezawa, and Daisuke Yamamoto. 2011. "Female Contact Activates Male-Specific Interneurons That Trigger Stereotypic Courtship Behavior in *Drosophila*." *Neuron* 69 (3): 498–508.
- Kohl, Johannes, Aaron D. Ostrovsky, Shahar Frechter, and Gregory S. X. E. Jefferis. 2013. "A Bidirectional Circuit Switch Reroutes Pheromone Signals in Male and Female Brains." *Cell* 155 (7): 1610–23.
- Koh, Tong-Wey, Zhe He, Srinivas Gorur-Shandilya, Karen Menuz, Nikki K. Larter, Shannon Stewart, and John R. Carlson. 2014. "The *Drosophila* IR20a Clade of Ionotropic Receptors Are Candidate Taste and Pheromone Receptors." *Neuron*.  
<https://doi.org/10.1016/j.neuron.2014.07.012>.
- Konsolaki, M., M. Sanicola, T. Kozlova, V. Liu, B. Arcà, C. Savakis, W. M. Gelbart, and F. C. Kafatos. 1992. "FLP-Mediated Intermolecular Recombination in the Cytoplasm of *Drosophila* Embryos." *The New Biologist* 4 (5): 551–57.
- Krupp, Joshua J., Clement Kent, Jean-Christophe Billeter, Reza Azanchi, Anthony K-C So, Julia A. Schonfeld, Benjamin P. Smith, Christophe Lucas, and Joel D. Levine. 2008. "Social Experience Modifies Pheromone Expression and Mating Behavior in Male *Drosophila Melanogaster*." *Current Biology: CB* 18 (18): 1373–83.
- Kuo, Tsung-Han, Joanne Y. Yew, Tatyana Y. Fedina, Klaus Dreisewerd, Herman A. Dierick, and Scott D. Pletcher. 2012. "Aging Modulates Cuticular Hydrocarbons and Sexual Attractiveness in *Drosophila Melanogaster*." *The Journal of Experimental Biology* 215 (Pt 5): 814–21.
- Kurtovic, Amina, Alexandre Widmer, and Barry J. Dickson. 2007. "A Single Class of Olfactory Neurons Mediates Behavioural Responses to a *Drosophila* Sex Pheromone." *Nature* 446 (7135): 542–46.
- Kwon, Jae Young, Anupama Dahanukar, Linnea A. Weiss, and John R. Carlson. 2014. "A Map of Taste Neuron Projections in the *Drosophila* CNS." *Journal of Biosciences* 39 (4): 565–74.
- Laughlin, Simon. 1981. "A Simple Coding Procedure Enhances a Neuron's Information Capacity." *Zeitschrift Für Naturforschung C*. <https://doi.org/10.1515/znc-1981-9-1040>.
- Lebreton, Sébastien, Veit Grabe, Aman B. Omondi, Rickard Ignell, Paul G. Becher, Bill S. Hansson, Silke Sachse, and Peter Witzgall. 2014. "Love Makes Smell Blind: Mating Suppresses Pheromone Attraction in *Drosophila* Females via Or65a Olfactory Neurons." *Scientific Reports* 4 (November): 7119.
- Lee, T., and L. Luo. 2001. "Mosaic Analysis with a Repressible Cell Marker (MARCM) for *Drosophila* Neural Development." *Trends in Neurosciences* 24 (5): 251–54.
- Lehmann, F. O., and M. H. Dickinson. 1997. "The Changes in Power Requirements and Muscle Efficiency during Elevated Force Production in the Fruit Fly *Drosophila Melanogaster*." *The Journal of Experimental Biology* 200 (Pt 7): 1133–43.
- Leitch, Katherine, Francesca Ponce, Floris van Breugel, and Michael H. Dickinson. 2020. "The Long-Distance Flight Behavior of *Drosophila* Suggests a General Model for Wind-Assisted Dispersal in Insects." <https://doi.org/10.1101/2020.06.10.145169>.
- Li, Feng, Jack W. Lindsey, Elizabeth C. Marin, Nils Otto, Marisa Dreher, Georgia Dempsey, Ildiko Stark, et al. 2020. "The Connectome of the Adult *Drosophila* Mushroom Body

- Provides Insights into Function.” *eLife* 9 (December).  
<https://doi.org/10.7554/eLife.62576>.
- Li, P. H., Larry F. Lindsey, Michał Januszewski, Zhihao Zheng, Alexander Shakeel Bates, István Taisz, Mike Tyka, et al. 2020. “Automated Reconstruction of a Serial-Section EM *Drosophila* Brain with Flood-Filling Networks and Local Realignment.”  
<https://doi.org/10.1101/605634>.
- Liu, Tony X., Pasha A. Davoudian, Kristyn M. Lizbinski, and James M. Jeanne. 2022. “Connectomic Features Underlying Diverse Synaptic Connection Strengths and Subcellular Computation.” *Current Biology: CB* 32 (3): 559–69.e5.
- Longair, Mark H., Dean A. Baker, and J. Douglas Armstrong. 2011. “Simple Neurite Tracer: Open Source Software for Reconstruction, Visualization and Analysis of Neuronal Processes.” *Bioinformatics* 27 (17): 2453–54.
- Loudon, C., and M. A. Koehl. 2000. “Sniffing by a Silkworm Moth: Wing Fanning Enhances Air Penetration through and Pheromone Interception by Antennae.” *The Journal of Experimental Biology* 203 (Pt 19): 2977–90.
- Luan, Haojiang, Nathan C. Peabody, Charles R. Vinson, and Benjamin H. White. 2006. “Refined Spatial Manipulation of Neuronal Function by Combinatorial Restriction of Transgene Expression.” *Neuron* 52 (3): 425–36.
- Maimon, Gaby, Andrew D. Straw, and Michael H. Dickinson. 2008. “A Simple Vision-Based Algorithm for Decision Making in Flying *Drosophila*.” *Current Biology: CB* 18 (6): 464–70.
- Malnic, B., J. Hirono, T. Sato, and L. B. Buck. 1999. “Combinatorial Receptor Codes for Odors.” *Cell* 96 (5): 713–23.
- Marin, Alina Cristina, Andreas T. Schaefer, and Tobias Ackels. 2021. “Spatial Information from the Odour Environment in Mammalian Olfaction.” *Cell and Tissue Research* 383 (1): 473–83.
- Marin, E. C., Gregory S. X. E. Jefferis, Takaki Komiyama, Haitao Zhu, and Liqun Luo. 2002. “Representation of the Glomerular Olfactory Map in the *Drosophila* Brain.” *Cell* 109 (2): 243–55.
- Mathis, Alexander, Pranav Mamidanna, Kevin M. Cury, Taiga Abe, Venkatesh N. Murthy, Mackenzie Weygandt Mathis, and Matthias Bethge. 2018. “DeepLabCut: Markerless Pose Estimation of User-Defined Body Parts with Deep Learning.” *Nature Neuroscience*. <https://doi.org/10.1038/s41593-018-0209-y>.
- Mazzoni, Valerio, Gianfranco Anfora, and Meta Virant-Doberlet. 2013. “Substrate Vibrations during Courtship in Three *Drosophila* Species.” *PloS One* 8 (11): e80708.
- McKellar, Claire E., Joshua L. Lillvis, Daniel E. Bath, James E. Fitzgerald, John G. Cannon, Julie H. Simpson, and Barry J. Dickson. 2019. “Threshold-Based Ordering of Sequential Actions during *Drosophila* Courtship.” *Current Biology: CB* 29 (3): 426–34.e6.
- Meier, Matthias, and Alexander Borst. 2019. “Extreme Compartmentalization in a *Drosophila* Amacrine Cell.” *Current Biology: CB* 29 (9): 1545–50.e2.
- Meissner, Geoffrey W., Zachary Dorman, Aljoscha Nern, Kaitlyn Forster, Theresa Gibney, Jennifer Jeter, Lauren Johnson, et al. 2020. “An Image Resource of Subdivided *Drosophila* GAL4-Driver Expression Patterns for Neuron-Level Searches.”  
<https://doi.org/10.1101/2020.05.29.080473>.
- Mercier, Damien, Yoshiko Tsuchimoto, Kazumi Ohta, and Hokto Kazama. 2018. “Olfactory Landmark-Based Communication in Interacting *Drosophila*.” *Current Biology: CB* 28 (16): 2624–31.e5.
- Mohamed, Ahmed A. M., Bill S. Hansson, and Silke Sachse. 2019. “Third-Order Neurons in the Lateral Horn Enhance Bilateral Contrast of Odor Inputs Through Contralateral Inhibition in *Drosophila*.” *Frontiers in Physiology*.

- <https://doi.org/10.3389/fphys.2019.00851>.
- Münch, Daniel, and C. Giovanni Galizia. 2016. “DoOR 2.0--Comprehensive Mapping of *Drosophila Melanogaster* Odorant Responses.” *Scientific Reports* 6 (February): 21841.
- “NoRMCorre: An Online Algorithm for Piecewise Rigid Motion Correction of Calcium Imaging Data.” 2017. *Journal of Neuroscience Methods* 291 (November): 83–94.
- Olsen, Shawn R., Vikas Bhandawat, and Rachel I. Wilson. 2007. “Excitatory Interactions between Olfactory Processing Channels in the *Drosophila* Antennal Lobe.” *Neuron* 54 (1): 89–103.
- Olsen, Shawn R., and Rachel I. Wilson. 2008. “Lateral Presynaptic Inhibition Mediates Gain Control in an Olfactory Circuit.” *Nature*. <https://doi.org/10.1038/nature06864>.
- Otsuna, Hideo, Masayoshi Ito, and Takashi Kawase. 2018. “Color Depth MIP Mask Search: A New Tool to Expedite Split-GAL4 Creation.” <https://doi.org/10.1101/318006>.
- Park, Annie, Tracy Tran, Elizabeth A. Scheuermann, Dean P. Smith, and Nigel S. Atkinson. 2020. “Alcohol Potentiates a Pheromone Signal in Flies.” *eLife*. <https://doi.org/10.7554/elife.59853>.
- Pavlou, Hania J., and Stephen F. Goodwin. 2013. “Courtship Behavior in *Drosophila Melanogaster*: Towards a ‘courtship Connectome.’” *Current Opinion in Neurobiology*. <https://doi.org/10.1016/j.conb.2012.09.002>.
- Payne, Alex. 1986. *Mechanisms in Insect Olfaction*. Oxford University Press, USA.
- Peña, J. L., and M. Konishi. 2001. “Auditory Spatial Receptive Fields Created by Multiplication.” *Science* 292 (5515): 249–52.
- Pereira, Talmo D., Diego E. Aldarondo, Lindsay Willmore, Mikhail Kislin, Samuel S-H Wang, Mala Murthy, and Joshua W. Shaevitz. 2019. “Fast Animal Pose Estimation Using Deep Neural Networks.” *Nature Methods* 16 (1): 117–25.
- Pfeiffer, B. D., A. Jenett, A. S. Hammonds, T. T. Ngo, S. Misra, C. Murphy, A. Scully, et al. 2008. “Tools for Neuroanatomy and Neurogenetics in *Drosophila*.” *Proceedings of the National Academy of Sciences of the United States of America* 105 (28). <https://doi.org/10.1073/pnas.0803697105>.
- Pfeiffer, B. D., Teri-T B. Ngo, Karen L. Hibbard, Christine Murphy, Arnim Jenett, James W. Truman, and Gerald M. Rubin. 2010. “Refinement of Tools for Targeted Gene Expression in *Drosophila*.” *Genetics* 186 (2): 735–55.
- Phelps, Jasper S., David Grant Colburn Hildebrand, Brett J. Graham, Aaron T. Kuan, Logan A. Thomas, Tri M. Nguyen, Julia Buhmann, et al. 2021. “Reconstruction of Motor Control Circuits in Adult *Drosophila* Using Automated Transmission Electron Microscopy.” *Cell* 184 (3): 759–74.e18.
- Philipsborn, Anne C. von, Anne C. von Philipsborn, Tianxiao Liu, Jai Y. Yu, Christopher Masser, Salil S. Bidaye, and Barry J. Dickson. 2011. “Neuronal Control of *Drosophila* Courtship Song.” *Neuron*. <https://doi.org/10.1016/j.neuron.2011.01.011>.
- Pologruto, Thomas A., Bernardo L. Sabatini, and Karel Svoboda. 2003. “ScanImage: Flexible Software for Operating Laser Scanning Microscopes.” *BioMedical Engineering OnLine*. <https://doi.org/10.1186/1475-925x-2-13>.
- Poulet, James F. A., and Berthold Hedwig. 2005. “Auditory Orientation in Crickets: Pattern Recognition Controls Reactive Steering.” *Proceedings of the National Academy of Sciences of the United States of America* 102 (43): 15665–69.
- Rajan, Raghav, James P. Clement, and Upinder S. Bhalla. 2006. “Rats Smell in Stereo.” *Science* 311 (5761): 666–70.
- Ribeiro, Inês M. A., Michael Drews, Armin Bahl, Christian Machacek, Alexander Borst, and Barry J. Dickson. 2018. “Visual Projection Neurons Mediating Directed Courtship in *Drosophila*.” *Cell* 174 (3): 607–21.e18.
- Rideout, Elizabeth J., Anthony J. Dornan, Megan C. Neville, Suzanne Eadie, and Stephen F.

- Goodwin. 2010. "Control of Sexual Differentiation and Behavior by the Doublesex Gene in *Drosophila Melanogaster*." *Nature Neuroscience* 13 (4): 458–66.
- Robie, Alice A., Jonathan Hirokawa, Austin W. Edwards, Lowell A. Umayam, Allen Lee, Mary L. Phillips, Gwyneth M. Card, et al. 2017. "Mapping the Neural Substrates of Behavior." *Cell* 170 (2): 393–406.e28.
- Ronderos, David S., and Dean P. Smith. 2010. "Activation of the T1 Neuronal Circuit Is Necessary and Sufficient to Induce Sexually Dimorphic Mating Behavior in *Drosophila Melanogaster*." *The Journal of Neuroscience: The Official Journal of the Society for Neuroscience* 30 (7): 2595–99.
- Root, Cory M., Kaoru Masuyama, David S. Green, Lina E. Enell, Dick R. Nässel, Chi-Hon Lee, and Jing W. Wang. 2008. "A Presynaptic Gain Control Mechanism Fine-Tunes Olfactory Behavior." *Neuron* 59 (2): 311–21.
- Ruta, Vanessa, Sandeep Robert Datta, Maria Luisa Vasconcelos, Jessica Freeland, Loren L. Looger, and Richard Axel. 2010. "A Dimorphic Pheromone Circuit in *Drosophila* from Sensory Input to Descending Output." *Nature* 468 (7324): 686–90.
- Saalfeld, Stephan, Albert Cardona, Volker Hartenstein, and Pavel Tomancak. 2009. "CATMAID: Collaborative Annotation Toolkit for Massive Amounts of Image Data." *Bioinformatics* 25 (15): 1984–86.
- Sánchez-Alcañiz, Juan Antonio, Ana Florencia Silbering, Vincent Croset, Giovanna Zappia, Anantha Krishna Sivasubramaniam, Liliane Abuin, Saumya Yashmohini Sahai, et al. 2018. "An Expression Atlas of Variant Ionotropic Glutamate Receptors Identifies a Molecular Basis of Carbonation Sensing." *Nature Communications* 9 (1): 4252.
- Scheffer, Louis K., C. Shan Xu, Michal Januszewski, Zhiyuan Lu, Shin-Ya Takemura, Kenneth J. Hayworth, Gary B. Huang, et al. 2020. "A Connectome and Analysis of the Adult Central Brain." *eLife* 9 (September). <https://doi.org/10.7554/eLife.57443>.
- Schindelin, Johannes, Ignacio Arganda-Carreras, Erwin Frise, Verena Kaynig, Mark Longair, Tobias Pietzsch, Stephan Preibisch, et al. 2012. "Fiji: An Open-Source Platform for Biological-Image Analysis." *Nature Methods* 9 (7): 676–82.
- Schlegel, Philipp, Alexander Shakeel Bates, Tomke Stürner, Sridhar R. Jagannathan, Nikolas Drummond, Joseph Hsu, Laia Serratos Capdevila, et al. 2021. "Information Flow, Cell Types and Stereotypy in a Full Olfactory Connectome." *eLife* 10 (May). <https://doi.org/10.7554/eLife.66018>.
- Schlegel, Philipp, Marta Costa, and Gregory Sxe Jefferis. 2017. "Learning from Connectomics on the Fly." *Current Opinion in Insect Science*. <https://doi.org/10.1016/j.cois.2017.09.011>.
- Schlieff, Michelle L., and Rachel I. Wilson. 2007. "Olfactory Processing and Behavior Downstream from Highly Selective Receptor Neurons." *Nature Neuroscience* 10 (5): 623–30.
- Schretter, Catherine E., Yoshinori Aso, Alice A. Robie, Marisa Dreher, Michael-John Dolan, Nan Chen, Masayoshi Ito, et al. 2020. "Cell Types and Neuronal Circuitry Underlying Female Aggression in." *eLife* 9 (November). <https://doi.org/10.7554/eLife.58942>.
- Seeholzer, Laura F., Max Seppo, David L. Stern, and Vanessa Ruta. 2018. "Evolution of a Central Neural Circuit Underlies *Drosophila* Mate Preferences." *Nature* 559 (7715): 564–69.
- Seelig, Johannes D., M. Eugenia Chiappe, Gus K. Lott, Anirban Dutta, Jason E. Osborne, Michael B. Reiser, and Vivek Jayaraman. 2010. "Two-Photon Calcium Imaging from Head-Fixed *Drosophila* during Optomotor Walking Behavior." *Nature Methods* 7 (7): 535–40.
- Seelig, Johannes D., and Vivek Jayaraman. 2013. "Feature Detection and Orientation Tuning in the *Drosophila* Central Complex." *Nature* 503 (7475): 262–66.

- Si, Guangwei, Jacob Baron, Yu Feng, and Aravinthan D. T. Samuel. 2021. “An Olfactory Pattern Generator for on-Demand Combinatorial Control of Receptor Activities.” <https://doi.org/10.1101/2021.05.31.446433>.
- Spieth, Herman T. 1952. *Mating Behavior Within the Genus Drosophila (Diptera)*.
- Stocker, R. F., M. C. Lienhard, A. Borst, and K. F. Fischbach. 1990. “Neuronal Architecture of the Antennal Lobe in *Drosophila Melanogaster*.” *Cell and Tissue Research* 262 (1): 9–34.
- Strother, James A., Shiu-an-Tze Wu, Allan M. Wong, Aljoscha Nern, Edward M. Rogers, Jasmine Q. Le, Gerald M. Rubin, and Michael B. Reiser. 2017. “The Emergence of Directional Selectivity in the Visual Motion Pathway of *Drosophila*.” *Neuron* 94 (1): 168–82.e10.
- Tachibana, Shin-Ichiro, Kazushige Touhara, and Aki Ejima. 2015. “Modification of Male Courtship Motivation by Olfactory Habituation via the GABAA Receptor in *Drosophila Melanogaster*.” *PloS One* 10 (8): e0135186.
- Takasaki, Tetsuya, Shigehiro Namiki, and Ryohei Kanzaki. 2012. “Use of Bilateral Information to Determine the Walking Direction during Orientation to a Pheromone Source in the Silkmoth *Bombyx Mori*.” *Journal of Comparative Physiology. A, Neuroethology, Sensory, Neural, and Behavioral Physiology* 198 (4): 295–307.
- Takemura, Shin-Ya, Aljoscha Nern, Dmitri B. Chklovskii, Louis K. Scheffer, Gerald M. Rubin, and Ian A. Meinertzhagen. 2017. “The Comprehensive Connectome of a Neural Substrate for ‘ON’ Motion Detection in *Drosophila*.” *eLife*. <https://doi.org/10.7554/elife.24394>.
- Tinbergen, Nikolaas. 1951. *The Study of Instinct*. Oxford University Press, London.
- Tirian, Laszlo, and Barry J. Dickson. 2017. “The VT GAL4, LexA, and Split-GAL4 Driver Line Collections for Targeted Expression in the *Drosophila* Nervous System.” <https://doi.org/10.1101/198648>.
- Tobin, William F., Rachel I. Wilson, and Wei-Chung Allen Lee. 2017. “Wiring Variations That Enable and Constrain Neural Computation in a Sensory Microcircuit.” *eLife* 6 (May). <https://doi.org/10.7554/eLife.24838>.
- Tsubouchi, Asako, Tomoko Yano, Takeshi K. Yokoyama, Chloé Murtin, Hideo Otsuna, and Kei Ito. 2017. “Topological and Modality-Specific Representation of Somatosensory Information in the Fly Brain.” *Science* 358 (6363): 615–23.
- Tuthill, John C., and Rachel I. Wilson. 2016. “Mechanosensation and Adaptive Motor Control in Insects.” *Current Biology: CB* 26 (20): R1022–38.
- Vosshall, L. B., A. M. Wong, and R. Axel. 2000. “An Olfactory Sensory Map in the Fly Brain.” *Cell* 102 (2): 147–59.
- Wang, and Anderson. 2010. “Identification of an Aggression-Promoting Pheromone and Its Receptor Neurons in *Drosophila*.” *Nature*. <https://doi.org/10.1038/nature08678>.
- Wang, Fei, Kaiyu Wang, Nora Forknall, Christopher Patrick, Tansy Yang, Ruchi Parekh, Davi Bock, and Barry J. Dickson. 2020. “Neural Circuitry Linking Mating and Egg Laying in *Drosophila* Females.” *Nature*. <https://doi.org/10.1038/s41586-020-2055-9>.
- Wang, Jian, Christopher T. Zugates, Inray H. Liang, Ching-Hsien J. Lee, and Tzumin Lee. 2002. “*Drosophila* Dscam Is Required for Divergent Segregation of Sister Branches and Suppresses Ectopic Bifurcation of Axons.” *Neuron* 33 (4): 559–71.
- Wang, Kaiyu, Fei Wang, Nora Forknall, Tansy Yang, Christopher Patrick, Ruchi Parekh, and Barry J. Dickson. 2021. “Neural Circuit Mechanisms of Sexual Receptivity in *Drosophila* Females.” *Nature* 589 (7843): 577–81.
- Wang, Liming, Xiaoqing Han, Jennifer Mehren, Makoto Hiroi, Jean-Christophe Billeter, Tetsuya Miyamoto, Hubert Amrein, Joel D. Levine, and David J. Anderson. 2011. “Hierarchical Chemosensory Regulation of Male-Male Social Interactions in

- Drosophila.” *Nature Neuroscience* 14 (6): 757–62.
- White, J. G., E. Southgate, J. N. Thomson, and S. Brenner. 1986. “The Structure of the Nervous System of the Nematode *Caenorhabditis Elegans*.” *Philosophical Transactions of the Royal Society of London. Series B, Biological Sciences* 314 (1165): 1–340.
- Wilson, Rachel I. 2013. “Early Olfactory Processing in *Drosophila*: Mechanisms and Principles.” *Annual Review of Neuroscience* 36 (July): 217–41.
- Wilson, Rachel I., Glenn C. Turner, and Gilles Laurent. 2004. “Transformation of Olfactory Representations in the *Drosophila* Antennal Lobe.” *Science* 303 (5656): 366–70.
- Wolf, H., and M. Burrows. 1995. “Proprioceptive Sensory Neurons of a Locust Leg Receive Rhythmic Presynaptic Inhibition during Walking.” *The Journal of Neuroscience: The Official Journal of the Society for Neuroscience* 15 (8): 5623–36.
- Zhang, Stephen X., Lauren E. Miner, Christine L. Boutros, Dragana Rogulja, and Michael A. Crickmore. 2018. “Motivation, Perception, and Chance Converge to Make a Binary Decision.” *Neuron* 99 (2): 376–88.e6.
- Zheng, Zhihao, J. Scott Lauritzen, Eric Perlman, Camenzind G. Robinson, Matthew Nichols, Daniel Milkie, Omar Torrens, et al. 2018. “A Complete Electron Microscopy Volume of the Brain of Adult *Drosophila Melanogaster*.” *Cell* 174 (3): 730–43.e22.
- Zhou, Chuan, Yufeng Pan, Carmen C. Robinett, Geoffrey W. Meissner, and Bruce S. Baker. 2014. “Central Brain Neurons Expressing Doublesex Regulate Female Receptivity in *Drosophila*.” *Neuron* 83 (1): 149–63.
- Zill, Sasha N., Josef Schmitz, Sumaiya Chaudhry, and Ansgar Büschges. 2012. “Force Encoding in Stick Insect Legs Delineates a Reference Frame for Motor Control.” *Journal of Neurophysiology* 108 (5): 1453–72.

## Appendix

The appended paper was under review at the time of submission, and appeared as a preprint on the biorxiv server (P. H. Li et al. 2020). This study introduces Flood Filling Neural Network based automated image segmentation methods for connectomic reconstruction. It also presents novel data augmentation and alignment techniques to deal with missing EM sections and local misalignment. I contributed to this work by showing how this segmentation facilitates finding the most relevant synaptic partners of a neuron. In brief, prior best practice was annotating all (pre- or post-) synapses of a neuron, and randomly sampling connected profiles. Due to the random nature of the sampling the partners with most synaptic connections are the most likely to be found. This strategy can be improved with the segmentation: once synapses are annotated, the segments can be ranked by the number of overlapping connections. By following the ranking to reconstruct connected segments, neurons with strong synaptic weights can be found with tracing out five times fewer neurons than with random sampling (Figure 7D, E in the paper). We used this method to find presynaptic partners to aSP-g neurons and G2N-SLP1 (Figure 18). This approach can be leveraged by connectomic researchers working with CATMAID on any segmented EM dataset by using the R `catnat` package and the functions: `segments_ranked_post`, and `segments_ranked_pre`; <https://github.com/jefferislab/catnat>.

## **Automated Reconstruction of a Serial-Section EM *Drosophila* Brain with Flood-Filling Networks and Local Realignment**

Peter H. Li<sup>1</sup>, Larry F. Lindsey<sup>1</sup>, Michał Januszewski<sup>1</sup>, Zhihao Zheng<sup>2,5</sup>, Alexander Shakeel Bates<sup>3</sup>, István Taisz<sup>3</sup>, Mike Tyka<sup>1</sup>, Matthew Nichols<sup>2</sup>, Feng Li<sup>2</sup>, Eric Perlman<sup>2</sup>, Jeremy Maitin-Shepard<sup>1</sup>, Tim Blakely<sup>1</sup>, Laramie Leavitt<sup>1</sup>, Gregory S.X.E. Jefferis<sup>3,4</sup>, Davi Bock<sup>2,6</sup>, Viren Jain<sup>1</sup>

<sup>1</sup> Google Research

<sup>2</sup> Janelia Research Campus, Howard Hughes Medical Institute, Ashburn, VA, USA

<sup>3</sup> Neurobiology Division, MRC Laboratory of Molecular Biology, Cambridge, UK

<sup>4</sup> Department of Zoology, University of Cambridge, Cambridge, UK

<sup>5</sup> Solomon H. Snyder Dept. of Neuroscience, Johns Hopkins University, Baltimore, MD, USA

<sup>6</sup> Current address: Dept. of Neurological Sciences, University of Vermont, Burlington, VT, USA

**Abstract:**

Reconstruction of neural circuitry at single-synapse resolution is a key target for improving understanding of the nervous system in health and disease. Serial section transmission electron microscopy (ssTEM) is among the most prolific imaging methods employed in pursuit of such reconstructions. We demonstrate how Flood-Filling Networks (FFNs) can be used to computationally segment a forty-teravoxel whole-brain *Drosophila* ssTEM volume. To compensate for data irregularities and imperfect global alignment, FFNs were combined with procedures that locally re-align serial sections as well as dynamically adjust and synthesize image content. The proposed approach produced a largely merger-free segmentation of the entire ssTEM *Drosophila* brain, which we make freely available. As compared to manual tracing using an efficient skeletonization strategy, the segmentation enabled circuit reconstruction and analysis workflows that were an order of magnitude faster.

## Introduction:

The description of neural function in terms of the circuit architecture of individual neurons and their connections remains a fundamental goal in neurobiology (Shepherd and Grillner 2018). Progress towards this goal has recently been enabled by advances in “connectomics”, specifically nanometer-resolution volume imaging as well as computational methods for visualizing and annotating 3d image data. Scale, however, remains a fundamental constraint: most connectomic studies have been limited to imaging volumes that are millions of cubic microns or less, and in many cases only a fraction of the imaged data have been reconstructed and analyzed (Kornfeld and Denk 2018). In practice this has meant limiting connectomics studies to, for example, fractions of mouse (Bock et al. 2011; Helmstaedter et al. 2013; Kim et al. 2014; Kasthuri et al. 2015; W.-C. A. Lee et al. 2016), rat (Schmidt et al. 2017), rabbit (Anderson et al. 2011), songbird (Kornfeld et al. 2017), zebrafish (Wanner et al. 2016), or *Drosophila* (Takemura et al. 2013; Takemura, Aso, et al. 2017; Takemura, Nern, et al. 2017; Shan Xu et al. 2020) brains, or else characterizing complete but smaller brains such as *C. elegans* (White et al. 1986; Varshney et al. 2011) or larval *Drosophila* (Ohyama et al. 2015).

A recent imaging milestone provides both completeness and significantly increased scale compared to previous synapse-resolution connectomic studies: a serial section transmission electron microscopy (ssTEM) volume of a complete adult *Drosophila* brain imaged at 4x4 nm resolution and sectioned at 40 nm thickness, known as the “full adult fly brain” (FAFB) dataset (Zheng et al. 2018). This trove of image data has the potential to reveal fundamental aspects of the structure and function of the *Drosophila* central nervous system, provided that significant hurdles related to the manual and automated reconstruction of the neurons and their connections can be mitigated or overcome (Funke et al. 2016).

For example, a complication of ssTEM and serial section microscopy in general is the necessity and difficulty of computationally aligning independently imaged sections into a coherent three-dimensional volume, in which physical structures in the tissue are represented at stable XY locations across consecutive imaging planes. In fact, large serial section electron microscopy datasets often require warping, or elastic alignment algorithms (Saalfeld et al. 2012), as well as specific compensation for data irregularities that invariably occur such as tears, folds, cracks, and contaminant particles (Wetzel et al. 2016; Zheng et al. 2018). For large datasets, complete identification and compensation for artifacts is historically intractable, with some misalignments generally persisting throughout subsequent analysis efforts. When tracing over these misalignments, there is a significantly increased danger of introducing errors such as mergers (in which two or more processes are erroneously connected to one another), for both automated algorithms as well as trained human annotators (Schneider-Mizell et al. 2016).

In order to compensate for imperfections in global alignment of the full adult fly brain (FAFB) ssTEM data, we integrated a new “local realignment” procedure into the flood-filling network (FFN) segmentation method (Michał Januszewski et al. 2018), which operates on local subvolumes as an intermediate step towards building a whole volume segmentation. Local realignment improved the alignment quality of subvolumes provided to the FFN, and when

combined with a procedure that further gated FFN segmentation depending on resulting data quality, reduced total merge errors by an order of magnitude (Fig. 3). In an additional “irregular section substitution” process, we automatically detected data irregularities that persisted after local realignment and, where possible, replaced affected regions with data from neighboring sections. This reduced split errors (where two processes are erroneously disconnected from one another) and thus tripled the “expected run length” (Michał Januszewski et al. 2018) (Fig. 4). Finally, for severe situations in which multiple sections of raw data were missing, we used a Segmentation-Enhanced CycleGAN (SECGAN) to synthesize replacement imagery (Michał Januszewski and Jain 2019).

In the following we (1) describe a multi-scale FFN segmentation pipeline for FAFB, (2) show how local realignment and irregular section substitution can be used to deal with imperfect alignment and artifacts, (3) characterize reconstruction accuracy using ground truth skeletons, and (4) show how the automated segmentation results can be used to assist and accelerate manual reconstruction and analysis of neural circuits. We provide the complete segmentation and accompanying metadata such as derived skeletons as a public resource to assist further efforts related to FAFB, *Drosophila* connectomics, and connectomic algorithm development.

## Results:

### **Flood-filling segmentation of FAFB**

The primary result presented here is an automated segmentation of neuronal processes densely covering the entire FAFB dataset (Fig. 1), which contains 40 teravoxels of tissue within a 995x537x283  $\mu\text{m}$  EM volume resulting from a correlation- and feature-based deformable alignment of  $\sim 21$  million raw ssTEM camera images (Zheng et al. 2018; Khairy, Denisov, and Saalfeld 2018). We segmented FAFB via a multistage pipeline whose workhorse was the FFN (detailed below), operating in a coarse-to-fine mode that reduced computational cost by an order of magnitude.

The segmentation result, referred to as “FAFB-FFN1”, is largely an oversegmentation, in which each neuron in the dataset corresponds to multiple automated segments. Conversely, merge errors, in which a single segment overlaps multiple neurons, are rare. We evaluated these properties by comparing the segmentation to a set of 525 ground truth neuronal skeletons produced by human tracers (Zheng et al. 2018, 2020) (Fig. 2). For each ground truth skeleton, we found all FFN segments that overlapped skeleton node positions; ground truth skeletons could then be visualized alongside their overlapping segments to assess the quality of segmentation coverage for each neuron (Fig. 2B-C). We also checked whether each segment overlapped only a single skeleton, versus erroneously merging multiple skeletons together. Finally, for each ground truth skeleton we analyzed the percent of total path length correctly covered by merge-free segments versus the percent impacted by merge errors (Fig. 2D). Out of 525 ground truth skeletons, 509 had negligible merge errors.

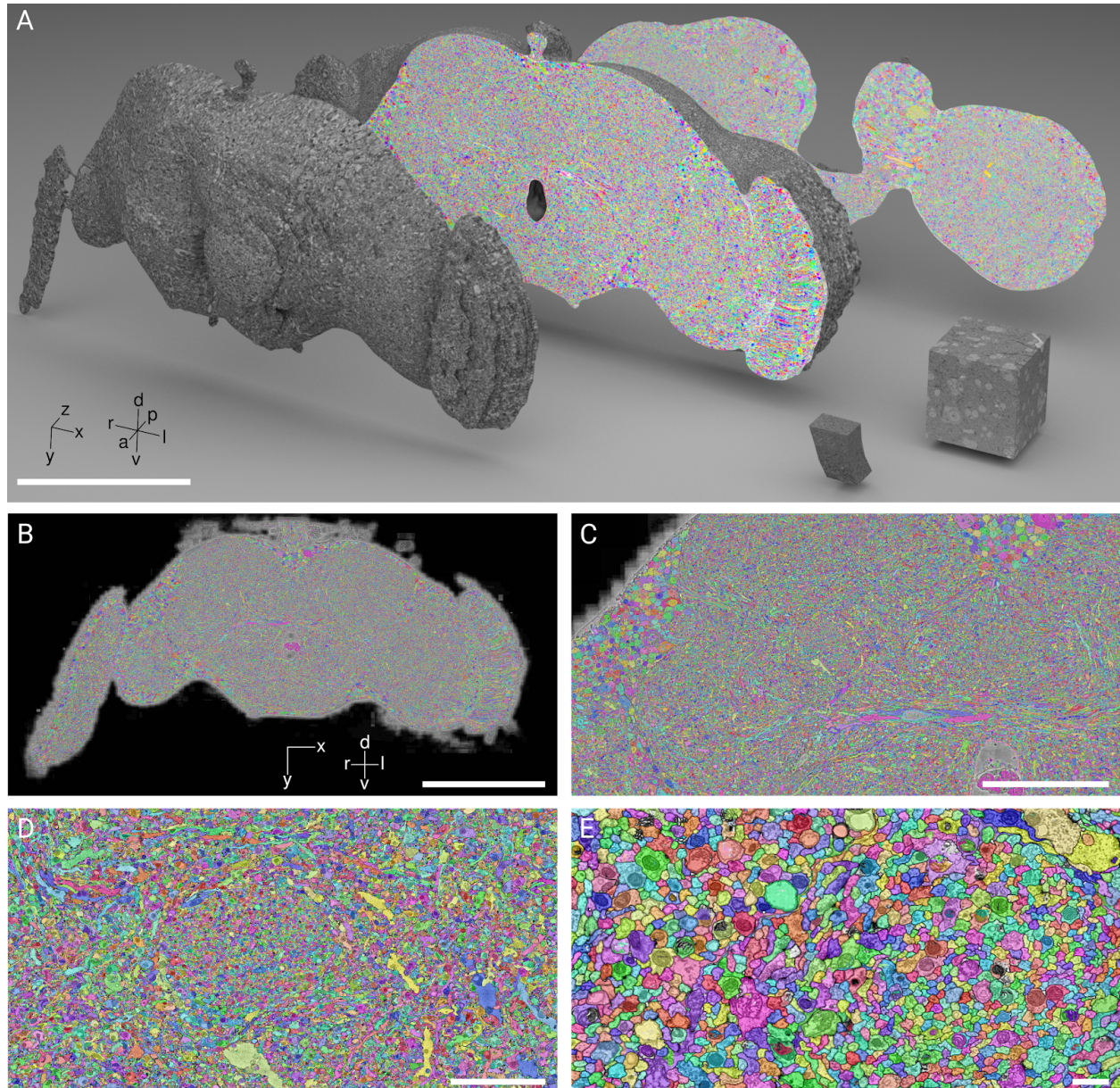


**Figure 1. Dense segmentation of the entire fly brain via FFNs.** (A) 3D rendering of a smoothed tissue mask of the FAFB dataset. Arbitrary coronal sections (dataset XY plane) reveal the FAFB-FFN1 segmentation throughout the interior. In the lower right, two recent dense segmentation benchmarks, from the songbird tectum (Michał Januszewski et al. 2018) and *Drosophila* optic lobe (Takemura et al. 2015), for comparison. Scale bar 200 µm. Exterior surface of FAFB is pseudo-textured. (B-E) Increasing zoom levels of coronal sections intersecting the mushroom body peduncular tract (right hemisphere), FAFB-FFN1 segmentation overlaid on CLAHE processed raw data. Scale bars 200, 50, 10, 1 µm. d, dorsal; v, ventral; a, anterior; p, posterior; r, right hemisphere; l, left hemisphere.

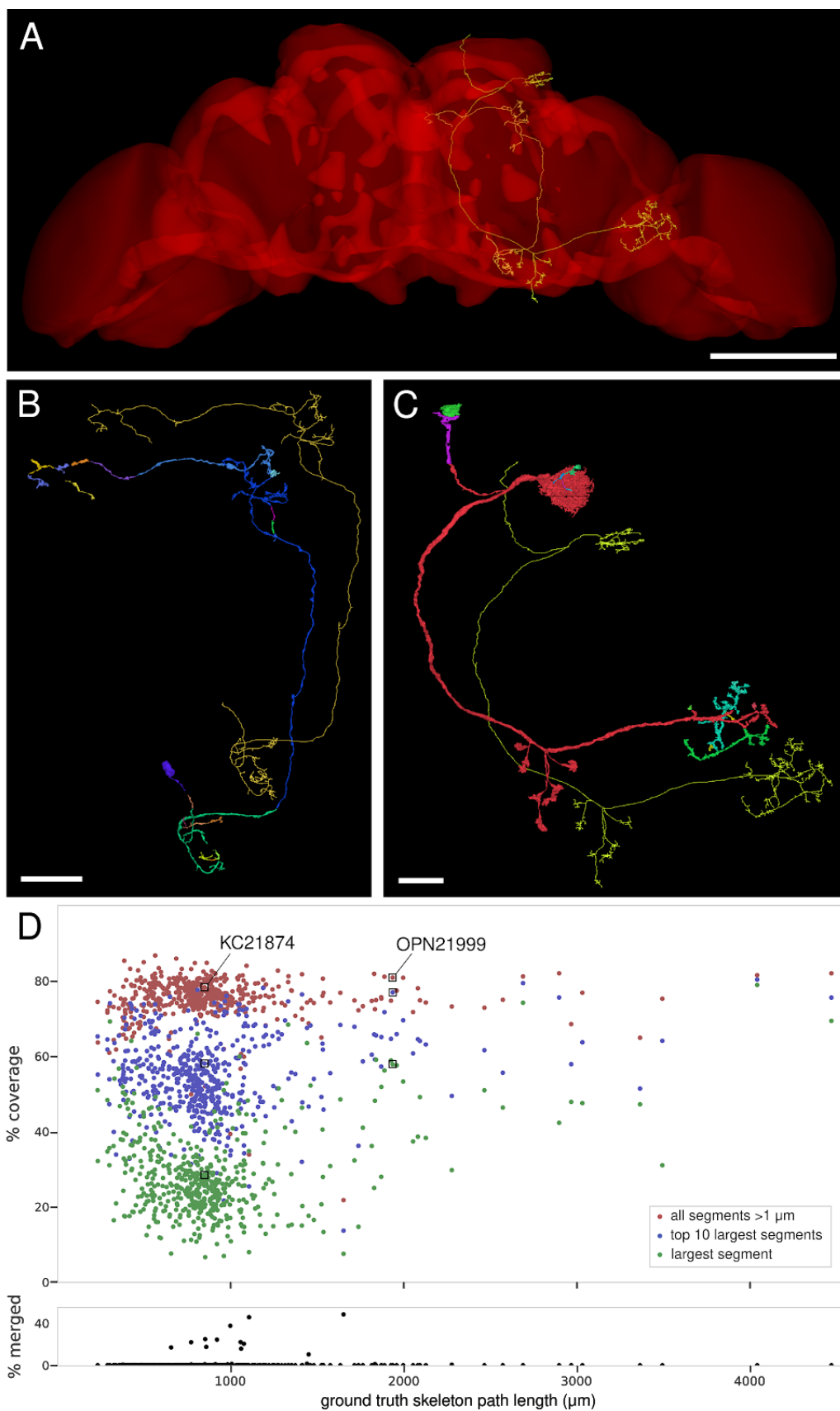


**Figure 2. Automated neuron reconstructions validated against manual neuron tracings. (A)** Manual skeleton tracings of Kenyon cell (KC) 12874 and olfactory projection neuron (OPN) 21999 (Zheng et al. 2018), overlaid on the reference fly brain (Jefferis 2018a). Scale bar 120  $\mu\text{m}$ . **(B)** The same KC12874 skeleton as in (A), displayed alongside the 23 FFN segments that overlap with it for more than 3  $\mu\text{m}$  of path length (offset for clarity, segments colored arbitrarily). FFN segments cover significant skeleton path length without erroneously merging into any neighboring neurites. Scale bar 20  $\mu\text{m}$ . **(C)** As (B), for the 14 segments that overlap OPN21999. **(D)** Top, for each ground truth skeleton ( $n=525$ ), three points showing coverage of the skeleton by FFN segments as a percent of total path length. The point groups are: just the largest segment (by path length covered) for each skeleton (green), the summed path length covered by the five largest segments per skeleton (blue), or the summed path length per skeleton for all segments greater than 1  $\mu\text{m}$  (red). Points for KC12874 and OPN21999 are indicated. Bottom, for each skeleton, the percent of total path length covered by segments that erroneously merge multiple skeletons. For 478 out of 525 cells there are zero merge errors, and for 509 cells the merged path length is  $< 1\%$ .

We further quantified FAFB-FFN1 final segmentation quality using summary metrics based on the ground truth skeletons (Michał Januszewski et al. 2018). *Edge accuracy* categorizes skeleton edges as either correctly reconstructed, or else falling into one of three error categories: split, omitted, or merged. FAFB-FFN1 achieves edge accuracies of 91.5% correct, 4.4% split, and 3.3% omitted, with only 0.82% merged. *Expected run length (ERL)*, computes the expected error-free path length in the segmentation given a uniformly sampled starting point along a ground truth skeleton. FAFB-FFN1 achieves an ERL of 199  $\mu\text{m}$ , comparable to the path error rates computed between multiple expert human tracers in adult (61  $\mu\text{m}$  / error) and larval (27  $\mu\text{m}$  / error) *Drosophila* brain volumes (Zheng et al. 2018; Schneider-Mizell et al. 2016). We also used the skeleton metrics extensively to evaluate the quality of intermediate results throughout the development of the detailed FAFB-FFN1 pipeline described below (Figs. 3-5).

### Handling input data irregularities

To segment FAFB, it was critical to address misalignments and data irregularities such as damaged, occluded, missing, or distorted sections. While these issues affect most connectomic datasets, they are particularly prevalent in serial-section data. FFN segmentation without specific procedures to address irregularities resulted in unacceptably high error rates, particularly for merge errors (Fig. 3). One strategy to handle irregularities is simply to prevent the FFN from moving into any field of view where irregularities are detected (Michał Januszewski et al. 2018). This reduces merge errors while increasing splits. More critically, it can also result in significant omission errors, where regions of the dataset are left unsegmented (Figs. 3A, 4A). Therefore, we addressed these issues more directly via three “preprocessing” steps (attempting to correct issues in the raw inputs before they are passed to the FFN): *Local Realignment (LR)*, *Irregular Section Substitution (ISS)*, and *Segmentation-Enhanced CycleGAN (SECGAN)*.

LR sidesteps the difficulties inherent in globally aligning large serial-section datasets by correcting residual misalignment within each local subvolume block just prior to segmentation (Fig. 3A). We first automatically estimated residual misalignment in the globally aligned dataset via neighboring section cross-correlation template matching (see Methods). The resulting

section-to-section shift estimates allowed each local subvolume block to be realigned on-the-fly prior to FFN segmentation, with additional raw image context drawn as needed per section from the underlying dataset. LR significantly improved segmentation, correcting many merge errors and splits (Fig. 3B-E).

ISS was also applied on-the-fly prior to FFN segmentation, to address the problems of damaged, occluded, missing, and distorted areas by selectively replacing these areas with data from neighboring sections (Fig. 4). We again used section-to-section cross-correlation, now to detect all classes of irregularity remaining after LR (e.g. Fig. 4A-B). We then evaluated, for each detected irregular section, whether the cross-correlation would be improved within the local subvolume block by replacing the irregular section with a copy of the previous neighboring section. Accepting substitutions that passed this evaluation and applying them prior to FFN segmentation significantly improved contiguity and completeness of the result (Fig. 4C), nearly tripling expected run length (Fig. 4D). While ISS did incur an increase in merge errors, this negative impact was effectively nullified by the later oversegmentation consensus stage (see below). For any areas where detected irregularities persisted after both LR and evaluation for ISS, we fell back to simply preventing the FFN from moving into the area. This corrected some remaining merge errors, at the cost of omission and split errors that were addressed via later fill-in and agglomeration stages (see below).

Finally, in three locations in the volume where multiple consecutive sections were partially or completely missing, we trained a SECGAN to synthesize (i.e., “hallucinate”) missing data (Fig. 4E). The SECGAN enabled the FFN to trace through about 60% of the neurites in such locations, on average.

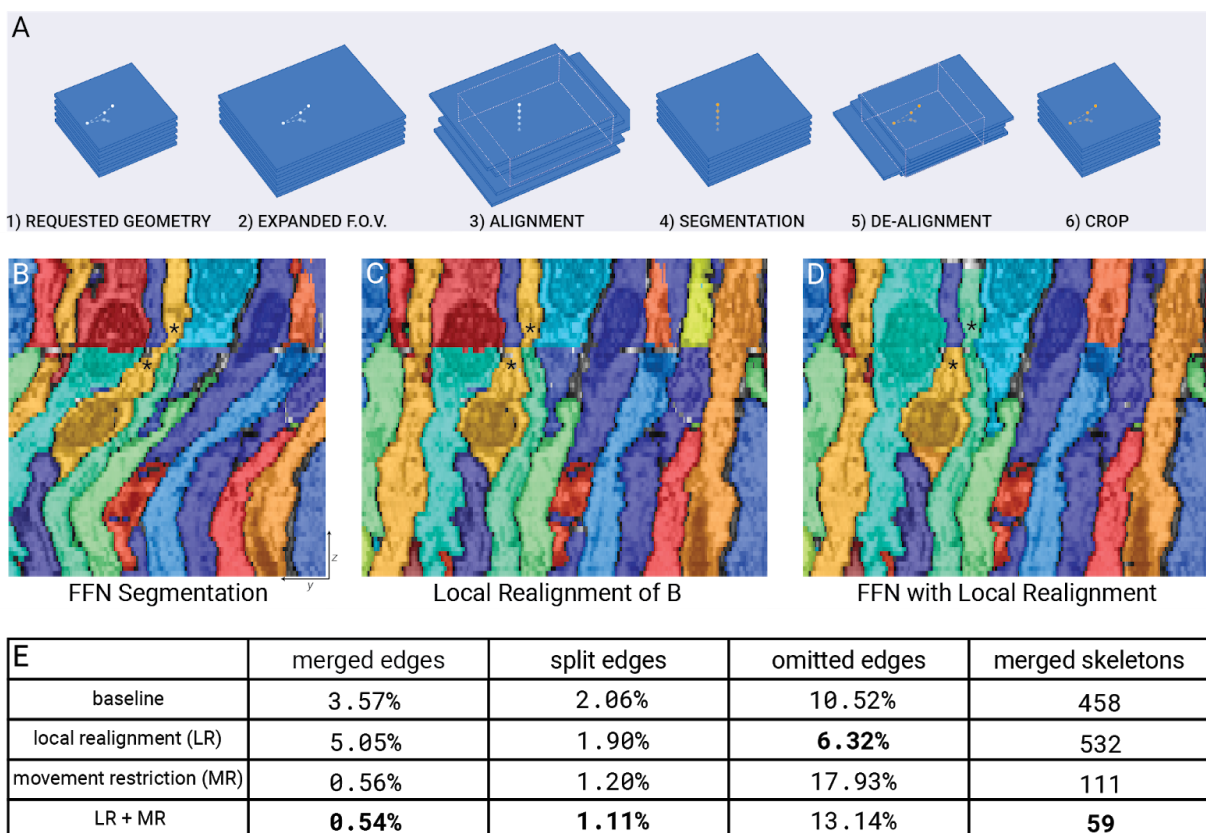


**Figure 3. Local realignment (LR).** (A) LR procedure; a local subvolume is requested for FFN inference (1-2); this is aligned according to section image content (3) and then cropped and segmented (4); the segmentation output is then dealigned (5) and cropped back to the original requested subvolume dimensions for incorporation into a coherent output volume (6). The expansion of the subvolume bounds in (2) is computed to account for the two subsequent rounds of cropping. (B) YZ view of FFN segmentation at for example location in FAFB without LR. (C) The same segmentation result as (B), with LR applied *post-hoc*. This reveals more clearly the impact of the discontinuity in section alignment, including many clear split errors as well as a merge error (stars). (D) Segmentation of the same location as (B) and (C), now with LR applied as a preprocessing step prior to segmentation. This fixes the merge error as well as most splits. (E) Impact of LR on skeleton metrics for 16x16x40 nm resolution FFN segmentation of the Sample E mushroom body cutout. LR fixes many merge and split errors, but cannot correct heavily distorted areas or other types of data irregularity such as damaged or occluded sections. In combination with movement restriction to address these other cases, LR reduced merge errors by an order of magnitude while minimizing splits and omitted areas.

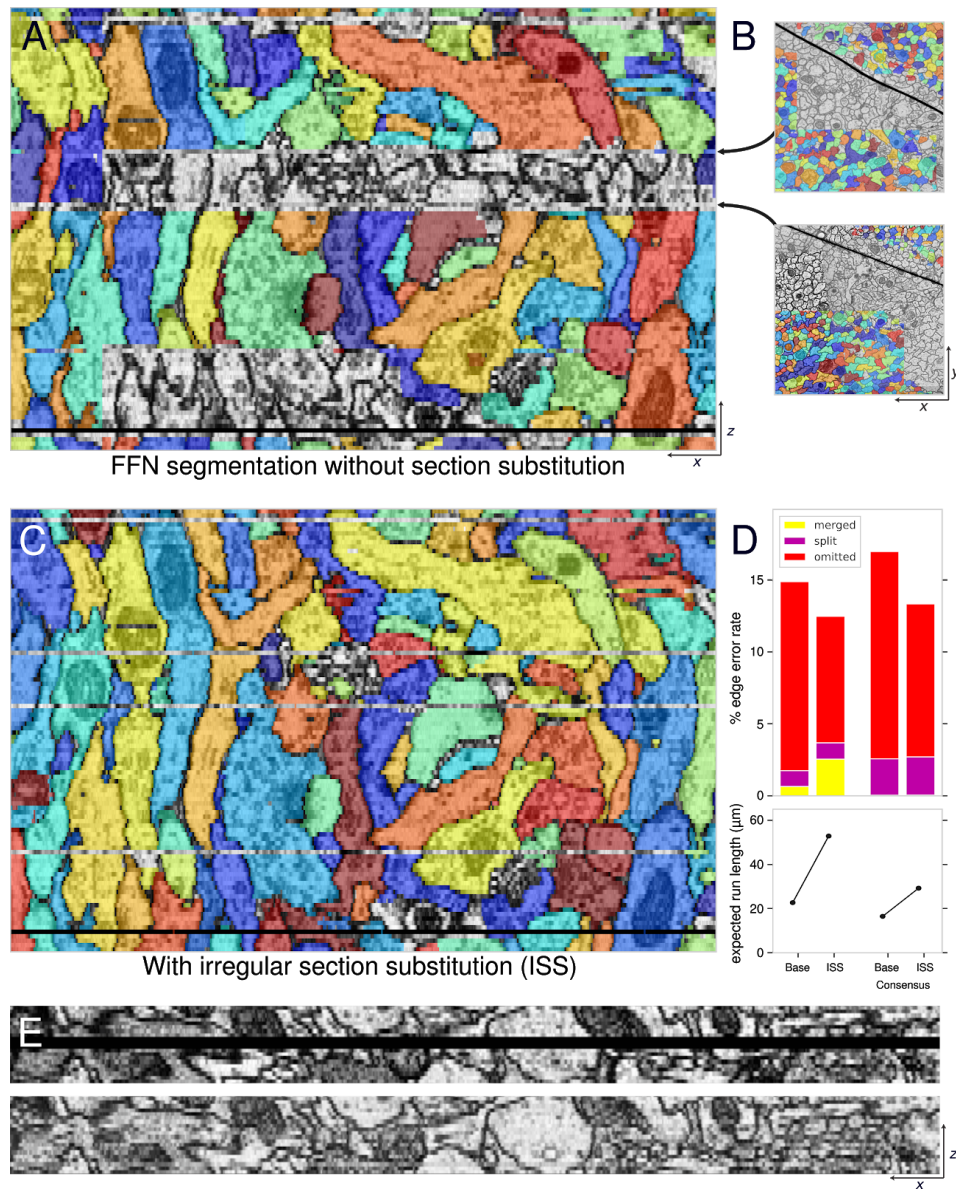


**Figure 4. Irregular section substitution (ISS) and SECGAN.** (A) XZ view of FFN segmentation for an example location in FAFB, with LR and movement restriction preprocessing (Fig. 3). Segments are interrupted at multiple sections due to data artifacts incompletely addressed by LR. When artifacts occur on nearby sections, movement restriction can cause the whole area to be left unsegmented. (B) XY views of two sections from (A) showing tissue fold artifacts. (C) The same view as (A), but with automatic ISS applied prior to segmentation. (D) Impact of ISS on skeleton metrics for 16x16x40 nm resolution FFN segmentation of Sample E. Top, percent remaining skeleton edge errors by subtype. Bottom, expected run length, the average error-free path length of segments under uniform sampling along skeletons. ISS substantially reduces omission errors and nearly triples expected run length, but also causes some new merge errors. However, the increased merge error effect is nullified by later oversegmentation consensus procedure (Fig. 5). (E) Top, XZ view of three consecutive missing sections (Z indices 3595-3597). Bottom, SECGAN interpolation replaces the missing sections with synthesized imagery.

## Overall FAFB segmentation pipeline

FFN segmentation was first performed at reduced resolution (16x16x40 nm) to efficiently handle large structures at the scale of the whole fly brain, before switching to higher resolutions to fill in remaining gaps and capture finer structures (Fig. 5A). As a result, the FFN considered 2.2 teravoxels of tissue for each complete run at 16x16x40 nm resolution, but only 1.5 teravoxels of remaining unlabeled tissue at 8x8x40 nm (versus 8.8 teravoxels total) and only 4.2 teravoxels of remaining unlabeled tissue at 4x4x40 nm (versus 35.2 teravoxels total). Furthermore, resolution was selectively reduced within, but not across, tissue sections (i.e. in the X and Y, but not Z dimensions). This rendered most pipeline inputs more isotropic than the raw data, allowing network architectures previously developed on more isotropic datasets to be successfully redeployed.

The full segmentation pipeline consisted of three major stages: *consensus*, *fill-in*, and *agglomeration* (Fig. 5A). Each stage used the FFN in a different mode, and primarily addressed a different class of segmentation error (merges, omissions, and splits) as revealed in the skeleton metric evaluations (Fig. 5B). Every step involving FFN evaluation (Fig. 5A, rounded boxes) also included LR and ISS preprocessing, except the SECGAN computations which handled misalignment and data irregularity separately.

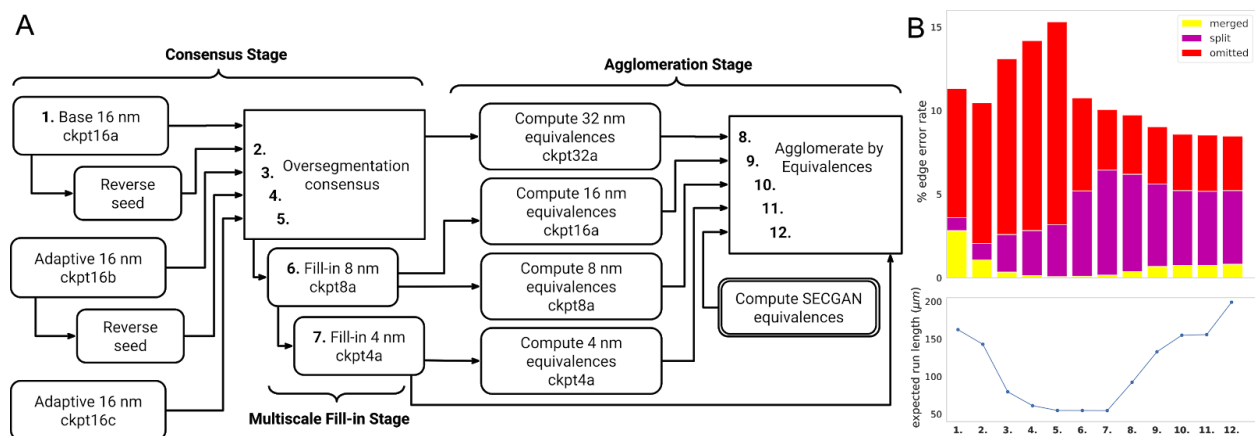


**Figure 5. Overall FAFB-FFN1 segmentation pipeline. (A)** Detailed pipeline steps and major stages, bold numerals highlight selected intermediate volumes in the pipeline used for evaluations in (B). Rounded boxes indicate FFN inference stages. Each FFN step indicates the model checkpoint used. **(B)** Evaluation metrics relative to ground truth skeletons at progressive stages of the pipeline, columns corresponding to pipeline stages with bold numeral labels in (A). Top, percent remaining skeleton edge errors by subtype. Bottom, expected run length.

In the initial stage, we ran the FFN multiple times at 16x16x40 nm resolution from different starting conditions to produce five separate segmentations of the entire FAFB volume. We then combined these results via an “oversegmentation consensus” procedure that breaks segments at any location where the input segmentations disagree (Michał Januszewski et al. 2018). The resulting consensus segmentation has a very low merge error rate at the cost of accumulating split errors (Fig. 5B), as merge errors are retained only when present in *all* input segmentations, whereas split errors in *any* input carry through.

In the second stage, the FFN was only allowed to fill-in remaining empty areas while leaving pre-existing consensus segments unchanged, thus reducing omission errors without introducing significant new merge errors. The primary cause of omissions was inadequate image resolution; FFNs trained and run at 16x16x40 nm resolution were unable to follow some finer structures, leaving these regions empty. FFNs trained and run at 8x8x40 or 4x4x40 nm were able to fill in most of these areas (Fig. 5, steps 6-7).

In the third stage, we used the FFN to evaluate whether selected abutting segments from prior fill-in results should be merged together (i.e. automatically agglomerated). For each evaluation, we extracted small subvolumes (60x60x30 voxels) surrounding a local interface between two candidate segments from both the image volume and the segmentation, seeded the FFN from several points on each side of the interface, and accepted a merge for the segments if the FFN was able to flood significantly and consistently across the interface from both directions (Michał Januszewski et al. 2018).

We evaluated agglomeration candidates at multiple resolutions. For segments in the 16 nm segmentation (Fig. 5A, step 5) we evaluated candidates using an FFN trained and run at 32x32x40 nm. Segments in the 8 nm segmentation (Fig. 5A, step 6), including those created in consensus and fill-in stages, were agglomerated using FFNs trained at both 16x16x40 and 8x8x40 nm resolution. Segments in the 4 nm segmentation (Fig. 5A, step 7) were agglomerated at 4 nm. The automated agglomeration process corrected 30% of the remaining splits in the segmentation (1.5% of total edges), and was tuned to avoid committing significant new merge errors (Figure 5B).

Finally, we used SECGAN synthesized imagery in three regions of the volume to bridge multiple consecutive missing or irregular sections. Without SECGAN replacement, these areas split crossing processes for most of the neurons across the entire XY extent of the volume. We analyzed FFN segmentation of the SECGAN replacement imagery to agglomerate non-SECGAN segments across the gaps, repairing 150,000 splits and improving final ERL from 156 to 199  $\mu\text{m}$  (Fig. 5B).

### **Application of automated segmentation to circuit tracing workflows**

Experiments with human tracers demonstrated the benefit of using FFN segmentation to assist typical biological analysis workflows. We assessed raw speed-up of neuron tracing in several brain areas (Fig. 6) as well as benefits for trans-synaptic circuit tracing efforts (Fig. 7). Some neuron tracing experiments (Fig. 6) were conducted using earlier preliminary versions of the FFN segmentation, with ERLs of 40-50  $\mu\text{m}$  (see Methods); because of the human effort involved these were not repeated using the more complete final FAFB-FFN1. In some cases, tracers worked directly with FFN segments, while for other workflows we first automatically skeletonized the segmentation via blockwise TEASAR (Sato et al. 2000) and the tracers then worked with the skeleton fragments. Depending on the specific workflow, observed benefits ranged from several-fold to more than an order of magnitude in human effort saved.

As part of an ongoing effort to characterize the network connectivity of the mushroom body calyx (Zheng et al. 2020), we traced the dendritic arbors of 1,146 Kenyon cells (KCs) to determine the complement of olfactory projection neuron (OPN) inputs to each (Fig. 6A). All tracing was done in the CATMAID environment (Saalfeld *et al.*, Schneider-Mizell *et al.*) (see Methods). An initial group of 545 KCs was traced entirely via manual node marking, with each arbor reconstructed completely. For a second group of 601 KCs, the arbor was instead reconstructed by manually concatenating segmentation-derived skeleton fragments, with limited manual node marking to link between automated skeletons as needed. In this case, the arbor was traced only to the completeness necessary to positively identify all OPN inputs (Fig. 6A, inset). FFN concatenation is a feasible approach in part due to the very low merge error rate in the segmentation (Fig. 5B) as well as the high coverage of the larger ( $\geq 1 \mu\text{m}$  path length) automated skeleton fragments that tracers find convenient to work with (Fig. 2B-D). Comparing tracing speeds (person-minutes per  $\mu\text{m}$  path length) shows a 5.4x speed-up on average from using FFN skeletons.

In a separate tracing effort, a variety of neurons in the lateral horn (Frechter et al. 2018) and gnathal ganglion (Hsu and Bhandawat 2016) were also reconstructed either manually or via FFN concatenation (Fig. 6B). In this case, the goal of tracing was primarily to allow cell type identification; this generally requires lower levels of completeness, e.g. just the cell body fiber and the major axonal and dendritic branches. Comparing tracing speeds for this workflow shows an 14.6x speed-up on average from using FFN skeletons.

Another common biological analysis workflow is trans-synaptic tracing. In this setting, the goal is to determine for a given neuron how its input and output synapses are distributed, and what the complement of upstream and downstream synaptic partner neurons are. Often there is a particular emphasis on identifying strong partners, e.g. those making five or more synaptic connections with the given neuron.

We assessed the benefits of using FFN segmentation to assist trans-synaptic tracing (Fig. 7). For these experiments, we assumed that a neuron of interest had already been traced, whether manually or via FFN concatenation (Fig. 6), but its upstream and downstream partner neurons had not. We further assumed that all input and output synapse locations had been marked; in this case marking was done manually, but an automated approach (Kreshuk et al. 2015; Buhmann et al. 2018; Heinrich et al. 2018; Huang, Scheffer, and Plaza 2018; Buhmann et al. 2019) would also be viable.

First, we asked how many input synapses onto a given neuron are associated with non-trivial (overlapping at least 3 consecutive manually traced skeleton nodes) upstream FFN segments. Starting from 82 manually traced neurons in the lateral horn, we found that on average 84% of upstream synaptic connections could be recovered by concatenating FFN segments (Fig. 7A). For a number of traced partners recovery was close to 100%, and in some cases synapses were found in the FFN segmentation that had been missed in manual tracing.

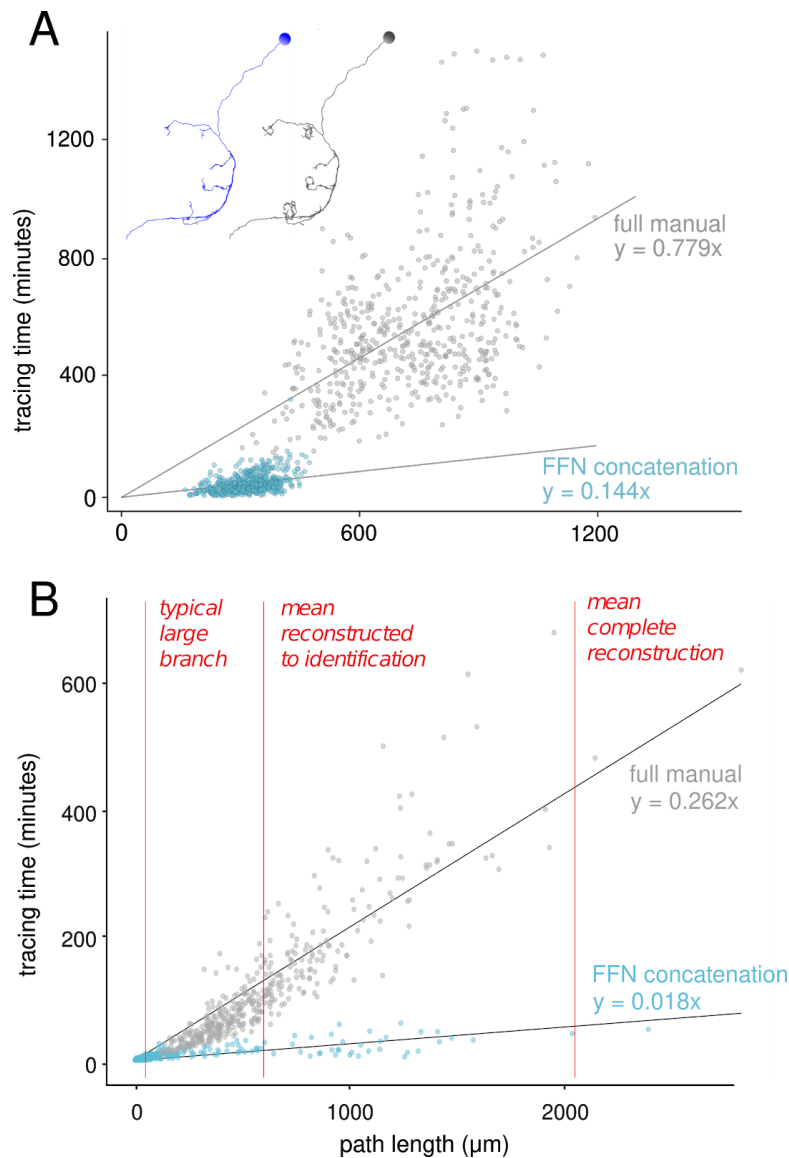


**Figure 6. Segmentation-assisted neuron tracing. (A)** Tracing speed (person-minutes per  $\mu\text{m}$  path length) for Kenyon cells in the mushroom body calyx. Cells are grouped according to the reconstruction methodology: “full manual” (gray points,  $n=545$ ) or “FFN concatenation” (blue points,  $n=601$ ), in which FFN segmentation-derived skeleton fragments were linked together. Inset illustrates for one cell the targeted level of reconstruction completeness for the concatenation methodology (blue) versus the complete dendritic arbor (gray). **(B)** Tracing speeds for various neurons in the lateral horn and gnathal ganglion, traced to lower levels of completeness primarily for cell type identification (mean path length for different completeness indicated for reference). Cells are grouped by reconstruction methodology as in (A). Linear fits indicate tracing speed-ups from using FFN concatenation of 5.4x (A) and 14.6x (B).

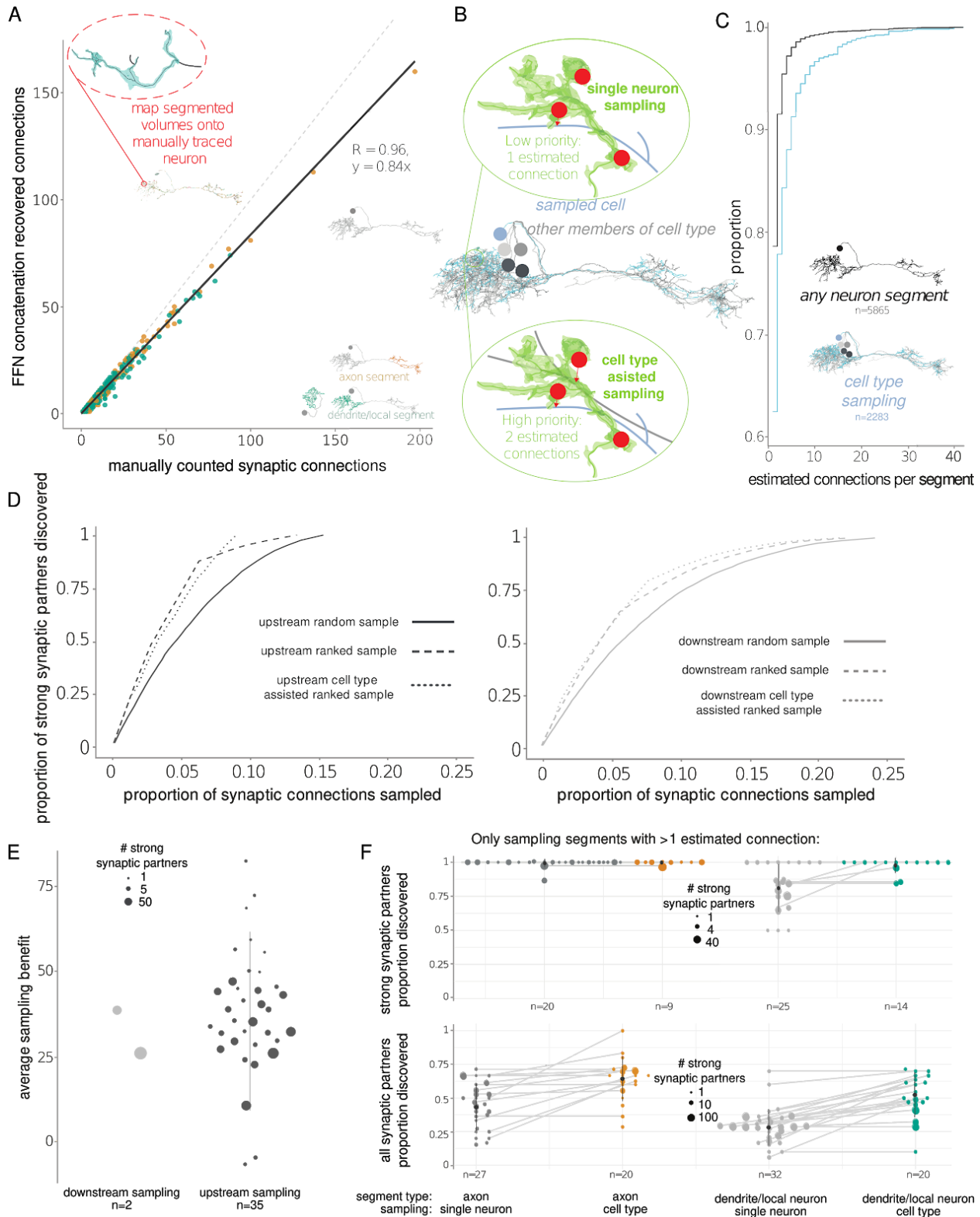


**Figure 7. Trans-synaptic circuit tracing.** (A) For a set of manually traced neurons in the lateral horn (LH,  $n=82$ ), the number of incoming synapses recovered per upstream partner by concatenating FFN segments, versus ground truth synapse total from manual search. Upstream partners have either axonal

morphology (orange points) or dendritic morphology consistent with a local interneuron (green points). Points along the dashed gray unity line indicate near-perfect synapse recovery. The linear fit indicates 84% recovery on average. **(B)** Illustration of two ways to use FFN segments to recover strong upstream synaptic partners. For a traced neuron of interest (blue), we use the FFN segments (top) to search for clusters of marked incoming synapses (red spheres) that originate from a single upstream partner; these are probable strong connections. If other cells of the same type have also been traced (gray), we can also identify FFN segments containing multiple synapses onto any cell of the type of interest as probable strong partners (bottom). **(C)** Cumulative density plot for the proportion of upstream fragments discovered, and the number of connections they have with the given neuron. FFN segmentation-assisted sampling upstream of single starter neurons (black, n=82) and sampling by cell type (blue, n=54 neurons that have >1 neuron in their cell type traced). **(D)** Example average sampling curves for finding strongly connected partners (connected by five or more synapses) of LH neurons. Left, sampling curves for downstream partners of a DA2 projection neuron (Huoviala et al. 2018). We assessed the recovery of strongly connected synaptic partners with different synapse sampling strategies (n=100); solid line: completely random sampling; dashed line: a sample of downstream FFN segments ranked by the number of estimated connections (“ranked sampling”); dotted line: a sample of downstream FFN segments ranked by the number of estimated connections from all five members of this cell type (“cell type assisted ranked sampling”). Right, sampling curves for upstream partners of a PD2a1 LH output neuron (Dolan et al. 2018). Again, five neurons of the same cell type were used for cell type assisted ranked sampling. **(E)** Tracing benefit, i.e. the average proportion of randomly sampled synapses from which one would no longer need to reconstruct (to discover the same number of strong synaptic partners) if using the ranked sampling approach. **(F)** Top, swarm plots of the proportion of strongly connected upstream partners that can be recovered by sampling only from FFN segmented fragments that contain two or more connections to the neuron of interest (gray) or to any neurons of the same cell type (color). Bottom, proportion of all partners, strong or weak. Left, neurons whose upstream segment has axonic morphology. Right, upstream segments with dendritic morphology, consistent with local interneurons.

Availability of FFN segmentation also allowed more efficient, targeted sampling for strong synaptic partners (Fig. 7B-F). The baseline workflow for strong partner discovery is simply to sample input/output synapses for a given neuron in arbitrary order, and reconstruct each corresponding upstream/downstream partner iteratively to find those making multiple synapses onto the neuron of interest, which implies greater significance to the neural circuit (Frechter et al. 2018). However, if an existing automated segment connects multiple synapses together, then that partner can immediately be prioritized for reconstruction as a likely strong partner. This can be extended if the neuron of interest is one of a class of neurons that have also already been traced; in this case an upstream segment that contains multiple synapses onto the neuron of interest *or any other neurons of the same class* is a likely strong partner (Fig. 7B-D). Segmentation-assisted ranked sampling allowed faster recovery of strong connections for a given level of reconstruction effort, for both upstream and downstream partners and especially for partner axons (Fig. 7D-F). In sum, this allowed human tracers to skip as many as 80% of FFN fragments that were not multiply connected (Fig. 7C) to the neuron of interest and still recover the large majority of strongly connected partners (median 97.6% recovered for cell type ranked sampling with axonic partners; 100% for dendritic partners; Fig. 7F, top).

### Discussion:

We have demonstrated that it is possible to segment a complete ssTEM volume of a *Drosophila* brain using a combination of Flood-Filling Networks and novel procedures that compensate for imperfections in the raw data and its initial global alignment. To our knowledge, FAFB-FFN1 is the largest dense segmentation of a central nervous system that has been publicly released, and the first “whole brain” dataset that has been densely segmented by computational means.

The approaches introduced here handle data irregularities explicitly, detecting them and preprocessing on the fly to correct them before the segmentation model sees the data. An alternative approach is to train the segmentation model to take irregularities in stride, e.g. via training data augmentations that simulate the spectrum of issues present in the dataset (K. Lee et al. 2017). We found that while including these augmentations during FFN training improved segmentation robustness, it was not sufficient to allow competitive segmentation of FAFB without explicit handling of irregularities.

FAFB-FFN1 is largely an “over-segmentation” in which each neuron in the automated segmentation is composed of a number of separate segments, each of which average 199  $\mu\text{m}$  in path (run) length when sampled uniformly. Experiments with human tracers have shown that it is more efficient, by an order of magnitude, for humans to manually concatenate automatically-generated segments, as compared to performing manual skeletonization. Moreover, some highly useful biological inferences, such as identification of neuronal cell type, can be performed using FAFB-FFN1 in minutes or seconds per neuron, as compared to hours in the purely manual case. Experiments also demonstrated the applicability of FAFB-FFN1 to circuit tracing and connectomic analyses; these studies combine segmentation with an accounting of the synaptic connections between neurons, for which large-scale automated methods on *Drosophila* tissue are an active research area (Kreshuk et al. 2015; Buhmann et al. 2018; Heinrich et al. 2018; Huang, Scheffer, and Plaza 2018; Buhmann et al. 2019).

Further improvements in the automated reconstruction of volumes such as FAFB may be driven by advances in segmentation methodology. However, a survey of errors in FAFB-FFN1 that persist even after preprocessing for data irregularities suggests that further improvement to global or local alignment methods could improve results even with the same segmentation approach. Furthermore, the FFNs used to generate FAFB-FFN1 were trained primarily on a small subset of the volume located in one particular region of the fly brain (Funke et al. 2016), augmented with a handful of sparsely proof-read neurons sampled from other regions. Training on additional ground truth that represents greater coverage of distinct regions and cell types in the fly brain may also improve reconstruction accuracy. One alternative segmentation of FAFB based on further refinement of the global alignment and an expanded training dataset has recently been released through the open-access, centrally-managed FlyWire tracing environment (Dorkenwald et al. 2020). Although not free to download, this resource will further enhance circuit analyses. Given that error modes between FAFB-FFN1 and FlyWire are

frequently uncorrelated, there is also an opportunity to combine both resources in tracing workflows, provided their differences in global alignment and data accessibility can be reconciled.

In addition to accelerating the reconstruction and study of *Drosophila* neurons and circuits, FAFB-FFN1 may provide a useful resource for the development of novel computational tools. For example, there is a largely unexplored opportunity to develop novel segment agglomeration algorithms that exploit truly brain-wide neuron shape representations and priors. Large-scale morphometric analysis of *Drosophila* neurites and neuron shapes (Sümbül et al. 2014; Zhao and Plaza 2014; Costa et al. 2016; Kanari et al. 2018; Chandrasekhar and Navlakha 2019), along with efforts to model detailed biophysics, such as second messenger dynamics along neurites (Rangamani et al. 2019), may also immediately benefit from sampling segments within FAFB-FFN1.

## Methods:

### **Input and training data**

The raw image and training data were all derived from the Full Adult Fly Brain (FAFB) dataset described by (Zheng et al. 2018). The dataset was acquired at 4x4x40 nm nominal resolution, while our segmentation pipelines additionally used volumes downsampled to 8x8x40, 16x16x40, 32x32x40, and 64x64x40 nm via non-overlapping boxcar-mean filtering. Prior to training and inference it was helpful to normalize all raw imagery via Contrast Limited Adaptive Histogram Equalization (CLAHE) (Zuiderveld 1994), with kernel sizes of 2048x2048 nm followed by 1120x1120 nm.

### **Evaluation data and metrics**

To evaluate automated segmentation quality, we compared our results to manually-traced ground-truth neuronal skeletons (Fig. 2). We used the set of 166 ground-truth skeletons from the mushroom body region, described in (Zheng et al. 2018), as well as a partially overlapping larger collection of 405 Kenyon cells and 123 olfactory projection neurons (Zheng et al. 2020). Where we list IDs for specific FAFB neurons (Fig. 2, and below), they are taken from the FAFB public skeleton IDs (Zheng et al. 2018). We further quantified the agreement between automated segments and ground-truth skeletons via *skeleton metrics*. As described previously (Michał Januszewski et al. 2018), these metrics consist of *edge accuracies* and *expected run lengths* (ERLs).

Briefly, *edge accuracies* count the proportion of ground-truth skeleton edges falling into four non-overlapping categories: correct edges, whose ends are both within one segment; merge errors, where either end is within a segment that erroneously joins two ground truth skeletons; split errors, whose ends are in two different merge-free segments; and omission errors, where either end is in an unsegmented area. ERL computes the expected error free path length (the linear distance connected by correct skeleton edges) in the segmentation given a uniformly sampled starting position along a ground-truth skeleton.

Dataset	Description	Visualization links	Download link	Citations
FAFB	The v14 aligned Full Adult Fly Brain dataset	<a href="https://fafb.catmaid.virtualflybrain.org">https://fafb.catmaid.virtualflybrain.org</a> <a href="#">Neuroglancer</a>	<a href="http://temca2data.org/">http://temca2data.org/</a>	(Zuiderveld 1994; Zheng et al. 2018)
FAFB CLAHE	FAFB with CLAHE contrast normalization	<a href="#">Neuroglancer</a>	<a href="http://fafb-ffn1.storage.googleapis.com/landing.html">http://fafb-ffn1.storage.googleapis.com/landing.html</a>	(Zuiderveld 1994)
CREMI	Training data from the CREMI challenge, based on an earlier alignment of FAFB		<a href="https://cremi.org/data/">https://cremi.org/data/</a>	(Funke et al. 2016)
FAFB-FFN1	FAFB FFN segmentation	<a href="#">Neuroglancer</a>	<a href="http://fafb-ffn1.storage.googleapis.com/landing.html">http://fafb-ffn1.storage.googleapis.com/landing.html</a>	here
FAFB-FFN1 Skeletonization	Automated skeletonization	<a href="#">Neuroglancer</a>	<a href="http://fafb-ffn1.storage.googleapis.com/landing.html">http://fafb-ffn1.storage.googleapis.com/landing.html</a>	(Sato et al. 2000; Silversmith 2019)
FAFB tissue mask	Semantic segmentation mask of different tissue types	<a href="#">Neuroglancer</a>	<a href="http://fafb-ffn1.storage.googleapis.com/landing.html">http://fafb-ffn1.storage.googleapis.com/landing.html</a>	here
FAFB cross-correlation	Section-to-section cross-correlation volume	<a href="#">Neuroglancer</a>	<a href="http://fafb-ffn1.storage.googleapis.com/landing.html">http://fafb-ffn1.storage.googleapis.com/landing.html</a>	here

**Table 1. Input data and results.**

The training data consisted of 3 densely labeled cutouts from the Mushroom Body region of an earlier FAFB global alignment, provided by the MICCAI Challenge on Circuit Reconstruction from Electron Microscopy Images (CREMI) (Funke et al. 2016). Each cutout totals 1250x1250x125 labeled voxels at 4x4x40 nm. We downsampled these cutouts to train networks at reduced resolutions. To generate additional training data at 16x16x40 nm resolution, we additionally proofread 201.3 megavoxels of an earlier segmentation result to rough topological completion. For segmentation pipeline development (Figs. 3, 4) we also used a larger (120,000 x 120,000 x 75,040 nm) unlabeled cutout, referred to as “Sample E”, from around the mushroom body of the v14 alignment (starting offset 376,000 x 80,000 x 158,200 nm).

It was helpful to erode the ground truth skeletons by 1 node back from all branch endpoints, due to many cases where the manually placed endpoint nodes were directly on the border between neighboring cells. We also ignored merge errors that involved fewer than 3 ground truth skeleton nodes (Berning, Boergens, and Helmstaedter 2015). These smallest detected mergers often reflected errors in ground truth skeleton node placement, or were expected due to irregular section substitution changing the positions of neurons within substituted sections, or else were real segmentation errors but were too minor to impact biological interpretation or subsequent processing. After inspecting a subset of manual tracings, we also removed 169 nodes that were reported as larger merge errors but were found to be misplaced, as well as all

nodes occurring in sections 4411 and 4423, which were subject to irregular section substitution across most of the XY extent of the manual tracings.

In a handful of exceptional cases we also excluded entire ground truth neurons from evaluations. Olfactory projection neurons 30791 and 51886 were found to be legitimately fused together over about 25  $\mu\text{m}$  within the medial antenna lobe tract (mALT). This apparent biological aberration or tissue preparation artifact was reported as a merge error if included in the metrics. Olfactory projection neuron 28876 had abnormally dark cytoplasm, possibly due to cell damage (Fiala, Spacek, and Harris 2002), leading to many split and omission errors as well as a few mergers.

### **Misaligned and irregular section detection**

Misalignments and irregular data regions were detected via section-to-section cross-correlation template matching (Lewis 1995). Overlapping image patches of about  $4 \times 4 \mu\text{m}$  were extracted at  $32 \times 32 \text{ nm}$  resolution and  $128 \times 128 \text{ nm}$  stride across each section, and cross-correlated against patches from the following section. For each image pair, the offset of the peak of the correlation surface was taken as the local section-to-section shift.

We found that cross-correlations based on simple zero-padded search windows, without extended image context or cumulative sum normalization (Lewis 1995), were more robust to areas with data irregularities or coherent lateral movement of neural processes (e.g. fiber tracts running transverse to the cutting plane). Therefore we simply zeroed the image mean prior to cross-correlation, found the peak of the unnormalized correlation surface, and then post-normalized the peak value by the autocorrelation magnitude to generate a measure of template match quality.

The cross-correlation procedure produces a subsampled, quantized section-to-section flow field for the entire volume. In areas of misalignment or coherent lateral movement of neural processes, the flow field reveals the magnitude of local section-to-section shifts. It also detects irregular data areas such as tissue cracks and folds by the characteristic sharp discontinuities in their flow fields, and damaged or occluded sections by their large, inconsistent shift values and low template match quality values.

### **Misaligned and irregular section handling**

Movement restriction (Michał Januszewski et al. 2018) blocks the FFN during inference from moving through or evaluating on any field of view where flow field shift magnitudes exceed threshold. For FAFB segmentation we set relatively tolerant thresholds of 64-128 nm, but this still resulted in significant movement restriction over the volume. Restriction generally causes local split errors, but when two restricted areas are close to each other it can prevent an area from being segmented at all (Fig. 4A) and thus also causes omitted edge errors.

Local realignment (LR) instead attempts to allow FFN evaluation through misaligned areas by dynamically correcting alignment at inference time (Fig. 3). Before the FFN considers each local

subvolume (generally 400x400x100 voxels, or 60x60x30 voxels for agglomeration) we compute a translation-only realignment transform based on the weighted median flow field shift over each section, with cross-correlation match quality used as weights. Excessive section-to-section shifts usually reflect data irregularities rather than misalignments, so we set a threshold of 128-256 nm, above which we discard the shift for a given section, resetting it to zero. Applying the computed realignment transform to the subvolume results in a view of the data in which errors in the global alignment of the input are nominally corrected. The FFN operates on the corrected data, and we then reverse the transform to return the segmentation output back to the global coordinate space.

An important requirement is that the subvolume provided to the FFN after realignment should be cropped to a rectilinear shape containing only valid data, so that the FFN is afforded free movement and has valid context. Similarly, the reverse transformed segmentation output should be cropped rectilinear and valid, so that output subvolumes can be reassembled into a coherent segmentation volume. To compensate for cropping, each subvolume has its bounds expanded before the forward realignment is applied, with the amount of additional context needing to be drawn from the input volume dependent on the largest accumulated XY shifts in the given transform.

Following realignment, the flow field of the subvolume is also recomputed, so that any large remaining shifts can still trigger FFN movement restriction. This is important in cases where highly distorted, cracked, or folded sections can only be adequately realigned over a portion of the subvolume XY extent, as well as for data irregularities that realignment cannot address such as missing or occluded sections. In preliminary experiments, we found that replacing translation-only LR with an affine alignment approach could successfully address some of these areas. However, affine LR proved more difficult to regularize.

For data issues inadequately addressed by LR, irregular section substitution (ISS) attempts to allow FFN evaluation through the area by replacing the affected section locally within the subvolume with data from a neighboring section (Fig. 4). The criterion for considering a section for substitution is whether the magnitude of flow field shifts for the unsubstituted section triggers significant movement restriction (defined as restriction over more than 3% of the section extent within the subvolume). If so, the section is replaced with the preceding section, and the cross-correlation flow field with respect to the following section is recomputed. If the new flow field results in a significant reduction in movement restriction (defined as 50% or more reduction), the candidate substitution is accepted and the LR transform is updated to reflect the new flow field.

Thus ISS is only allowed when the sections on either side of an irregularity can be adequately realigned to each other. The anisotropy of the FAFB dataset makes it rare for this to be effective across more than a single consecutive section. For FAFB-FFN1, we considered only single section substitutions, except for the 32x32x40 nm agglomeration stage, where we allowed up to 3 consecutive sections to be substituted.

### **Flood-filling network training and inference**

FFNs were trained as described previously (Michał Januszewski et al. 2018) and as publicly released (Michał Januszewski 2019). Briefly, a deep 3d convolutional neural network was trained in TensorFlow via asynchronous stochastic gradient descent. The network field of view was 33x33x17 voxels except networks trained at full 4x4x40 nm resolution, where the field of view was 33x33x9. The network architecture consisted of a series of 18 convolutional layers with 3x3x3 kernels and 32 feature channels, paired off into 9 residual units with no downsampling, resulting in 472,353 trainable parameters. All three CREMI cutouts of ground-truth labels were used for training, downsampled to the appropriate resolution as needed.

FFN seeding and movement policies for training and inference were as described previously. Due to the anisotropy of serial-section data, we also found that a 2d variant of the Sobel-Feldman peak distance seeding procedure (Michał Januszewski et al. 2018) was effective for filling in small processes in later inference runs. FFN inference hyperparameters were set similarly to previously described: initial field-of-view fill value 0.05; movement threshold 0.9; segment threshold 0.6. The base movement step size was 8x8x4 voxels.

Network weights were checkpointed periodically during training, and convergence was assessed at each checkpoint by running test inference on a small cutout from the mushroom body calyx (“calyx1”) and evaluating skeleton metrics against the resulting segmentation. We then selected a subset of the checkpoints whose calyx1 evaluations had zero merge errors and high overall edge accuracy for inference over the larger Sample E mushroom body cutout. Finally, we selected the checkpoints with the lowest merge error rates and highest overall edge accuracies from these evaluations for inference over all of FAFB (Fig. 5). Two additional checkpoints were selected for oversegmentation consensus (Michał Januszewski et al. 2018) at 16x16x40 nm by reevaluating all checkpoints over an additional small area (“adaptive1”) where the base segmentation had remaining merge errors, and selecting checkpoints that corrected these errors while maintaining high edge accuracy.

### **Segmentation-Enhanced CycleGAN for Triple-Section Interpolation**

A SECGAN (Michał Januszewski and Jain 2019) was trained to synthesize missing data in the raw FAFB volume at 16x16x40 nm voxel resolution. Both “input” dataset X and “target” dataset Y were sampled from regions within FAFB. Samples for X were chosen from regions containing data with no known irregularities, and samples from Y were specifically chosen within regions that contained three consecutive missing or irregular sections. The field of view of the generator was 33x33x33 voxels, using a ResNet-like architecture previously described (Michał Januszewski and Jain 2019), and a ResNet18 discriminator architecture (He et al. 2016). During training, the central 3 sections of every training example were excluded from the Y cycle loss, and were zeroed-out in the input of the Y discriminator. The Y images were also altered by filling the empty sections with the contents of the directly preceding non-empty section.

For SECGAN inference, the raw image data around the missing sections was first elastically realigned (Saalfeld et al. 2012) via an iterative procedure. First, the flow field between the two sections directly preceding and following the gap was estimated from downsampled imagery at 64x64 nm in-plane pixel resolution using patch-wise cross-correlation (patch size 160 pixels, stride 40 pixels), and used to relax a 2-section (ignoring the gap) elastic mesh. The procedure was then repeated at 32 x 32 nm in-plane resolution to obtain the final alignment.

After running FFN segmentation within 200-section subvolumes centered on the SECGAN substituted region, overlaps were computed between the SECGAN segments and the preexisting segments on either side of the substituted gap. For each SECGAN segment, the maximally overlapping pre- and post-gap preexisting segments were determined, and these two segment IDs were then joined if both overlaps exceeded 1000 voxels. By construction, this approach can only link a single pre-gap segment to a single post-gap segment for each SECGAN segment, which limits the ability to fully address neurites that branch within the substituted block. However, we found this constraint to be important for avoiding new merge errors.

### **Overall segmentation pipeline details**

The overall pipeline comprised a series of FFN segmentation steps, selected to maximize overall skeleton edge accuracy and ERL while minimizing merge errors, as described previously (Michał Januszewski et al. 2018) and above. For filtering agglomeration decisions, we found that it was more effective to require the proportion of deleted voxels to be below threshold for both segment A and B (operation AND), rather than for either segmentation A or B (operation OR) as done previously.

Some experiments with human tracers (Fig. 6) were carried out using earlier segmentations, referred to as FAFB-FFN0 and SAMPLE-E-FFN0. Detailed hyperparameters for the different pipelines are given in Table 2.

	FAFB-FFN1 (Figs. 1-5, 7)	FAFB-FFN0 (Figs. 6B)	SAMPLE-E-FFN0 (Fig. 6A)
Consensus input segmentations	ckpt16a peaks2d forward, ckpt16a peaks2d reverse, ckpt16b peaks2d forward, ckpt16b peaks2d reverse, ckpt16c peaks2d forward	ckpt16d peaks3d forward, ckpt16d peaks3d reverse, ckpt16e peaks2d forward unwhitened	ckpt16d peaks3d forward, ckpt16d peaks3d reverse, ckpt16e peaks2d forward
Fill-in segmentations	ckpt8a peaks2d ckpt4a peaks2d	ckpt16d peaks2d, ckpt8b peaks2d	ckpt8b peaks2d
Image normalization	CLAHE 2x	CLAHE	CLAHE
Cross-correlation normalization	post-normalized	whitened, except as noted above	unwhitened

### Agglomeration 1

Checkpoint	ckpt32a	ckpt16d	ckpt16d
Decision point radius	80x80x80 nm	48x48x32 nm	48x48x32 nm
Decision point min segment size	16,000 voxels		
Fidelity minimums (segment A & B)	0.85	0.6	0.6
Jaccard minimum	0.7	0.7	0.7
Deleted proportion maximums (segment A & B)	0.01	0.02	0.02
Deleted proportion combination operation	AND	OR	OR

### Agglomeration 2

Checkpoint	ckpt16a
Decision point radius	80x80x32 nm
Decision point min segment size	16,000 voxels
Fidelity minimums	0.95
Jaccard minimum	0.7
Deleted proportion maximums	0.01

### Agglomeration 3

Checkpoint	ckpt8a
Decision point radius	80x80x32 nm
Decision point min segment size	16,000 voxels
Fidelity minimums	0.85
Jaccard minimum	0.5
Deleted proportion maximums	0.02

#### Agglomeration 4

Checkpoint	ckpt8a
Decision point radius	80x80x32 nm
Decision point min segment size	3,000 voxels
Decision point min overlap 16 nm	5,000 voxels
Fidelity minimums	0.9
Jaccard minimum	0.5
Deleted proportion maximums	0.02

#### Agglomeration 5

Checkpoint	ckpt4a
Decision point radius	150x150x150 nm
Decision point min segment size	5,000 voxels
Decision point min overlap 8 nm	5,000 voxels
Fidelity minimums	0.85
Jaccard minimum	0.85
Deleted proportion maximums	0.02

#### Agglomeration 6

Checkpoint	secgan16a
Z-sections	1564-1566; 2176-2178; 3595-3597
Couplet overlap minimums	0.75

**Table 2. FFN pipeline hyperparameters.** All checkpoint names include the XY resolution used in training and inference.

peaks3d, 3d Sobel-Feldman peak seeding; peaks2d, 2d Sobel-Feldman peak seeding; forward, normal seed order; reverse, reversed seed order; post-normalized, post-normalized cross-correlation (see Methods); whitened, square-root frequency amplitude normalized image cross-correlation; unwhitened, cumulative sum normalized image cross-correlation.

### Tissue Masking

We trained a convolutional network to predict whether a voxel belonged to one of six categories that represented general structural features of the image volume. We manually labeled 10.7 million voxels at 2x reduced lateral resolution as either neuropil (4.6M voxels), cell body (1.6M voxels), glia (0.11M voxels), black border (0.7M voxels), resin (1.6M voxels), or tissue border (1.9M voxels). Annotations were sparsely created using a custom web-based tool (“Armitage”) that enabled manual painting of voxels with a modifiable brush size.

We then used TensorFlow to train a 3d convolutional network to classify a 65x65x5 patch centered on each manually labeled voxel. The network contained three “convolution-pooling” modules consisting of convolution (3x3x1 kernel size, 64 feature channels, VALID mode where

convolution results are only computed where the image and filter overlap completely) and max pooling (2x2x1 kernel size, 2x2x1 stride, VALID mode), followed by one additional convolution (3x3x1 kernel size, 16 feature maps, VALID), a fully connected layer that combines information from all 5 slices (512 nodes), and a six-class softmax output layer. We trained the network by stochastic gradient descent with a minibatch size of 32 and 6 replicas. During training, each of the six classes was sampled equally often. Training was terminated after 0.5 million updates.

Inference with the trained network was applied to all voxels in the image volume using dilated convolutions, which is several orders of magnitude more efficient than a naive sliding-window inference strategy. Inference on the whole volume at 16x16x40nm resulted in 1.97 teravoxels of predicted neuropil, 0.25 teravoxels of soma, 0.24 teravoxels of glia, 0.24 teravoxels of black border, 0.46 teravoxels of resin, and 0.41 teravoxels of tissue border.

Tissue masking predictions were used during FFN inference to block FFN evaluations centered at locations with less than 12% predicted neuropil probability and less than 50% predicted soma probability. This improved efficiency of segmentation and prevented some segmentation errors in areas such as glia with textures underrepresented in the training set. Class-wise voxel counts from the tissue masking volume were used to estimate the total dataset size of 39.4 teravoxels of combined neuropil, soma, and glial tissue at full 4x4x40 nm resolution. These three classes were also combined to generate a whole brain mesh for visualization (Fig. 1).

### **Automated skeletonization**

Some biological analysis workflows require a neuron skeleton representation (Fig. 2A-C, Fig. 6A inset) rather than volumetric segments. We used the TEASAR algorithm (Sato et al. 2000) to automatically convert the FFN segmentation to a skeleton representation. Earlier versions of the segmentation were skeletonized via a different pipeline than the final release; the differences are detailed in Table 3.

The scale of FAFB required that TEASAR be run block-wise and at downsampled resolution. To reconnect skeletons at block boundaries, a simple heuristic was used to join the nearest neighbor nodes on either side provided their separation distance was below a fixed threshold. Occasionally this heuristic failed to reconnect across blocks, in which case a single skeleton ID in the result might comprise multiple components. In a few cases, large irregular bodies such as glia, trachea, somas, or non-biological material created highly fragmented skeletons; skeletons with total number of components above a fixed threshold were discarded.

Skeletons were further post-processed to enhance suitability for FFN concatenation workflows (Fig. 6). First, we eroded skeletons back from all endpoints. Skeleton branches with a low path length relative to average diameter often reflect thickening or bumps at the surface of neurites, rather than true neuronal branches; these were either pruned off (for length / diameter < 10; earlier releases) or were excluded from skeletonization by increasing the invalidation radius scale factor (FAFB-FFN1 final release). Finally skeletons were sparsified to a target distance

between nodes within unbranched sections. After these post-processing steps, all resulting skeletons greater than 1  $\mu\text{m}$  path length were exported to the tracing environment.

	FAFB-FFN1 (Fig. 7)	FAFB-FFN0; SAMPLE-E-FFN0 (Fig. 6)
Block size	256x256x256	512x512x256
Resolution (nm)	32x32x40	32x32x40
Maximum reconnection distance (nm)	50	165
Max fragments per skeleton	1,000,000	10,000
Endpoint erosion (nm)	100	250
Node sparsification distance (nm)	300	250
Length / diameter minimum ratio	NA	10
Invalidation radius scale factor	4	NA
TEASAR implementation	(Silversmith 2019)	(Funke 2017)

**Table 3. Skeletonization parameters**

### Neuron skeleton tracing and trans-synaptic analysis

All neuron skeleton tracing (Fig. 6) was done in the FAFB CATMAID environment (Saalfeld et al. 2009). CATMAID provides an interface for exploring the EM image volume, and neurons can be traced manually by marking a series of node points (Schneider-Mizell et al. 2016). The TEASAR-generated skeletons of FFN segments were also imported into CATMAID, and tools were provided for linking skeleton fragments together (“FFN concatenation”) and quickly jumping to fragment endpoints to check for missing continuations of neurites.

Neuronal reconstruction in mushroom body calyx (Fig. 6A) was typically done by two team members, an initial tracer and a subsequent proofreader who validated the tracing, potentially sending issues back to the tracer to iterate on. Neurites in the fly brain can be classified into larger, microtubule-containing neurites (“backbones”) and fine, microtubule-free neurites (“twigs”) (Schneider-Mizell et al. 2016). Microtubules were used as guides during manual tracing and FFN concatenation to ensure quick reconstruction of backbones of the neurons, which is often sufficient for cell type identification.

The CATMAID environment automatically records the amount of time spent tracing each neuron. When the FFN concatenation tracing methodology was introduced, there was a ramping-up period while human tracers adjusted and software tools for efficient concatenation matured. Thus, out of 916 total Kenyon cells (KCs) traced via FFN concatenation, the first 315 had an average tracing speed of 20 seconds per  $\mu\text{m}$  path length with a standard deviation of 13 seconds, while the remaining 601 KCs from the later mature period averaged 9 seconds per  $\mu\text{m}$  with a standard deviation of 5 seconds. In the Results section, we therefore exclude the ramping-up period from the analysis.

Trans-synaptic analysis combined use of both skeletons and volumetric segments. Software tools for mapping between CATMAID skeletons and the FFN segments are available publicly (Jefferis 2018b). To simulate the recovery of strong synaptic partners using different sampling strategies over synaptic connections (Fig. 7D-E), we started from a fully traced neuron of interest. We also traced at least the local arbor and cell body fiber of all upstream or downstream synaptic partners for purposes of simulation. We then picked a single synaptic connection from which to run simulated tracing, sampled either randomly or using FFN segments to rank multiply connected partners higher *a priori*. For each sampled connection, we recorded whether it corresponded to a strong partner (at least 5 synaptic connections). We also marked all other connections for that partner as visited, under the assumption that they would be discovered in tracing the partner to identification, or else would be trivially connected to the partially traced partner if sampled subsequently. Sampling was then repeated until all strong partners were discovered for the neuron of interest, and the entire procedure was repeated for each starter neuron.

### Acknowledgements

This work was supported by core support from the MRC (MC-U105188491) and an ERC Consolidator (649111) grant (to GSXEJ); the Howard Hughes Medical Institute and a National Institutes of Health BRAIN Initiative (1RF1MH120679-01) grant (DB); and a Wellcome Trust Collaborative Award (203261/Z/16/Z to GSXEJ, DB). We thank FAFB tracers J. Ali, S. Calle-Schuler, J. Hsu, N. Masoodpanah, C. Fisher, N. Sharifi, L. Kmecova, J. Ratliff, S. Imtiaz, B. Gorko, A. Boyes, A. John, E. Moore, B. Koppenhaver, P. Ranft, B. Harrison, S. Murthy, A. Haddad, A. Adesina, A. Scott, C. Marlin, E. Wissell, Z. Gillis, S. Ali, G. Allred, S. Waters, A. Scott, L. Marin, S. Mohr, M. Lingelbach, E. Spillman, A. Smith, T. Ngo, B. Gampah, M. Ryan, J. Dunlap, N. Reddy, A. Fischel, M. Pleijzier, A. Sheridan, K. A. Jahjah, A. Edmondson-Stait, R. Parekh, I. Salaris, A. Warner, S. Lauritzen, R. Roberts, L. Bueld, C. Ardekani, J. Gonzales, R. Rais, W. Chen, N. Ribeiro, and T. Neves for their work reconstructing neurons in mushroom body. We thank I. Varela, B. Morris, S. N. Bailey, and R. J. V. Roberts for their tracing work in lateral horn and gnathal ganglion. We thank T. L. Dean, A. Pope, N. Apthorpe, and J. Shlens for technical contributions and discussions.

### References

- Anderson, James R., Bryan W. Jones, Carl B. Watt, Margaret V. Shaw, Jia-Hui Yang, David Demill, James S. Lauritzen, et al. 2011. "Exploring the Retinal Connectome." *Molecular Vision* 17 (February): 355–79.
- Berning, Manuel, Kevin M. Boergens, and Moritz Helmstaedter. 2015. "SegEM: Efficient Image Analysis for High-Resolution Connectomics." *Neuron* 87 (6): 1193–1206.
- Bock, Davi D., Wei-Chung Allen Lee, Aaron M. Kerlin, Mark L. Andermann, Greg Hood, Arthur W. Wetzell, Sergey Yurgenson, Edward R. Soucy, Hyon Suk Kim, and R. Clay Reid. 2011. "Network Anatomy and in Vivo Physiology of Visual Cortical Neurons." *Nature* 471 (7337): 177–82.
- Buhmann, Julia, Renate Krause, Rodrigo Ceballos Lentini, Nils Eckstein, Matthew Cook,

- Srinivas Turaga, and Jan Funke. 2018. "Synaptic Partner Prediction from Point Annotations in Insect Brains." *arXiv [cs.CV]*. arXiv. <http://arxiv.org/abs/1806.08205>.
- Buhmann, Julia, Arlo Sheridan, Stephan Gerhard, Renate Krause, Tri Nguyen, Larissa Heinrich, Philipp Schlegel, et al. 2019. "Automatic Detection of Synaptic Partners in a Whole-Brain Drosophila EM Dataset." *bioRxiv*. <https://doi.org/10.1101/2019.12.12.874172>.
- Chandrasekhar, Arjun, and Saket Navlakha. 2019. "Neural Arbors Are Pareto Optimal." *Proceedings of the Royal Society B: Biological Sciences* 286 (1902): 20182727.
- Costa, Marta, James D. Manton, Aaron D. Ostrovsky, Steffen Prohaska, and Gregory S. X. E. Jefferis. 2016. "NBLAST: Rapid, Sensitive Comparison of Neuronal Structure and Construction of Neuron Family Databases." *Neuron* 91 (2): 293–311.
- Dolan, Michael-John, Ghislain Belliard-Guérin, Alexander Shakeel Bates, Shahar Frechter, Aurélie Lampin-Saint-Amaux, Yoshinori Aso, Ruairí J. V. Roberts, et al. 2018. "Communication from Learned to Innate Olfactory Processing Centers Is Required for Memory Retrieval in Drosophila." *Neuron* 100 (3): 651–68.e8.
- Dorkenwald, Sven, Claire McKellar, Thomas Macrina, Nico Kemnitz, Kisuk Lee, Ran Lu, Jingpeng Wu, et al. 2020. "FlyWire: Online Community for Whole-Brain Connectomics." <https://doi.org/10.1101/2020.08.30.274225>.
- Fiala, John C., Josef Spacek, and Kristen M. Harris. 2002. "Dendritic Spine Pathology: Cause or Consequence of Neurological Disorders?" *Brain Research. Brain Research Reviews* 39 (1): 29–54.
- Frechter, Shahar, Alexander S. Bates, Sina Tootoonian, Michael-John Dolan, James D. Manton, Arian Jamasb, Johannes Kohl, Davi Bock, and Gregory S X. 2018. "Functional and Anatomical Specificity in a Higher Olfactory Centre." *bioRxiv*. <https://doi.org/10.1101/336982>.
- Funke, Jan. 2017. *Imageprocessing*. Github. <https://github.com/funkey/imageprocessing>.
- Funke, Jan, Stephan Saalfeld, Davi Bock, Srini Turaga, and Eric Perlman. 2016. "CREMI: Challenge on Circuit Reconstruction from Electron Microscopy Images." May 1, 2016. <http://cremi.org/>.
- Heinrich, Larissa, Jan Funke, Constantin Pape, Juan Nunez-Iglesias, and Stephan Saalfeld. 2018. "Synaptic Cleft Segmentation in Non-Isotropic Volume Electron Microscopy of the Complete Drosophila Brain." *arXiv [cs.CV]*. arXiv. <http://arxiv.org/abs/1805.02718>.
- He, Kaiming, Xiangyu Zhang, Shaoqing Ren, and Jian Sun. 2016. "Deep Residual Learning for Image Recognition." In *Proceedings of the IEEE Conference on Computer Vision and Pattern Recognition*, 770–78.
- Helmstaedter, Moritz, Kevin L. Briggman, Srinivas C. Turaga, Viren Jain, H. Sebastian Seung, and Winfried Denk. 2013. "Connectomic Reconstruction of the Inner Plexiform Layer in the Mouse Retina." *Nature* 500 (7461): 168–74.
- Hsu, Cynthia T., and Vikas Bhandawat. 2016. "Organization of Descending Neurons in Drosophila Melanogaster." *Scientific Reports* 6 (February): 20259.
- Huang, Gary B., Louis K. Scheffer, and Stephen M. Plaza. 2018. "Fully-Automatic Synapse Prediction and Validation on a Large Data Set." *Frontiers in Neural Circuits* 12: 87.
- Huoviala, Paavo, Michael-John Dolan, Fiona Love, Shahar Frechter, Ruairí J. V. Roberts, Zane Mitrevica, Philipp Schlegel, et al. 2018. "Neural Circuit Basis of Aversive Odour Processing in Drosophila from Sensory Input to Descending Output." <https://doi.org/10.1101/394403>.
- Januszewski, Michal. 2019. *FFN: Flood-Filling Networks*. Github. <https://github.com/google/ffn>.
- Januszewski, Michal, and Viren Jain. 2019. "Segmentation-Enhanced CycleGAN." *bioRxiv*. <https://doi.org/10.1101/548081>.
- Januszewski, Michał, Jörgen Kornfeld, Peter H. Li, Art Pope, Tim Blakely, Larry Lindsey, Jeremy

- Maitin-Shepard, Mike Tyka, Winfried Denk, and Viren Jain. 2018. "High-Precision Automated Reconstruction of Neurons with Flood-Filling Networks." *Nature Methods* 15 (8): 605–10.
- Jefferis, Gregory. 2018a. *Elmr*. Github. <https://github.com/jefferis/elmr>.
- . 2018b. *Fafbseg*. Github. <https://github.com/jefferis/fafbseg>.
- Kanari, Lida, Paweł Dłotko, Martina Scolamiero, Ran Levi, Julian Shillcock, Kathryn Hess, and Henry Markram. 2018. "A Topological Representation of Branching Neuronal Morphologies." *Neuroinformatics* 16 (1): 3–13.
- Kasthuri, Narayanan, Kenneth Jeffrey Hayworth, Daniel Raimund Berger, Richard Lee Schalek, José Angel Conchello, Seymour Knowles-Barley, Dongil Lee, et al. 2015. "Saturated Reconstruction of a Volume of Neocortex." *Cell* 162 (3): 648–61.
- Khairy, Khaled, Gennady Denisov, and Stephan Saalfeld. 2018. "Joint Deformable Registration of Large EM Image Volumes: A Matrix Solver Approach." *arXiv [cs.CV]*. arXiv. <http://arxiv.org/abs/1804.10019>.
- Kim, Jinseop S., Matthew J. Greene, Aleksandar Zlateski, Kisuk Lee, Mark Richardson, Srinivas C. Turaga, Michael Purcaro, et al. 2014. "Space-Time Wiring Specificity Supports Direction Selectivity in the Retina." *Nature* 509 (7500): 331–36.
- Kornfeld, Jörgen, Sam E. Benezra, Rajeevan T. Narayanan, Fabian Svava, Robert Egger, Marcel Oberlaender, Winfried Denk, and Michael A. Long. 2017. "EM Connectomics Reveals Axonal Target Variation in a Sequence-Generating Network." *eLife* 6 (March). <https://doi.org/10.7554/eLife.24364>.
- Kornfeld, Jörgen, and Winfried Denk. 2018. "Progress and Remaining Challenges in High-Throughput Volume Electron Microscopy." *Current Opinion in Neurobiology* 50 (June): 261–67.
- Kreshuk, Anna, Jan Funke, Albert Cardona, and Fred A. Hamprecht. 2015. "Who Is Talking to Whom: Synaptic Partner Detection in Anisotropic Volumes of Insect Brain." In *Medical Image Computing and Computer-Assisted Intervention -- MICCAI 2015*, 661–68. Springer International Publishing.
- Lee, Kisuk, Jonathan Zung, Peter Li, Viren Jain, and H. Sebastian Seung. 2017. "Superhuman Accuracy on the SNEMI3D Connectomics Challenge." *arXiv [cs.CV]*. arXiv. <http://arxiv.org/abs/1706.00120>.
- Lee, Wei-Chung Allen, Vincent Bonin, Michael Reed, Brett J. Graham, Greg Hood, Katie Glattfelder, and R. Clay Reid. 2016. "Anatomy and Function of an Excitatory Network in the Visual Cortex." *Nature* 532 (7599): 370–74.
- Lewis, J. P. 1995. "Fast Template Matching." *Vision Interface* 95 (May). <http://dx.doi.org/>.
- Ohyama, Tomoko, Casey M. Schneider-Mizell, Richard D. Fetter, Javier Valdes Aleman, Romain Franconville, Marta Rivera-Alba, Brett D. Mensh, et al. 2015. "A Multilevel Multimodal Circuit Enhances Action Selection in *Drosophila*." *Nature* 520 (7549): 633–39.
- Rangamani, Padmini, Miriam Bell, Andrea Cugno, Donya Ohadi, Thomas M. Bartol, Ravi Iyengar, and Terrence J. Sejnowski. 2019. "Dendritic Spine Geometry and Ultrastructure Dictate the Spatiotemporal Dynamics of Second Messengers." *Biophysical Journal*. <https://doi.org/10.1016/j.bpj.2018.11.1651>.
- Saalfeld, Stephan, Albert Cardona, Volker Hartenstein, and Pavel Tomancak. 2009. "CATMAID: Collaborative Annotation Toolkit for Massive Amounts of Image Data." *Bioinformatics* 25 (15): 1984–86.
- Saalfeld, Stephan, Richard Fetter, Albert Cardona, and Pavel Tomancak. 2012. "Elastic Volume Reconstruction from Series of Ultra-Thin Microscopy Sections." *Nature Methods* 9 (7): 717–20.

- Sato, M., I. Bitter, M. A. Bender, A. E. Kaufman, and M. Nakajima. 2000. "TEASAR: Tree-Structure Extraction Algorithm for Accurate and Robust Skeletons." In *Proceedings the Eighth Pacific Conference on Computer Graphics and Applications*, 281–449. [ieeexplore.ieee.org](http://ieeexplore.ieee.org).
- Schmidt, Helene, Anjali Gour, Jakob Straehle, Kevin M. Boergens, Michael Brecht, and Moritz Helmstaedter. 2017. "Axonal Synapse Sorting in Medial Entorhinal Cortex." *Nature* 549 (7673): 469–75.
- Schneider-Mizell, Casey M., Stephan Gerhard, Mark Longair, Tom Kazimiers, Feng Li, Maarten F. Zwart, Andrew Champion, et al. 2016. "Quantitative Neuroanatomy for Connectomics in *Drosophila*." *eLife* 5 (March). <https://doi.org/10.7554/eLife.12059>.
- Shan Xu, C., Michal Januszewski, Zhiyuan Lu, Shin-Ya Takemura, Kenneth J. Hayworth, Gary Huang, Kazunori Shinomiya, et al. 2020. "A Connectome of the Adult *Drosophila* Central Brain." *bioRxiv*. <https://doi.org/10.1101/2020.01.21.911859>.
- Shepherd, Gordon M., and Sten Grillner. 2018. *Handbook of Brain Microcircuits*. Oxford University Press.
- Silversmith, Will. 2019. *Kimimaro*. Github. <https://github.com/seung-lab/kimimaro>.
- Sümbül, Uygur, Sen Song, Kyle McCulloch, Michael Becker, Bin Lin, Joshua R. Sanes, Richard H. Masland, and H. Sebastian Seung. 2014. "A Genetic and Computational Approach to Structurally Classify Neuronal Types." *Nature Communications* 5 (March): 3512.
- Takemura, Shin-Ya, Yoshinori Aso, Toshihide Hige, Allan Wong, Zhiyuan Lu, C. Shan Xu, Patricia K. Rivlin, et al. 2017. "A Connectome of a Learning and Memory Center in the Adult *Drosophila* Brain." *eLife* 6 (July). <https://doi.org/10.7554/eLife.26975>.
- Takemura, Shin-Ya, Arjun Bharioke, Zhiyuan Lu, Aljoscha Nern, Shiv Vitaladevuni, Patricia K. Rivlin, William T. Katz, et al. 2013. "A Visual Motion Detection Circuit Suggested by *Drosophila* Connectomics." *Nature* 500 (7461): 175–81.
- Takemura, Shin-Ya, Aljoscha Nern, Dmitri B. Chklovskii, Louis K. Scheffer, Gerald M. Rubin, and Ian A. Meinertzhagen. 2017. "The Comprehensive Connectome of a Neural Substrate for 'ON' Motion Detection in *Drosophila*." *eLife* 6 (April). <https://doi.org/10.7554/eLife.24394>.
- Takemura, Shin-Ya, C. Shan Xu, Zhiyuan Lu, Patricia K. Rivlin, Toufiq Parag, Donald J. Olbris, Stephen Plaza, et al. 2015. "Synaptic Circuits and Their Variations within Different Columns in the Visual System of *Drosophila*." *Proceedings of the National Academy of Sciences of the United States of America* 112 (44): 13711–16.
- Varshney, Lav R., Beth L. Chen, Eric Paniagua, David H. Hall, and Dmitri B. Chklovskii. 2011. "Structural Properties of the *Caenorhabditis Elegans* Neuronal Network." *PLoS Computational Biology* 7 (2): e1001066.
- Wanner, Adrian A., Christel Genoud, Tafheem Masudi, Léa Siksou, and Rainer W. Friedrich. 2016. "Dense EM-Based Reconstruction of the Interglomerular Projectome in the Zebrafish Olfactory Bulb." *Nature Neuroscience* 19 (6): 816–25.
- Wetzel, A. W., J. Bakal, M. Dittrich, D. G. C. Hildebrand, J. L. Morgan, and J. W. Lichtman. 2016. "Registering Large Volume Serial-Section Electron Microscopy Image Sets for Neural Circuit Reconstruction Using FFT Signal Whitening." In *2016 IEEE Applied Imagery Pattern Recognition Workshop (AIPR)*, 1–10.
- White, J. G., E. Southgate, J. N. Thomson, and S. Brenner. 1986. "The Structure of the Nervous System of the Nematode *Caenorhabditis Elegans*." *Philosophical Transactions of the Royal Society of London. Series B, Biological Sciences* 314 (1165): 1–340.
- Zhao, Ting, and Stephen M. Plaza. 2014. "Automatic Neuron Type Identification by Neurite Localization in the *Drosophila* Medulla." *arXiv [q-bio.NC]*. arXiv. <http://arxiv.org/abs/1409.1892>.

- Zheng, Zhihao, J. Scott Lauritzen, Eric Perlman, Camenzind G. Robinson, Matthew Nichols, Daniel Milkie, Omar Torrens, et al. 2018. "A Complete Electron Microscopy Volume of the Brain of Adult *Drosophila Melanogaster*." *Cell* 174 (3): 730–43.e22.
- Zheng, Zhihao, Feng Li, Corey Fisher, Iqbal J. Ali, Nadiya Sharifi, Steven Calle-Schuler, Joseph Hsu, et al. 2020. "Structured Sampling of Olfactory Input by the Fly Mushroom Body." *bioRxiv*. <https://doi.org/10.1101/2020.04.17.047167>.
- Zuiderveld, Karel. 1994. "Contrast Limited Adaptive Histogram Equalization." In *Graphics Gems IV*, edited by Paul S. Heckbert, 474–85. San Diego, CA, USA: Academic Press Professional, Inc.